

**Electrolyte Supply Methods in Anion Exchange Membrane Water Electrolysis  
Cells with Custom Inkjet Printed Catalyst Layers**

by

Jasper Eitzen

A thesis submitted in partial fulfillment of the requirements for the degree of

Master of Science

Department of Mechanical Engineering

**University of Alberta**

©Jasper Eitzen, 2023

# Abstract

This work was concerned with the construction and testing of anion exchange membrane water electrolysis (AEMWE) cells to study the effect of electrolyte feed method. Each cell used a catalyst-coated membrane (CCM) fabricated in-house by inkjet printing catalyst layers onto Aemion+ membranes using a Fujifilm Dimatix DMP-2831 printer. Inkjet printing allowed for precise control in the deposition of catalyst layer materials, but necessitated that printable inks containing catalyst nanopowder (platinum supported on carbon and iridium oxide) and ionomer (Aemion+ AP2-HNN5-00-X) be formulated. To develop ink formulae, a procedure was followed that began by selecting a base of propylene glycol and isopropanol with a dynamic viscosity and surface tension close to that required for printing. The ionomer solution was then added, and the mixture was re-characterized to ensure it still had the required rheology. Any necessary adjustments were made and the catalyst powder was finally added. This process resulted in inks that were successfully printed without the need to produce multiple complete inks, reducing the waste of expensive catalyst and ionomer.

Initial in-situ AEMWE cell tests were run to ensure that cell performance was repeatable. Five cells were tested, achieving this goal as the last four all performed similarly. Cell construction was altered between some of these cells, most notably the type of Aemion+ membrane was changed, i.e., increasing the thickness from 50 to 75  $\mu\text{m}$  and altering the reinforcement type, the cathode porous transport layer (PTL) was changed from carbon to nickel, and the bipolar plate material was changed from titanium to nickel 400 alloy. These changes slightly improved cell performance by reducing the ohmic losses caused by resistance within the cells. Cells were tested by feeding 1 M potassium hydroxide (KOH) and compared to literature. The performance of the cells was similar to state of the art CCM cells using

Aemion+, achieving a current density of 900 mA/cm<sup>2</sup> at 2 V. Once good, repeatable cell performance was achieved, the same cell construction was used for the study on electrolyte feed method.

Four cells were used to study the effect of feeding aqueous 1 M potassium hydroxide solution to both electrodes, just the cathode, and just the anode was done for the first time in AEMWE cells. A reference electrode was also connected to the cell membrane using a strip of membrane passed out the side of the cell. Challenges were encountered with the experimental setup that resulted in some inconsistent measurements from the reference electrode, caused by cell operation. Despite this, it did allow for separate anode and cathode overpotentials to be measured. The cells tested in this work performed similarly with two-electrode and anode-only feed, resulting in 900 mA/cm<sup>2</sup> at 2 V, whereas cathode-only feed achieve the lower 550 mA/cm<sup>2</sup> at 2 V. Six hour constant-current stability tests also resulted in increased degradation for cathode-only feed. The change was due to poor anode performance, as the separate electrode potentials obtained using the reference electrode showed an increase in anode overpotential in this feed configuration. The lack of electrolyte in the anode catalyst layer possibly resulted in increased ionic resistance as the electrolyte normally supports this, or a loss of reactant hydroxide that would normally be supplied by the electrolyte.

**Keywords:** anion exchange membrane water electrolysis, inkjet printing, ink development, printed catalyst layers, repeatability, nickel 400, reference electrode, cell feed method

# Acknowledgements

Thank you to my supervisor, Marc Secanell for your guidance and support throughout my project, my colleges in the Energy Systems Design Lab for all the assistance they provided me, and to Future Energy Systems for funding this project. Thank you to my defence committee, Natalia Semagina, Mohtada Sadrzadeh, and committee chair Tim Weis, as well.

I would additionally like to thank my colleges Scott Storbaken, Jiafei Lui, Manas Mandal, Eric Beaulieu, Luis Padilla, Wei Fei, and Aslan Kosakian for your direct assistance with my work, whether it was teaching me how to use equipment in the lab, how to run experiments and analyse the results, or the discussions we had related to the results and conclusions of my work. Specifically, thank you to Scott Storkbakken for building the anion exchange membrane water electrolyzer test setup, teaching me how to use it, and for showing me all the steps necessary for building and testing electrolysis cells, and Jiafei Liu for the anion exchange membrane strip test data used in Figure 2.14 of this work.

Most importantly, thank you to my parents. Without your support, encouragement, and assistance I would not have been able to complete this project.

# Table of Contents

<b>1</b>	<b>Introduction</b>	<b>1</b>
1.1	Background & Motivation . . . . .	1
1.1.1	Anion Exchange Membrane Water Electrolysis . . . . .	3
1.1.2	Electrolysis Cell Characterization . . . . .	5
1.2	Literature Review . . . . .	7
1.2.1	Anion Exchange Membrane Catalyst Layer Fabrication . . . . .	7
1.2.2	In-situ Cell Component Materials and Operational Methods . . . . .	9
1.2.3	In-situ Cell Characterization Methods . . . . .	12
1.2.4	Integration of a Reference Electrode into an In-situ Electrochemical Cell	13
1.3	Objectives . . . . .	15
<b>2</b>	<b>Experimental Methodology</b>	<b>16</b>
2.1	Ink Formulation Process . . . . .	16
2.2	Ink Characterization . . . . .	20
2.2.1	Density Characterization . . . . .	20
2.2.2	Dynamic Viscosity Characterization . . . . .	21
2.2.3	Surface Tension Characterization . . . . .	24
2.2.4	Particle Size Measurement . . . . .	28
2.3	Inkjet Printing Catalyst Coated Membranes . . . . .	30
2.4	Electrolysis Cell Configuration . . . . .	33
2.4.1	Cell Construction . . . . .	33
2.4.2	Test Station Equipment . . . . .	34
2.4.3	Electrode Feed Method Testing . . . . .	36
2.4.4	Reference Electrode Integration . . . . .	37
2.5	Electrolysis Cell Characterization . . . . .	42
2.5.1	Cell Conditioning . . . . .	42
2.5.2	Polarization Curves . . . . .	46
2.5.3	Electrochemical Impedance Spectroscopy . . . . .	48
2.5.4	Cell Stability Testing . . . . .	51

<b>3</b>	<b>Results and Discussion</b>	<b>52</b>
3.1	Ink Development and Catalyst Layer Fabrication . . . . .	52
3.1.1	Propylene Glycol & Isopropyl Alcohol Mixtures . . . . .	53
3.1.2	Iridium Oxide Ink Development & Characterization . . . . .	54
3.1.3	Iridium Oxide Ink Printing . . . . .	57
3.1.4	Platinum-Carbon Ink Development & Characterization . . . . .	60
3.1.5	Platinum-Carbon Ink Printing . . . . .	61
3.1.6	Summary of the Ink Development Process . . . . .	63
3.2	In-situ Electrolysis Cell Characterization . . . . .	65
3.2.1	Obtaining Repeatable In-situ Cell Results using Aemion+ Membranes and Ionomer . . . . .	65
3.2.2	Reference Electrode Integration . . . . .	78
3.2.3	Cell Feed Method Study . . . . .	87
3.2.4	Summary of AEMWE Cell Testing . . . . .	97
<b>4</b>	<b>Conclusions and Future Work</b>	<b>101</b>
4.1	Conclusions . . . . .	101
4.2	Future Work . . . . .	103
	<b>References</b>	<b>105</b>
<b>A</b>	<b>Equipment Information</b>	<b>115</b>
A.1	Cannon Instrument Company Zeitfuchs Cross-Arm Viscometer Certificate of Calibration . . . . .	116
A.2	Pine Research Ag/AgCl Reference Electrode . . . . .	117
A.3	Metal Print Guide Solidworks Drawing . . . . .	119
A.4	Nickel 400 Bipolar Plate Solidworks Drawings . . . . .	120
<b>B</b>	<b>Measurement Error and Confidence Interval Calculations</b>	<b>122</b>
B.1	Density Measurement Uncertainty . . . . .	124
B.2	Dynamic Viscosity Measurement Uncertainty . . . . .	124
B.3	Surface Tension Measurement Uncertainty . . . . .	124
B.4	HFR Uncertainty . . . . .	125
<b>C</b>	<b>Altered Test Profiles for Cells Operating Under Cathode-Only Feed</b>	<b>126</b>
<b>D</b>	<b>Additional Equations used in this Work</b>	<b>129</b>
D.1	Conversion of Ink Recipes from a Weight Percent Basis to a Mass Basis . . .	129

D.2	Calculation of the Mass of Solid Potassium Hydroxide needed to make an Aqueous 1 M Solution . . . . .	131
<b>E</b>	<b>Additional Experimental Results</b>	<b>132</b>
E.1	Cell Voltage and Current During Conditioning . . . . .	132
E.2	Individual Viscosity Measurements for Ink Development Solutions . . . . .	137
E.3	Individual Polarization Curve Results . . . . .	138
E.4	Polarization Curve Voltage over Time Plots . . . . .	144
E.5	Individual HFR Measurements - measured between anode and cathode . . .	151
E.6	Individual HFR Measurements - measured between one electrode and reference electrode . . . . .	155
E.7	Polarization Curve Step Time Test . . . . .	158
E.8	Stability Tests with the Reference Electrode . . . . .	159
E.9	Cell Component Resistance Measurements . . . . .	163
E.10	Electrochemically Active Surface Area Measurements . . . . .	164

# List of Tables

1.1	Literature sources testing in-situ AEMWE cells with non-PGM components.	11
1.2	AEMWE cell performance in literature with water and alkaline electrolyte feed.	12
1.3	Reference electrode integration methods used for in-situ electrochemical cells in literature. . . . .	14
2.1	Overview of the testing order used for the cells in this work. . . . .	42
2.2	Galvanostatic profile used for cell conditioning. . . . .	45
2.3	Short conditioning profile used to displace air from the GDUs. . . . .	45
2.4	Galvanostatic profile used to obtain polarization curves. For curves run forward and backward, backward steps are denoted in parenthesis beside their forward counterparts. . . . .	47
2.5	Galvanostatic EIS profiles used following each polarization curve and stability test run on repeatability testing AEMWE cells. . . . .	49
2.6	Galvanostatic EIS profiles used following each polarization curve and stability test run on feed method testing AEMWE cells. . . . .	49
3.1	Properties of the Aemion ionomers and membranes used in this work. Information obtained from Ionomr Innovations. . . . .	52
3.2	IrO <sub>x</sub> ink recipe in both a weight % and a mass basis. . . . .	56
3.3	Catalyst loading data collected during two prints of the AP2 IrO <sub>x</sub> ink formulation to loadings of 1.0 mg/cm <sup>2</sup> . . . . .	58
3.4	Pt/C ink recipe in both a weight % and a mass basis. . . . .	61
3.5	Catalyst loading data collected during two prints of the AP2 Pt/C ink to loadings of 0.2 mg/cm <sup>2</sup> and 0.1 mg/cm <sup>2</sup> . . . . .	63
3.6	Comparison of construction and operational parameters used for the cells tested in this work to obtain repeatability. . . . .	67
3.7	HFR values obtained using equivalent circuit fits with the EIS measurements made on Cell 5. . . . .	70

3.8	Average HFR values obtained for Cells 2 to 5 following each polarization curve and stability test. Values averaged across all measured current densities. Errors represent a 95% confidence interval. . . . .	72
3.9	CCM resistance for the repeatability cells calculated as the difference of the average HFR and component resistance (resistance of the bipolar plates and PTLs) of each. . . . .	72
3.10	Comparison of construction and operational parameters used for Cell 5 and cells from literature used for comparison. . . . .	75
3.11	Comparison of construction and operational parameters used for the cells in this work tested using a reference electrode and different feed methods along with the literature source used for reference electrode comparison. . . . .	80
3.12	Average HFR measurements made on Cells 6, 7, and 8 between the anode and cathode compared to the average measurements between the anode/cathode and reference electrode. . . . .	86
3.13	Total cell HFR values obtained using equivalent circuit fits with the EIS measurements made on cell 6. . . . .	90
3.14	Average total cell HFR values measured on the feed method cells following each polarization curve and stability test for all tested feed methods. Errors represent a 95% confidence interval. . . . .	91
B.1	Table of Student's <i>t</i> -values . . . . .	123
C.1	Galvanostatic profile used to obtain polarization curves under cathode-only feed. For curves run forward and backward, backward steps are denoted in parenthesis beside their forward counterparts. . . . .	127
C.2	Galvanostatic EIS profiles used following each polarization curve and stability test run on the studied AEMWE cells when operating in Cathode-only feed. . . . .	128
D.1	Ink formulae definitions. . . . .	130
D.2	Definitions for the variables used to convert ink recipes from a weight percent basis to a mass basis. . . . .	130
E.1	Individual, consecutive measurements of dynamic viscosity made during ink development. . . . .	137
E.2	HFR values obtained using equivalent circuit fits with the EIS measurements made on cell 2. . . . .	151
E.3	HFR values obtained using equivalent circuit fits with the EIS measurements made on cell 3. . . . .	151

E.4	HFR values obtained using equivalent circuit fits with the EIS measurements made on cell 4. . . . .	151
E.5	Total cell HFR values obtained using equivalent circuit fits with the EIS measurements made on cell 7. . . . .	152
E.6	Total cell HFR values obtained using equivalent circuit fits with the EIS measurements made on cell 8. . . . .	153
E.7	Total cell HFR values obtained using equivalent circuit fits with the EIS measurements made on cell 9. . . . .	154
E.8	Separate anode and cathode HFR values obtained using equivalent circuit fits with the EIS measurements made on Cell 6. . . . .	155
E.9	Separate anode and cathode HFR values obtained using equivalent circuit fits with the EIS measurements made on Cell 7. . . . .	156
E.10	Separate anode and cathode HFR values obtained using equivalent circuit fits with the EIS measurements made on Cell 8. . . . .	157
E.11	Test profile used to characterize the drift in OCV on Cell 9. . . . .	162
E.12	ECSA values calculated for the feed method cells using cyclic voltammetry measurements. . . . .	164

# List of Figures

1.1	Diagram of an AEMWE cell layout. . . . .	4
1.2	Diagram of a polarization curve with the major types of losses separated and labelled. . . . .	6
1.3	Box and whisker plot comparing AEMWE cell performance in literature using CCM and CCS catalyst layer fabrication methods, reproduced from Miller et al. . . . .	9
2.1	Flowchart of the ink formula development process. . . . .	19
2.2	Test setup used to measure kinematic viscosity at a controlled temperature using a Zeitfuchs cross-arm glass capillary viscometer. . . . .	22
2.3	Balance of surface tension and gravitational forces for a droplet hanging at the end of a capillary. . . . .	25
2.4	Experimental setup used to measure fluid surface tension by the drop weight method. . . . .	27
2.5	Example outputs from the Kalliope software when analysing DLS measurements. . . . .	30
2.6	Pictures of the Fujifilm Dimatix inkjet printer and associated cartridges used in this work. . . . .	31
2.7	Metal print guide used to hold Aemion+ membranes in place while printing. Shown here with completed CCMs. . . . .	32
2.8	Pourbaix diagrams showing the stable phases for titanium and graphite at varied potentials and pH values. . . . .	34
2.9	Exploded view of the AEMWE cell components. . . . .	35
2.10	Diagram of the connections made between a tested AEMWE cell and the test station equipment, including both the electrolyte feed system and potentiostat. . . . .	36
2.11	Diagram of a standard 3-electrode electrochemical system. . . . .	38
2.12	Exploded view of the AEMWE cell components with an integrated reference electrode. . . . .	40
2.13	Picture of an AEMWE cell assembled with the reference electrode and connected to the AEMWE cell test station. . . . .	41

2.14	Potential measured between two Ag/AgCl reference electrodes in saturated KCl solutions connected by a strip of AEM. a) AEM exposed to atmosphere. b) AEM covered with KCl soaked lab wipes. c) AEM laminated. . . . .	43
2.15	Lamination sheet layout used to hold in place and keep hydrated the membrane strip that connected to the reference electrode. Lamination sheets were only laminated to the left of the red dashed line and cutouts were made along the green lines. . . . .	44
2.16	Conditioning process for Cell 6. Current was applied based on the profile in Table 2.2, and the cell voltage was measured. . . . .	46
2.17	Example Nyquist plot with regions of interest representing kinetic, ohmic, and mass transport losses labeled. Based on O’Hayre et al. [66]. . . . .	50
2.18	Equivalent circuit layout used to fit data obtained by EIS measurements between the anode and cathode in this work using resistors (R), CPEs (Q), and inductors (L). . . . .	50
2.19	Equivalent circuit layout used to fit data obtained by EIS measurement between one cell electrode and the reference electrode in this work using resistors (R), CPEs (Q), and inductors (L). . . . .	51
3.1	Densities of the characterized PG:IPA mixtures. Error bars represent a 95% confidence interval. . . . .	54
3.2	Dynamic viscosities of the characterized PG:IPA mixtures. Error bars represent a 95% confidence interval. . . . .	55
3.3	Surface tensions of the characterized PG:IPA mixtures. Error bars represent a 95% confidence interval. . . . .	55
3.4	Dynamic viscosities of the characterized IrO <sub>x</sub> no-catalyst ink solutions compared with the PG:IPA mixtures. Error bars represent a 95% confidence interval. . . . .	56
3.5	Intensity-weighted particle distribution obtained by DLS for the IrO <sub>x</sub> ink. . .	57
3.6	Images taken of the IrO <sub>x</sub> catalyst layers printed using the ink developed in this work at 10 times zoom. . . . .	59
3.7	Images taken of a bare Aemion+ AF2-HWP8-75-X membrane at 10 times zoom. The pattern of the reinforcement layer is visible on both sides, but is more prominent on the rougher anode side. . . . .	59
3.8	Dynamic viscosities of the characterized Pt/C ink solutions compared with the PG:IPA mixtures. Error bars represent a 95% confidence interval. . . .	61
3.9	Intensity-weighted particle distribution obtained by DLS for the Pt/C ink. .	62

3.10	Images taken of the Pt/C catalyst layers printed using the ink developed in this section at 10 times zoom. . . . .	64
3.11	(a) Poor polarization curve results obtained from Cell 1 compared with the results for Cell 2, (b) and the resulting damaged carbon paper PTL. . . . .	68
3.12	Polarization curves measured on Cell 5. Backward curves plotted with dashed lines. . . . .	68
3.13	Average polarization curves run on Cells 2 through 5. Error bars represent the minimum and maximum individual polarization curves from each cell. Backward curves plotted with dashed lines and no error bars, iR-free curves plotted with thinner, partly transparent lines. . . . .	70
3.14	Results of the EIS measurements made on cell 5 following polarization curve 1 with equivalent circuit fits plotted as lines. (a) Nyquist plot of all 3 measurements. (b) Nyquist plot zoomed in to show the details of the 300 and 600 mA/cm <sup>2</sup> measurements. (c) -Im(Z) versus log(frequency) plot of all 3 measurements. . . . .	71
3.15	Stability test results for Cells 2 through 5. Each test was run for 6 hours at a constant cell potential of 1.8 V. . . . .	74
3.16	Box and whisker plot comparing AEMWE cell performance in literature, adapted from Miller et al., with the performance obtained for Cell 5 from this work included. . . . .	74
3.17	Comparison of the performance achieved by Cell 5 and literature sources that also used Aemion membranes and ionomer. iR-free curves provided for Cell 5, Koch et al., and Fortin et al. data with thinner, partly transparent lines. (a) polarization curves with standard area-normalized current densities. (b) polarization curves with current densities normalized by the sum of IrO <sub>x</sub> and Pt loading. . . . .	77
3.18	Average polarization curves measured on the feed method cells. Both electrodes fed with 1 M KOH solution. Error bars represent the minimum and maximum individual polarization curves from each cell. Backward curves plotted with dashed lines and no error bars. (a) Total cell overpotential. (b) Separated electrode overpotentials. . . . .	81
3.19	Plots of the separated electrode overpotential versus time during the two TEF polarization curves (denoted “Curve 1” and “Curve 2”) run on (a) Cell 6, (b) Cell 7, and (c) Cell 8 (forward sweeps). . . . .	84
3.20	Comparison of the separated polarization curves measured on the feed method cells with both electrodes fed to the results from Xu et al. . . . .	85

3.21	Average polarization curves across cells 6 to 8 for each of the feed methods tested. Error bars represent the minimum and maximum individual polarization curves from these cells. Backwards curves plotted as dashed lines without error bars, iR-free curves plotted with thinner, partly transparent lines. . . .	89
3.22	Average polarization curves across Cells 6, 8, & 9 of the separated electrode overpotentials for TEF and COF. Error bars represent the minimum and maximum individual polarization curves from these cells. Backwards curves plotted as dashed lines without error bars. . . . .	91
3.23	Results of the EIS measurements made on cell 6 following TEF polarization curve 1 with equivalent circuit fits plotted as lines. (a) Nyquist plot of all 5 measurements. (b) Nyquist plot zoomed in to show the details of the higher current density measurements. (c) $-\text{Im}(Z)$ versus $\log(\text{frequency})$ plot of all 5 measurements. . . . .	92
3.24	Six hour stability tests run on feed method cells at a constant $300 \text{ mA/cm}^2$ . Tests were performed in the order of the legend. . . . .	94
3.25	6 hour stability tests run on Cell 8 at a constant $1000 \text{ mA/cm}^2$ . Tests were run in the electrode-feed order of TEF, AOF, COF. . . . .	95
3.26	Test of five current density levels on Cell 9, each held for one hour under TEF and AOF. . . . .	96
3.27	Polarization curves from test cells used to determine if the order of the feed method tests had a large effect. Test 1 was run AOF first, then COF, and test 2 was run in the opposite order. Error bars represent the minimum and maximum individual polarization curves from each cell. Backward sweeps plotted as dashed lines without error bars. . . . .	96
E.1	Conditioning process for Cell 1. Current was applied and the cell voltage was measured. This cell was tested before the final conditioning profile was decided.	133
E.2	Conditioning process for Cell 2. Current was applied and the cell voltage was measured. This cell was tested before the final conditioning profile was decided.	133
E.3	Conditioning process for Cell 3. Current was applied based on the profile in Table 2.2, and the cell voltage was measured . . . . .	134
E.4	Conditioning process for Cell 4. Current was applied based on the profile in Table 2.2, and the cell voltage was measured . . . . .	134
E.5	Conditioning process for Cell 5. Current was applied based on the profile in Table 2.2, and the cell voltage was measured . . . . .	135
E.6	Conditioning process for Cell 7. Current was applied based on the profile in Table 2.2, and the cell voltage was measured. . . . .	135

E.7	Conditioning process for Cell 8. Current was applied based on the profile in Table 2.2, and the cell voltage was measured. . . . .	136
E.8	Conditioning process for Cell 9. Current was applied based on the profile in Table 2.2, and the cell voltage was measured. . . . .	136
E.9	Polarization curves measured on Cell 2. . . . .	138
E.10	Polarization curves measured on Cell 3. Backward curves plotted with dashed lines. . . . .	139
E.11	Polarization curves measured on Cell 4. Backward curves plotted with dashed lines. . . . .	139
E.12	Polarization curves measured on Cell 6 with all electrode feed configurations. Backward curves plotted with dashed lines. . . . .	140
E.13	Polarization curves of the separate anode and cathode overpotentials measured on Cell 6 with TEF and COF configurations. Backward curves plotted with dashed lines. . . . .	140
E.14	Polarization curves measured on Cell 7 with all electrode feed configurations. Backward curves plotted with dashed lines. . . . .	141
E.15	Polarization curves measured on Cell 8 with all electrode feed configurations. Backward curves plotted with dashed lines. . . . .	141
E.16	Polarization curves of the separate anode and cathode overpotentials measured on Cell 8 with TEF and COF configurations. Backward curves plotted with dashed lines. . . . .	142
E.17	Polarization curves measured on Cell 9 with TEF and COF configurations. Backward curves plotted with dashed lines. . . . .	142
E.18	Polarization curves of the separate anode and cathode overpotentials measured on Cell 9 with TEF and COF configurations. Backward curves plotted with dashed lines. . . . .	143
E.19	Plot of the voltage versus time during the two TEF polarization curves (denoted “Curve 1” and “Curve 2”) run on Cell 6 (forward sweep). . . . .	144
E.20	Plot of the voltage versus time during the two TEF polarization curves (denoted “Curve 1” and “Curve 2”) run on Cell 6 (backward sweep). . . . .	145
E.21	Plot of the separated electrode overpotential versus time during the two TEF polarization curves (denoted “Curve 1” and “Curve 2”) run on Cell 6 (backward sweep). . . . .	145
E.22	Plot of the voltage versus time during the two TEF polarization curves (denoted “Curve 1” and “Curve 2”) run on Cell 7 (forward sweep). . . . .	146
E.23	Plot of the voltage versus time during the two TEF polarization curves (denoted “Curve 1” and “Curve 2”) run on Cell 7 (backward sweep). . . . .	146

E.24 Plot of the separated electrode overpotential versus time during the two TEF polarization curves (denoted “Curve 1” and “Curve 2”) run on Cell 7 (backward sweep). . . . .	147
E.25 Plot of the voltage versus time during the two TEF polarization curves (denoted “Curve 1” and “Curve 2”) run on Cell 8 (forward sweep). . . . .	147
E.26 Plot of the voltage versus time during the two TEF polarization curves (denoted “Curve 1” and “Curve 2”) run on Cell 8 (backward sweep). . . . .	148
E.27 Plot of the separated electrode overpotential versus time during the two TEF polarization curves (denoted “Curve 1” and “Curve 2”) run on Cell 8 (backward sweep). . . . .	148
E.28 Plot of the voltage versus time during the two TEF polarization curves (denoted “Curve 1” and “Curve 2”) run on Cell 9 (forward sweep). . . . .	149
E.29 Plot of the voltage versus time during the two TEF polarization curves (denoted “Curve 1” and “Curve 2”) run on Cell 9 (backward sweep). . . . .	149
E.30 Plot of the separated electrode overpotential versus time during the two TEF polarization curves (denoted “Curve 1” and “Curve 2”) run on Cell 9 (forward sweep). . . . .	150
E.31 Plot of the separated electrode overpotential versus time during the two TEF polarization curves (denoted “Curve 1” and “Curve 2”) run on Cell 9 (backward sweep). . . . .	150
E.32 Comparison between the results of 90 and 120 second polarization curve step lengths on the same cell. . . . .	158
E.33 Stability test results for the feed method cells with electrolyte feed to both electrodes. Tests were run at a constant 300 mA/cm <sup>2</sup> for 6 hours. (a) Total cell potential. (b) Separated electrode overpotentials. . . . .	160
E.34 Change in the average voltage measured on Cell 9 for the 10 mA/cm <sup>2</sup> current holds for the OCV drift test following the profile in Table E.11. . . . .	161
E.35 Cell component resistance tests performed by assembling cells without a CCM and applying a series of current holds. . . . .	163
E.36 Cyclic voltammetry measurements run on Cell 6 before and after characterization. . . . .	164
E.37 Cyclic voltammetry measurements run on Cell 7 before and after characterization. . . . .	165
E.38 Cyclic voltammetry measurements run on Cell 8 before and after characterization. . . . .	165

# Abbreviations

**AC** alternating current.

**AEM** anion exchange membrane.

**AEMWE** anion exchange membrane water electrolysis.

**AOF** anode-only feed.

**CCM** catalyst-coated membrane.

**CCS** catalyst-coated substrate.

**COF** cathode-only feed.

**CPE** constant phase element.

**DC** direct current.

**DLS** dynamic light scattering.

**ECSA** electrochemically active surface area.

**EIS** electrochemical impedance spectroscopy.

**ESDLab** Energy System Design Lab.

**GDU** gas disengagement unit.

**HER** hydrogen evolution reaction.

**HFR** high frequency resistance.

**IEC** ion exchange capacity.

**IPA** isopropyl alcohol.

**LSV** linear sweep voltammetry.

**NHE** normal hydrogen electrode.

**OCV** open circuit voltage.

**OER** oxygen evolution reaction.

**PEM** proton exchange membrane.

**PEMWE** proton exchange membrane water electrolysis.

**PG** propylene glycol.

**PGM** platinum-group metal.

**PTL** porous transport layer.

**RHE** reversible hydrogen electrode.

**SEM** scanning electron microscopy.

**SHE** standard hydrogen electrode.

**SOEC** solid oxide electrolyzer cell.

**TEF** two-electrode feed.

# Nomenclature

$C$  Capacitance.

$C_T$  Tate's law correction factor.

$C_v$  Zeitfuchs cross-arm viscometer calibration constant.

$D$  Diffusion coefficient.

$E$  Voltage/electrical potential.

$F$  Faraday constant.

$I$  Intensity of scattered light.

$L$  Inductance.

$R$  Resistance.

$R_g$  Ideal gas constant.

$R_h$  Hydrodynamic radius.

$T$  temperature.

$V$  Volume.

$Z$  Impedance.

$\Gamma$  Decay rate.

$\eta$  Overpotential.

$\gamma$  Surface tension.

$\lambda_0$  Laser wavelength.

$\mu$  Dynamic viscosity.

$\nu$  Kinematic viscosity.

$\omega$  Radial frequency.

$\phi$  Phase shift.

$\rho$  Density.

$\tau$  Correlation/delay time.

$\theta$  Light scattering angle.

$a$  Activity.

$i$  Current.

$j$  Square root of  $-1$ .

$k_B$  Boltzmann's constant.

$m$  Mass.

$n$  Refractive index.

$r$  Radius.

$s^0$  Standard entropy.

$t$  Time.

$v$  Number of moles normalized per mole reactant.

**CO<sub>2</sub>** Carbon dioxide.

**H<sup>+</sup>** Proton or hydrogen cation.

**H<sub>2</sub>O** Water.

**H<sub>2</sub>** Hydrogen.

**IrO<sub>x</sub>** Iridium oxide.

**Ir** Iridium.

**K<sub>2</sub>CO<sub>3</sub>** Potassium carbonate.

**KCl** Potassium chloride.

**KOH** Potassium hydroxide.

**LiOH** Lithium hydroxide.

**NaOH** Sodium hydroxide.

**O<sub>2</sub>** Oxygen.

**OH<sup>-</sup>** Hydroxide anion.

**Pt/C** Platinum supported on carbon.

**Pt** Platinum.

# Chapter 1

## Introduction

### 1.1 Background & Motivation

Hydrogen is an extremely useful molecule, both as a chemical feedstock and as an energy storage mechanism that has the potential to solve issues of storing energy produced by intermittent renewable sources such as wind and solar [1]. Most hydrogen produced today is used in industry for fertilizer production, metallurgy, electronics fabrication, hydrogenating fats and oils, and even filling weather balloons [2]. Currently however, most hydrogen is mass-produced through reforming of fossil fuels, which also produces carbon dioxide ( $\text{CO}_2$ ) as a bi-product [3]. The splitting of water to produce hydrogen, or water electrolysis, has the potential to produce hydrogen using just electricity and water and, if this electricity is provided by renewable sources, there are zero  $\text{CO}_2$  emissions. Utilizing water electrolysis in the production of hydrogen has the potential to reduce  $\text{CO}_2$  emissions in many industries, and facilitate the long-term storage of renewable energy, as stored hydrogen can efficiently be converted back to electricity through the use of fuel cells [4, 5]. Current water electrolysis technologies, however, are prohibitively expensive, especially in the capital costs required to build the cells, and so reducing the cost of materials and improving electrolysis cell lifetime is the main target for commercialization [3].

Water electrolysis has been used for over a century to produce high-purity hydrogen gas, with liquid alkaline water electrolysis being the first method used [6]. This process utilizes an electrochemical cell with the anode and cathode submerged in an aqueous alkaline solution and separated by a diaphragm that allows for the transport of hydroxide anions ( $\text{OH}^-$ ) across it. Water is split when a voltage greater than  $1.229\text{ V}$  is applied across the cell, with the hydrogen evolution reaction (HER) occurring at the cathode side, and the oxygen evolution reaction (OER) occurring at the anode side [7]. These systems are relatively simple to build, and are still used today as they can utilize relatively inexpensive metal catalysts, such as nickel and iron, at the electrodes and have a long lifetime [5, 8]. The disadvantages

of liquid alkaline electrolysis include the use of a highly alkaline electrolyte solution, and a high crossover of the produced gases from one electrode to the other, which will either react to form water again, lowering efficiency, or result in a mixing of hydrogen and oxygen gases, resulting in an explosion hazard. This crossover manifests as the electrodes must be positioned close together to reduce the distance needed for  $\text{OH}^-$  ions to travel due to their poor mobility, and so separating the electrodes also lowers the efficiency of the system [8].

In the time since the invention of liquid alkaline water electrolysis cells, proton exchange membrane water electrolysis (PEMWE) and solid oxide electrolyzer cell (SOEC) technologies have been developed to overcome some of the drawbacks of liquid alkaline electrolysis [9]. PEMWE improves the liquid alkaline system by replacing the caustic liquid electrolyte with a proton conducting polymer membrane, usually a material called Nafion, which conducts hydrogen cations ( $\text{H}^+$ ) from anode to cathode, completing the electrolysis reaction and creating an acidic cell environment. The use of a solid polymer electrolyte has the benefits of eliminating the liquid electrolyte, creating a more compact cell layout with reduced crossover, and increasing overall efficiency since the thin membrane reduces ohmic losses [8–10]. PEMWE cells can also be operated with a pressure differential across the membrane, allowing for the produced hydrogen gas at the cathode to be electrochemically compressed while the reactant water can be fed to the anode side at atmospheric pressure [9]. The drawbacks of these cells include the use of expensive materials such as platinum-group metal (PGM) catalysts, and platinum-coated titanium porous transport layer (PTL)s and bipolar plates due to the acidic environment and high cell potential, as well as a lower lifetime compared to liquid alkaline cells [9, 10].

Both liquid alkaline and PEM water electrolysis are examples of low-temperature electrolysis, as they operate between room temperature and  $100^\circ\text{C}$ , whereas SOEC technology operates between  $800$  and  $1000^\circ\text{C}$ . A SOEC, as its name implies, utilizes a solid oxide electrolyte, usually yttria-stabilized zirconia. Instead of conducting hydroxide or hydrogen ions, oxygen anions are conducted through the solid electrolyte, which is only conductive at high temperatures, resulting in the major difference in these types of cells [11]. SOECs do not require expensive PGM catalysts, as the high temperatures improve reaction kinetics, and cells can be operated under high pressures. There are some significant disadvantages for SOECs, however, aside from the additional complexity of providing the heat necessary to reach operating temperatures. SOECs suffer from poor long-term cell durability and other complications due to the brittle ceramics used in construction, and material choice is limited at the operating temperatures [9, 11].

In the past decades, durable, high-ionic conductivity hydroxide ( $\text{OH}^-$ ) conducting polymers have been developed, such as Aemion and PiperION [12, 13], opening the door to a new electrolyzer technology that combines the benefits of liquid alkaline electrolysis, such as

the possibility to use abundant and cost-effective catalysts and materials, with the use of a thin, low gas crossover membrane, similar to that used in PEMWE cells. This technology is called anion exchange membrane water electrolysis (AEMWE). The aim of this work is to study the suitability of this novel technology.

### 1.1.1 Anion Exchange Membrane Water Electrolysis

At a fundamental level, an AEMWE single-cell consists of two electrodes where the gas evolution reactions take place separated by an anion-conducting polymer membrane. When power is supplied to the electrodes, electrons flow from anode to cathode, resulting in the HER progressing at the cathode and the OER progressing at the anode. Figure 1.1 provides a diagram outlining the major components of an AEMWE cell, and the half-reactions that occur at the electrodes. At the center of the cell is the AEM that conducts  $\text{OH}^-$  ions from cathode to anode, completing the electrical circuit and allowing for the electrolysis reaction to progress. The reactions themselves occur in the catalyst layers, made of a composite material that catalyses the reaction, conducts electricity and ions, and is porous to increase catalyst active area, or the sites where reactions can occur [14]. Catalyst layers are generally made very thin by depositing them onto the membrane or the porous transport layer (PTL)s to reduce the use of expensive catalyst and ohmic losses. PTLs are the next layer out, consisting of a porous network of metal or graphite fibers that conduct electricity and allow for the flow of water and gases between the catalyst layers and the flow channels of the bipolar plates, which in turn are themselves made of metal or graphite and are connected to the power supply and fluid transport lines that supply the water and collect the produced gases.

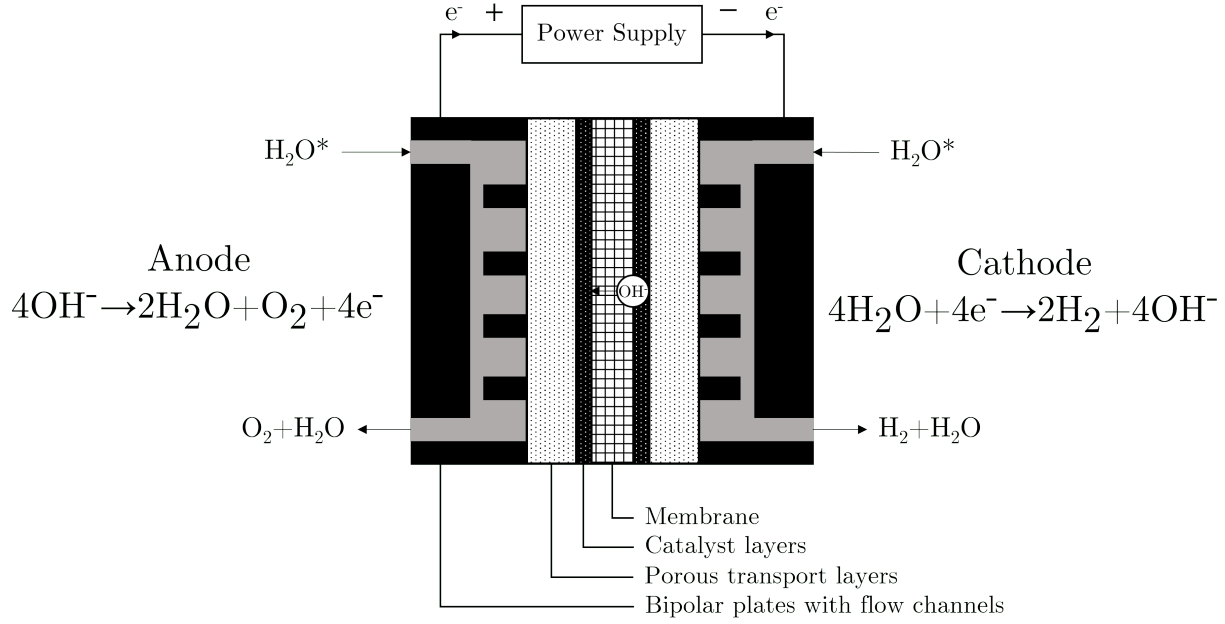
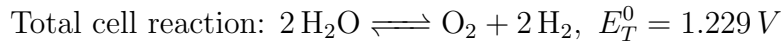
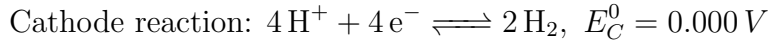


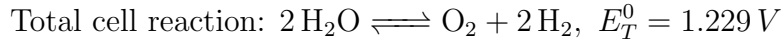
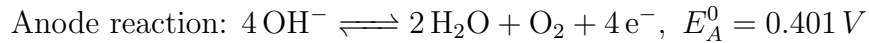
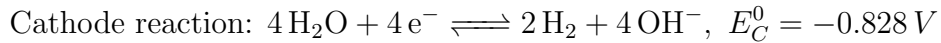
**Figure 1.1** – Example layout of an AEMWE cell. \*In this work, water is supplied to one or both of the electrodes during cell operation.

AEMWE cells are similar in construction to PEMWE cells, both utilising a solid polymer membrane as the electrolyte to separate the electrodes, however, they differ in the ions which these membranes conduct. The proton exchange membrane (PEM) in a PEMWE cell, usually made of Nafion, conducts  $\text{H}^+$  cations from anode to cathode, whereas an anion exchange membrane (AEM) conducts  $\text{OH}^-$  anions from cathode to anode instead. The reactions that take place at the cathode and anode in PEMWE and AEMWE cells are [15]:

PEMWE



AEMWE



PEMWE cells require the use of platinum-group metal (PGM) catalysts, generally platinum supported on carbon (Pt/C) at the cathode and iridium oxide ( $\text{IrO}_x$ ) at the anode [9].

The reason for this is that they are, by far, the most active and stable catalyst for these reactions under acidic conditions. These are both expensive materials, and the use of  $\text{IrO}_x$  is especially of concern due to its scarcity [16, 17]. The high potentials required for the OER in acidic media also necessitates the use of titanium for many of the supporting materials of a PEMWE cell, which makes up the bulk of a cell’s mass, again increasing the cost [9]. The main benefit of the change to  $\text{OH}^-$  ions in AEMWE cells then, is the resulting alkaline cell environment, which requires a lower voltage in the anode thereby reducing the corrosive environment, eliminating the need for  $\text{IrO}_x$  catalysts and titanium components. This has the effect of allowing for the capital costs of water electrolysis to be lowered [5, 8, 10]. The disadvantage of this change in the conducted ion is that new polymers must be developed to function as AEMs, and of those that exist today, none have yet reached the durability of Nafion [10]. Additionally, most AEMWE cells reported in literature to date still use an alkaline electrolyte, usually aqueous KOH, instead of deionized water due to poor durability of the ion conducting polymer (ionomer) materials that exist for conducting  $\text{OH}^-$  [8].

### 1.1.2 Electrolysis Cell Characterization

To determine the operational capabilities of an electrolysis cell, in-situ and ex-situ characterization techniques are used such as polarization curves, stability tests, electrochemical impedance spectroscopy (EIS), and microscopy of the catalyst layers. In-situ techniques can show how a cell operates, with the most common technique, polarization curves, operating a cell over a range of current densities and logging the cell potential (voltage) required to obtain the tested currents. These can either be operated as a continuous sweep or with the cell held at discrete current densities, each for a set amount of time. An example polarization curve is given in Figure 1.2, with the major types of losses that occur during operation separated and labelled. As was discussed above, the standard potential for a water electrolysis reaction is  $E^0 = 1.229\text{ V}$  at  $25^\circ\text{C}$ , but at this potential, the reaction progresses in both directions equally, and to produce the desired products of hydrogen and oxygen gas, a higher potential must be applied. The difference between the equilibrium and operating potentials is called the overpotential, and it is desirable to keep this as low as possible to reduce power consumption. There are three types of overpotential that arise in an electrolysis cell as the current increases, kinetic, ohmic, and mass transport. As each type of loss dominates at different levels of current, polarization curves can have up to three distinct regions based on the dominant type of loss, depending on how high a current is tested. The in-depth process and equations used to calculate overpotentials in this work, both correcting for temperature and for comparing half-reaction potentials against any desired reference electrode are provided in Section 2.4.4.

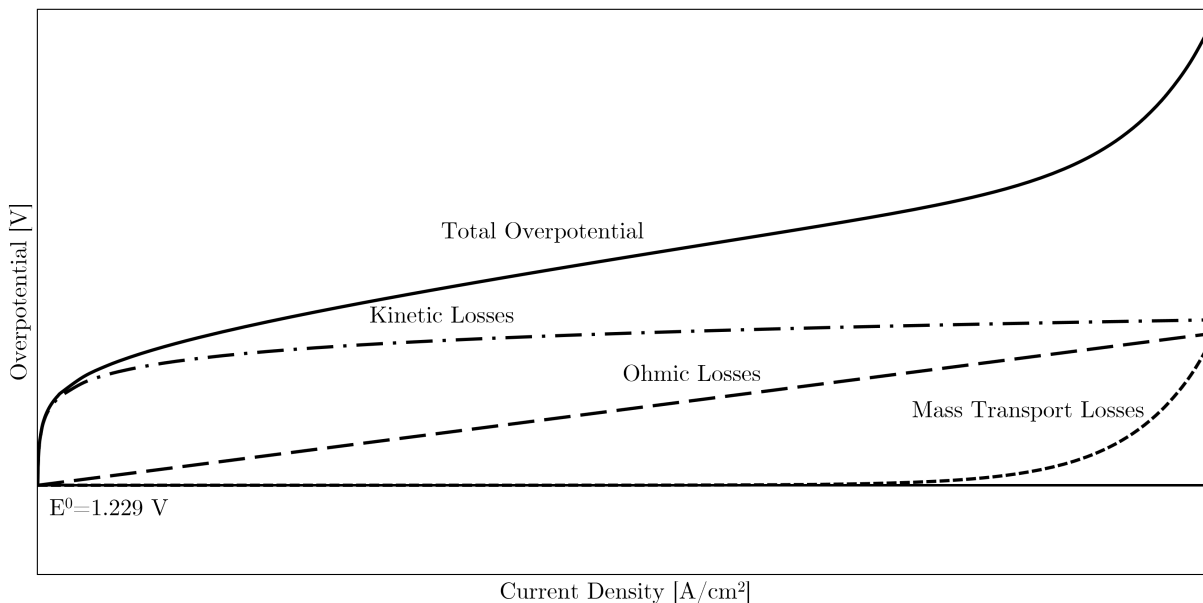


**Figure 1.2** – Diagram of a polarization curve with the major types of losses separated and labelled.

Stability and EIS tests are also run in-situ, also serving to characterize the operation of an electrolysis cell. A stability test holds the cell at a set current or voltage for multiple hours, measuring a common and unwanted slow decrease in performance over time. This occurs as either an increase in voltage, or decrease in current, whichever is being measured. This is distinct from very long-term durability tests, as these decreases in performance over the short-term are generally not permanent and will recover after the cell remains unused for some amount of time.

EIS is a more complicated technique where a voltage with an alternating current component is applied to the cell. Fundamentally, every physical process has a different dynamic response to an applied alternating current, and the dynamic response can be deconvoluted to understand the voltage losses due to each phenomenon. In its simplest form, the dynamic response of an electrolyzer can be approximated by equivalent electrical circuits composed of resistors, capacitors, and inductors, which can provide some insights about the underlying physical processes. In doing so, the losses observed in the polarization curve can be quantitatively characterized [18]. In-depth explanations of how these characterization techniques were used in this work are provided in sections 2.5.4 and 2.5.3.

As this work covers both the fabrication and use of AEMWE cell catalyst layers, some ex-situ characterization of these components was also done. As was shown in Figure 1.1, at the center of an AEMWE cell is the membrane and catalyst layers. Herein, catalyst layers were deposited directly onto the AEM by inkjet printing to create a catalyst-coated membrane

(CCM). Images of the catalyst layers deposited onto fabricated CCMs were then taken using optical microscopy and scanning electron microscopy (SEM), both before and after they were used in AEMWE cells. This was done as catalyst layers are porous, composite components, and imaging allows for a detailed examination of their microstructures. This is especially important as these components were fabricated in-house by inkjet printing, an uncommon technique.

## 1.2 Literature Review

The existing literature on AEMWE cells is limited, as in-situ research has only been ongoing since the early 2010s, and due to this, there are aspects of AEMWE cell operation that have not yet been fully investigated. This review will be divided into four sections: catalyst layer fabrication methods (1.2.1), in-situ AEMWE cell materials and operational methods (1.2.2), AEMWE cell characterization methods (1.2.3), and finally the integration of a reference electrode within these cells (1.2.4). Catalyst layer fabrication is important for this work, as the CCMs used were made in-house and then assembled into single cells. The latter three sections of this review cover all aspects of AEMWE cell construction and operation relevant to this work, including cell materials and test setup operation, characterization techniques, and the use of a reference electrode, as the testing of AEMWE cells is the primary focus of this work.

### 1.2.1 Anion Exchange Membrane Catalyst Layer Fabrication

The most common method used in literature to fabricate catalyst layers is spray coating, usually with an airbrush [19–29], but ultrasonic and plasma spraying have been used as well [30–32], along with alternate methods like electro-deposition [33–36], brush coating [20, 37, 38], and decal transfer [39]. An alternative technique to these is inkjet printing. Although this has so far only had limited use in fabricating catalyst layers of AEMWE cells [40], there is literature that covers the inkjet printing of catalyst layers for PEM fuel and electrolysis cells. Shukla et al. [41] and Mandal et al. [42] both showed that inkjet printed CCMs performed well in PEM cells, with the printing process resulting in an even distribution of catalyst and ionomer materials throughout the catalyst layers. Inkjet printing also allows for a fine control over the deposition of the inks used, allowing for the use of lower catalyst loadings and accurate deposition of materials onto the desired surface, reducing the amount of wasted catalyst. The reason this is not as widespread as spray coating, especially in AEMWE, is likely the difficulty of producing easily jettable inks and the long deposition times, resulting in most inkjet printed cells being low loading. For comparison, Fortin et

al. and Zignanni et al. [22, 29] achieved cathode Pt/C loadings of 1 mg/cm<sup>2</sup>, whereas the cathode Pt/C loadings used by Mandal et al. and Storbakken [40, 42] were only 0.1 mg/cm<sup>2</sup>. Higher loadings may be necessary for the future development of AEMWE cells as non-PGM catalyst are used more frequently, and due to their lower costs, higher loadings can be used [43]. As this was not a focus of this work, and due to the advantages of the system (little catalyst waste, no aerosol formation, and well-controlled deposition) and the knowledge base built up in the ESDLab, inkjet printing was the catalyst layer fabrication method chosen for this work.

Catalyst layers can be deposited on either the membrane directly using the CCM method [19, 24, 30, 38, 43], or onto the PTLs by the catalyst-coated substrate (CCS) method [20, 22, 25, 26, 31–36]. In theory, CCM catalyst layers are in direct contact with the membrane, allowing for a good connection between the ionomer material in the catalyst layers and the ion-conducting membrane [14, 44], improving performance compared to CCS catalyst layers. This is not necessarily the case when it comes to in-situ cells, however, as a comparison of published AEMWE cells performance numbers for both of these methods from Miller et al. [8] showed (Figure 1.3). The results from Miller et al. indicate similar overall performance between the two methods, however, this comparison did not account for differences in cell construction or operational conditions. CCS fabrication does have a distinct benefit when working with AEMs as the membranes can swell quite a bit when wetted during catalyst deposition. This was a challenge when working with first generation Aemion membranes, as discussed by Storbakken [40], but the second generation Aemion (Aemion+) membranes used in this work are reinforced and do not swell as much during catalyst layer deposition. Direct comparisons of these two methods were done by Storbakken and Park et al. [40, 45], the former resulting in very similar performance, and the latter finding CCM to perform better. As the results of these comparisons show similar performance, with those from Park et al. slightly favouring the CCM method, this was selected for use in this work.

The inks used to fabricate catalyst layers, whether by inkjet printing or other methods, contain suspended catalyst particles that are generally on a nanometre scale, and so the mixture is considered a colloid [46]. This complicates the inkjet printing deposition process, as it can take up to 6 hours to print the required loading of catalyst material, throughout which time the particles must remain suspended. Shukla et al. [47] found that isopropyl alcohol (IPA) worked well as a solvent for creating inks stable enough for printing using Pt/C catalyst particles and adding Nafion ionomer served to further stabilize the inks and lower average aggregate particles sizes. The work done by Shukla et al. and Mandal et al. [41, 42, 47, 48] form the basis for the ink formulation and printing process used here. Additionally, Storbakken [40] developed processes to produce inks for printing AEMWE cell catalyst layers, much of which is followed in this work, most notably the limits on solid

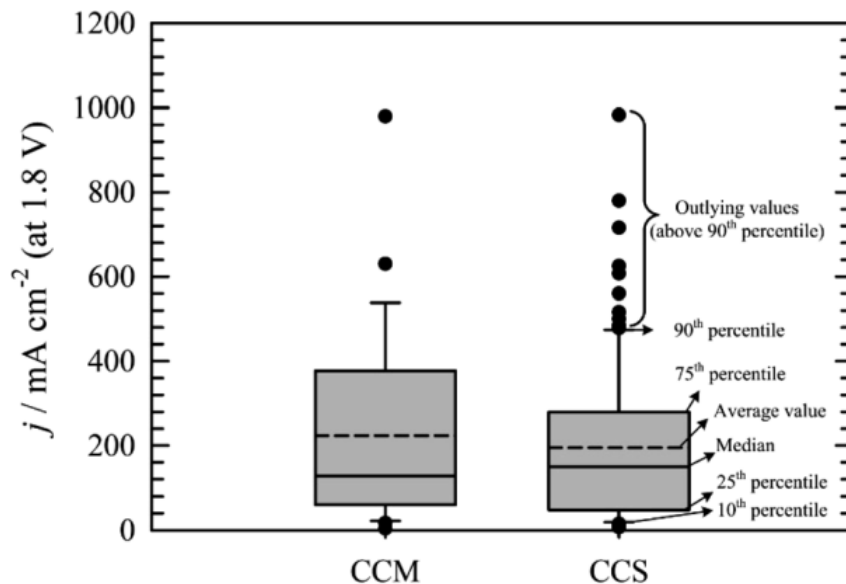


**Figure 1.3** – Box and whisker plot comparing AEMWE cell performance in literature using CCM and CCS catalyst layer fabrication methods, reproduced from Miller et al. [8].

content to 1.25 and 3.25 wt.% for Pt/C- and  $\text{IrO}_x$ -based inks, respectively, intended to ensure that catalyst particle aggregates do not become large enough to clog the printer nozzles. One major change that was made from Storbakken was the removal of water from inks, as it is recommended to not expose Aemion+ ionomer to pure water [49]. The ink formulation processes covered in Section 2.1 of this work was adapted from these sources.

## 1.2.2 In-situ Cell Component Materials and Operational Methods

In recent years, newly available commercial AEMs such as Aemion, Sustainion, and PiperION have allowed for AEMWE cells to be constructed that result in relatively good and consistent performance [12, 13]. There are few performance comparisons between AEMs made from these newer materials, but the review by Henkensmeier et al. [12] showed similar results for cells using Aemion and Sustainion membranes. Lindquist et al. [13] tested AEMWE cells with Aemion, Sustainion, and PiperION, with pure water fed to the cell, and again obtained similar results between Aemion and Sustainion, but both were out-performed by PiperION. Despite the performance differences, Aemion was selected to be used as the membrane material in this work since the ESDLab had prior experience with Aemion from the work by Storbakken [40], and it was an opportunity to use a new material, as the new Aemion+ membranes have, at the time of writing, been used for in-situ AEMWE cells in very few publications.

The selection of the catalyst and ionomer used in the catalyst layer inks was informed

by the works of Shukla et al., Mandal et al., and Storbakken [40–42, 47, 48], with the ink for the cathode catalyst being considered first. The single most common cathode catalyst material that has been used in in-situ AEMWE cells is Pt/C or platinum black [21–27, 29, 30, 50–55], with nickel-based catalysts also being a popular choice [19, 20, 28, 31–36, 38, 39, 43, 56–59]. The use of nickel as an AEMWE catalyst makes sense, as a major benefit of the technology is the ability to use non-PGM catalysts, however, this has already been reported quite a bit in the literature, some sources of which are compared in Table 1.1. Also, as there are more sources that use the standard Pt/C catalyst, including Fortin et al. and Koch et al. [22, 30], that also used similar membranes to those used here, Pt/C was chosen so that results obtained here could be compared with other sources. The other component of the cathode catalyst ink to be selected was the ionomer material, and the concentration of it in the ink. Aemion+ AP2-HNN5-00-X ionomer was used to match with the Aemion+ membrane discussed earlier. As for the amount of ionomer in the ink, work by Koch et al. [30], Faid et al. [60], and Huang et al. [61] optimized the cathode ionomer content to be 10 wt.%, and so this is the cathode ionomer fraction used in this work.

The most common material used for AEMWE cell anode catalyst layers is Ir or IrO<sub>x</sub> [22, 24, 25, 27, 30, 34, 43, 53–55], although many non-PGM catalyst, usually nickel- or cobalt-based, have also been tested in-situ at the anode [19–21, 23, 26, 28, 29, 31–33, 35, 36, 38, 39, 50, 51, 56–59]. The performance of some of these sources is compared in Table 1.1. The push to use non-PGM catalyst at the anode is in part due to the scarcity of iridium [16, 17], as demonstrated by the number of sources that have investigated this. For the same reasons as the selection of the cathode catalyst, the ability to compare with sources using the more common material, IrO<sub>x</sub> was used as the anode catalyst in this work. Aemion+ AP2-HNN5-00-X ionomer was also used at the anode to match the membrane material. Koch et al [30] tested ionomer contents of 15, 10, 7, and 4 wt.%, and found that lowering the ionomer content resulted in performance gains. Huang et al. also investigated the anode ionomer content [62], where their results were similar to Koch et al., with cell performance improving as the anode ionomer loading decreased, although the lowest loading they tested was 15 wt.%. Based on these results, an anode catalyst loading of 5 wt.% was selected for this work.

As mentioned earlier, nickel- and cobalt-based alloys are being actively investigated as replacements for iridium as an anode catalyst material. Replacement of the PTL and bipolar plate materials, specifically at the anode-side, is also of interest. These components can make up a large amount of the total material used in electrolysis cells, and in PEMWE cells, the anode-side will generally use platinized titanium [8]. In AEMWE cells, these are often replaced with nickel or stainless steel which still maintain adequate performance [21, 26, 29, 31, 32, 38, 50, 58, 59]. Table 1.1 compiles the materials used for PTLs and bipolar plates

**Table 1.1** – Literature sources testing in-situ AEMWE cells with non-PGM components.

Source	Cathode			Anode			Current Density @ 1.8 V (mA/cm <sup>2</sup> )
	Catalyst	PTL	Bipolar Plate	Catalyst	PTL	Bipolar Plate	
Pandiarajan et al. (2015) [38]	Ni	Pt coated Ti	Stainless Steel	Ce <sub>0.2</sub> MnFe <sub>1.8</sub> O <sub>4</sub>	Pt coated Ti	Stainless Steel	300
Park et al. (2021) [31]	Ni-alloys/C	Carbon Cloth	Stainless Steel	CuCoO	Ni Foam	Stainless Steel	435
Parrondo et al. (2014) [26]	Pt Black	Carbon Paper	Graphite	Pb <sub>2</sub> Ru <sub>2</sub> O <sub>6.5</sub>	Carbon Paper	n/a	400
Pavel et al. (2014) [59]	ACTA 4030	Carbon Cloth	Stainless Steel	CuCoO <sub>3</sub>	Ni Foam	Stainless Steel	440
Wang et al. (2019) [32]	NiAlMo	Stainless Steel	Stainless Steel	Ni-alloys	Stainless Steel	Stainless Steel	1000
Wu et al (2011) [50]	Pt/C	Stainless Steel	n/a	Cu <sub>0.7</sub> Co <sub>2.3</sub> O <sub>4</sub>	Stainless Steel	n/a	1000
Xiao et al. (2012) [58]	NiMo	Stainless Steel	Stainless Steel	NiFe	Ni Foam	Stainless Steel	275
Xiao et al. (2021) [21]	Pt/C	Carbon Paper	Graphite	FeNiOOH-20F	Ni Foam	Titanium	1500 (@ 1.74 V)
Zignani et al. (2020) [29]	Pt/C	Carbon Cloth	Graphite	NiFeO <sub>x</sub> /C	Carbon Cloth	Nickel	280

in these sources. Park et al. [31], Pavel et al. [59], and Wang et al. [32] were able to achieve quite good results at 1.8 V with current densities of 435 mA/cm<sup>2</sup>, 440 mA/cm<sup>2</sup>, and 1000 mA/cm<sup>2</sup>, respectively, while using entirely non-PGM catalysts, PTLs, and bipolar plates. As it seems that non-PGM PTLs and bipolar plates have been reported to work well at the anode-side of AEMWE cells in literature, following some issues with the initial PEMWE-style PTLs and bipolar plates used in this work, nickel felt PTLs and a nickel 400 alloy bipolar plates were selected for use in both anode and cathode.

Cost savings in cell components is a benefit of AEMWE cells, but a drawback is that many cells reported in literature are operated using an aqueous alkaline electrolyte, commonly a 1 M (1 mol/L) solution of potassium hydroxide (KOH), instead of feeding pure or deionized water [8]. This increases the complexity of the system as the electrolyte must be made and handled properly as it is a corrosive solution. This aqueous electrolyte supplements the hydroxide-conducting ionomer in the catalyst layers to improve the performance and durability of the ionomer materials [14, 54]. The use of water-fed cells has been investigated in the literature, and some have performed quite well, although many sources that compare performance with an alkaline electrolyte find that operating with water negatively impacts performance [14, 45, 50, 54, 63]. Table 1.2 compares AEMWE cell performance obtained by sources that tested using water and an alkaline electrolyte. In addition, Kiessling et al. [54, 55] tested the use of various alkaline electrolytes at both the anode and cathode, including aqueous hydroxide solutions made using KOH, sodium hydroxide (NaOH), and lithium hydroxide (LiOH), potassium carbonate (K<sub>2</sub>CO<sub>3</sub>) solution, and water. The use of these electrolytes changed both the anions and cations in solution, which had an effect on the performance of the cells, with the best cell performance and durability being achieved when KOH electrolyte was used. The study of using pure water in AEMWE cells is interesting, as it would be the most convenient feed solution to use in operation, however only recently have AEMs that perform well with a pure water feed been developed [13], and as operation with water is not recommended for the Aemion+ membranes [49], a 1 M KOH solution will be used in this work.

**Table 1.2** – AEMWE cell performance in literature with water and alkaline electrolyte feed.

Source	Current Density @ 1.8 V (mA/cm <sup>2</sup> )		Electrolyte Used
	Water Feed	Alkaline Electrolyte Feed	
Hassan et al. (2022) [63]	435	1000 @ 1.72 V	0.3 M KOH
Kiessling et al. (2021) [54]	125 @ 1.7 V	1590	1 M KOH
Liu et al. (2021) [14]	290	1000	1 M KOH
Park et al. (2019) [45]	20	465	1 M KOH
Wu and Scott (2011) [50]	85	965	1 M KOH

A limited amount of work has been published on the feed method used with AEMWE cells, and there is no consensus or standard feed method currently used. Leng et al. [24] tested the operational lifetime of AEMWE cells in cathode-only feed (COF) and anode-only feed (AOF) with deionized water, and found the cells that used AOF lasted the longest, measured at 513 hours versus 196 hours for COF. Testing the difference between two-electrode feed (TEF) and cathode-only feed (COF) with 1 M KOH, Park et al. [45] observed that COF resulted in very poor performance compared to TEF, where at 1.8 V, the two configurations operated at 40 and 465 mA/cm<sup>2</sup>, respectively. Kiessling et al. and Cho et al. [55, 64] tested AOF and TEF, and found that AOF did not greatly impact cell performance, at least initially. Cho et al. additionally performed 100 voltage cycles, and found that AOF performance improved over time while TEF stayed relatively constant, although this enhanced cell durability was also due to the PTFE binder used in the catalyst layers.

It is understandable that a lack of electrolyte solution at one of the electrodes would decrease cell performance due to a decrease in ionic conductivity and therefore possible reaction sites, but the reason that the performance of AEMWE cells suffers so greatly when the anode is dry and not when the cathode is, which uses water as a reactant, is puzzling. It has been hypothesized to be because hydroxide ions are the reactant in the OER reaction, and so supplying OH<sup>-</sup> directly increases the reaction efficiency [45], however, there is a lack of studies on the subject of AEMWE cell feed methods, and none that have tested all three methods. Therefore, the question of what feed method works best will be investigated in this work.

### 1.2.3 In-situ Cell Characterization Methods

Multiple in-situ techniques are used to analyse the materials and methods used to construct AEMWE cells, the most common of which in literature are polarization curves [19–24, 26–39, 43, 50–59, 64, 65]. Polarization curves plot the cell potential as a function of cell current or current density. As current is directly proportional to the rate of water electrolysis [66],

and current times voltage is power, a lower voltage means a lower power consumption. Polarization curve are measured by controlling either voltage or current, and can be done in either a continuous sweep or a stepwise manner. For this work, current was controlled in a stepwise method, as this had the advantage that experiments could be performed identically whether using a reference electrode or not, as it was independent of the measured voltage, and some of the hardware used could not perform continuous sweeps.

Though not as common as polarization curves, short-term stability tests are used to observe how the performance of a cell decreases as it is operated continuously. Cell stability and degradation are terms generally used to quantify the difference between performance losses that are observed in the short-term and recovered when the cell is not in operation versus long-term, permanent losses. Various methods of testing the short-term stability of cells have been used in literature, commonly by holding a constant current [20–22, 24, 26, 27, 30–32, 36, 38, 39, 51, 52, 56–59, 65], or voltage [23, 25, 35, 38, 43] over time, or with the use of methods such as the cycling the voltage many times [29, 64]. The test format used initially was a 6 hour hold at a constant 1.8 V, as during this type of test, cell current would only decrease over time, and so was considered safer when cell stability was poor. Later the more common constant-current method would be used, holding cells at 300 mA/cm<sup>2</sup> for 6 hours.

Although the types of losses that occur in an electrochemical cell can be seen in polarization curve results, they can be better quantified through the use of EIS. Like polarization curves, these are quite commonly used in literature for AEMWE cells [22, 25, 27, 28, 30–32, 34, 35, 38, 43, 53–56, 64], mainly to separate kinetic and ohmic losses. EIS does require more specialized equipment however, as is performed by applying a small amplitude alternating current (AC) signal to the cell and measuring the response. By fitting this response to an electrical circuit model based on the cell, features of the cell such as its direct current (DC) resistance, or high frequency resistance (HFR), can be quantified. As EIS can provide this useful information, and the equipment to do so was available, it was used in this work.

#### 1.2.4 Integration of a Reference Electrode into an In-situ Electrochemical Cell

For much of the existing literature sources focused on the testing of AEMWE cells, only the total cell potential,  $E_{cell} = E_{anode} - E_{cathode}$ , is reported, as separating the anode and cathode potentials requires the integration of a reference electrode into the cell construction, which is not trivial due to the structure of polymer electrolyte electrochemical cells. The ability to measure the individual half-reaction potentials is desirable, as it allows for the overpotentials at each side of an electrochemical cell to be individually characterized, and

**Table 1.3** – Reference electrode integration methods used for in-situ electrochemical cells in literature.

Source	Cell Type	Reference Electrode Integration Method
Andre et al. (2010) [68]	PEMFC	Micro-electrode inserted into H <sub>2</sub> side of the flow channels
Faid et al. (2020) [60]	AEMWE	Membrane strip in contact with AEM through bipolar plate
Hartig-Weiß et al. (2021) [69]	PEMWE	Electrode laminated between two PEMs
He and Nguyen (2004) [67]	PEMFC	Membrane strip in contact with PEM through side of cell
Johnston-Haynes (2018) [70]	PEMWE	Membrane strip in contact with PEM through bipolar plate
Jung et al. (2009) [71]	PEMFC	Membrane strip in contact with PEM through side of cell
Smith (2015) [72]	PEM & AEMFC	Electrode laminated between two PEMs/AEMs
Xu et al. (2021) [53]	AEMWE	Membrane strip in contact with AEM through side of cell

a better understanding of the ongoing processes at either side can be gained [67]. This has been investigated in literature sources for AEMWE and similar cells, and those that were reviewed here are given in Table 1.3 [53, 60, 67–72]. In this work, it was decided to integrate a reference electrode into some of the AEMWE cells tested to improve the understanding of the anode and cathode overpotentials.

The sources covered in Table 1.3 utilize three main types of reference electrode integration methods: a membrane strip “ionic bridge”, a metallic electrode placed between two ion-exchange membranes at the cell center, and a metallic electrode integrated into the hydrogen-side flow channels. The use of a membrane strip ionic bridge was ultimately selected for this work, as it has been used successfully by He et al., Jung et al., and Xu et al. [53, 67, 71] and required the fewest number of modifications to the existing cell hardware. The only precaution that must be taken is ensuring that the membrane strip remains hydrated during use. Johnston-Haynes and Faid et al. [60, 70] used a modified version of this method where the ionic bridge was inserted through a hole in a bipolar plate, but this would require extensive cell hardware modifications. Placing a reference electrode, such as a piece of platinum metal, in the hydrogen-side flow channel can also be achieved with little hardware modifications, and would create a pseudo-reference electrode [69], but in an electrolysis cell the concentration of hydrogen in the channel depends on cell operation, and so this may lead to inconsistent measurements.

Xu et al. [53] was able to implement a reference electrode in an AEMWE cell, and was successful in measuring the potentials of the two electrodes individually for polarization curves, although longer term testing was not performed. They utilized a membrane strip that made contact with the AEM inside the cell and with a reference electrode outside the cell. Based on this success, and the minimal cell modification necessary, the setup used in this work will be based on that from Xu et al. As ion and water transport are important factors in the operation of ion-exchange membrane cells, it was of interest in this work to also study longer-term cell operation with a reference electrode.

An ideal reference electrode will not alter the way the cell operates, nor will cell operation change the reference potential. Electrodes connected by the edge of the ion-exchange membrane should have little effect on cell operation, whereas those connected between the catalyst layers may interrupt the transport of hydroxide or water through the membrane and influence how different feed methods affect cell performance [72]. The distribution of electrical potential within an ion-exchange membrane during cell operation has been modelled [67, 72, 73], with the results finding that the gradient in potentials between the electrodes extended beyond the area of membrane in contact with the electrodes. As long as a reference electrode is connected a certain distance from the edge of the working and counter electrodes, at least three times the membrane thickness, the potential measured by the reference electrode is equal to the potential at the center-point of the membrane. The potential distribution in the membrane could become asymmetrical, and therefore the potential sensed by the reference electrode could change, during cell operation however, due to a misalignment in the working and counter electrodes of more than one membrane thickness, or due to differences in the reaction kinetics of the two electrodes [67, 73]. These factors present potential challenges that must be considered for the integration of a reference electrode, and for the accuracy of the measurements.

### 1.3 Objectives

The work herein was performed with the objective of understanding the limitations of AEMWE single-cells. The main objective of this work is to study how cell performance is affected by different feed methods. To do this study, catalyst inks will be developed, catalyst layers fabricated by inkjet printing, and cells characterized using different feed methods. The objectives of this work are summarized as follows:

1. Formulate inks containing Aemion+ ionomer and catalyst nanoparticles, both platinum supported on carbon and iridium oxide, that conform to the recommended specifications for inkjet printing for a Fujifilm Dimatix DMP 2850 printer. Use this ink to print Aemion+ catalyst coated membranes.
2. Construct single-cell anion exchange membrane water electrolysis cells and characterize their performance in-situ. Obtain consistent performance between cells through the use of robust ionomer materials and cell test procedures.
3. Characterize cell performance with electrolyte fed to one or both electrodes to understand the effect of electrolyte supply methods on AEMWE cell operation. Additionally, make measurements using a reference electrode integrated into the cell to study anode and cathode performance separately.

# Chapter 2

## Experimental Methodology

The major objectives of this work required the testing of AEMWE single-cells, which themselves had to be constructed. The first step in this process was to develop ink recipes containing catalyst nanoparticles that could be inkjet printed to fabricate the CCMs used within the cells. Once a printable ink formula was developed, inks were printed onto Aemion+ membranes to form  $\text{IrO}_x$  anode and Pt/C cathode catalyst layers. Cells were then assembled using the CCMs and connected to the test station for operation, where electrolyte was fed to the cells, the produced gasses removed, and the cells operated using a potentiostat. With this completed, cells could be characterized using procedures laid out here to integrate a reference electrode and study the effects of cell feed method.

### 2.1 Ink Formulation Process

To fabricate the AEMWEs, a catalyst was coated onto an AEM. To coat the catalyst, an inkjet printer was used. Herein is the process used to formulate catalyst inks suitable for inkjet printing from the base components: catalyst powder, solid Aemion+ ionomer, methanol, acetone, propylene glycol (PG), and isopropyl alcohol (IPA). The inks used in this work were always made in batches of 3 g, so the formulae covered here are for this amount. Inks were defined based on the weight percent of their components, but when inks were made, the mass of each component was used. The formulae used to convert from weight percent to mass are provided in Appendix D.1.

Before inks were made, the ionomer solution to be used in the ink were formulated. The ionomer solution for both the anode and cathode inks were made from Aemion+ AP2-HNN5-00-X<sup>1</sup> solid ionomer (Ionomr Innovations) dissolved in a 50%/50% mixture of methanol and

---

<sup>1</sup>Aemion product numbers use the following format: AAB-CCCD-EE-X, where AA is either AF for membranes or AP for ionomer; B is 1 or 2 for the Aemion generation (Aemion or Aemion+); CCC is the reinforcement type, D is the relative IEC; EE is the thickness in  $\mu\text{m}$  with 00 used for ionomer; and the trailing -X denotes that the material is in pre-production.

acetone by volume, which was prepared by measuring out 1 mL of each solvent into a container, as this was be more than enough to make a batch of ink. To then produce the ionomer solution for the anode ink, 14.6 mg of solid ionomer and 731.3 mg of the methanol/acetone solution were added to a vial, and stirred on a magnetic stir plate set to 350 rpm and a temperature of 50°C for 20-60 minutes, until the ionomer was dissolved. The same process was used for the cathode ink ionomer solution, but with 11.3 mg of ionomer and 562.5 mg of the methanol/acetone solution. The ionomer solution was then passed through a 5  $\mu\text{m}$  filter to remove undissolved particles. An excess of ionomer solution is made because some loss occurs during filtration.

A test was done to determine how much ionomer and solvent was lost during the filtration process. For this test, a 2 wt.% ionomer solution containing 12.0 mg of ionomer and 602.1 mg of the acetone/methanol solvent was made. The total mass of the solution and the mass of the filter were measured before filtration. Following filtration, the filter was allowed to dry before it, and the remaining solution, were again measured. This difference in the filter mass was used to calculate that 10.8 % of the ionomer was trapped in the filter following filtration. Similarly, the difference in the total solution mass (taking the lost ionomer into account) was used to estimate that 8.6 % of the liquid solvent was also lost during filtration. With this information, the ionomer content of the filtered ionomer solution was calculated to be 1.9 wt.%. Based on this value, all ionomer solutions used in this work were considered to contain the same 1.9 wt.% solid ionomer following filtration, and this was taken into account when calculating the ionomer content of the inks and printed catalyst layers.

To fabricate the anode catalyst ink, the components used were: 92.6 mg of  $\text{IrO}_x$  powder ( $\text{IrO}_x$  nanopowder from Tanaka Kikinzoku Kogyo (TKK) Company, Japan), 2073.0 mg of PG, 590.6 mg of IPA, and 243.8 mg of ionomer solution. This achieved the desired 3.25 wt.% of solid content in the ink, with 5 wt.% ionomer within the solid content. The catalyst powder was added in a vial and weighed using a mass balance (Entris 124i-1S by Sartorius, 0.1 mg resolution). To the catalyst, a portion of the total amount of PG was added, equal to the total mass of IPA to be added. The mixture was then stirred with a magnetic stir plate set to 350 rpm for 5 minutes. The IPA was added next and the mixture was again stirred at 350 rpm at room temperature until the PG and IPA were mixed (about 5 minutes). The ionomer solution was then added in a drop-wise manner, waiting 15 seconds between drops, while the mixture was bath sonicated (Branson 1800, 40 kHz). The temperature of the bath sonicator was not allowed to rise much above room temperature (25 to 28°C maximum) to prevent evaporation of volatile solvents. After the ionomer solution was added to the ink, it was allowed to bath sonicate for an additional 30 minutes before the remaining PG was added and the ink was again stirred at 350 rpm for 5 minutes. Finally, the ink was probe sonicated (Qsonica S-4000, 2 minutes on, 1 minute off, 15 minutes total, 20% amplitude) and

then degassed for 60 minutes using the same bath sonicator as earlier set to degas mode. To prevent evaporation of volatile solvents, the ink container was kept closed whenever possible, and during probe sonication, parafilm wax was used to seal the gap between the ink container and probe. Between formulation and use, the ink was stored on a magnetic stir plate set to 350 rpm.

To fabricate the cathode catalyst ink, the components used were: 33.8 mg of Pt/C powder (Pt/C nanopowder from Tanaka Kikinzo Kogyo (TKK) Company, Japan as 46.7 wt.% Pt supported on carbon black), 2085.0 mg of PG, 693.8 mg of IPA, and 187.5 mg of ionomer solution. This achieved the desired 1.25 wt.% of solid content in the ink, with 10 wt.% ionomer within the solid content. The process of making the cathode ink was the same as described for the anode ink, just with these different amounts of each component.

The total solid weight percent was set at 3.25 wt.% and 1.25 wt.% for the anode and cathode inks, respectively based on previous work using Aemion AP1-HNN8-00-X ionomer by Storbakken [40]. These levels were high enough that the desired catalyst loading could be printed in a reasonable number of layers, and low enough that the ink would not clog the printhead nozzles. A notable change from the formulae used by Storbakken was the removal of water, as it was recommended by Ionomr Innovations that the Aemion+ ionomer not be exposed to pure water [49]. This process for making the inks was adapted from those utilized previously at the ESDLab [40, 41, 74].

To successfully print a catalyst layer, an ink had to be developed that could inkjet printed and contained enough solid material to deposit the necessary amount of catalyst in a reasonable time period, as material was deposited slowly when printing. To fabricate CCMs in this work, a Dimatix DMP-2831 drop-on-demand inkjet printer was used with DMC-11610 printheads, which suggested using an ink viscosity of 10 to 12 mPa·s and surface tension of 28 to 33 mN/m to achieve optimal printing performance [75, 76]. In addition to these parameters, the dimensionless Ohnesorge number is traditionally used to determine the ability of a fluid to be inkjet printed. This number is defined as [77, 78]:

$$Oh = \frac{\mu}{\sqrt{\rho\gamma L}} \quad (2.1)$$

or a ratio of dynamic viscosity,  $\mu$ , to the surface tension,  $\gamma$ , density,  $\rho$ , and characteristic length,  $L$ , usually the diameter of the droplets or printhead nozzle.  $Oh$  therefore physically represents a ratio the viscous forces to surface tension and inertial forces. A fluid with an  $Oh$  value between 0.1 and 1 is able to form stable droplets and can be considered printable by inkjet [78]. A range of  $Oh$  values valid for printing with the Fujifilm Dimatix for the DMC-11610 printheads was calculated using the viscosity and surface tension ranges provided by Fujifilm as well as the effective nozzle diameter of 21  $\mu\text{m}$  [76]. Fujifilm also recommends a density close to 1, and so this value was used for the following calculations:

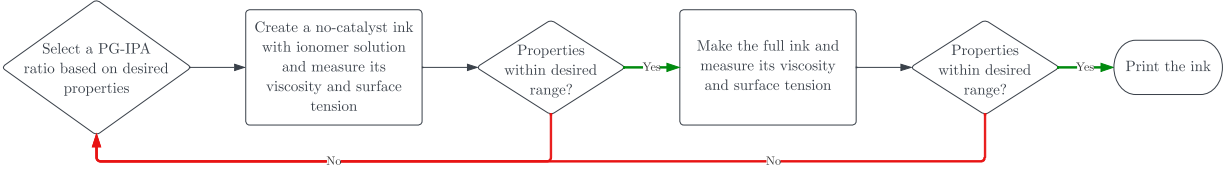


**Figure 2.1** – Flowchart of the ink formula development process.

$$Oh_{min} = \frac{(10 \text{ mPa} \cdot \text{s})}{\sqrt{(1 \text{ g/mL})(33 \text{ mN/m})(21 \text{ } \mu\text{m})}} = 0.38$$

$$Oh_{max} = \frac{(12 \text{ mPa} \cdot \text{s})}{\sqrt{(1 \text{ g/mL})(28 \text{ mN/m})(21 \text{ } \mu\text{m})}} = 0.49$$

The primary way inks in this work were analysed was by comparing their dynamic viscosity and surface tension to those recommended by the printer, however, since these values were already being measured, the Ohnesorge number was also be calculated and compared to this range of  $0.38 < Oh < 0.49$ .

To develop the ink formulae that met these requirements, a multi-step process was used, where one component of the ink was added at a time, and at each step the mixture was characterized using the methods covered in Section 2.2, with measurements of density, dynamic viscosity, and surface tension made. The first step was to make mixtures of PG and IPA, representing the ink “base”. Solutions with PG:IPA mass ratios of 1:1, 1.5:1, 2:1, 2.5:1, 3:1, and 3.5:1 were made and characterized for this purpose. A PG:IPA ratio would then be selected based on the recommended dynamic viscosity and surface tension values. Using this ratio, an ink with no catalyst was made by following all the ink formulation steps given earlier, but leaving out the catalyst powder. This new solution was again characterized to ensure its viscosity and surface tension were within the desired ranges, and if not, a different PG:IPA ratio was selected and a new ink with no catalyst was made. Finally, once the desired properties were achieved, a full ink was made with ionomer and catalyst, of which the dynamic viscosity and surface tension would once more be measured to ensure addition of the catalyst did not change the properties too much before the ink was used to print catalyst coated membranes. This process is summarized in the flow chart in Figure 2.1. The particle sizes within the final inks were also measured using dynamic light scattering (DLS) to ensure the ink would not clog the printhead nozzles. The Dimatix user guide recommends a particle size of less than  $0.2 \text{ } \mu\text{m}$ , however, the nozzles of the DMC-11610 printheads have an effective diameter of  $21 \text{ } \mu\text{m}$  [76], and so larger particles could in theory be tolerated without blocking the nozzle, although smaller particle sizes were desired. The use of this process to develop the ink formulae used in this work is covered in Section 3.1.

During the process of making inks, standard operating procedures and appropriate safety precautions were followed. These included assessing material safety data sheets for all ink components, and storing chemicals in material-compatible containers. When possible, all work with volatile chemicals, such as acetone, was done in a fume hood. Only small quantities of these chemicals (<10 g) were removed from the fume hood when necessary, and were kept within sealed containers whenever not in use. Additionally, a half-mask respirator was worn when handling dry catalyst nanoparticles to protect against inhalation.

## 2.2 Ink Characterization

The inks developed utilizing the process described in Section 2.1 were characterized using the processes covered in this section. As the inks used in this work contained multiple solvents (PG, IPA, methanol, acetone) as well as solid ionomer and catalyst, their rheology had to be determined experimentally, and the particle sizes of the solids also measured to ensure they could be printed. Ink formulae were therefore characterized to ensure their properties matched the viscosity and surface tension ranges provided by the Dimatix user guide, and catalyst particle size was measured to ensure printhead nozzles would not become blocked during printing.

### 2.2.1 Density Characterization

Ink density was required for the measurements of both dynamic viscosity and surface tension, and as inks were generally made in small batches of 3 g to minimize the use of PGM catalysts, it was desirable to use minimal ink for these tests. Density measurements used a mass balance (Entris 124i-1S by Sartorius, 0.1 mg resolution) to measure the mass of 1 mL of fluid, itself contained within a 1 mL volumetric flask (Kimble Kimax 1 mL,  $\pm 0.01$  mL). The small volume of the flask served to lower the error in the volume caused when the meniscus of the measured fluid was not visible. The volumetric flask was filled so the meniscus of the fluid reached a demarcated line, but as the catalyst inks were opaque, the inability to line this up exactly introduced an error. Use of a small and thin volumetric flask served to reduce this error by increasing the total height of the fluid column, thereby reducing the fraction of the height occupied by the meniscus. By knowing the mass,  $m$ , and volume,  $V$ , the density,  $\rho$ , was then be calculated as:

$$\rho = \frac{m}{V} \quad (2.2)$$

where  $V$  is the 1 mL volume of fluid used.

For each fluid that was tested, six replicate measurements were made to obtain the uncertainty in the mass measurement. As there was no source of bias uncertainty in this

experiment, the total uncertainty in density was entirely a precision uncertainty. The full density uncertainty calculation is provided in Appendix B.1.

To ensure this method resulted in accurate results, it was tested using water and IPA. These fluids were selected as their densities are known, and the densities of produced inks fell between those of these fluids. Using this method, densities of  $0.989 \pm 0.010$  g/mL and  $0.776 \pm 0.008$  g/mL were measured for water and IPA, resulting in experimental errors of 0.603% and 1.15%, respectively (The known densities of water and IPA used were 0.995 g/mL [79] and 0.785 g/mL [80] at 25°C). Verification measurements were done at  $23.5 \pm 0.5$ °C. These errors were small enough to be considered acceptable for the measurements that were made in this work.

Samples tested using this procedure were at room temperature throughout testing as this method did not allow for sample temperature to be controlled, but any error caused by the difference were small enough to neglect. The temperature of the inks in this work during printing was 32°C, and so ideally, ink properties should have been measured at this temperature. The difference, however, between the density of water at 23.5°C and 32.0°C is only 0.002 g/mL [81], and for IPA over the same temperature range is 0.0073 g/mL [82]. This difference is quite small, and so measurements of density at room temperature were considered sufficiently accurate.

### 2.2.2 Dynamic Viscosity Characterization

A dynamic viscosity range of 10 to 12 mPa·s was recommended for inks that would be printed using the DMC-11610 printheads that were used for this work [75], and so inks had to be developed that had dynamic viscosities within this range. To measure the viscosity of the inks, a reverse-flow glass viscometer (Zeitfuchs Cross-arm Glass Capillary Viscometer Size No.2) was used. The viscometer was placed in a heated water bath set to a temperature of 32°C. The water bath consisted of a beaker (4 L PYREX glass beaker), heater (Model 3150SS 1150 W immersion heater from Electra), temperature probe (TMT316SS-125U-12 from Omega), and heater controller (10 A temperature control box, built in-house). It was necessary to use a reverse-flow viscometer where fluid only flows in one direction, as the inks that were tested in this work were opaque. A heated water bath was used as it was important to hold the samples at the printing temperature of 32°C for the viscosity measurements, since viscosity can be quite sensitive to changes in temperature [83]. Only about 1 mL of fluid was needed for this viscometer, so this method could be used without needing to produce more ink than normal, minimizing the waste of expensive PGM catalyst. An image of the viscometer in the experimental setup is shown in Figure 2.2.

It was important that the viscometer was aligned vertically in the water bath when it was

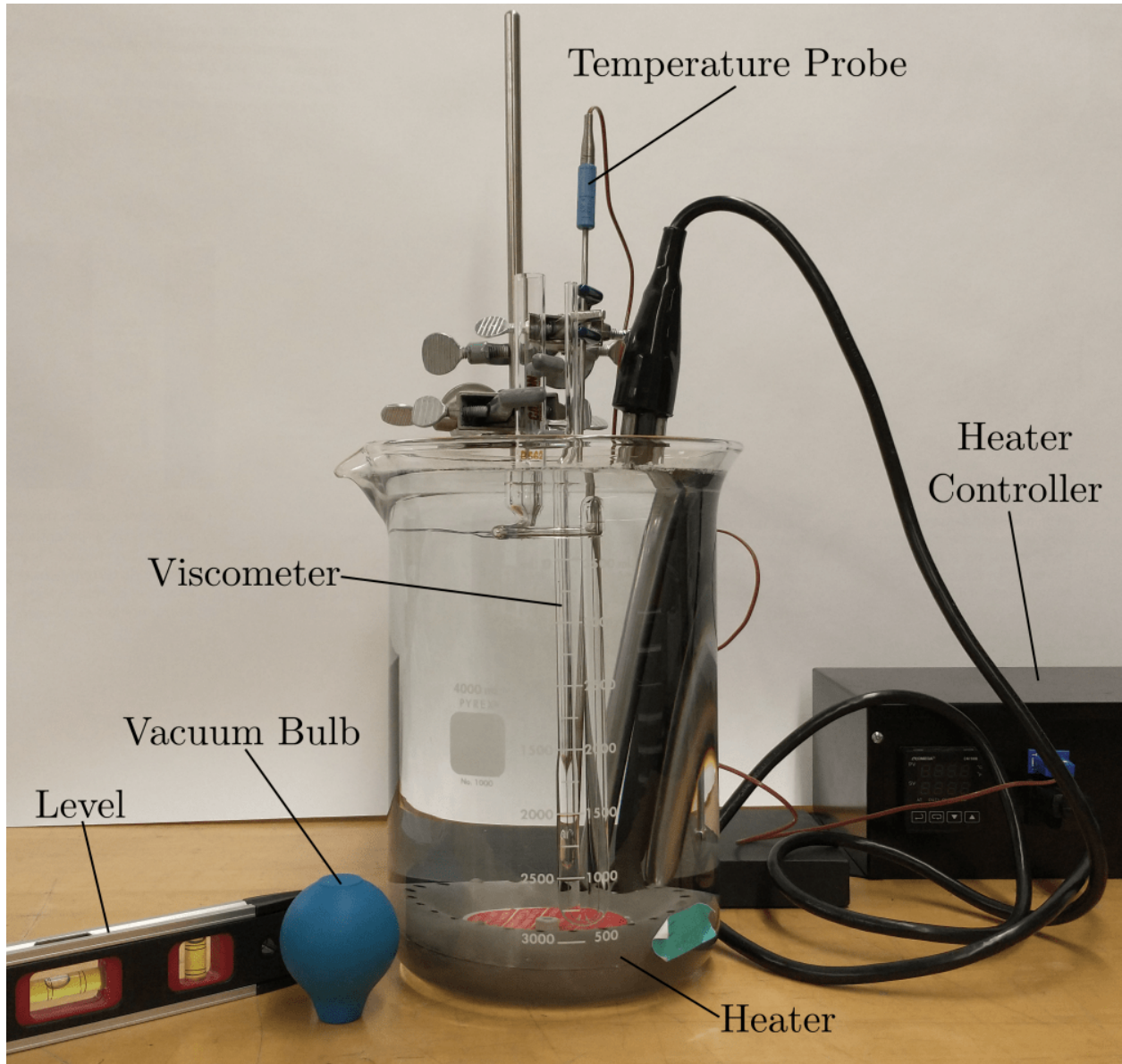


**Figure 2.2** – Test setup used to measure kinematic viscosity at a controlled temperature using a Zeitfuchs cross-arm glass capillary viscometer.

set up to ensure that the following measurements would be accurate. This alignment was done using a level to ensure the top of the viscometer was perfectly flat. The temperature of the water bath was also monitored using an external thermometer (Kessler 76 mm partial immersion thermometer) to double-check the temperature before beginning the experiment. As labelled in Figure 2.2, the sample was loaded into the larger tube on the viscometer. It was then allowed at least 15 minutes to reach equilibrium at 32°C, at which point the vacuum bulb was used to apply pressure to the inlet tube and force the sample into the capillary tube. The fluid was allowed to travel through the U-tube, where a timer was started when the sample passed the first timing line and stopped when it passed the second. The kinematic viscosity,  $\nu$ , was calculated using the elapsed time,  $t$ , and the viscometer conversion constant,  $C_v$  as:

$$\nu = tC_v$$

where the calibration constant for the Zeitfuches cross-arm viscometer was given by its calibration certificate in Appendix A.1 as  $C_v = 0.009463 \text{ mm}^2/\text{s}^2$ , but this was corrected using the local gravitational constant to be:

$$C_{v,corrected} = \frac{9.812}{9.801} \cdot 0.009463 = 0.009474 \text{ mm}^2/\text{s}^2$$

where the local gravitational constant at the University of Alberta was taken to be  $g = 9.812 \text{ m/s}^2$  [84].

Using the measured value of kinematic viscosity and the previously measured density, the dynamic viscosity,  $\mu$  could then be calculated [85]:

$$\mu = \nu\rho \tag{2.3}$$

Following each measurement, the viscometer was then cleaned and replaced in the water bath for the next measurement.

These measurements took a significant amount of time, so only two replicates were run to ensure the measured value was accurate. Since the percent difference between replicate viscosity measurements was generally less than 1%, further measurements on each sample were not considered to be necessary. The standard deviation of the replicate kinematic viscosity measurements was then used to calculate the uncertainty in the dynamic viscosity, as covered in Appendix B.2.

The measurement range of the viscometer used in this work was 2 and 10  $\text{mm}^2/\text{s}$ , although viscosities up to approximately 13  $\text{mm}^2/\text{s}$  were measured. To verify that these higher measurements would be accurate, the viscosity of ethylene glycol was measured. Ethylene glycol was used as its dynamic viscosity can be found in literature and is close to that of the inks used in this work. Therefore, if this measurement was accurate, the measured ink

viscosities should also be accurate. For this test, the known dynamic viscosity of ethylene glycol was taken as 13.61 mPa · s from Bohne et al. [86] at 29.9°C. As viscosity can be quite temperature-sensitive, the verification test was run at 29.9°C for comparison. The density of ethylene glycol was also obtained from Bohne et al. as 1.10569 g/mL. Following the procedure laid out above, two replicate measurements were performed on samples of ethylene glycol, resulting in a dynamic viscosity of 13.01 mPa · s at 29.9°C. This resulted in an error of 4.57% compared to the literature value, so this testing method should be accurate withing 5% error for the inks tested in this work.

### 2.2.3 Surface Tension Characterization

The surface tension of a fluid can be measured using multiple methods such as pendant drop, Du Noüy ring, Wilhelmy plate, capillary rise, and droplet weight or volume [87–89] and is important in determining ink printability. Surface tension is a component of the Ohnesorge number and the DMC-11610 printhead recommended the surface tension of an ink be between 28 and 33 mN/m [75]. Many of these measurement techniques could not be used as they required specialty equipment that the ESDLab did not have access to. The droplet weight method was ultimately selected as it was relatively simple and allowed for the use of small sample sizes [90], which was important as the inks used in this work were made in batches of 3 to 4 mL. A simple method described by Riba and Esteban [87] was used which only required a burette with a known outlet capillary diameter. The basic idea behind this method is that a droplet hanging at the end of a capillary is in perfect balance with gravity the moment before it falls. This balance is visualized in Figure 2.3, and can be represented by summing the forces of surface tension and gravity to zero:

$$F_{net} = F_{st} - F_g = 0$$

which can be expanded to obtain Tate’s law [87, 88, 90]:

$$F_{st} = F_g \rightarrow 2\pi r\gamma = mg \tag{2.4}$$

where  $r$  is the capillary radius where the droplet forms,  $\gamma$  is the droplet surface tension,  $m$  is the droplet mass, and  $g$  is the gravitational constant. To achieve the surface tension in the desired units of mN/m, the droplet mass should be in mg, the gravitational constant in m/s<sup>2</sup>, and the capillary radius in mm.

The experimental procedure to measure the surface tension of a sample fluid using Equation (2.4) by the drop weight method is based on the fact that Tate’s law holds true for the moment at which the droplet falls due to the force of gravity. If the mass of this droplet is then measured, the fluid surface tension can be calculated. The capillary radius must also

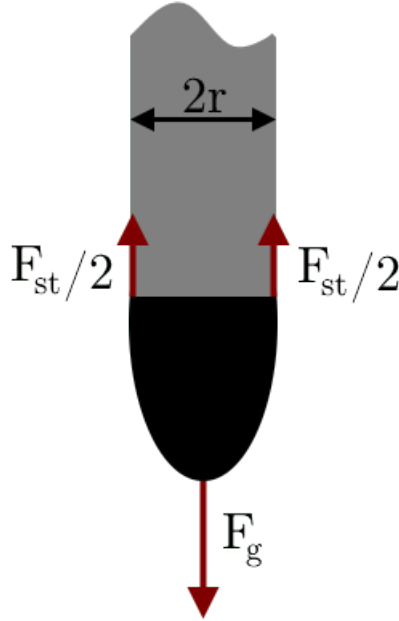


**Figure 2.3** – Balance of surface tension and gravitational forces for a droplet hanging at the end of a capillary.

be known by prior measurement, and can be either the inner or outer radius of the capillary, whichever the droplet forms on. If Tate’s law is used directly, however, the measured surface tension will be lower than expected, as upon dropping, some of the droplet will remain attached to the capillary. This can be accounted for by the use of an empirical correction factor,  $C_T$ , resulting in a modified version of Tate’s law [88]:

$$C_T \cdot 2\pi r \gamma = mg \rightarrow \gamma = \frac{mg}{2\pi r C_T} \quad (2.5)$$

This correction factor was calculated as a function of the capillary radius,  $r$ , and the droplet volume,  $V$ , to the power of 1/3 using the equation:

$$C_T = f(r/V^{1/3}) = 1 - 0.9121(r/V^{1/3}) - 2.109(r/V^{1/3})^2 + 13.38(r/V^{1/3})^3 \\ - 27.29(r/V^{1/3})^4 + 27.53(r/V^{1/3})^5 - 13.58(r/V^{1/3})^6 + 2.593(r/V^{1/3})^7$$

which is valid for  $0 < C_T < 1.2$  [87, 88]. Droplet volume was calculated using the measured droplet mass and fluid density, itself measured using the method described in Section 2.2.1.

Using the drop weight method, the droplet contact angle does not need to be accounted for, so long as the droplet forms only on the end of the capillary. As long as this is the case, the point of attachment of the droplet will have the same radius as the capillary, and Equation (2.4) holds true since the force of surface tension acts along the length of the attachment radius. Depending on the properties of the tested fluid, the droplet can begin to “creep” up

the capillary. This effect generally occurs for droplets with a value of  $r/V^{1/3} < 0.4$ , and can be confirmed by visual inspection during testing [88]. For the capillary radius and samples used in this work, droplets did not show this creeping behaviour, and so the contact angle should not influence the results.

The test setup used consisted of a glass burette (Eisco Labs 10 mL burette with PTFE Needle Valve Stopcock) with a syringe tip attached at its end, and a glass sample collection vial, all shown in Figure 2.4. A syringe tip was used as the capillary since the burette tip was tapered, and so did not have the constant radius that was necessary for use in Equation (2.5). Before testing, the vial was weighed so its dry mass was known. In order to improve the droplet mass measurements as each individual droplet could be quite small, at least 30 droplets were collected and their total mass measured [90]. When performing the experiment, it was also important to allow at least 30 seconds between each droplet to avoid hydrodynamic effects that could influence droplet size [91]. The needle stopcock of the burette was useful to this effect, as it allowed for fine control over fluid flow. Following the collection of 30 droplets, the vial with the droplets was weighed (Entris 124i-1S by Sartorius, 0.1 mg resolution) and the average mass of a single droplet calculated. The surface tension of the fluid was then calculated using Equation (2.5), and this process was repeated three times to obtain an average value.

Validation tests were done on the surface tension setup using PG and IPA to ensure that this test procedure was accurate. These fluids were used for testing as their nominal surface tension values are above and below the recommended range of the Dimatix printer, respectively. The PG test resulted in a surface tension of  $35.3 \pm 0.3$  mN/m, which had an error of 3.80% compared to the literature value of 36.6 mN/m [92]. Likewise, the IPA test resulted in a value of  $20.9 \pm 0.6$  mN/m, with an error of 1.99% compared to the literature value of 21.34 mN/m [93]. Both of these measurements resulted in small enough errors that the measured results could be considered adequately accurate. The method used to calculate the uncertainty in surface tension measurements is covered in Appendix B.3.

This method does not allow for the temperature to be controlled during testing and so the resulting surface tensions were measured at room temperature. From 20°C and 35°C the surface tension of IPA changes by 6.9% [94], and between 22.4°C and 40°C the surface tension of PG changes by 4.4% [95]. As these were the primary components of the inks that would be characterized in this work, similar errors will be assumed between the measured surface tension values and the actual values at the printing temperature of 32°C.

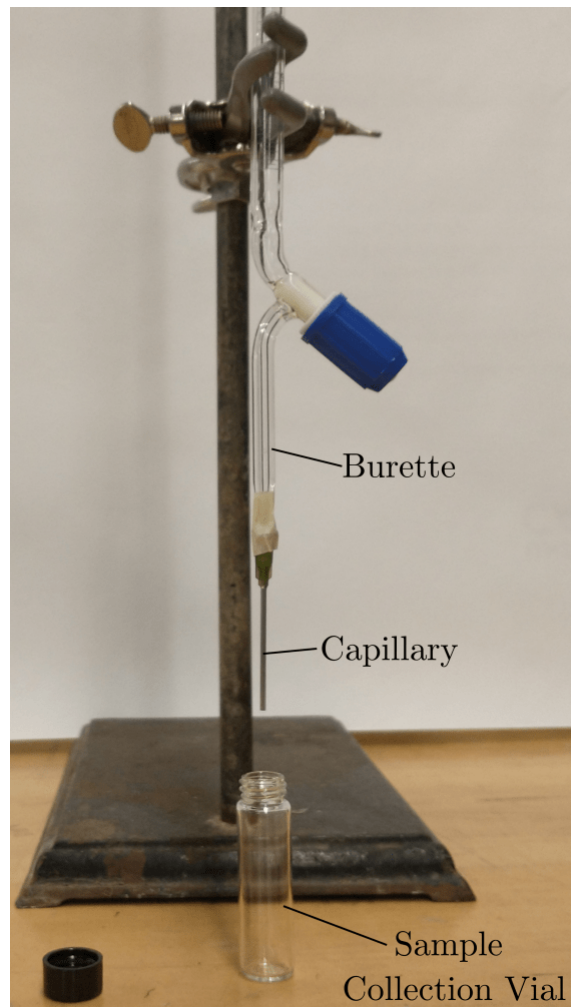


**Figure 2.4** – Experimental setup used to measure fluid surface tension by the drop weight method.

## 2.2.4 Particle Size Measurement

The size of solid particles in the inks was measured by dynamic light scattering (DLS) (Particle Analyzer Litesizer 500, Anton Paar, 658 nm wavelength laser, controlled with Kalliope Software version 2.28.0). DLS functions by aiming a laser light source at the sample and measuring fluctuations in the scattered laser light over time. The light is scattered by particles in the sample and over a short time span, from  $t$  to  $t + \tau$ , the scattered light measurements are correlated [96]. The small time span  $\tau$  is referred to as the correlation time or delay time. For a very small  $\tau$ , on the order of microseconds, the measurements will be similar, but as  $\tau$  increases, the correlation between measurements decreases [97]. The reason for this is the Brownian motion of the particles in the sample causes the light to scatter differently over time as the particles move from where they were for the initial measurement. Brownian motion describes the random movement of particles, from the scale of subatomic to colloidal particles, and for colloids is caused by the kinetic energy of the molecules that make up a fluid constantly contacting the larger particles and pushing them around [98]. The speed at which particles move under Brownian motion is inversely related to the size of the particles, as well as dependent on solvent temperature and dynamic viscosity, these measurements can be used to determine the size of the particles in the sample [96].

To obtain the particle diameter following the measurements of scattered laser light, the Kalliope software that interfaces with the Litesizer 500 performs multiple calculations on the light scattering data. A cumulant model is used to generate a correlation function based on the measured intensity of the scattered light, and from this the average hydrodynamic radius of the particles in the sample can be determined. The procedure used by the Kalliope software is based on the algorithm described by ISO 22412 [97], however, in this work the “advanced” algorithm provided in the software was used, which modifies the ISO standard, but how it does this is not explained entirely by the software. In any case, it begins with the correlation function based on the intensity of the scattered light measured over time [97]:

$$G^{(2)}(\tau) = \langle I(t) \cdot I(t + \tau) \rangle$$

where  $I(t)$  is the intensity of the scattered light as a function of time, and the  $\langle \rangle$  brackets represent an average of their contents over time  $t$ .  $G^{(2)}(\tau)$  is an exponential decaying function in the form of [97]:

$$G^{(2)}(\tau) = A[1 + B \exp(-2\Gamma\tau)]$$

where  $A$  is the “baseline”, a constant proportional to  $\langle I \rangle^2$ ,  $B$  is a constant defined by the instrument that has a value  $\leq 1$ , and  $\Gamma$  is the decay rate. An example of what this correlation function looks like when fit to an actual measurement is provided in Figure 2.5a. From this function, the decay rate,  $\Gamma$ , can be obtained and subsequently used to calculate the diffusion

coefficient,  $D$ , through [97]:

$$\Gamma = D \left[ \frac{4\pi n}{\lambda_0} \sin(\theta/2) \right]^2 \quad (2.6)$$

where  $n$  is the solvent refractive index,  $\lambda_0$  is the laser wavelength, and  $\theta$  is the scattering angle. Finally, the Stokes-Einstein equation relates the diffusion coefficient to the hydrodynamic radius, given that the temperature and dynamic viscosity of the solvent are known [96, 97]:

$$D = \frac{k_B T}{6\pi\mu R_h} \quad (2.7)$$

where  $k_B$  is Boltzmann’s constant,  $T$  is the solvent temperature,  $\mu$  is the solvent dynamic viscosity, and  $R_h$  is the particle hydrodynamic radius. In this work, the solvent temperature was held at 32°C within the Litesizer 500 during testing, and the dynamic viscosity was measured using the techniques covered in Section 2.2.2. The hydrodynamic radius calculated this way was an average for the entire sample however, as mentioned before, the actual algorithm used by the software may be modified from the theory laid out here.

To supplement the average hydrodynamic radius of a given sample, the Kalliope software also calculates a particle distribution, which was useful for the inks in this work. In addition to the calculation of average particle size, it is also useful to have an estimation of the largest particles in the sample. The process of obtaining this distribution for a sample is not covered in detail here, as Anton Paar does not provide a breakdown of the process, only explaining that they used a combination of non-negative least squares and Tikhonov regularization methods [96]. The results of the DLS measurements were then represented as a plot of particle distribution vs particle size. An example of this is given in Figure 2.5b. In this work, intensity weighted particle distributions were used, meaning the distribution of particles will be weighted by the amount of light scattered by particles of varying sizes. This is the default distribution provided by the Kalliope software used to operate the Litesizer 500 device, but the software can also calculate volume and number weighted distributions, which can be useful in determining the sizes of particles present in the inks. These distributions will not be used in this work, however, as DLS results are only used here to check that there are no particles too large to print and that the particle distribution is narrow. These additional distributions would also require the refractive index and absorption index of the particles, which are not known.

For additional information on how wide the particle distribution is, the polydispersity index, given as a percentage value, is also calculated using the cumulant model. A polydispersity index less than 10% indicates the particles in solution are mostly uniform in size, and the distribution become broader as the value increases [96]. A uniform distribution is desired as it indicates that there are no large agglomerates forming in the solution however, it does not provide information on the shape of the particle distribution.

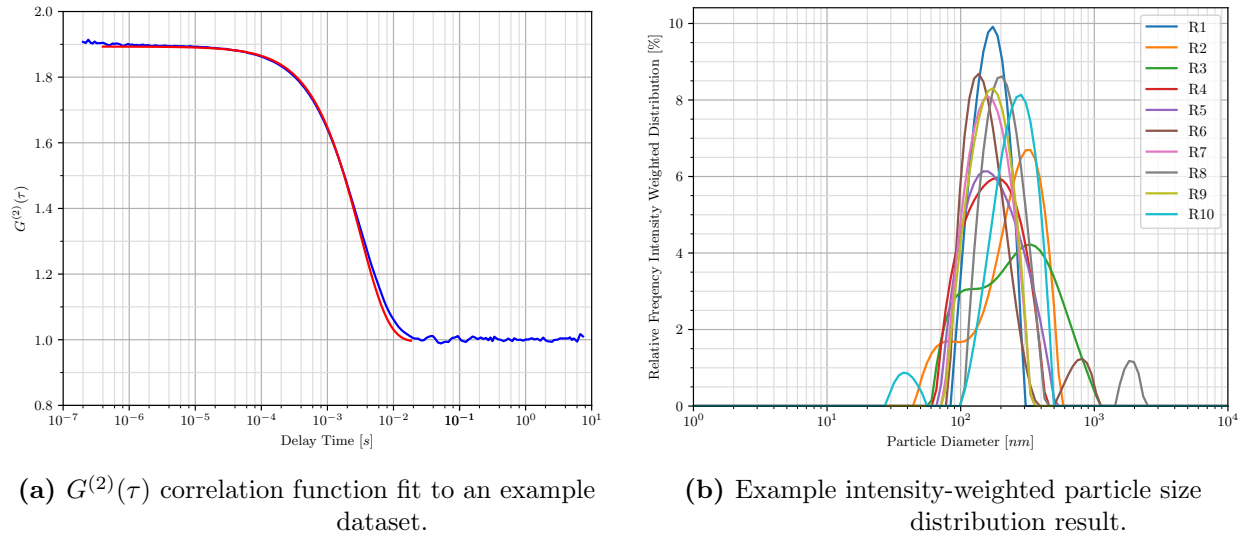


**Figure 2.5** – Example outputs from the Kalliope software when analysing DLS measurements.

As was mentioned, temperature, dynamic viscosity, and laser wavelength were known, and additionally, a back scattering angle of  $175^\circ$  was used as that works best for turbid samples such as inks [96]. The solvent refractive index however, was not known, which was an issue as this value was needed for Equation (2.6). As inks are made up of multiple liquid components with various refractive indices, the value for the ink would have to be determined experimentally. This could be done using the Litesizer 500, but previous results attempting to do this by Storbakken resulted in large errors [40]. Due to this, a refractive index of 1.39, corresponding to a 1:1 mixture of water and PG by weight, was used for measurements in this work, as it should have been close to the actual refractive index of the inks used. Storbakken performed tests on particle size data obtained by DLS to determine that the maximum error to be expected when using this approximation of the refractive index, and it was noted to be approximately 15%. As DLS results were only used as a rough estimate of the particle size distribution, this was deemed an acceptable result.

## 2.3 Inkjet Printing Catalyst Coated Membranes

After an ink was formulated and its properties met the requirements for printing, it was then used to fabricate CCMs that in turn were used to assemble AEMWE cells. The use of an ink to print CCMs was also the final test in determining if an ink formula was successful. Although the properties of an ink formula were measured before printing to ensure they match the requirements provided by Fujifilm Dimatix [75, 76], actually being able to print layers with the necessary amount of ink to produce a CCM determined if the ink was truly



(a) Fujifilm Dimatix DMP-2831 drop-on-demand inkjet printer.



(b) DMC-11610 cartridge printhead (above) and reservoir (below).

**Figure 2.6** – Pictures of the Fujifilm Dimatix inkjet printer and associated cartridges used in this work.

usable. Inkjet printing was used for CCM fabrication in this work as it allowed for accurate deposition of the catalyst material directly onto the AEM. The process used for printing inks described here was developed in an effort to ensure consistent printing performance of the catalyst inks between batches of CCMs.

The printing process utilized in this work was based on previous work done in the ESDLab [40, 42]. Inks were ideally printed soon after they were made, with most inks in this work being made and printed the same day to prevent changes to the rheology of the inks that may occur if they were stored for an extended period of time [99]. If an ink had to be stored between when it was made and printed, it was stored on a magnetic stir plate set at 350 rpm in an effort to prevent the dissolved ionomer and catalyst nanoparticles from settling and the fluid properties from changing. Prior to printing, the ink that would be used was degassed in an ultrasonic water bath for 1 hour (Branson 1800, set to degas mode). Then, 2 to 3 mL of ink was loaded into a DMC-11610 cartridge for use with the DMP-2831 inkjet printer. The cartridge printheads each had 16  $21 \times 21 \mu\text{m}$  nozzles spaced  $254 \mu\text{m}$  apart that each utilized piezoelectric crystals to produce 10 pL droplets. During printing, droplet spacing was set to  $20 \mu\text{m}$ . Pictures of the DMP-2831 printer along with the cartridge are provided in Figure 2.6. Piezoelectric drop-on-demand inkjet printing functions by placing a small piezoelectric crystal within a capillary upstream of the nozzle. When actuated, the crystal pulses and pushes out a small amount of ink to generate the desired droplet [77].

Using inkjet printing allowed for catalyst material to be deposited accurately and evenly over the desired area, which in the case of this work was a  $5 \text{ cm}^2$  area arranged in a  $22.37$

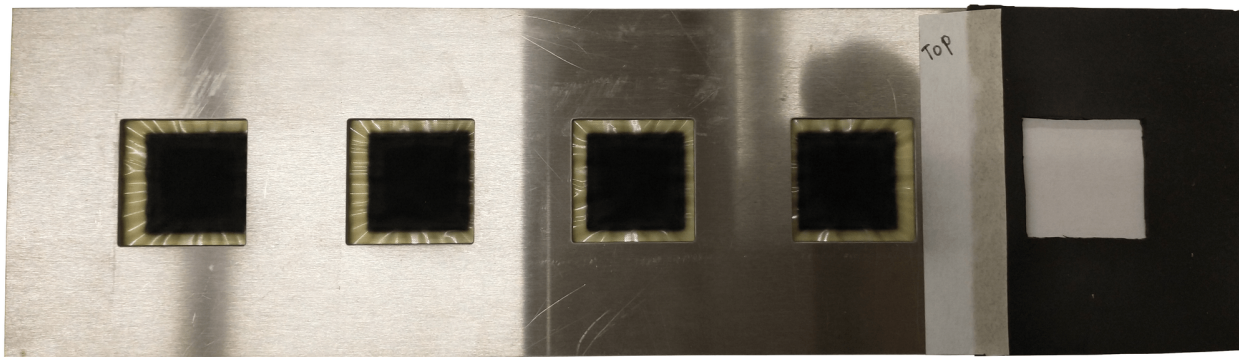


**Figure 2.7** – Metal print guide used to hold Aemion+ membranes in place while printing. Shown here with completed CCMs.

× 22.37 mm square pattern. As preparing the printing process took a significant amount of time, up to four CCMs would be printed simultaneously onto Aemion+ membranes with serial number AF2-HLE8-50-X or AF2-HWP8-75-X, both of which were used in this work. Additionally, it could take up to 6 hours to print all layers necessary to achieve the desired catalyst loading, and over this time the membranes would swell due to the absorption of ink solvents and subsequently contract as the liquid evaporated. This would cause the membrane to wrinkle which could slightly shift its position, leading to a misalignment with the print pattern. The solution to this was to fix the membrane in place as well as possible by taping it to a metal print guide that would remain rigid during printing and could in turn be taped to the printer platen. A picture of the print guide used along with completed CCMs is provided in Figure 2.7, and the drawing used to fabricate the print guide is given in Appendix A.3.

As can be seen in Figure 2.7, in addition to the 4 holes used for printing CCMs, a piece of rubber with another hole of the same size was attached to the metal print guide and was used to hold a piece of aluminium foil. The same pattern used to print catalyst layers onto the membrane was used to print an equal amount of ink onto the aluminium foil, which could be weighed to determine the current catalyst loading after any number of layers. This way, the loading could be checked throughout the printing process and the number of layers adjusted to compensate for variability in printing. Before weighing, the aluminium foil was dried in an oven at 80°C.

The anode side catalyst layer was printed first, as the 1 mg/cm<sup>2</sup> IrO<sub>x</sub> loading used would required 2 to 3 times more layers to be printed compared to the 0.1 mg/cm<sup>2</sup> Pt loading for the cathode side. The extra layers would result in additional membrane wrinkling which could be partly mitigated as the membrane was still attached to the plastic backing sheet that it shipped with. After detaching the Aemion+ AF2-HWP8-75-X membrane from the backing sheet it did not stick back onto it again, and so it was decided that the most layers should be printed while the membrane was still attached to the backing.

## 2.4 Electrolysis Cell Configuration

Following the fabrication of CCMs, single cells would be assembled, each using one CCM along with a Scribner redox flow cell test fixture so that the cell performance could be characterized in-situ. This test fixture could be installed in the AEMWE cell test station by connecting the cell inlets and outlets to their respective gas disengagement unit (GDU), each serving as an electrolyte reservoir and to separated the electrolyte and produced gasses leaving the cell. The cell was electrically connected to one of two potentiostats used throughout this work so that it could be characterized by the techniques described in Section 2.5. In addition, cells were characterized in different electrode feed configurations, where only one electrode would be fed at a time, and a reference electrode was integrated into the cell.

### 2.4.1 Cell Construction

Cells were constructed using a Scribner redox flow cell test fixture, custom-made bipolar plates with serpentine flow channels, PTFE gaskets, and PTLs, on either side of the CCM. The redox flow cell test fixture was used instead of a standard fuel cell test fixture because the inlet and outlet tubes of the redox flow cell were made of chemically resistant plastics and passed directly through the aluminium back plates. This was necessary for AEMWE cells in order to avoid contact between aluminium metal and the alkaline electrolyte fed into the cell. Initial cell tests presented in this work used bipolar plates with integrated serpentine flow channels made from graphite on the cathode side and titanium on the anode side. Under the high pH conditions of the cells however, these materials were not optimal given the respective half-reaction potentials that they were subject to (0.401 V at the anode, -0.828 V at the cathode, both versus SHE [15]), as seen in the Pourbaix diagrams in Figure 2.8. Due to this, the bipolar plates were eventually replaced with plates made from corrosion-resistant nickel 400 alloy that used the same serpentine flow channels. The drawings used to fabricate these plates are given in Appendix A.4. For the same reason, nickel felt (Bekipor) was used as the PTL on both sides of the cell, although early cells used carbon paper at the cathode side.

Cells were assembled by layering each component on top of the last, beginning at the cathode side. Figure 2.9 provides an exploded view of all these components. Following the Scribner back plates were the gold-plated current collectors that were also part of the redox flow cell test fixture. All potentiostat connections were made with the top part of these plates that stick out above the cell, as they were in electrical contact with the bipolar plates. There was also an insulating layer on the current collectors between themselves and the back plates. After the bipolar plates, gaskets were used to seal the space around the PTLs. Rigid PTFE-reinforced gaskets of 10 mil thickness were used prior to reference electrode integration, but this arrangement was changed as described in Section 2.4.4 due to the use

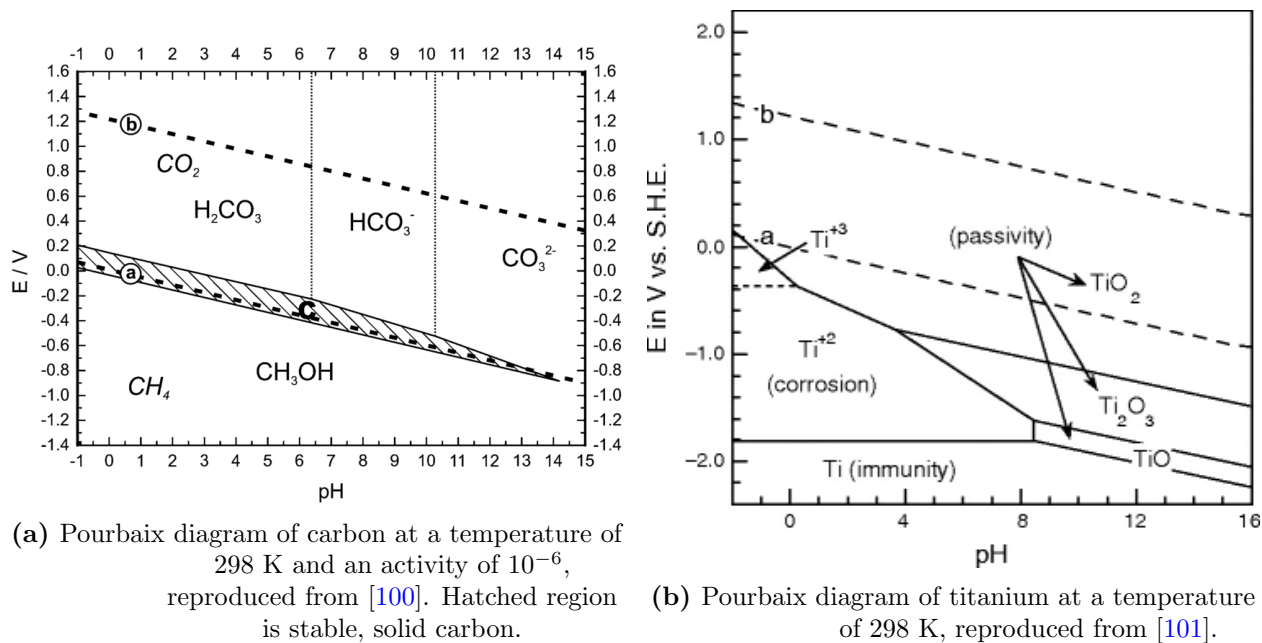


**Figure 2.8** – Pourbaix diagrams showing the stable phases for titanium and graphite at varied potentials and pH values.

of lamination sheets with the reference electrode. Nickel felt and/or carbon paper PTLs were cut to fit within the gasket center holes and make contact with the electrocatalyst layers previously printed onto either side of the CCM at the center of the cell. Following the assembly of these parts, the screws from the test fixture were used to apply compression and hold the cell together. For cells tested in this work, a torque wrench set to 50 in·lb was used to consistently tighten these screws.

## 2.4.2 Test Station Equipment

Following AEMWE cell assembly, the cell was connected to both the KOH electrolyte feed system and potentiostat used for taking the measurements. Aqueous 1 M KOH solutions was fed to both electrodes, or either electrode individually. These solutions were prepared from deionized water and solid KOH (Fischer Scientific P250-1 Potassium Hydroxide) (Equations used to calculate the necessary solid KOH are covered in Appendix D.2). The system used to feed electrolyte to the cell consisted of two GDUs that would each be filled with 500 mL of 1 M KOH solution, and pumped through the cell using a peristaltic pump (Gilson Minipuls 3). In effect, this setup created two closed loops; electrolyte was fed into the cell and a mixture of electrolyte and produced gas exited the cell and returned to the GDUs, where they would separate. Oxygen gas was vented to the atmosphere and hydrogen was vented to a hydrogen disposal line, both through 1/3 psi check valves. These check valves stopped air from entering the GDUs in an effort to prevent atmospheric carbon dioxide from reacting

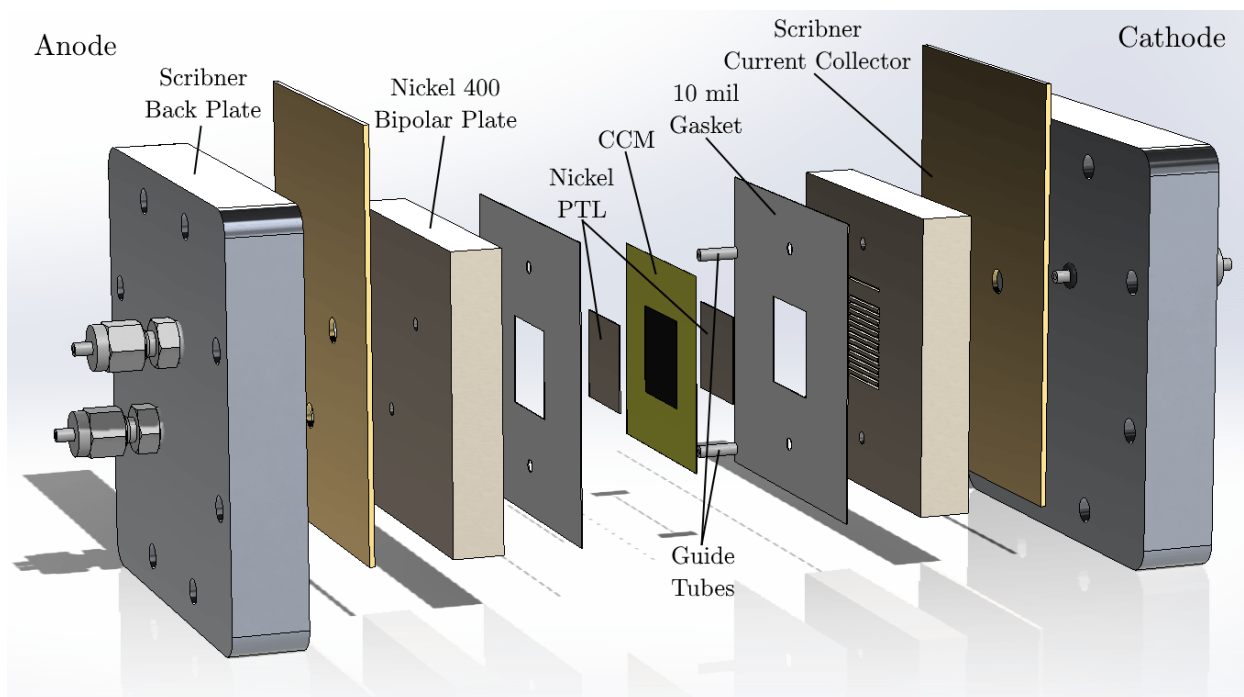


**Figure 2.9** – Exploded view of the AEMWE cell components.

with the KOH in the electrolytes. The GDUs and cell had integrated heaters to maintain the system at a constant 60°C. Figure 2.10 provides a representation of the connections between the test cell and the electrolyte feed system, as well as the electrical connections made with the potentiostat. All electrolyte-containing equipment was also kept within spill trays in case of a leak of the KOH electrolyte.

Throughout cell testing in this work, the cell potential was controlled and measured with either an in-house built system (BK Precision 9202 power supply and Arduino UNO) or a Biologic SP-300 potentiostat. The in-house system was used to perform cell conditioning, polarization curves and stability tests on AEMWE cells prior to the integration of a reference electrode. This system was more cost-effective and was dedicated to the AEMWE cell test station compared to the Biologic potentiostat that was shared between test stations, but was not able to perform tests that required AC or a smooth voltage ramp such as EIS or LSV. The Biologic potentiostat was therefore used for these tests, as well as for all testing of cells that used a reference electrode. The connections for the potentiostats are shown in Figure 2.10. Both systems used separate power application and voltage measurement leads, and only one system was connected to a cell at a time.

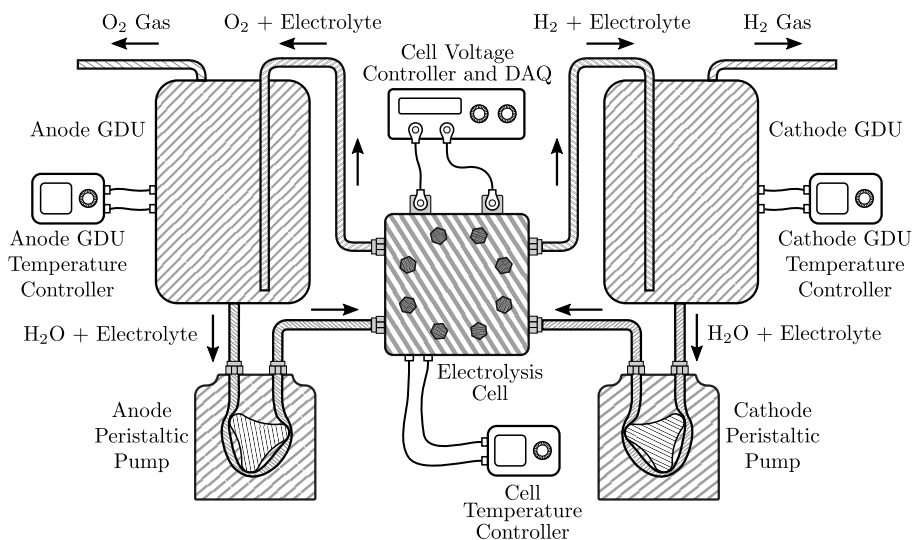


**Figure 2.10** – Diagram of the connections made between a tested AEMWE cell and the test station equipment, including both the electrolyte feed system and potentiostat, reproduced from Storbakken [40].

### 2.4.3 Electrode Feed Method Testing

When testing the effect of cell feed method, a cell would be tested in three configurations: two-electrode feed (TEF), anode-only feed (AOF), and cathode-only feed (COF), with TEF being tested both before and after the two single-electrode feed configurations. Additionally, when switching to either of the single-electrode feed configurations, the 1 M KOH solution that would be fed to the electrode in question was replaced to maintain consistency with the refresh of KOH following normal conditioning. The GDUs for the electrode that was not fed was disconnected from the cell inlet side, but the outlet remained connected for disposal of the produced gas. As the GDUs would be opened and exposed to atmosphere when switching feed methods, the short conditioning profile covered in Section 2.5.1 was run before testing a cell in a new configuration.

As discussed in Section 1.2.2, little work has been done to date on the operation of AEMWE cells under single-electrode feed and how this affects cell operation. Single-electrode operation may cause a decrease in cell performance due to loss of reactant and electrolyte at the electrodes, but with the potential benefit of hydrogen production at high pressure. Changes to cell performance were characterized in this work, but cell durability was not, as the longest cell tests done were only be six hours in length.

## 2.4.4 Reference Electrode Integration

When performing the tests covered in Section 2.5 with a standard AEMWE cell, the responding variable was the cell voltage or electrical potential,  $E$ , (cell current,  $i$ , was the responding variable for constant voltage stability tests). While this provides useful information on how performance changes based on cell construction and operational parameters, additional information could be obtained if the potentials of the two electrodes was separated. In an electrochemical system, this is done by adding a third electrode of constant, known potential, and measuring the potential difference between this reference electrode and the working electrode. A diagram showing the layout of a standard 3-electrode system is provided in Figure 2.11. In this work, the anode of an AEMWE cell was considered the working electrode, and the cathode the counter electrode. The total cell voltage was measured as the potential difference between anode and cathode,  $E_1$ , and the anode voltage was measured as the potential difference between anode and reference,  $E_2$ . The relationship between these two measured potentials can be represented mathematically as:

$$E_1 = E_{cell} = E_{working} - E_{counter}$$

$$E_2 = E_{working} - E_{reference}$$

and the counter electrode potential relative to the reference electrode was calculated as:

$$E_2 - E_1 = (E_{working} - E_{reference}) - (E_{working} - E_{counter}) = E_{counter} - E_{reference}$$

This allowed the two electrode potentials to be measured relative to the reference electrode potential. Additional calculations could be made to obtain the electrode overpotentials, or the difference between the measured and equilibrium potentials, and to find the electrode potentials versus any desired standard such as the standard hydrogen electrode (SHE) or reversible hydrogen electrode (RHE).

The potential measured when no current flows and the reaction is at equilibrium is known as the open circuit voltage (OCV), and the change in potential when a current is applied is called an overpotential,  $\eta$ . Overpotential is a measure of the efficiency of an electrochemical cell, and indicates energy above that which is theoretically expected to drive a reaction. Overpotential can be represented as:

$$\eta = E - E^{eq} \tag{2.8}$$

where  $E$  is the applied electrode potential and  $E^{eq}$  is the theoretical equilibrium potential of the reaction or half reaction. The equilibrium potential must be calculated using the standard potential,  $E^0$ , and the Nernst equation [66, 102]:

$$E^{eq} \simeq E^0 - \frac{R_g T}{v_e F} \ln \left( \frac{\prod_i^N a_i^{v_i}}{\prod_j^M a_j^{v_j}} \right) + \frac{\Delta s^0}{v_e F} (T - T^0) \tag{2.9}$$

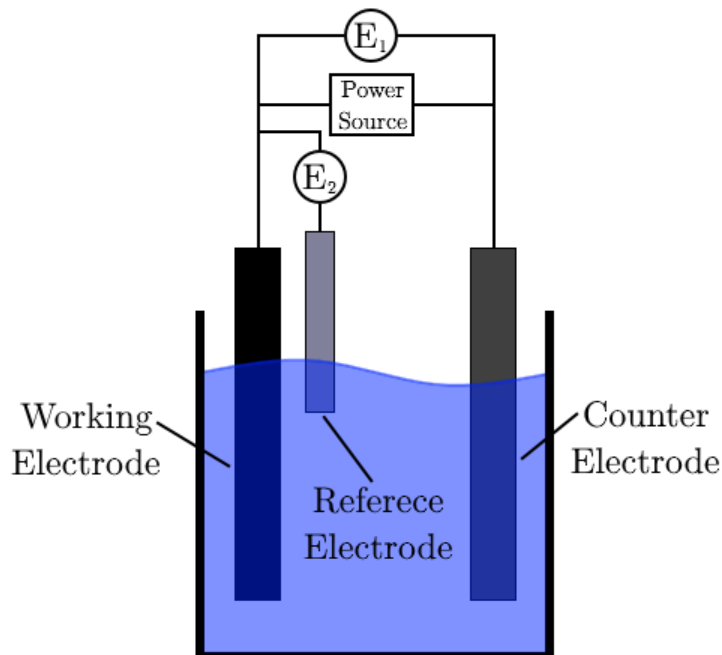


**Figure 2.11** – Diagram of a standard 3-electrode electrochemical system.

where  $R_g$  is the ideal gas constant,  $T$  is the temperature in Kelvins,  $v_e$  is the moles of electrons transferred per mole of reactant,  $F$  is the Faraday constant,  $a_i$  and  $a_j$  are the activities of the reduced and oxidized species, respectively, each raised to the number of moles of that species per mole reactant,  $\Delta s^0$  is the change in specific entropy, and  $T^0$  is the standard temperature ( $T^0 = 298.15$  K). It was important for this work to include the entropy term in Equation (2.9) to account for the effect of temperature, as experiments were run at  $60^\circ\text{C}$ , which lowered the value of  $E^{eq}$ . The change in specific entropy at standard atmospheric pressure and temperature for a half reaction can be calculated as [66]:

$$\Delta s^0 = \sum_i^N (v_i s_i^0)_{reduced} - \sum_j^M (v_j s_j^0)_{oxidized}$$

where  $v$  and  $s^0$  are the number of moles per mole reactant and specific entropy of each species in a given half-reaction. The two  $\Delta s^0$  values from the half-reactions can then be used to obtain the change in specific entropy for the overall reaction as  $\Delta s_T^0 = \Delta s_C^0 - \Delta s_A^0$ . Using Equation (2.9), the equilibrium potentials of the anode and cathode were calculated to be  $E_{anode}^{eq} = 374$  mV and  $E_{cathode}^{eq} = -826$  mV at  $60^\circ\text{C}$ , respectively.

In this work, separated anode and cathode overpotentials were calculated using Equation (2.8). This however, results in values with respect to the reference electrode used to measure the separate potentials. To change the “base” reference electrode, the values of  $E^{eq}$  for both the reference electrode used and the desired reference electrode must be known, and can also

be calculated using Equation (2.9). The electrode overpotentials can then be corrected to any reference electrode by:

$$E_{RE2} = E_{RE1} - (E_{eq,RE2} - E_{eq,RE1}) \quad (2.10)$$

where  $E_{RE1}$  is the measured potential with respect to reference electrode 1 (the electrode used to obtain the measurement), and  $E_{RE2}$  is the measured potential with respect to reference electrode 2 (the electrode to be compared against). In this work, overpotentials were converted to be relative to the SHE, where  $E_{SHE}^{eq} = 0$  V at all temperatures [103].

A modification to the cell construction was required to implement a reference electrode in the system. A Ag/AgCl reference electrode (Pine Research Ag/AgCl in 4 M KCl gel,  $E^0 = +0.199$  V vs NHE, information sheet in Appendix A.2) was used and integrated using the layout selected in Section 1.2.4. Unlike the setup that Xu et al. [53] used, the cell hardware in this work had to use vertically aligned plates due to the inlet & outlet tubing, so some modifications had to be made to integrate the reference electrode. Instead of placing the container with electrolyte on top of the membrane strip, the strip was run from inside the cell into a bottle filled with 1 M KOH solution, into which the Ag/AgCl reference electrode was also inserted. Figure 2.12 shows an exploded view of this setup, and Figure 2.13 shows a picture of the assembled cell attached to the test station. In order to integrate the membrane strip that ionically connected the CCM to the reference electrode, different gaskets were used in the cell. The membrane strip itself was cut from the 15  $\mu$ m thick Aemion+ AF2-HLF8-15-X to ensure the cell stayed sealed during use.

Although Ag/AgCl electrodes are not intended for use in alkaline media, they were cheaper and easier to handle compared to Hg/HgO electrodes. To ensure the reference potential of the Ag/AgCl electrode did not drift over time due to being exposed to the 1 M KOH solution, drift tests were performed at least once before and once after each cell that used it was tested. Drift tests consisted of placing the Ag/AgCl electrode used as a reference into the same aqueous saturated KCl solution as a second Ag/AgCl electrode. This second electrode was always kept in a saturated KCl solution and so was assumed to have a constant potential. The OCV between these electrodes would be measured, and if the difference stayed below 5 mV, the reference electrode potential was considered to be acceptable.

As was covered in Section 2.4, when not using the reference electrode, gaskets of 10 mil thickness were used on either side of the CCM, but when using a reference electrode, lamination sheets of 3 mil thickness each were used and partially laminated to hold the membrane strip in place. This also served to maintain hydration of the membrane strip by isolating it from the atmosphere, which was important for maintaining ionic conductivity. Xu et al. [53] used an alternate method to maintain membrane strip hydration where they placed moistened wipes over the exposed portion of the strip. To verify that the laminated

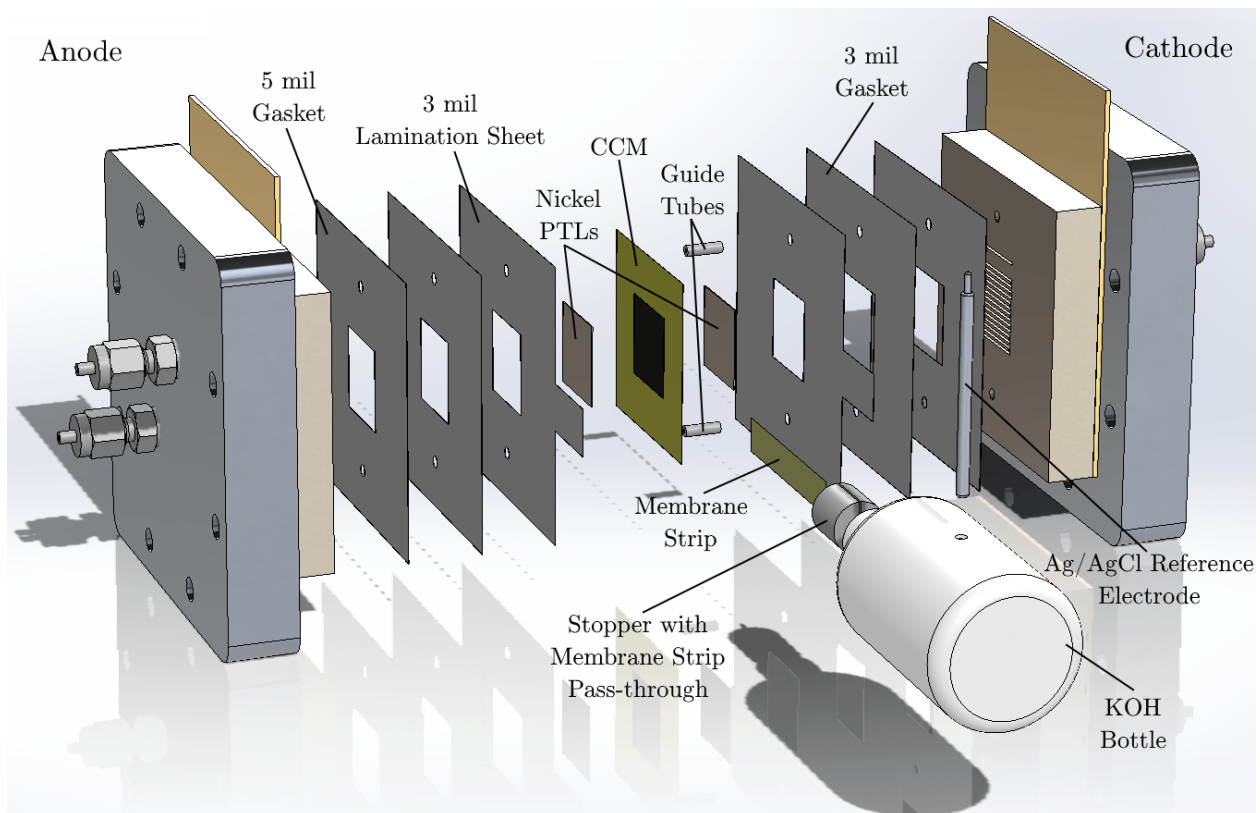


**Figure 2.12** – Exploded view of the AEMWE cell components with an integrated reference electrode.

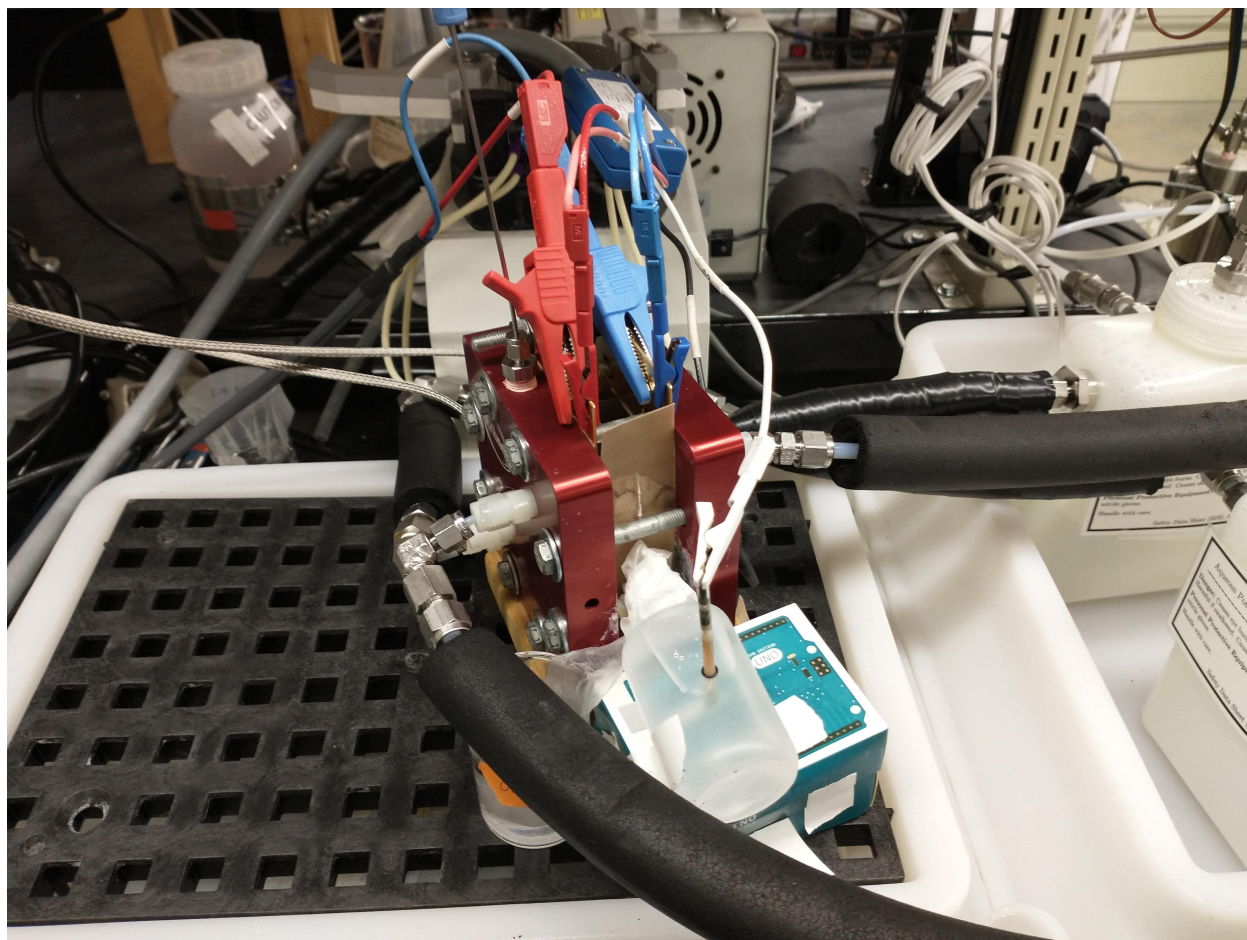


**Figure 2.13** – Picture of an AEMWE cell assembled with the reference electrode and connected to the AEMWE cell test station.

**Table 2.1** – Overview of the testing order used for the cells in this work.

Repeatability Cell Testing		Feed Method Cell Testing	
Number	Test	Number	Test
0	Conditioning	0	Conditioning
1	Polarization curve	1	Polarization curve
2	EIS	2	EIS
3	Polarization curve	3	Polarization curve
4	EIS	4	EIS
5	Polarization curve	5	Stability
6	EIS	6	EIS
7	Polarization curve	7	Repeat for other feed methods
8	EIS		
9	Stability		
10	EIS		

strips would work, a laminated strip, a strip wrapped in KCl soaked wipes, and a bare control strip, were tested by using them to bridge two solutions of KCl, and measuring the potential between Ag/AgCl electrodes placed in the two solutions. The results of these tests are given in Figure 2.14. The fact that the potential measured between the two electrode remained stable for the laminated strip confirmed that this technique would be adequate. A diagram showing placement of the membrane strip in the lamination sheets is provided in Figure 2.15. Since the addition of these lamination sheets added material between the bipolar plates, the gasket thickness had to be reduced to compensate and maintain an acceptable level of compression. To do this, the 10 mil gaskets were replaced with a 3 mil and a 5 mil gasket on both sides of the CCM, which provided an ideal amount of compression.

## 2.5 Electrolysis Cell Characterization

By altering cell construction or operational parameters and performing the tests covered in this section, the effect that these had on cell performance could be studied with the goal of understanding the parameters that influence cell operation in-situ. Table 2.1 provides an overview of the typical testing procedure for the cells tested in this work. Note that for the feed method cells, TEF was tested first, followed by AOF, then COF.

### 2.5.1 Cell Conditioning

Electrochemical cells are generally conditioned prior to operation in order to stabilize and improve performance through a decrease in both kinetic and ohmic overpotentials. This is

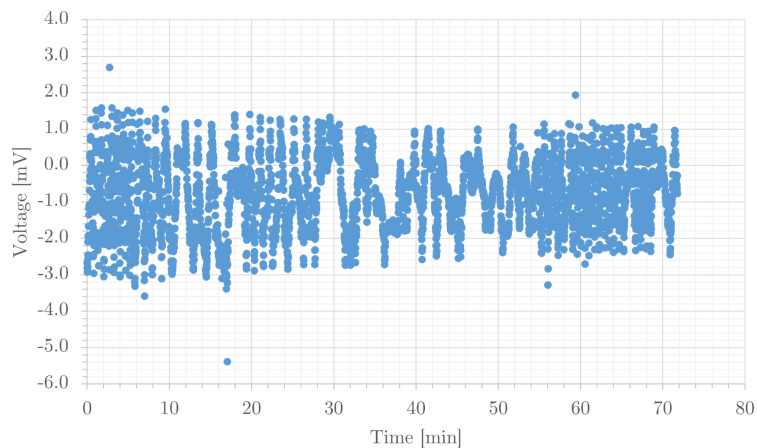
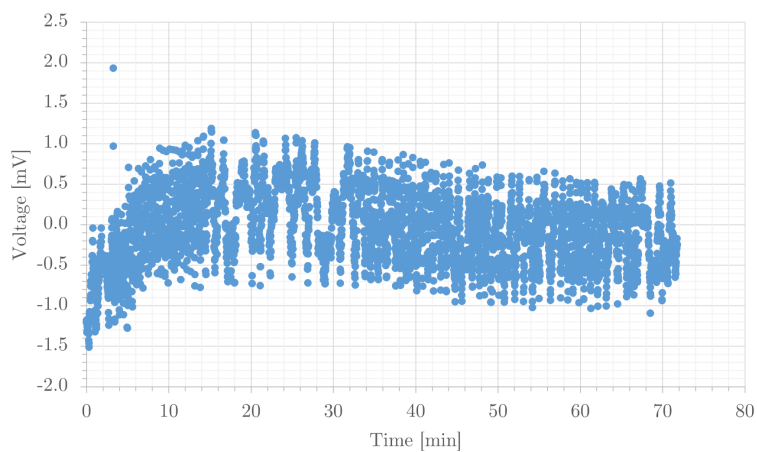
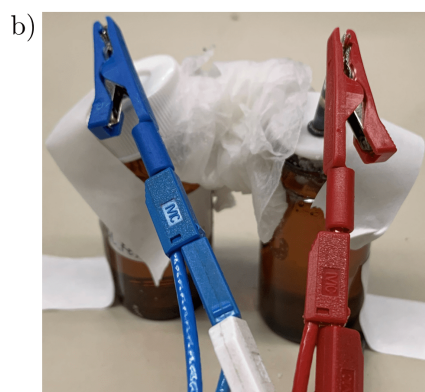
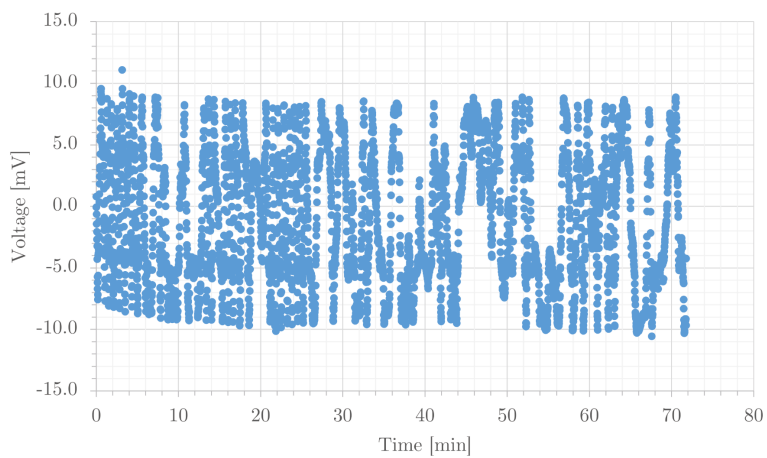
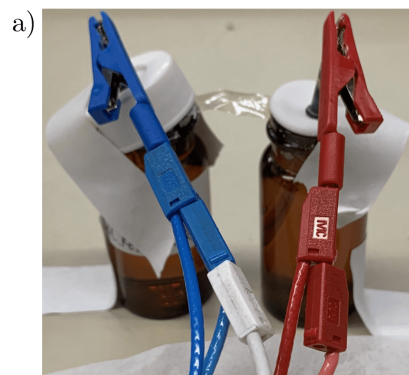


**Figure 2.14** – Potential measured between two Ag/AgCl reference electrodes in saturated KCl solutions connected by a strip of AEM. a) AEM exposed to atmosphere. b) AEM covered with KCl soaked lab wipes. c) AEM laminated.

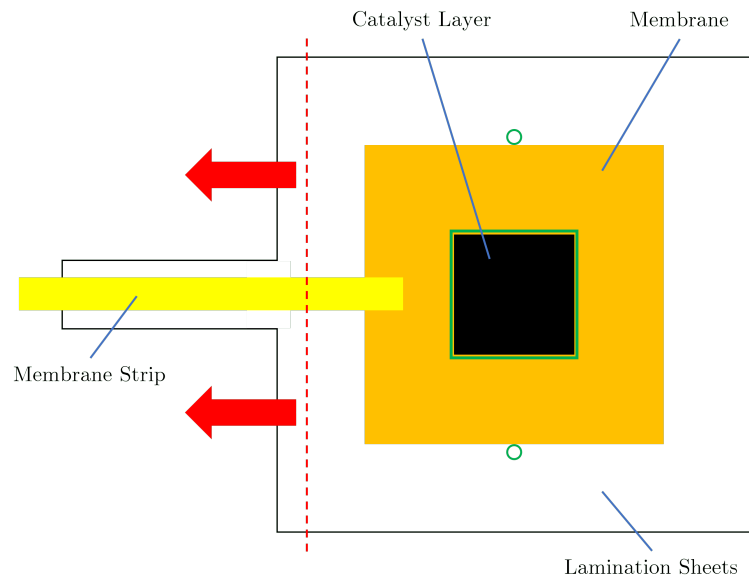


**Figure 2.15** – Lamination sheet layout used to hold in place and keep hydrated the membrane strip that connected to the reference electrode. Lamination sheets were only laminated to the left of the red dashed line and cutouts were made along the green lines.

achieved by removing impurities on the catalyst surfaces, increasing the amount of reaction sites and oxidising the anode catalyst layer through regular cell operation [104]. Cells tested when first implementing Aemion+ membranes were not conditioned as prior results using first generation Aemion membranes showed a significant decrease in performance after operating for even a short time [40]. Due to the increased stability afforded by Aemion+ membranes however, it was decided that a conditioning process would be implemented.

The conditioning profile utilized for cell 3 onwards is provided in Table 2.2, and consisted of multiple long galvanostatic holds stepping up over time, each with short rest periods in between. This profile allowed for the cell to operate at moderate current levels in an effort to achieve the desired effects of cell conditioning (improved stability and activity). As conditioning was the first step in cell operation, the AEMWE test station GDUs was filled with 1 M KOH solution prior to operation. As a standard for cell testing in this work, this 1 M KOH solution was refreshed between cell conditioning and characterization. This profile was based on the conditioning process used for PEMWE cells in the ESDLab [105], as little information has to date been published concerning the conditioning of in-situ AEMWE cells, although lower current densities were used due to the lower performance of AEMWE cells.

During each step of the conditioning process, for the set current value, the cell potential should stabilize. A plot of the applied current and resulting voltage over time for the conditioning process of a cell discussed in this work (Cell 6) is provided in Figure 2.16. For this

**Table 2.2** – Galvanostatic profile used for cell conditioning.

Step	Time [min]	Current [mA]	Current Density [mA/cm <sup>2</sup> ]
0	5	0	0
1	30	50	10
2	5	0	0
3	60	500	100
4	5	0	0
5	60	1250	250
6	5	0	0
7	60	2500	500
8	5	0	0

**Table 2.3** – Short conditioning profile used to displace air from the GDUs.

Step	Time [min]	Current [mA]	Current Density [mA/cm <sup>2</sup> ]
0	5	0	0
1	2	100	20
2	2	500	100
3	2	1000	200
4	2	2000	400
5	60	3000	600
6	5	0	0

case, the cell performance actually deteriorated during conditioning instead of improving. The potential of the cell increased over time, but at the last step, the cell voltage appeared to stabilize. This was consistent throughout all AEMWE cells in this work, and so they were considered to have stabilized during the conditioning process.

The exact procedure used for conditioning was developed while testing the first three cells. Cells 1, 2, and 3 were conditioned using slightly different profiles, but all followed a process of four to six current holds, each increasing in value. It was decided that the conditioning profile used on cell 3 would be repeated on all future cells. Voltage and current plots for the conditioning results of the cells discussed in this work are provided in Figure 2.16 (Cell 6) and Appendix E.1.

As the 1 M KOH solution was refreshed following conditioning, the GDUs would contain atmospheric air following the refresh. This was also true following the change in cell feed method, as the GDUs were opened during this process. To displace the air in the GDUs and bring the system to the same state that it would be in during normal operation, a short conditioning profile was run any time after the GDUs were opened. This profile followed the steps in Table 2.3.

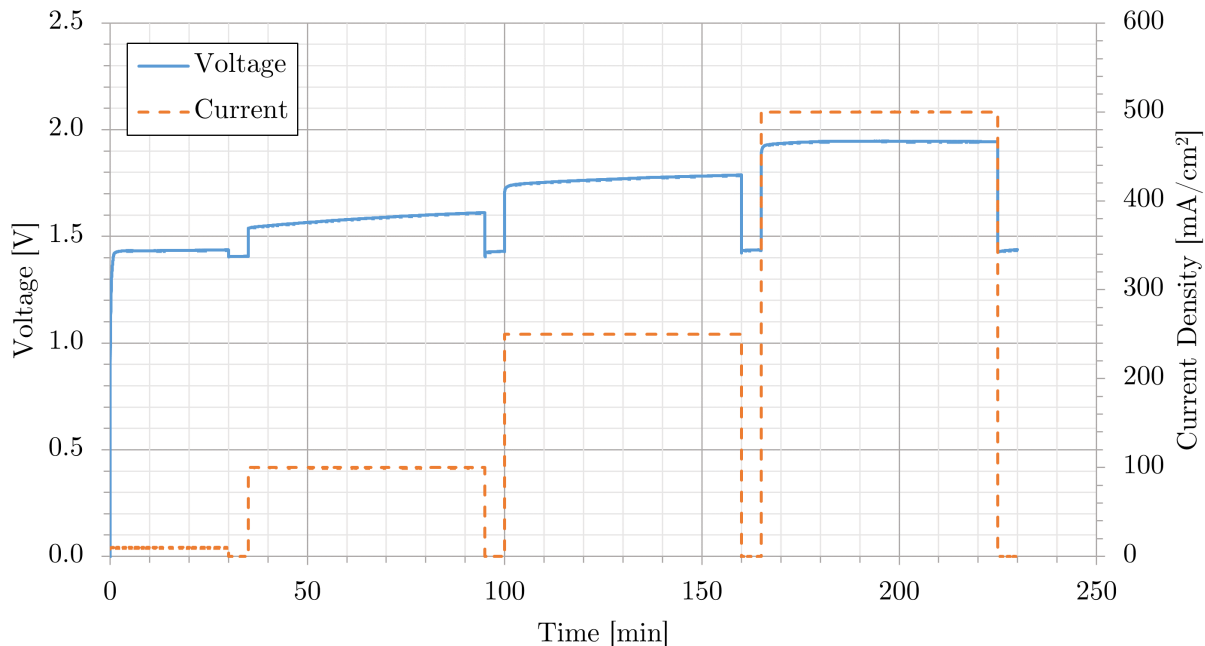


**Figure 2.16** – Conditioning process for Cell 6. Current was applied based on the profile in Table 2.2, and the cell voltage was measured.

## 2.5.2 Polarization Curves

Cells in this work were primarily characterized by polarization curves, and these were the first tests to be performed followed cell conditioning. This technique allowed for the analysis of cell performance at set current values. Specified currents were applied in a stepwise profile, and the cell potential was measured at each step. The maximum applied current was limited so that the cell potential would not exceed 2.3 V to prevent damage.

Either two or three polarization curves were run on one cell in a day depending on if the curves were run only forward or forward and backward, the latter of which was used on later cells to characterize short-term performance hysteresis. The standard stepwise current-based profile used for these tests is provided in Table 2.4. Most steps were held for 90 seconds to allow the cell potential to become reasonably stable, and the last 9 points would be averaged to obtain the polarization curve plots presented in this work (This represents the last 10% of points, as a sampling rate of 1 second was used). As will be discussed later, the data from Cell 9 was much noisier than the other cells, and so for that cell, the last 85 points were averaged to compensate for the noise. When studying single-electrode feed, cells experienced higher losses under COF and could not be operated to the same high current densities. In this case, the reduced polarization curve profile given in Table C.1 was used. Each polarization curve was followed by an EIS measurement, as cell performance could change slightly over a single day of testing.

**Table 2.4** – Galvanostatic profile used to obtain polarization curves. For curves run forward and backward, backward steps are denoted in parenthesis beside their forward counterparts.

Step (Backward Step)	Time [s]	Current [mA]	Current Density [mA/cm <sup>2</sup> ]
0 (64)	300	0	0
1 (63)	300	5	1
2 (62)	90	25	5
3 (61)	90	50	10
4 (60)	90	75	15
5 (59)	90	100	20
6 (58)	90	125	25
7 (57)	90	150	30
8 (56)	90	200	40
9 (55)	90	250	50
10 (54)	90	375	75
11 (53)	90	500	100
12 (52)	90	625	125
13 (51)	90	750	150
14 (50)	90	875	175
15 (49)	90	1000	200
16 (48)	90	1250	250
17 (47)	90	1500	300
18 (46)	90	1750	350
19 (45)	90	2000	400
20 (44)	90	2250	450
21 (43)	90	2500	500
22 (42)	90	2750	550
23 (41)	90	3000	600
24 (40)	90	3500	700
25 (39)	90	4000	800
26 (38)	90	4500	900
27 (37)	90	5000	1000
28 (36)	90	5500	1100
29 (35)	90	6000	1200
30 (34)	90	6500	1300
31 (33)	90	7000	1400
32	90	7500	1500

### 2.5.3 Electrochemical Impedance Spectroscopy

Electrochemical impedance spectroscopy (EIS) was performed with the objective of obtaining additional information on cell losses, and was used in this work mainly to obtain the cell resistance, or ohmic loss. Galvanostatic EIS, where the current is controlled, was used here so the same tests could be run no matter the reference electrode used. This functions through the application of a constant current plus a sinusoidal current perturbation to the cell and measuring the voltage response to obtain the overall cell impedance. The amplitude of the applied wave is small, generally 10 to 20% of the applied constant current value as it must be large enough to avoid noise, but small enough for the response to be linear. This applied current perturbation can be expressed as:

$$i(t) = i_0 \cos(\omega t)$$

where  $i_0$  is the amplitude of the current,  $\omega$  is the radial frequency, and  $t$  is time. This results in a voltage response of the form:

$$E(t) = E_0 \cos(\omega t + \phi)$$

where  $\phi$  represents the phase-shift in the response. This then results in a complex impedance that will consist of real and imaginary components that can be written as:

$$Z = \frac{E_0 \cos(\omega t + \phi)}{i_0 \cos(\omega t)} = \frac{E_0 e^{j\omega t + j\phi}}{i_0 e^{j\omega t}} = \frac{E_0}{i_0} e^{j\phi} = Z_0 e^{j\phi} = Z_0(\cos \phi + j \sin \phi)$$

where  $Z_0$  is the magnitude of the impedance ( $\frac{E_0}{i_0}$ ), and  $j$  is the imaginary number  $\sqrt{-1}$  [66].

As galvanostatic EIS required a sinusoidal current wave be applied, these tests could not be run using a DC power supply and so were performed with a Biologic SP-300 potentiostat. EIS tests were run following each polarization curve and stability test in order to detect any changes in cell operation that may have occurred over time. Depending on the cell, EIS tests were run at three to five current densities, for the repeatability and feed method testing cells, respectively. The parameters used for these test profiles are provided in Tables 2.5 and 2.6. Note that each of the test profiles used an amplitude of 10% of the current density, except the 20 mA/cm<sup>2</sup> test, which used a 20% amplitude. Additionally, before each test, the current density was held for 90 seconds to allow the cell voltage to stabilize. The alternate EIS test profiles provided in Table C.2 were used for cathode-feed only experiments, reducing the highest current density tested at from 1000 to 900 mA/cm<sup>2</sup>.

A Nyquist plot is often used as the primary method of analysing EIS data, as it displays the real and imaginary components of impedance. The Nyquist plot can then be broken into different regions representing the various losses within an electrochemical cell. A representative plot is shown in Figure 2.17 with these regions labeled. Since a Nyquist plot does

**Table 2.5** – Galvanostatic EIS profiles used following each polarization curve and stability test run on repeatability testing AEMWE cells.

Current Density (mA/cm <sup>2</sup> )	Amplitude (mA/cm <sup>2</sup> )	Starting Frequency (kHz)	Ending Frequency (mHz)	Points Measured per Frequency Decade
20	4	200	20	15
300	30	200	100	15
600	60	200	100	15

**Table 2.6** – Galvanostatic EIS profiles used following each polarization curve and stability test run on feed method testing AEMWE cells.

Current Density (mA/cm <sup>2</sup> )	Amplitude (mA/cm <sup>2</sup> )	Starting Frequency (kHz)	Ending Frequency (mHz)	Points Measured per Frequency Decade
20	4	200	20	15
150	15	200	50	15
300	30	200	100	15
600	60	200	100	15
1000	100	200	100	15

not contain any information on the frequency range used, they will often be accompanied by Bode or  $-\text{Im}(Z)$  versus  $\log(\text{frequency})$  plots to show the tested frequency range. Note also that Nyquist plots must use orthonormal axes to maintain the correct shape of the data.

To quantitatively obtain values for the impedance of a cell tested using EIS from the Nyquist plot data, the cell can be represented as an equivalent circuit constructed from circuit elements [66]. An equivalent circuit modeling aims to fit a representative circuit constructed from elements such as resistors, capacitors, and inductors to the impedance response data in order to obtain the characteristics of these elements, and in doing so obtain information about the tested cell. For the electrolysis cells tested in this work, the equivalent circuits used consisted of an inductor to account for the inductance of the measurement cables, a resistor to account for ohmic loss, or the resistance to the flow of current through the cell components, and two elements with a resistor in parallel with constant phase element (CPE) to account for kinetic losses in each electrode (Figure 2.18). Of the parallel components, the CPE accounts for the double layer capacitance at the electrode-electrolyte interface, and the resistor accounts for the reaction kinetic, or charge transfer, resistance [66].

The impedance,  $Z$ , of an inductor is  $Z_L = j\omega L$ , where  $L$  is inductance, the impedance of a resistor is  $Z_R = R$ , where  $R$  is the resistance, and the impedance of a capacitor is  $Z_C = \frac{1}{j\omega C}$ , where  $C$  is the capacitance [66]. An inductor element was included in series to account for inductive effects at the highest and lowest ends of the frequency range, appearing as a positive imaginary impedance. To account for the non-ideal behavior of the reaction interface, CPEs were used instead of capacitors. A CPE has an impedance of  $Z_{CPE} = \frac{1}{(j\omega)^{\alpha} Q}$ .

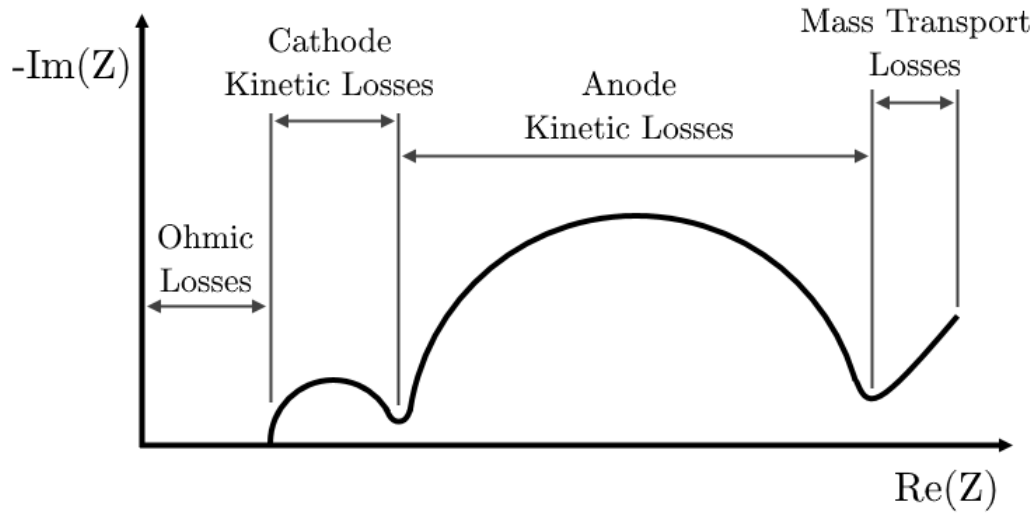


**Figure 2.17** – Example Nyquist plot with regions of interest representing kinetic, ohmic, and mass transport losses labeled. Based on O’Hayre et al. [66].

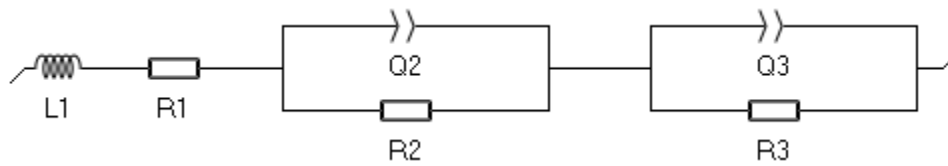


**Figure 2.18** – Equivalent circuit layout used to fit data obtained by EIS measurements between the anode and cathode in this work using resistors (R), CPEs (Q), and inductors (L).

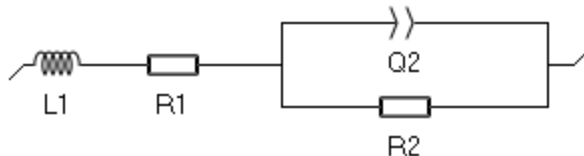


**Figure 2.19** – Equivalent circuit layout used to fit data obtained by EIS measurement between one cell electrode and the reference electrode in this work using resistors (R), CPEs (Q), and inductors (L).

A CPE is a generalized circuit element that can represent any standard element depending on the values of the constants  $a$  and  $Q$  [18].  $Q$  represents a generalized circuit element quantity with units of  $F \cdot s^{(a-1)}$  such that if  $a = 1$ , the CPE will represent a capacitor and  $Q$  will have units of farads (F), if  $a = 0$  the CPE will be represent a resistor, and if  $a = -1$  the CPE will be represent an inductor. When using CPEs to fit non-ideal capacitive behaviour, the value of  $a$  will be between 0 and 1, where the closer it is to 1 the closer the capacitor is to ideal. On a Nyquist plot, this non-ideal behavior manifests as a flattening of the semicircles that appear in the data.

The equivalent circuit provided in Figure 2.18 was used for measurements between the anode and cathode, but EIS measurements were also made between these electrodes and the reference electrode. As these measurements contained one fewer reaction interfaces, the modified equivalent circuit in Figure 2.19 was used instead.

### 2.5.4 Cell Stability Testing

Stability was studied by running constant voltage tests at 1.8 V for a 6 hour period to characterize how cell performance decreased in the initial hours of operation. This format was used as a fixed cell current could result in a dramatic increase in the cell potential, leading to permanent cell damage. After enough testing of Aemion+ membranes and ionomer however, it was determined that due to the observed increase in stability, the cell current could be held constant instead, and the stability tests were changed to run at 300 mA/cm<sup>2</sup> (1500 mA) for 6 hours. This change was implemented for the testing of the feed method cells.

These stability test procedures were based on literature that used similar short-term stability tests. These types of tests performed on AEMWE cells in literature used either a constant voltage hold [23, 35, 43] or constant current hold [22, 24, 26, 30, 38, 52, 57, 65], and ranged from three to 24 hours in length. Stability tests were generally run at the higher end of cell operational ranges, with cells either held at a voltage at or greater than 1.6 V, or a current density selected to achieve this voltage range based on how well a given cell performed.

# Chapter 3

## Results and Discussion

### 3.1 Ink Development and Catalyst Layer Fabrication

The Aemion AP1-HNN8-00-X ionomer used previously in the ESDLab was replaced with Aemion+ AP2-HNN5-00-X ionomer which presented a challenge as the manufacturer, Ionomr Innovations Inc. [49], recommended it not be exposed to water. As Aemion+ membranes are a bulk form of this same second-generation ionomer material, inks used to print directly onto them should also not contain water. Properties of these membranes and ionomers are given in Table 3.1. The ionomer solution was created by dissolving the solid ionomer in a mixture of 50% methanol and 50% acetone by volume.

The process of developing new inks with Aemion+ ionomer used the density, viscosity, and surface tension characterization methods laid out in Section 2.2. These were measured to ensure they fell within the recommended dynamic viscosity (10 to 12 mPa·s) and surface tension (28 to 33 mN/m) ranges recommended for the Dimatix DMP-2831 printer when using a DMC-11610 printhead [75]. The development of PG and IPA solutions, inks with no catalyst, and printing using the complete inks is covered in this section. An ink formulated by this process was considered successful if it could be used to print a CCM to the desired catalyst loading in a number of layers consistent with previous work done in the ESDLab on both AEM and PEM fuel cells and electrolyzers. Previous work using Aemion AP1-HNN8-00-X ionomer required approximately 15 layers to be printed to achieve a cathode Pt loading of 0.1 mg/cm<sup>2</sup> and approximately 30 layers to achieve an anode IrO<sub>x</sub> loading of 1.0

**Table 3.1** – Properties of the Aemion ionomers and membranes used in this work. Information obtained from Ionomr Innovations [106].

	Membrane Thickness (μm)	Reinforcement	IEC (meq/g)	Area Resistance (mΩ·cm <sup>2</sup> )
Aemion AP1-HNN8-00-X	n/a (ionomer)	n/a	2.5	n/a
Aemion+ AP2-HNN5-00-X	n/a (ionomer)	n/a	1.4-1.7	n/a
Aemion+ AF2-HLE8-50-X	50	Non-woven reinforcement	2.3-2.6	50-100
Aemion+ AF2-HWP8-75-X	75	Woven reinforcement	2.3-2.6	<150

mg/cm<sup>2</sup> [40]. An formulation ink was considered successful if it could achieve and repeat these metrics over multiple prints.

### 3.1.1 Propylene Glycol & Isopropyl Alcohol Mixtures

The inks used here were made using four components: IPA, PG, ionomer solution (itself made from methanol, acetone, and dissolved Aemion+ ionomer), and catalyst nanopowder. Ink development began by making and characterizing mixtures with different ratios of the base components, PG and IPA. Knowing the properties of the PG:IPA mixtures and the effects of adding the other components (ionomer solution and catalyst powder) a base solution can be selected that will result in a final ink with desired properties. This was done both to minimize the waste of catalyst nanopowder and ionomer, and because the amounts of PG and IPA used could be more easily adjusted, since the total solid content and the ratio of catalyst to ionomer solid were fixed. The first step in this process was to create a database of the densities and dynamic viscosities for multiple mixture ratios of PG and IPA. These solutions were labelled based on the mass ratio of PG to IPA that they contained. For all testing purposes, PG:IPA mixtures were made using a total of 3 g of liquid. Density, dynamic viscosity, and surface tension of PG:IPA mixtures were measured following the procedures laid out in Sections 2.2.1, 2.2.2, and 2.2.3, respectively.

The densities of PG:IPA mixtures and their respective uncertainties are provided in Figure 3.1. These results showed that density increased in a non-linear fashion as the relative mass of PG to IPA increased. Fujifilm Dimatix does not provide a recommended range for density, only noting that a “specific gravity greater than 1 is beneficial” [75]. As PG, the most dense ink solvent, has a specific gravity just above 1, the specific gravities of the inks used will always be less than 1, but higher ratios of PG to IPA will get close to this value.

Results of the dynamic viscosity measurements of PG:IPA mixtures and their respective uncertainties are provided in Figure 3.2 with the range of dynamic viscosities recommended by Fujifilm Dimatix of 10 to 12 mPa·s highlighted in red. These results showed a more linear increase with respect to the ratio of PG mass to IPA mass compared to the density results. The ionomer solution was measured to have a dynamic viscosity of  $3.5 \pm 0.4$  mPa·s. As this is quite a bit lower than the PG:IPA mixtures, it was expected to decrease the overall viscosity of the ink, and so it was expected that a PG:IPA ratio of 3.0:1 or 3.5:1 would be required.

Results of the surface tension measurements of PG:IPA mixtures and their respective uncertainties are provided in Figure 3.3, with the range recommended by Fujifilm Dimatix of 28 to 33 mN/m highlighted in red. These results showed higher variability as the procedure for these test procedure and the apparatus had not been fully developed at the time of these

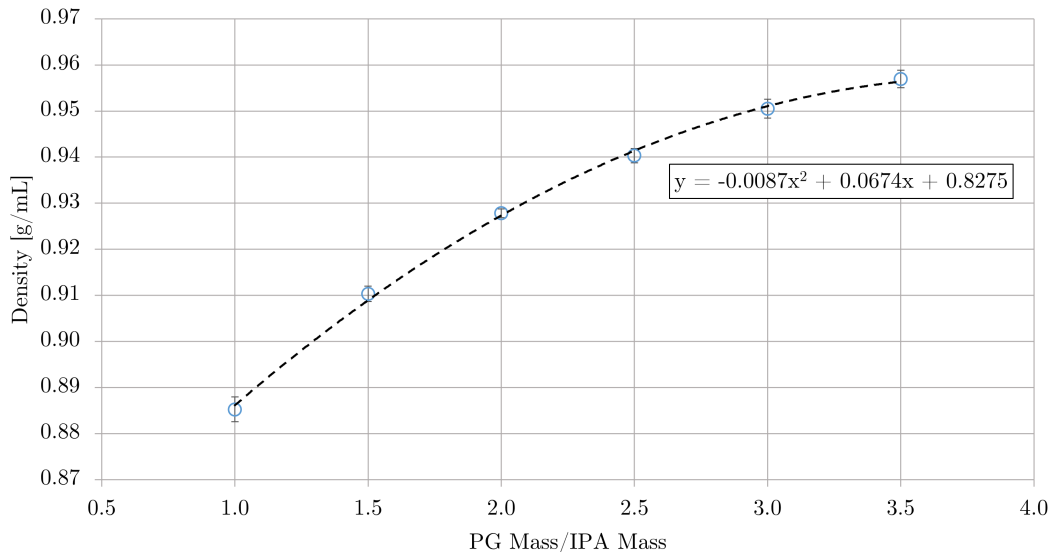


**Figure 3.1** – Densities of the characterized PG:IPA mixtures. Error bars represent a 95% confidence interval.

measurements. The trend in surface tension was non-linear, with the increase in surface tension slowing as the ratio of PG to IPA was increased. To obtain an ink within the desired range, a PG:IPA ratio greater than 2.5:1 was required.

### 3.1.2 Iridium Oxide Ink Development & Characterization

The first ink formula to be developed, using the process summarized in Figure 2.1, was the  $\text{IrO}_x$ -based ink used to print anode catalyst layers ( $\text{IrO}_x$  nanopowder acquired from Tanaka Kikinzoku Kogyo (TKK) Company, Japan). For the ink base, a PG:IPA ratio of 3:1 was chosen initially as it would be within the dynamic viscosity range of 10 to 12 mPa·s. To test the effect of the ionomer solution on the ink viscosity, ink with ionomer (but no catalyst) was made using a 3:1 PG:IPA ratio, and the dynamic viscosity measured. This result was compared with the PG:IPA solution viscosities (Figure 3.4, red square). The addition of the ionomer solution caused an 11% decrease in viscosity which was larger than expected. Therefore, a second ink with no catalyst was made using a 3.5:1 ratio of PG:IPA (Figure 3.4, green triangle). As the resulting solution had a dynamic viscosity ( $11.2 \pm 0.7$  mPa·s) and surface tension ( $28.5 \pm 0.3$  mN/m) both within the recommended range of the printer, this formula was chosen to make a full ink.

A batch of  $\text{IrO}_x$  ink was made using a 3.5:1 PG:IPA ratio and characterized. This formulation resulted in a density of  $0.940 \pm 0.002$  g/mL, viscosity of  $11.2 \pm 1.0$  mPa·s (Figure 3.4, yellow diamonds), surface tension of  $29.2 \pm 1.1$  mN/m, and an Ohnesorge number of  $Oh = 0.47 \pm 0.04$  (provided errors are a 95% confidence interval). These are within the

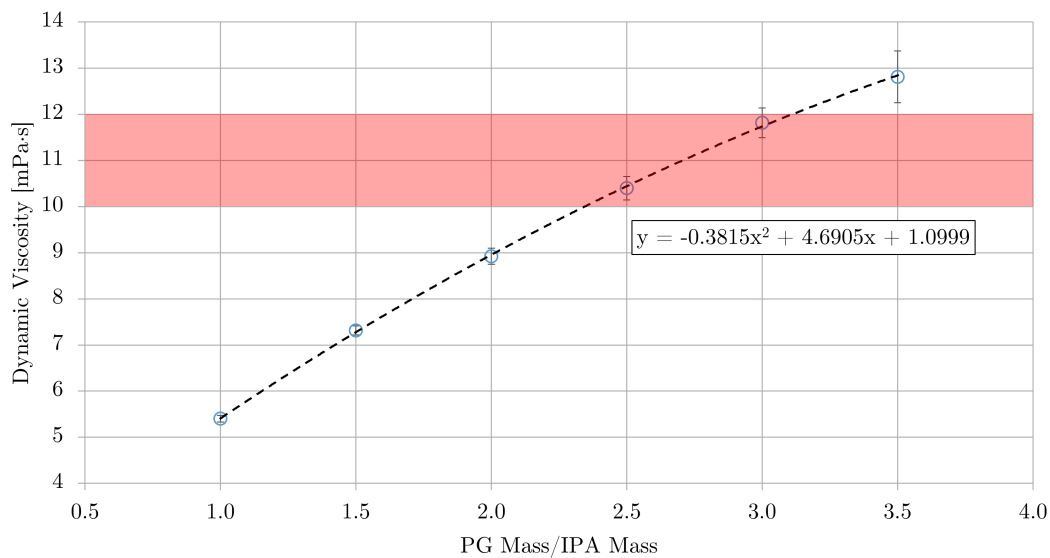


**Figure 3.2** – Dynamic viscosities of the characterized PG:IPA mixtures. Error bars represent a 95% confidence interval.

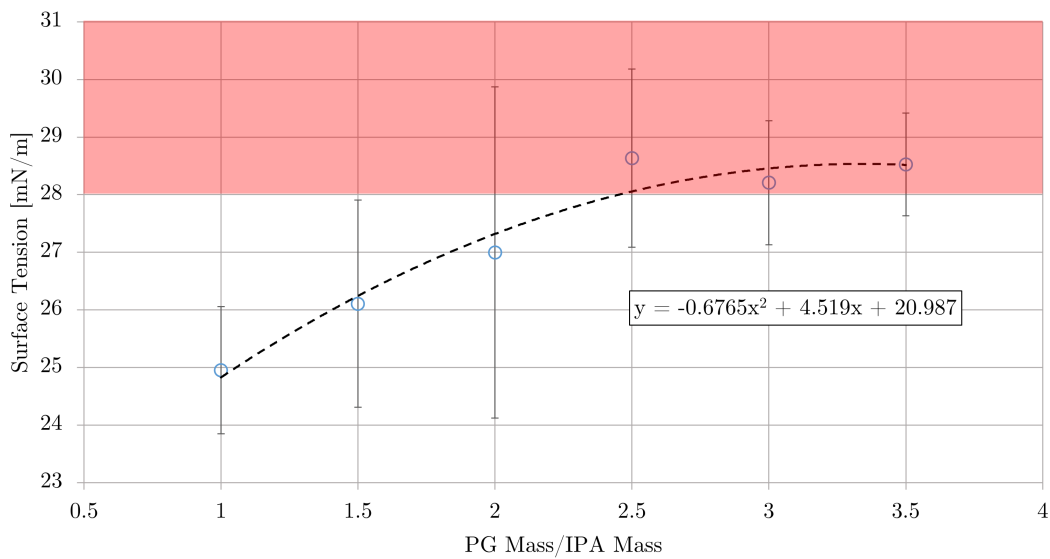


**Figure 3.3** – Surface tensions of the characterized PG:IPA mixtures. Error bars represent a 95% confidence interval.

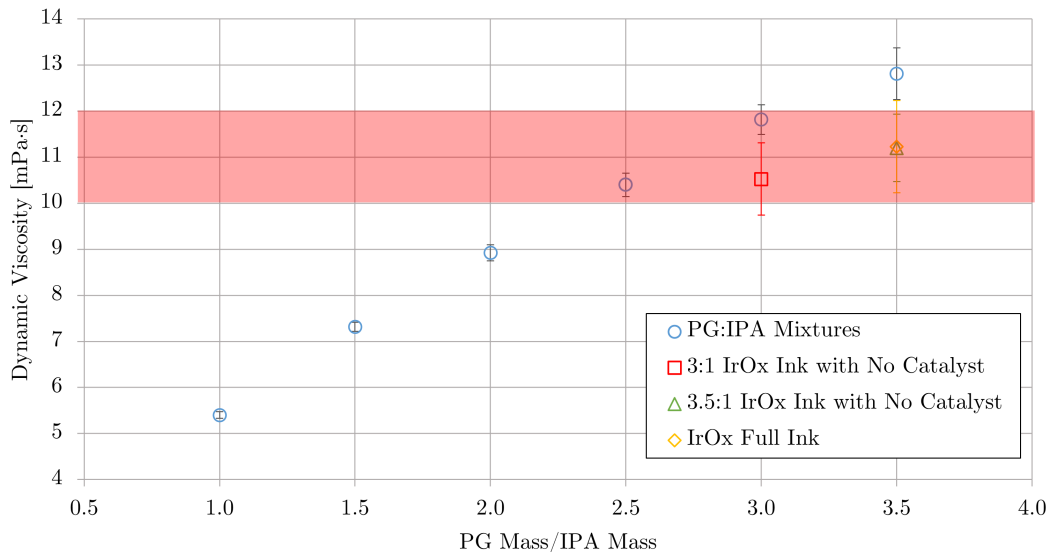


**Figure 3.4** – Dynamic viscosities of the characterized  $\text{IrO}_x$  no-catalyst ink solutions compared with the PG:IPA mixtures. Error bars represent a 95% confidence interval.

**Table 3.2** –  $\text{IrO}_x$  ink recipe in both a weight % and a mass basis.

Component		Amount [wt.%]	Mass [mg]
	TKK $\text{IrO}_x$	3.1	92.6
	PG	69.1	2073.0
	IPA	19.7	590.6
	Total	8.1	243.8
Ionomer Solution	Methanol & Acetone (50%/50% vol)	98.0	238.9
	AP2-HNN5-00-X	2.0	4.9

target ranges for the Fujifilm Dimatix DMP-2831 printer and DMC-11610 cartridges used in this work (dynamic viscosity of 10-12 mPa·s and surface tension of 28-33 mN/m). This ink was also analysed by DLS, resulting in the particle distribution shown in Figure 3.5. The average hydrodynamic diameter and polydispersity index were  $162 \pm 4$  nm and  $19.4 \pm 2.7\%$ , respectively. This particle distribution was quite uniform, and although there were some minor outlying measurements, most particles were smaller than 300 nm, which was similar to the recommended particle size (200 nm), and was significantly smaller than the 21  $\mu\text{m}$  nozzles of the cartridges and therefore was not expected to lead to clogging. As this ratio of PG to IPA resulted in the desired properties and the particle size distribution was adequately small, this formulation (Table 3.2) was used for  $\text{IrO}_x$  inks containing the Aemion+ AP2-HNN5-00-X ionomer.

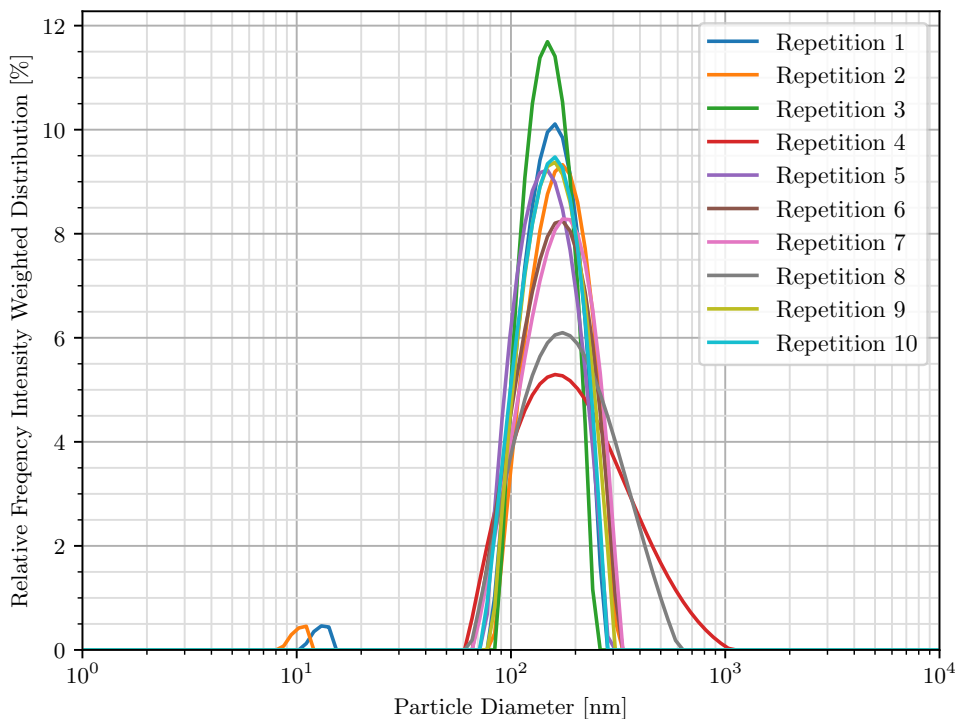


**Figure 3.5** – Intensity-weighted particle distribution obtained by DLS for the IrO<sub>x</sub> ink.

### 3.1.3 Iridium Oxide Ink Printing

The final test to determine whether the newly developed IrO<sub>x</sub> ink could be consistently printed using the Fujifilm Dimatix DMP-2831 and DMC-11610 cartridges was to attempt to reproducibly print CCMs to the desired loading of 1.0 mg/cm<sup>2</sup> IrO<sub>x</sub> in a similar number of layers and with consistent printing performance. To achieve this loading, it was expected to take approximately 30 print layers [40]. Two batches of CCMs were printed entirely using this ink formula, the first reaching the desired loading in 27 layers and the second in 32 layers, at a drop spacing of 20 μm, which were good results.

For both CCMs printed with this ink, one layer was initially printed, the mass of solid content deposited was measured, and the catalyst loading of the layer was calculated to obtain an initial estimate of the total number of layers that would be needed. As the amount of ink deposited per layer could vary throughout printing, the catalyst loading was checked multiple times so that the estimate of the remaining layers could be improved. Table 3.3 provides all the data collected during the printing of these two batches of CCMs, as well as the calculated per-layer loadings that were used to estimate the number of remaining layers. The average per-layer loading is calculated as the total loading divided by the total number of layers printed whereas the exclusive per-layer loading is calculated as the loading of just the new layers divided by the number of new layers. Loading was measured using

**Table 3.3** – Catalyst loading data collected during two prints of the AP2 IrO<sub>x</sub> ink formulation to loadings of 1.0 mg/cm<sup>2</sup>.

Total Layers	New Layers	$\sum \Delta m$ (mg)	$\Delta m$ (mg)	Loading (mg/cm <sup>2</sup> )	Average Per-layer Loading (mg/cm <sup>2</sup> /total layers)	Exclusive Per-layer Loading (mg/cm <sup>2</sup> /new layers)
Print 1						
1	1	0.2	0.2	0.04	0.04	0.038
6	5	1.2	1.0	0.23	0.038	0.038
16	10	3.0	1.8	0.57	0.036	0.034
25	9	5.0	2.0	0.95	0.038	0.042
27	2	5.4	0.4	1.0	0.038	0.038
Print 2						
1	1	0.1	0.1	0.02	0.02	0.02
10	9	1.4	1.3	0.27	0.027	0.027
20	10	3.2	1.8	0.61	0.030	0.034
28	8	4.7	1.5	0.89	0.032	0.036
32	4	5.3	0.6	1.0	0.032	0.029

a piece of aluminium foil onto which an additional catalyst layer was deposited. To ensure the measured mass was for only the solid material, the foil was dried in an 80°C oven for at least 10 minutes before each measurement, and overnight before the final measurement.

The amount of ink printed each layer was quite consistent for the prints, although they did vary slightly over time. These changes in per-layer loading are most likely caused by some of the nozzles on the printheads temporarily jetting more or less material, either because they became temporarily clogged or possibly due to changes in local fluid properties. The later option may in turn occur because of a lack of homogeneity in the colloidal inks or temperature changes, as the printhead would heat up during printing.

Images of the printed IrO<sub>x</sub> catalyst layers discussed above taken by stereo microscopy (Leica S8AP0 with a Leica MC170 HD camera) at 10 times zoom (Figure 3.6). Both images were similar, with cracks in the printed catalyst layers following the same pattern as the reinforcement material of the membrane. A white background was used behind the sample so the cracks could be better observed, as the light would reflect through the cracks and back to the camera. Images of a bare Aemion+ AP2-HWP8-75-X membrane are given in Figure 3.7 for comparison, with the side that the IrO<sub>x</sub> catalyst layers are printed on in Figure 3.7a. The woven reinforcement forms a grid throughout the membrane, and it seems that the cracks in these catalyst layers appear along these grid lines.

The IrO<sub>x</sub> ink was printed first on the top side of the membrane, which has a rougher texture compared to the other side. This was done as the IrO<sub>x</sub> catalyst layer took longer to print compared to the Pt/C, so it was preferable to do so while the membrane was still attached to the plastic backing sheet that it came with to minimize membrane swelling. The membrane texture was determined by physical inspection. It makes sense then, that there

would be thinning of the ink along these grid lines on the rougher side of the membrane, leading to the observed cracking pattern. Differences in the lighting of the images may have been due to a difference in the light levels and exposure time, as they were not controlled for between the pictures.

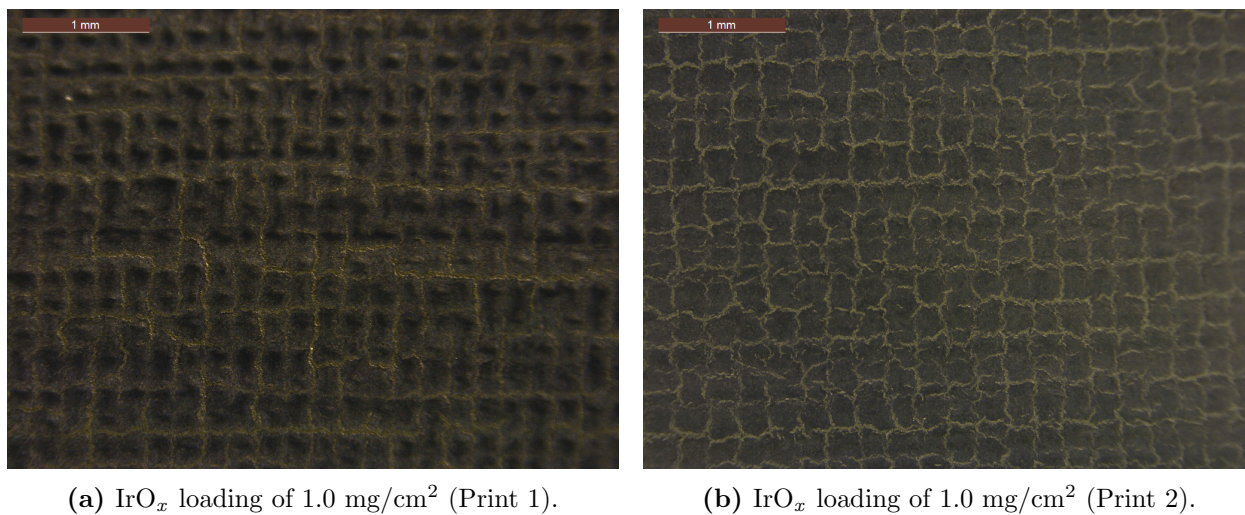


**Figure 3.6** – Images taken of the IrO<sub>x</sub> catalyst layers printed using the ink developed in this work at 10 times zoom.

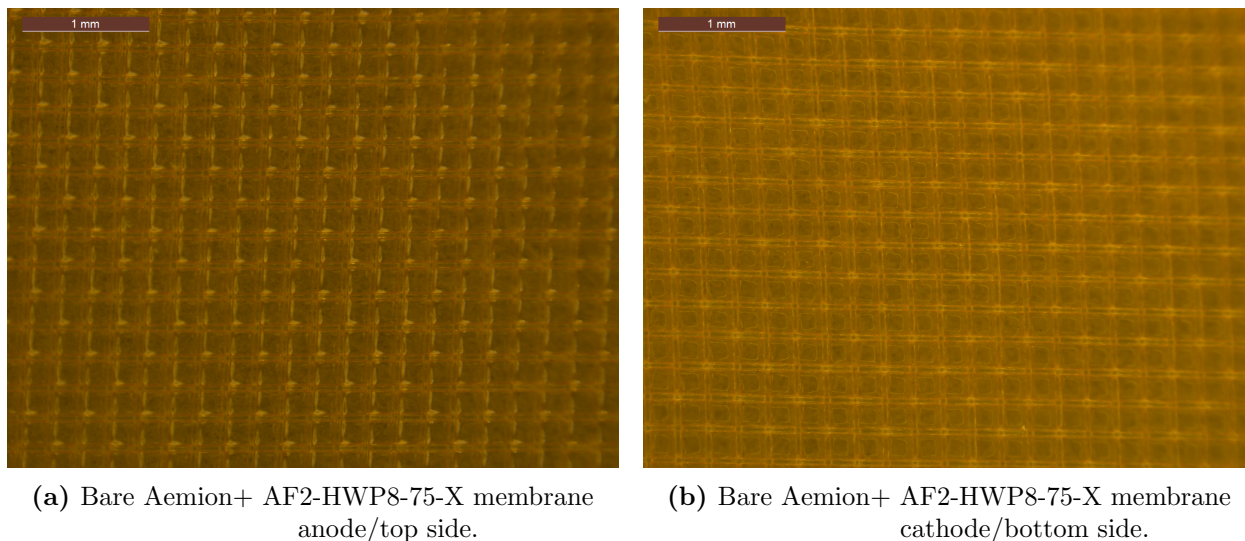


**Figure 3.7** – Images taken of a bare Aemion+ AF2-HWP8-75-X membrane at 10 times zoom. The pattern of the reinforcement layer is visible on both sides, but is more prominent on the rougher anode side.

### 3.1.4 Platinum-Carbon Ink Development & Characterization

Following the development of the IrO<sub>x</sub>-based ink using Aemion+ AP2-HNN5-00-X ionomer laid out in Section 3.1.2, the process was repeated to develop a Pt/C-based ink to be used for printing cathode catalyst layers (Pt/C nanopowder acquired from Tanaka Kikinzoku Kogyo (TKK) Company, Japan as 46.7 wt.% Pt supported on carbon black). Since the ionomer solution lowered the viscosity of the IrO<sub>x</sub> ink more than expected, a 3.5:1 ratio PG:IPA solution was initially selected for the Pt/C ink. An ink with no catalyst was then made using a 3.5:1 PG:IPA ratio and characterized, and its dynamic viscosity was compared with the PG:IPA mixtures (Figure 3.8, green triangle). For this ink, there was a much smaller reduction in dynamic viscosity when the ionomer solution was added because less ionomer solution was used. This was due to the lower solid content of the Pt/C ink formula compared to the IrO<sub>x</sub> formula (1.25 wt.% versus 3.25 wt.%). As this solution had a dynamic viscosity on the upper end of the acceptable range, another sample with a 3.0:1 PG:IPA ratio was made (Figure 3.8, red square).

The 3.0:1 Pt/C ink with no catalyst had an unexpectedly high dynamic viscosity at  $12.1 \pm 1.9$  mPa·s, and a large error (Figure 3.8, red square). This was likely due to evaporation of the ionomer solution solvents as this ink was exposed to atmosphere for longer than the others since unlike those solutions, its density was measured before its viscosity. This was confirmed by another viscosity test performed following the surface tension test (the surface tension measurement was  $28.5 \pm 0.1$  mN/m), which again exposed the ink to air for a prolonged period of time, where the resulting viscosity had increased to a value of 14.6 mPa·s. Based on these results, it was decided that a 3.0:1 PG:IPA ratio would be used for the Pt/C ink, exposure to air would be minimized, and separate inks would be made for characterization and printing to prevent unwanted changes to the ink that would be printed.

A batch of Pt/C ink with a 3.0:1 PG:IPA ratio was then made and characterized. This formulation resulted in a density of  $0.925 \pm 0.001$  g/mL, viscosity of  $9.2 \pm 0.5$  mPa·s (Figure 3.8, yellow diamond), surface tension of  $28.5 \pm 0.2$  mN/m, and an Ohnesorge number of  $Oh = 0.39 \pm 0.02$  (provided errors are a 95% confidence interval). This surface tension was within the target range, and although the dynamic viscosity was lower than desired, this ink formulation was still used as the viscosity was expected to increase due to ionomer solution solvent evaporation. This ink was also analysed by DLS, resulting in the particle distribution shown in Figure 3.9. The average hydrodynamic diameter and polydispersity index were  $396 \pm 37$  nm and  $23.8 \pm 4.9\%$ , respectively. This distribution was wider than that of the IrO<sub>x</sub> ink, as carbon is known to form fractal-like aggregates, but most particles were still below a diameter of 1 μm. This was larger than the diameter recommend by Dimatix, but it was hoped that this would not clog the 21 μm cartridge nozzles. As this ink met the

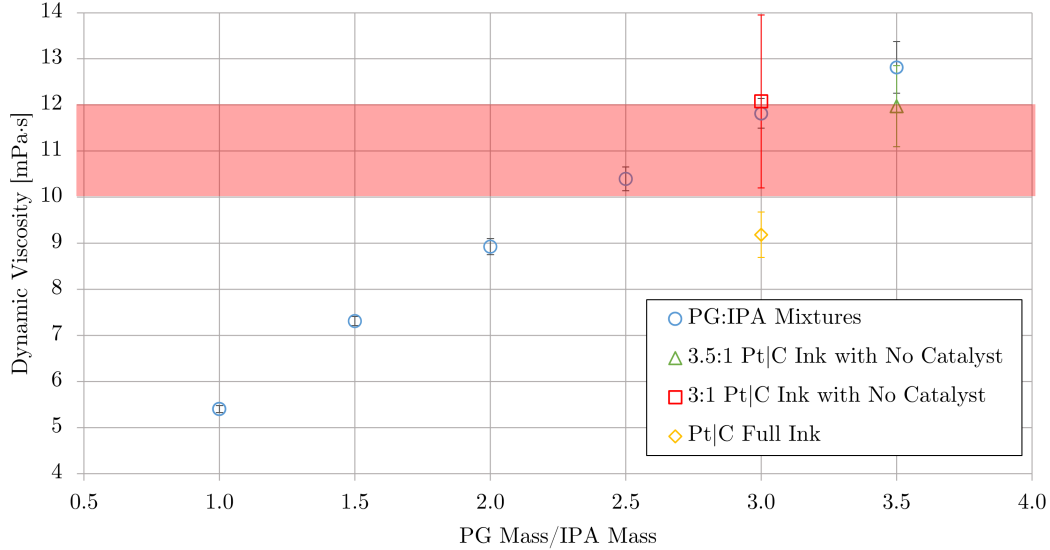


**Figure 3.8** – Dynamic viscosities of the characterized Pt/C ink solutions compared with the PG:IPA mixtures. Error bars represent a 95% confidence interval.

**Table 3.4** – Pt/C ink recipe in both a weight % and a mass basis.

Component		Amount [wt.%]	Mass [mg]
TKK 46.7 wt.% Pt/C		1.1	33.8
PG		69.5	2085.0
IPA		23.1	693.8
Total		6.3	187.5
Ionomer Solution	Methanol & Acetone (50%/50% vol)	98.0	183.7
	AP2-HNN5-00-X	2.0	3.8

desired properties, this formula (Table 3.4) was then used to print Pt/C catalyst layers.

### 3.1.5 Platinum-Carbon Ink Printing

The final test to determine whether the newly developed Pt/C ink could be consistently printed using the Fujifilm Dimatix DMP-2831 and DMC-11610 cartridges was to attempt to reproducibly print CCMs to the desired loading in a similar number of layers and with consistent printing performance. The two times this ink was used for printing were for two different catalyst loadings, first to  $0.2 \text{ mg/cm}^2$  Pt and second to  $0.1 \text{ mg/cm}^2$  Pt. To achieve a loading of  $0.1 \text{ mg/cm}^2$ , it was expected to take about 15 layers [40], and it was estimated to require twice that for  $0.2 \text{ mg/cm}^2$ . The two batches of CCMs that were printed using this ink took 36 and 16 layers to reach  $0.2 \text{ mg/cm}^2$  and  $0.1 \text{ mg/cm}^2$  loadings, respectively. While the second print was close to the expected 15 layers, the first was slightly higher than

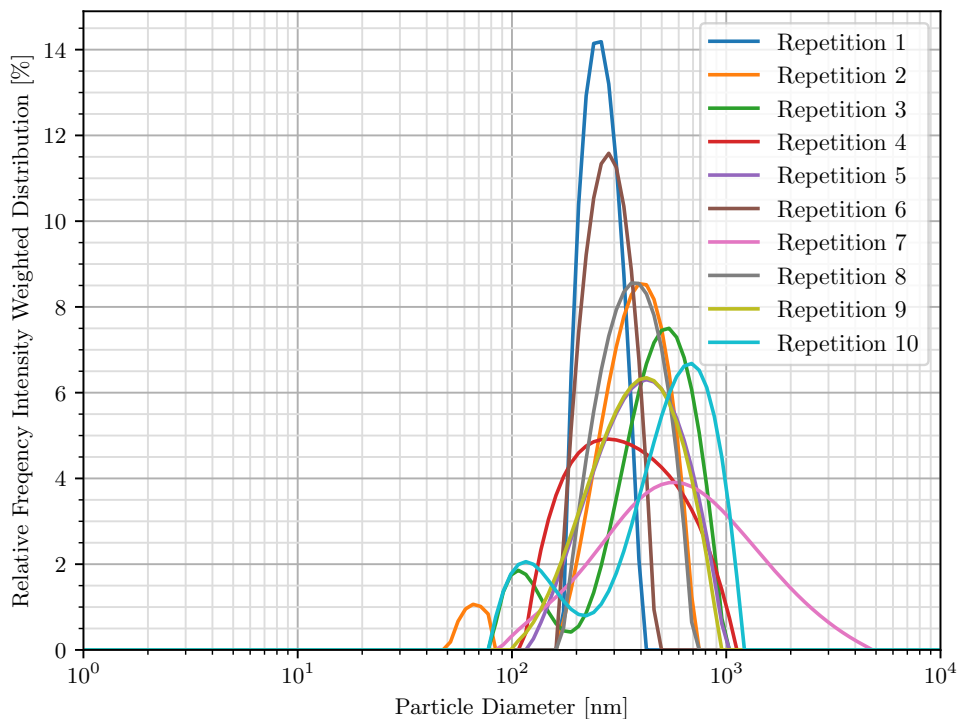


**Figure 3.9** – Intensity-weighted particle distribution obtained by DLS for the Pt/C ink.

expected, although this prediction was an extrapolation, and so the extra layers needed were not too concerning.

Like for the printing of the  $\text{IrO}_x$  ink, the catalyst loading would be calculated based on the measured mass of deposited solid content after a number of layers. Two layers were deposited before the first measurement since this ink contained a low solid content by weight percent (1.25 wt.% solid), and so less material was deposited per layer. Table 3.5 provides the measurements for the mass deposited per layer and the calculated per-layer loadings. Both inks performed relatively consistently throughout printing, with the per-layer loading increasing slightly from the start of both prints. For the  $0.2 \text{ mg/cm}^2$  print, the per-layer loading decreased significantly after layer 30, however, this was due to the cartridge running low on ink and having to be re-filled following layer 32. Printing performance still suffered following this, possibly due to ink drying in the printhead nozzles during the re-filling process.

Although the first print of this ink was to a catalyst loading of  $0.2 \text{ mg/cm}^2$ , by interpolating the data, it can be estimated to have achieved a  $0.1 \text{ mg/cm}^2$  catalyst loading after 18 layers, which is also close to the predicted 15 layers. Changes in the per-layer loadings for both prints were probably caused by the same effects as for the  $\text{IrO}_x$  ink; that is printhead nozzles being temporarily clogged, or due to local changes to the ink viscosity or surface tension from nonhomogeneous particle distributions or temperature changes.

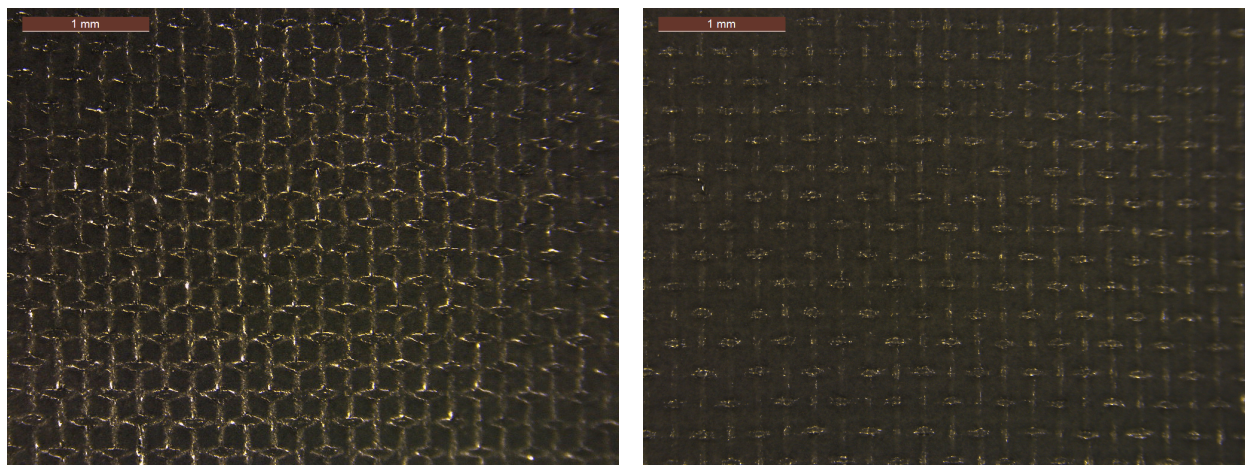
**Table 3.5** – Catalyst loading data collected during two prints of the AP2 Pt/C ink to loadings of 0.2 mg/cm<sup>2</sup> and 0.1 mg/cm<sup>2</sup>.

Total Layers	New Layers	$\sum \Delta m$ (mg)	$\Delta m$ (mg)	Loading (mg/cm <sup>2</sup> )	Average Per-layer Loading (mg/cm <sup>2</sup> /total layers)	Exclusive Per-layer Loading (mg/cm <sup>2</sup> /new layers)
Print 1						
2	2	0.1	0.1	0.008	0.004	0.004
8	6	0.5	0.4	0.04	0.005	0.006
20	12	1.4	0.9	0.12	0.0059	0.0063
30	10	2.2	0.8	0.18	0.0062	0.0067
32	2	2.3	0.1	0.19	0.0060	0.0042
36	4	2.4	0.1	0.20	0.0056	0.0021
Print 2						
2	2	0.1	0.1	0.01	0.004	0.004
10	8	0.8	0.7	0.07	0.007	0.007
15	5	1.1	0.3	0.092	0.0062	0.0050
16	1	1.25	0.2	0.11	0.0066	0.013

The resulting Pt/C catalyst layers were imaged by stereo microscopy (Leica S8AP0 with a Leica MC170 HD camera attached) in the same manner as the IrO<sub>x</sub> catalyst layers (Figure 3.10). Both images were quite similar, showing the same general pattern, despite the difference in catalyst loading and the number of printed layers. The pattern was more visible in the first print, but this was caused in part because of the angle at which the light is hitting the reflective catalyst layers. The pattern itself reveals the same grid as the images of the IrO<sub>x</sub> catalyst layers discussed previously, but instead of visible cracks along the reinforcement lines, there was a grid of “bumps”. Cracks may not have been visible since the Pt/C layer was printed second, and so light that would otherwise reflect back to the camera could have been blocked by the IrO<sub>x</sub> layer on the opposite side. The patterns in the Pt/C may have been less severe than for the IrO<sub>x</sub> layers since the Pt/C ink was printed second on the bottom side of the membranes, which is smoother than the top side that the IrO<sub>x</sub> ink was printed on. This difference in membrane texture is in turn due to the way the reinforcement material is distributed within the membrane. An image of the bare cathode-side of an AF2-HWP8-75-X membrane is given in Figure 3.7b for comparison.

### 3.1.6 Summary of the Ink Development Process

Due to the use of a new ionomer material, Aemion+ AP2-HNN5-00-X, and the restrictions on ink properties necessary for successful printing, an ink-development process was created and followed in this work to formulate printable inks. Two inks containing different catalyst nanopowders were developed, an IrO<sub>x</sub> ink for the anode and a Pt/C ink for the cathode, both of which were used to successfully print catalyst layers twice. This demonstrated that the ink formulation process was robust enough to develop inks with the desired dynamic



(a) Pt loading of  $0.2 \text{ mg/cm}^2$  (Print 1).

(b) Pt loading of  $0.1 \text{ mg/cm}^2$  (Print 2).

**Figure 3.10** – Images taken of the Pt/C catalyst layers printed using the ink developed in this section at 10 times zoom.

viscosity and surface tension properties required for printing without the need for trial and error with multiple ink solutions, which would waste expensive catalyst powder.

The  $\text{IrO}_x$  ink was developed first and it was noted that the variance in the dynamic viscosity of the test solutions increased quite a bit when the ionomer solution was added (Figure 3.4). This was again an issue when developing the Pt/C ink, as the 3.0:1 PG:IPA ratio ink with no catalyst had a higher viscosity than expected and a very large variance (Figure 3.8). This is thought to have been caused by evaporation of the methanol and acetone in the ionomer solution when the ink was exposed to atmosphere or at elevated temperatures.

Individual viscosity measurements for all the solutions discussed in this section are provided in Appendix E.2. From these measurements, it can be noted that the viscosity was always higher for the second measurement compared to the first, most likely due to evaporation of more volatile, less viscous solvents such as alcohols and acetone. Although this effect occurs for the PG:IPA mixtures, it is more pronounced for the samples that contained ionomer solution and therefore methanol and acetone. To account for this the following guidelines were appended to the ink formulation process: use ice baths to keep the ink at or slightly below room temperature during sonication, allow minimal time for atmospheric exposure, and perform the viscosity test before density or surface tension tests as it seemed to be the most sensitive property. These were followed when the full Pt/C ink was made, which resulted in a smaller variance in the viscosity measurements of this ink. Although the dynamic viscosity of the ink was lower than the recommended range, it was still used for printing as additional evaporation during use could lead to the viscosity increasing.

## 3.2 In-situ Electrolysis Cell Characterization

The printed CCMs were subsequently used to assemble AEMWE single-cells. These were characterized to determine the effect of cell construction and operational parameters of interest. The cell assembly and testing processes followed those laid out in Sections 2.4 and 2.5, respectively. The first cells characterized in this work were done to test the new Aemion+ membranes and ionomer with the objective of obtaining repeatable results between cells. Following this, a reference electrode was integrated into the AEMWE cells as this system provided an opportunity to improve cell characterization which has so far only seen limited use in AEMWE cells [53]. The objective of using a reference electrode was to gain additional information on the half-cell reaction overpotentials during electrode feed method testing. The study on electrolyte feed method was then performed to test three feed method configurations: two-electrode feed (TEF), anode-only feed (AOF), and cathode-only feed (COF) to determine how these operational method impacts cell performance.

### 3.2.1 Obtaining Repeatable In-situ Cell Results using Aemion+ Membranes and Ionomer

AEMWE cells were initially tested in an effort to understand what test configurations both worked well (comparable current density per unit voltage to literature results [22, 30, 40]), and resulted in repeatable performance between cells. This built off of the work done by Storbakken [40], with the first cells tested here using all the same components and test station equipment, except for the membrane and ionomer, which were upgraded from the first generation Aemion to the second generation Aemion+. The results obtained by Storbakken showed cell performance comparable to literature, but the performance was not repeatable, and they observed about a 30% failure rate using first generation Aemion membranes. Comparatively, all the cells tested using Aemion+ AEMs throughout this work (not all of which will be discussed) resulted in only a 7.1% failure rate, demonstrating the improved resilience of the fabrication process and reinforced Aemion+ membranes. Cell failure was defined as a failure to achieve water electrolysis at any point during characterization.

The AEMWE cells that will be discussed in this section were characterized with the goal of obtaining repeatable results. The cells are denoted as Cells 1 through 5. Cells 1, 2, and 3 used Aemion+ AF2-HLE8-50-X membranes (50  $\mu\text{m}$  thick) and AP2-HNN5-00-X ionomer, and were all printed together in the same batch. Following these cells, repeatability Cells 4 and 5 were printed in the next batch, using Aemion+ AF2-HWP8-75-X membranes (75  $\mu\text{m}$  thick) and the same ionomer as the first three cells, but with adjusted loadings. Table 3.6 compares the components and operating parameters used for Cells 1 through 5. Note that Cells 6 to 9, tested in Sections 3.2.2 and 3.2.3, used the same construction as Cells 4 and 5.

An ionomer loading of 5 wt.% was used at both electrodes for the first 3 cells before this was changed to 10 wt.% based on literature results [30, 60, 61]. Titanium and graphite bipolar plates were also used for the first three cells as nickel plates had not yet been obtained. Changes to the membrane and cathode catalyst in later batches were made due to a lack in the supply of these materials following production of the first batch of CCMs.

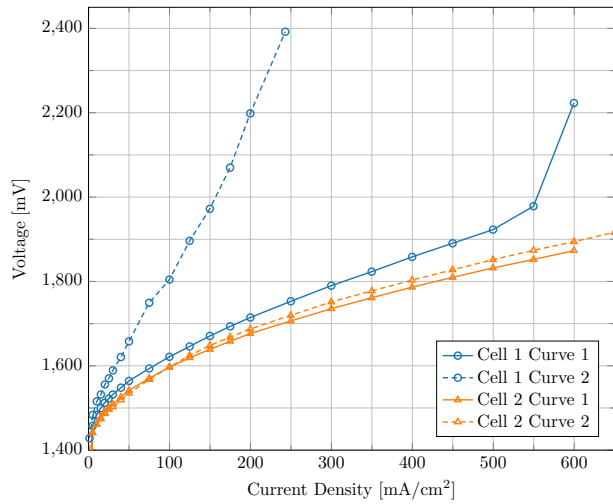
Cell 1, the first cell to be tested, used a carbon paper Sigracet 39AA PTL at the cathode side, but suffered from a large decrease in performance following the first polarization curve run on the cell. This is demonstrated in Figure 3.11a, where the first two polarization curves for Cells 1 and 2 are compared. When Cell 1 reached a current density of 600 mA/cm<sup>2</sup>, there was a sudden performance loss that the cell did not recover from for the second polarization curve. Upon post-operation inspection, it was found that there was damage to the structure of the carbon PTL used for Cell 1. A picture of the Sigracet 39AA PTL following cell testing is provided in Figure 3.11b. Based on the Pourbaix diagram for carbon, (Figure 2.8a [100]) at the near pH 14 conditions inside an AEMWE cell, carbon could corrode as soon as the potential deviated from the equilibrium potential for the HER. Therefore, it is likely that the cause of this sudden cell degradation was the corrosion of the carbon PTL once the overpotential was high enough, resulting in the weakening and subsequent breaking of the structure. Due to the complications with the carbon paper PTL, it was replaced with the same nickel PTL used at the anode for future cells, along with the graphite cathode bipolar plate being temporarily replaced with a titanium plate until bipolar plates made of nickel 400 alloy were acquired.

Once the change from carbon paper to nickel felt for the cathode-side PTL was made, the AEMWE cells tested in this work began to operate more consistently. This consistency is demonstrated by the four polarization curves that were run on Cell 5 (Figure 3.12), the final repeatability cell. All of these polarization curves were very similar, and so for future analysis all the polarization curves measured on a given cell will be averaged. Individual polarization curves for all cells discussed in this work are provided in Appendix E.3. Additionally, from these results it can be noted that there was a consistent hysteresis between forward and backward polarization curves. As will be discussed later, the reduced performance in the backward scan might be due to the lack of cell stability, with the cell performance slowly degrading over a period of six hours under constant operation.

The average polarization curves for Cells 2 through 5 (Figure 3.13) show that these cell all performed very similarly. Although performance across all four cells was not completely consistent, it was repeatable between the cells with the same construction, as the performance of Cells 2 and 3 consistently overlap, as do Cells 4 and 5. Cell 3 did perform slightly worse than Cell 2 in the ohmic region, possibly due to additional passivation of the titanium bipolar plates, which were re-used between these cells. Cell 4 also performed slightly worse in the

**Table 3.6** – Comparison of construction and operational parameters used for the cells tested in this work to obtain repeatability.

Cell Component/Parameter	Cell 1	Cells 2 & 3	Cells 4 & 5 (and 6 to 9)
Membrane	Aemion+ AF2-HLES-50-X	Aemion+ AF2-HLES-50-X	Aemion+ AF2-HWP8-75-X
Catalyst Layer Ionomer	Aemion+ AP2-HNN5-00-X	Aemion+ AP2-HNN5-00-X	Aemion+ AP2-HNN5-00-X
Anode Bipolar Plate	Ti Serpentine	Ti Serpentine	Ni 400 Serpentine
Anode PTL	Ni Felt (Bekipor)	Ni Felt (Bekipor)	Ni Felt (Bekipor)
Anode Catalyst	TKK IrO <sub>x</sub>	TKK IrO <sub>x</sub>	TKK IrO <sub>x</sub>
Anode Catalyst Loading (mg/cm <sup>2</sup> )	1.0	1.0	1.0
Anode Ionomer Loading (wt.%)	4.8	4.8	4.8
Cathode Bipolar Plate	Graphite Serpentine	Ti Serpentine	Ni 400 Serpentine
Cathode PTL	Sigracet 39 AA	Ni Felt (Bekipor)	Ni Felt (Bekipor)
Cathode Catalyst	Hyplat 40wt.% Pt/C	Hyplat 40wt.% Pt/C	TKK 46.7wt.% Pt/C
Cathode Catalyst Loading (mg/cm <sup>2</sup> )	0.1	0.1	0.1
Cathode Ionomer Loading (wt.%)	4.9	4.9	9.6
Cell Feed Method	Cathode & Anode	Cathode & Anode	Cathode & Anode
Feed Electrolyte	1 M KOH	1 M KOH	1 M KOH
Cell Operating Temperature (°C)	60	60	60
Catalyst Layer Fabrication Method	CCM	CCM	CCM
Cell area (cm <sup>2</sup> )	5	5	5



(a) First two polarization curves measured on Cells 1 and 2.

(b) Broken carbon paper PTL used in Cell 1. Membrane-facing side pictured.

**Figure 3.11** – (a) Poor polarization curve results obtained from Cell 1 compared with the results for Cell 2, (b) and the resulting damaged carbon paper PTL.

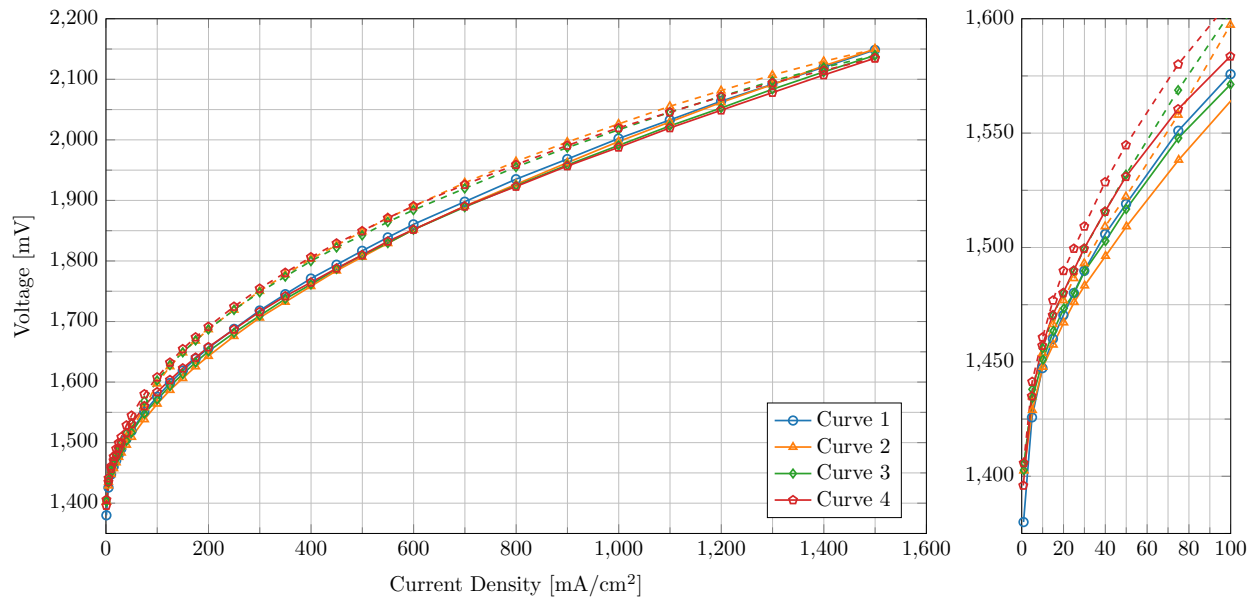


**Figure 3.12** – Polarization curves measured on Cell 5. Backward curves plotted with dashed lines.

kinetic region compared to Cell 5, but this difference is very minimal and may have been caused by inconsistencies in the CCMs from the printing process.

The overall cell performance improved for Cells 4 and 5 compared to Cells 2 and 3, even though a thicker AEM was used, which was expected to increase ohmic losses, thereby decreasing performance. Multiple parameters were altered at once that could contribute to this performance improvement, including a change in the cathode catalyst supplier, an increase in cathode ionomer content, and the switch from titanium to nickel 400 alloy bipolar plates. The catalyst difference was minor, and it is unlikely that the change in cathode ionomer content was the cause, as Koch et al. [30] found no significant change in AEMWE cell operation with ionomer contents of 10 and 20 wt.% in the cathode catalyst layer. It is possible that the change in bipolar plate material resulted in a decrease in high frequency resistance (HFR) as the surface of the nickel 400 plates may not have passivated as much as the titanium, thus counteracting the HFR increase that would have been caused by the thicker membrane.

The change in HFR between cells was taken into account by calculating iR-free polarization curves, where  $E_{iR\ free} = E_{measured} - i \cdot HFR$ . This was done for each measured polarization curve using the average HFR obtained as discussed below. The resulting average iR-free polarization curve for each cell were nearly identical (Figure 3.13). This suggests that most of the performance differences were caused by a decrease in ohmic resistance when the cell components were changed. There were still some notable differences in the kinetic region of the curves, where Cells 4 and 5 performed slightly better, meaning some of the changes made to cell construction may have had a minor impact on kinetic performance, or this may have been the result of differences between the two batches of CCMs.

HFR accounts for the resistance of the AEM, PTLs, bipolar plates, and the most conductive phase of the catalyst layers, and is obtained in this work by electrochemical impedance spectroscopy (EIS). EIS measurements were made following each polarization curve and stability test run on all cells in this work (procedure in Section 2.5.3). The EIS results of Cell 5 measured following polarization curve 1, along with the equivalent circuit fits used to obtain the values of HFR are provided in Figure 3.14. HFR is the real component of the impedance at high frequency, or  $HFR = \lim_{\omega \rightarrow \infty} Re(Z)$ . These results show that the HFR of the tested cells remained consistent over the current densities at the time that they were measured. The exact values of HFR obtained by equivalent circuit fit for Cell 5 (Table 3.7, similar tables for Cells 2, 3, and 4 are in Appendix E.5) are quite similar and do not follow a consistent trend. This was true for all cells in this work, and so the HFR of these cells was considered to not be dependent on current density. Therefore, the three measured HFR values obtained following each polarization curve were averaged, and used to estimate the average HFR for iR-free polarization curve calculations. The average HFR values for cells 2 to 5 are given in

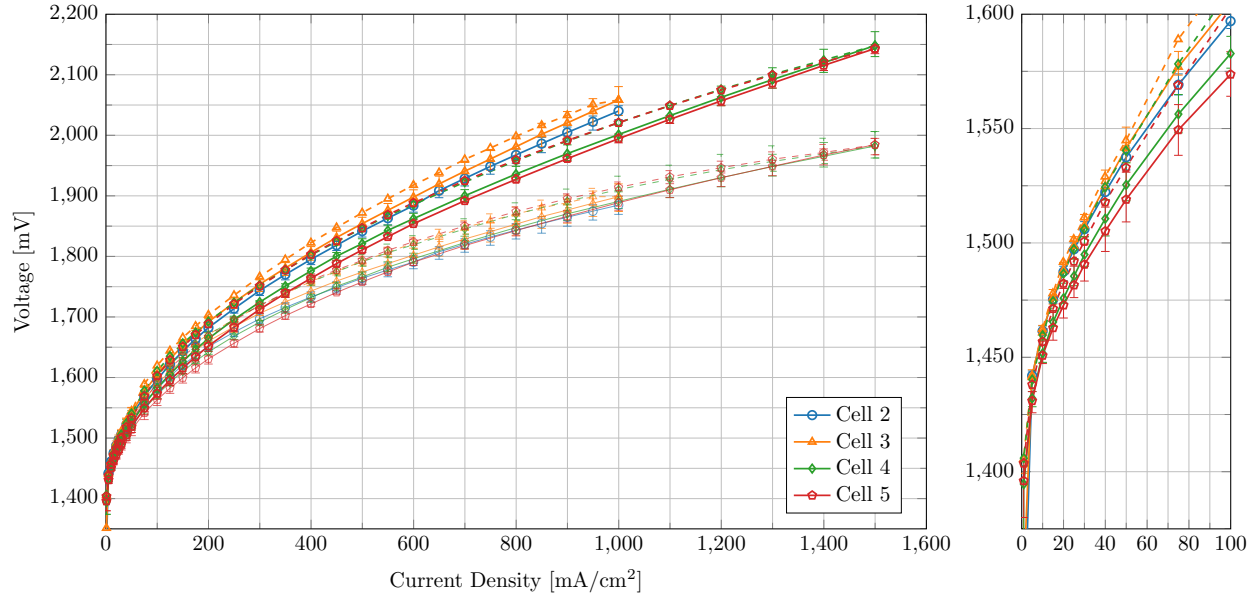


**Figure 3.13** – Average polarization curves run on Cells 2 through 5. Error bars represent the minimum and maximum individual polarization curves from each cell. Backward curves plotted with dashed lines and no error bars, iR-free curves plotted with thinner, partly transparent lines.

**Table 3.7** – HFR values obtained using equivalent circuit fits with the EIS measurements made on Cell 5.

Current Density [mA/cm <sup>2</sup> ]	HFR [mΩ·cm <sup>2</sup> ]				Stability
	Curve 1	Curve 2	Curve 3	Curve 4	
20	103	102	105	116	117
300	102	103	107	109	114
600	103	105	107	109	113
Average	102	103	106	111	114

Table 3.8 (95% confidence intervals were calculated as explained in Appendix B.4).

A final calculation was done using the HFR and cell component resistance to obtain the resistance of just the CCM, which can help to narrow down the cause of the performance difference between these cells. The cell component resistance, or the resistance of the parts of the cell other than the CCM was done using the data in Appendix E.9, and the results for the repeatability cells are provided in Table 3.9. This shows that the change in bipolar plate materials resulted in a minimal reduction in the overall cell resistance. Most of the HFR reduction between these cells, therefore must have been due to the change in membrane. Although a thicker membrane would be expected to increase the resistance, it is possible that the change in reinforcement layer counteracted this.

The repeatability cells were also compared using 6 hour stability tests (Figure 3.15). For

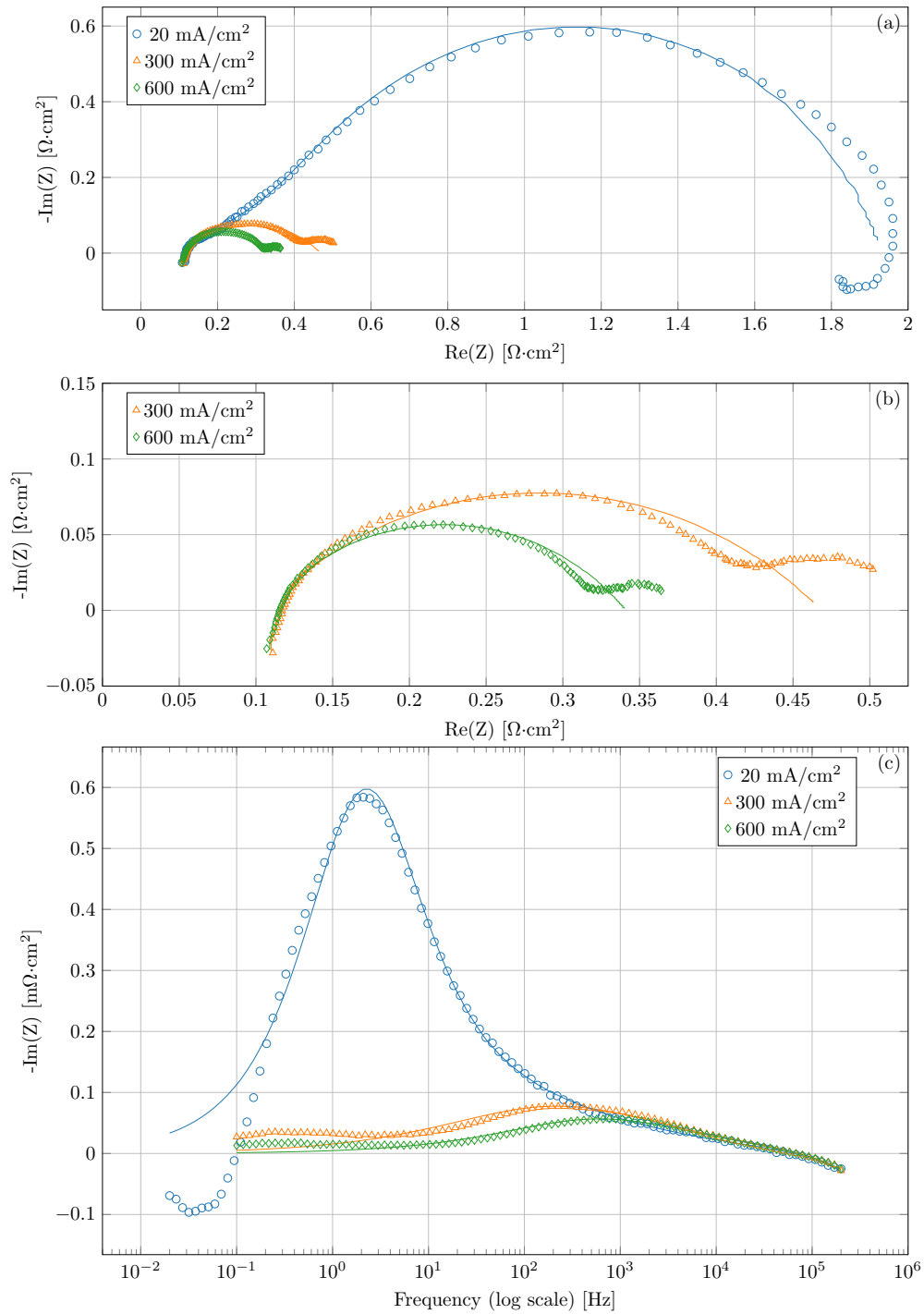


**Figure 3.14** – Results of the EIS measurements made on cell 5 following polarization curve 1 with equivalent circuit fits plotted as lines. (a) Nyquist plot of all 3 measurements. (b) Nyquist plot zoomed in to show the details of the 300 and 600 mA/cm<sup>2</sup> measurements. (c)  $-\text{Im}(Z)$  versus log(frequency) plot of all 3 measurements.

**Table 3.8** – Average HFR values obtained for Cells 2 to 5 following each polarization curve and stability test. Values averaged across all measured current densities. Errors represent a 95% confidence interval.

	Average HFR [ $\text{m}\Omega\cdot\text{cm}^2$ ]				
	Curve 1	Curve 2	Curve 3	Curve 4	Stability
Cell 2	$156 \pm 6$	$154 \pm 8$	$156 \pm 8$	$157 \pm 7$	$153 \pm 10$
Cell 3	$158 \pm 8$	$158 \pm 6$	$161 \pm 11$	$163 \pm 15$	$163 \pm 9$
Cell 4	$110 \pm 2$	$110 \pm 5$	$110 \pm 8$	$112 \pm 8$	$117 \pm 3$
Cell 5	$102 \pm 2$	$103 \pm 4$	$106 \pm 3$	$111 \pm 11$	$114 \pm 6$

**Table 3.9** – CCM resistance for the repeatability cells calculated as the difference of the average HFR and component resistance (resistance of the bipolar plates and PTLs) of each.

	Average HFR [ $\text{m}\Omega\cdot\text{cm}^2$ ]	Component Resistance [ $\text{m}\Omega\cdot\text{cm}^2$ ]	CCM Resistance [ $\text{m}\Omega\cdot\text{cm}^2$ ]
Cell 2	$155 \pm 4$	$5.32 \pm 0.01$	$150 \pm 4$
Cell 3	$161 \pm 5$	$5.32 \pm 0.01$	$156 \pm 5$
Cell 4	$112 \pm 3$	$1.510 \pm 0.007$	$110 \pm 3$
Cell 5	$108 \pm 3$	$1.510 \pm 0.007$	$106 \pm 3$

these tests, cells were held at a constant 1.8 V and the resulting cell current density was recorded (full procedure in Section 2.5.4). Stability tests were run using this method as it was uncertain how well the cells would perform over time, and so it was safer to use a constant voltage rather than a constant current. For these tests, the current densities of Cells 2 and 3 varied significantly, both from each other and from Cells 4 and 5, but for the latter two cells, the current densities were very similar. This change in performance was most likely due to the decrease in HFR after the membrane was changed between Cells 3 and 4 (Table 3.9). An additional conclusion from these tests was that the cells were stable enough to run at a constant current over this time period, and so the feed method testing cells discussed later in this chapter (Cells 5 to 9) will be characterized by constant current stability tests.

Throughout the stability tests, the current densities of Cells 2 to 5 followed similar trends of exponential decay. Cells 4 and 5 did decay slightly faster than Cells 2 and 3. The change in membrane reinforcement type from HLE8 (non-woven reinforcement) to HWP8 (woven reinforcement), that resulted in a decrease in HFR, might have the downside of slightly decreasing overall cell stability. These tests were however, too short to determine at what current the cells would eventually stabilize. Results from Moreno-González et al. [107] showed that similar AEMWE cells held at a set current would, in the long-term, reach a stable potential, but given the time constraints of the cells tested in this work, it was not

possible to run longer stability tests.

By the end of the 6 hour, 1.8 V stability tests, Cells 4 and 5 reached a current density of about 300 mA/cm<sup>2</sup>. In comparison, during their long-term stability tests, consisting of a constant current hold of 200 mA/cm<sup>2</sup> for over 8000 hours, Moreno-González et al. [107] observed quite stable cell performance at 2.0 V with similar construction (same membrane, catalyst materials, nickel PTLs, and 1 M KOH electrolyte). During the tests that Moreno-González et al. performed, they would stop cell operation for a short time once a week, and upon restarting cell operation, performance would recover before quickly returning to the previous stable performance level. This trend is similar to that observed in Figure 3.15, as the cell performance in this work also quickly decreases initially, before beginning to level off. Similar results can also be seen for Cells 6 to 8 in Figure 3.24 later in this work. This indicates that AEMWE cell performance quickly decreases during prolonged operation before stabilizing, possibly due to a depletion of OH<sup>-</sup> ions within the cell membrane before the system reaches an equilibrium where ions are absorbed as fast as they are consumed.

The stability test results show that the use of characterization methods in addition to just polarization curves may be necessary when testing AEMWE cells in order to get a complete overview of the effect of cell and operational parameters, since the stability tests magnified differences that did exist, but were very minor, in the polarization curves. The HFR of each cell was also measured following the stability tests (Table 3.8) to determine if the extended period of operation caused any changes. For all these cells, the value of HFR did not greatly increase or decrease following the stability tests, meaning that the extended operational period did not have a negative effect on the membrane.

The performance of the cells in this work obtained using the polarization curves were compared against that of literature cells provided by Miller et al. [8] to determine how well they performed (Figure 3.16). At 1.8 V, Cell 5 achieved a current density of 475 mA/cm<sup>2</sup>, resulting in the performance of this cell being above the 75th percentile of the CCM AEMWE cells in the literature reviewed by Miller et al. A comparison against a few select AEMWE cells in literature with similar materials was also done (Figure 3.17). Cell 5 was used as it had the same components as the cells discussed later in this work and performed the best of the repeatability cells. Results from Storbakken, Fortin et al., and Koch et al. [22, 30, 40] were selected for comparison as they all used Aemion membranes, although only Koch et al. used Aemion+. The components and operational parameters used for Cell 5 and the literature sources are compared in Table 3.10. The literature sources achieved higher performance than that presented here when normalized by area, but were similar when normalized by catalyst loading.

The catalyst loadings used in this work were quite low as inkjet printing CCM fabrication aims to lower catalyst loading and has a comparatively slow rate of material deposition. Due

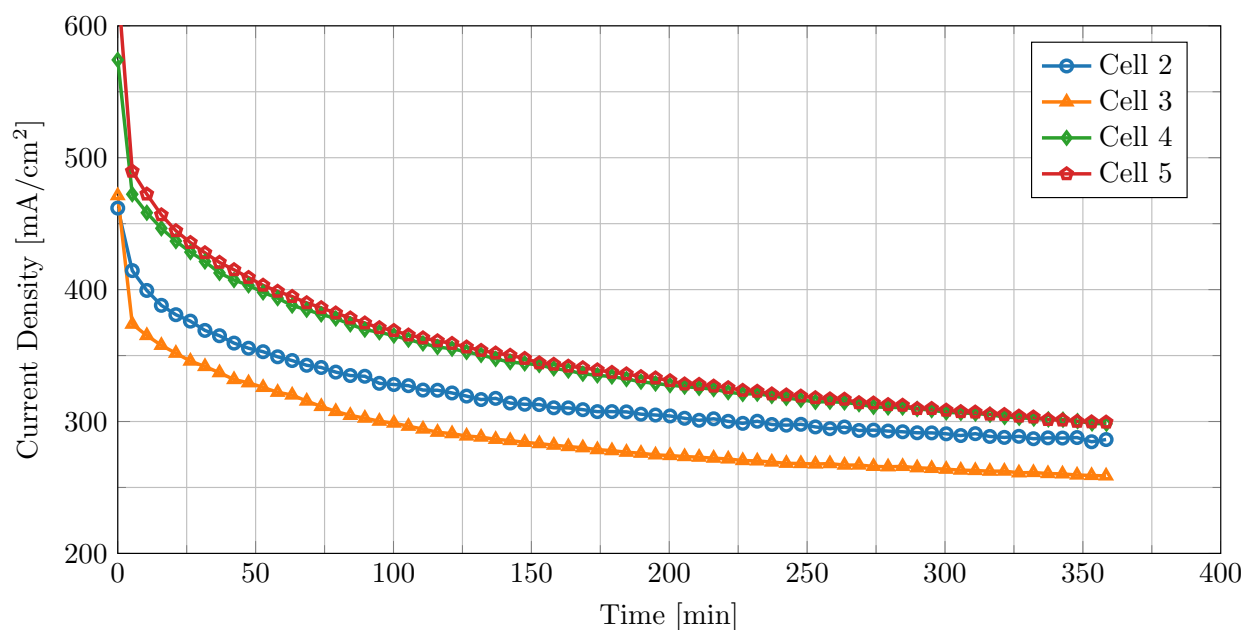


**Figure 3.15** – Stability test results for Cells 2 through 5. Each test was run for 6 hours at a constant cell potential of 1.8 V.

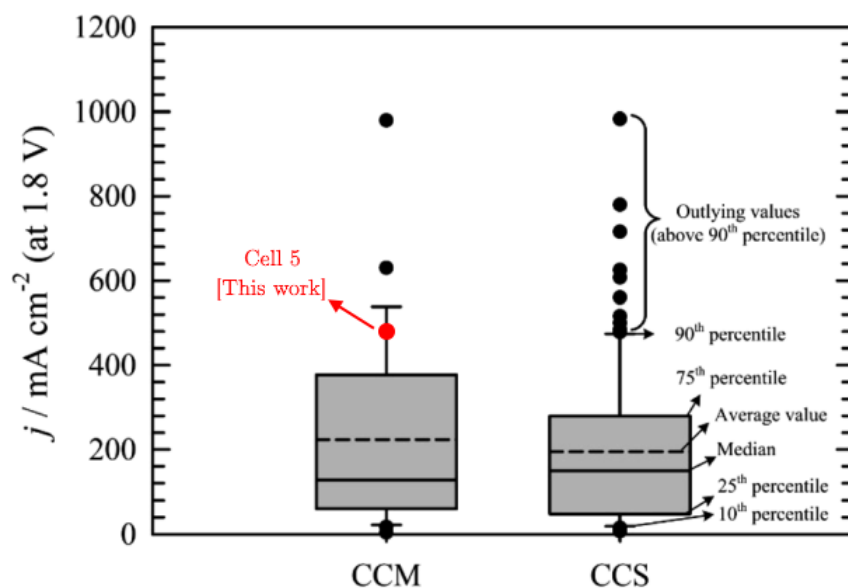


**Figure 3.16** – Box and whisker plot comparing AEMWE cell performance in literature, reproduced from Miller et al. [8], with the performance obtained for Cell 5 from this work included.

**Table 3.10** – Comparison of construction and operational parameters used for Cell 5 and cells from literature used for comparison.

Cell Component/Parameter	Eitzen Cell 5 [This work]	Storbakken [40]	Fortin et al. [22]	Koch et al. [30]
Membrane	Aemion+ AF2-HWP8-75-X	Aemion AF1-HNN8-50-X	AF1-HNN8-25-X	Aemion+ AF2-HLE7-25-X
Catalyst Layer Ionomer	Aemion+ AP2-HNN5-00-X	Aemion AP1-HNN8-00-X	Aemion AP2-HNN8-00	Aemion+ AP2-HNN6-00-X
Anode Bipolar Plate	Ni 400 Serpentine	Ti Serpentine	Gold-coated Ti	Gold-coated Ti
Anode PTL	Ni Felt (Bekipor)	Ni Felt (Bekipor)	Ti	Ti Felt
Anode Catalyst	TKK IrO <sub>x</sub>	TKK IrO <sub>x</sub>	Ir Black	IrO <sub>x</sub>
Anode Catalyst Loading (mg/cm <sup>2</sup> )	1.0	1	3.5 to 3.8	1
Anode Ionomer Loading (wt.%)	4.8	15	7	7
Cathode Bipolar Plate	Ni 400 Serpentine	Graphite Serpentine	Gold-coated Ti	Gold-coated Ti
Cathode PTL	Ni Felt (Bekipor)	Toray 90	Ti	Carbon Paper
Cathode Catalyst	TKK 46.7wt.% Pt/C	Hyplat 60wt.% Pt/C	60 wt.% Pt/C	60wt.% Pt/C
Cathode Catalyst Loading (mg/cm <sup>2</sup> )	0.1	0.1	1	0.5
Cathode Ionomer Loading (wt.%)	9.6	15	25	20
Cell Feed Method	Cathode & Anode	Cathode & Anode	Cathode & Anode	n/a
Feed Electrolyte	1 M KOH	0.85 M KOH	1 M KOH	1 M KOH
Cell Operating Temperature (°C)	60	60	50	60
Catalyst Layer Fabrication Method	CCM	CCM & CCS	CCS	CCM
Cell area (cm <sup>2</sup> )	5	5	25	4

to this difference, in addition to area-normalized current densities, performance comparisons were done with both catalyst loading-normalized current densities (Figure 3.17b), where  $i_{loading} = \frac{i_{area}}{Pt\ loading + IrO_x\ loading}$ , so that the resulting  $i_{loading}$  has units of  $\frac{mA}{mgPt+IrO_x}$  (An  $IrO_x$  loading of  $3.5\ mg/cm^2$  was used for the Fortin et al. data). Cell 5 performed better than the cell from Fortin et al. when normalized by catalyst loading, and was much closer to the cell from Koch et al., only performing slightly worse for current densities less than  $100\ mA/cm^2$ . Cell 5 from this work also surpassed the Koch et al. at current densities above  $600\ mA/mg$  since Koch et al. observed mass transport losses which were not seen in this work. Comparing to the results from Storbakken, kinetic losses are slightly worse for this work, which may be due to the different catalyst used in the cathode.

The performance of Cell 5 was similar to the literature cells at low current densities, but began to fall behind above about  $100\ mA/cm^2$ . The iR-free data in Figure 3.17 shows that this was not due to ohmic losses, as the literature sources still performed better when these were accounted for. This means that the performance difference must have been due to poorer reaction kinetics, and therefore kinetic losses, above  $100\ mA/cm^2$ , attributing the reason for the performance differences to the catalyst loadings or the catalyst manufacturers. As iR-free performance of the cells tested by Fortin et al. and Koch et al. still out-performed Cell 5 when normalized by catalyst loading, the performance differences may have instead been caused by differences in the electrode structure or catalyst manufacturer [105].

It is also possible that the way the cells were operated led to performance differences. The polarization curves run on these literature cells also used slightly different test profiles than this work. Fortin et al. and Koch et al. also used 60 second and 120 second long holds, respectively for the polarization curve steps. Results from this work did not always use the same polarization curve profile however, as it was changed between Cells 3 and 4 with no notable impact on performance. Additionally, Figure E.32 shows that changing the current step length resulted in only minor differences. It is possible that the conditioning procedures used in this work resulted in poorer cell performance as no conditioning processes were reported by Fortin et al. or Koch et al. The performance of the cells tested in this work only decreased during conditioning, although this decrease was not large enough to explain the entire performance difference between the cells in this work and literature.

It is interesting that despite using a membrane that was three times thinner, Koch et al. saw much larger ohmic losses when compared to this work. The HFR that Koch et al. measured was just under  $300\ m\Omega\cdot cm^2$ , nearly three times larger than that of Cell 5. This is puzzling, as there are not many factors that could have caused such a large difference. Koch et al. did use a slightly higher cathode catalyst loading, which would result in a thicker catalyst layer with higher resistance, and a lower relative IEC membrane, which would have cause lower ionic conductivity in the membrane, but these differences were quite

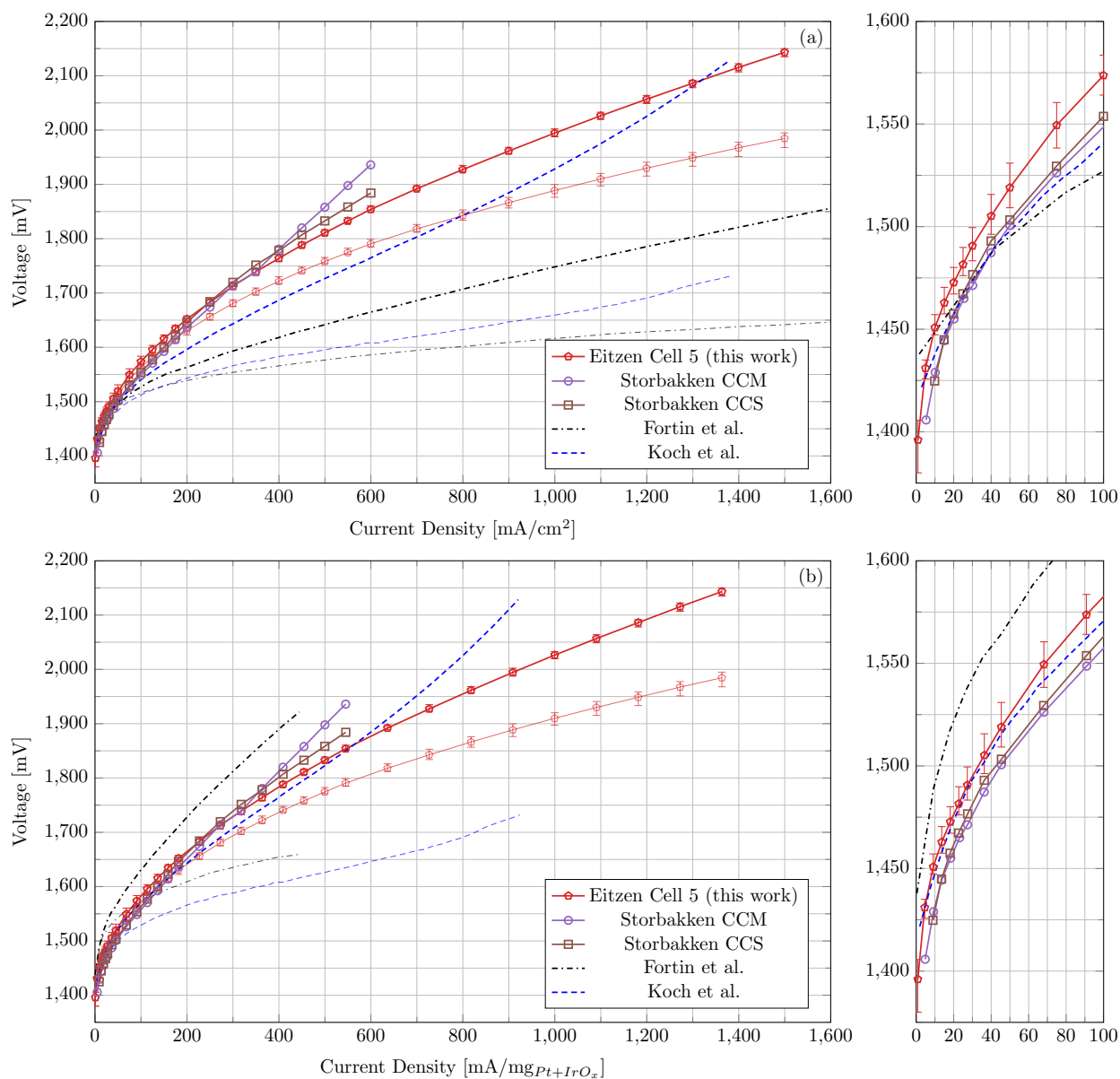


**Figure 3.17** – Comparison of the performance achieved by Cell 5 and literature sources that also used Aemion membranes and ionomer. *i*R-free curves provided for Cell 5, Koch et al., and Fortin et al. data with thinner, partly transparent lines. (a) polarization curves with standard area-normalized current densities. (b) polarization curves with current densities normalized by the sum of IrO<sub>x</sub> and Pt loading.

small. This leaves only cell hardware, the different catalyst manufacturers, or the lack of cell conditioning. For comparison, the HFR reported by Fortin et al. was about  $125 \text{ m}\Omega\cdot\text{cm}^2$ , which is only slightly higher than that measured for the cells in this work despite their much higher catalyst loadings.

### 3.2.2 Reference Electrode Integration

For a two electrode system, the potential between the anode and cathode, or total cell potential, can be measured, but the overpotential introduced at each electrode cannot. A reference electrode allows for the half-reaction overpotentials at the cathode and anode of an electrochemical cell to be analysed independently by measuring the electrode potential with respect to it. Ideally, no current flows through the reference electrode meaning it has zero overpotential, and all voltage variations can be attributed to the electrode being measured.

Integration of the reference electrode is a challenge for an AEMWE cell. A noted feature of AEMWE cells is their compact construction due to the thin polymer electrolyte membranes, that increase cell efficiency, but also cause difficulty when integrating a reference electrode, as it must be at the same electrolyte potential as the electrode being measured. As covered in section 1.2.4, various reference electrodes have been tested with similar cell layouts, including both the addition of an electrode inside the cell, and the use of an ionic bridge to connect to an external electrode. In this work, a similar method was used to that tested by Xu et al. [53], where a Ag/AgCl electrode was immersed in a 1 M KOH solution, from which a thin strip of AEM was extended to the inside of the cell, where it could contact the membrane of the CCM. Further details on the integration of the reference electrode and the way separated electrode overpotentials were calculated are provided in Section 2.4.4.

The reference electrode used in this work was a Ag/AgCl electrode (Pine Research) as this type of electrode is inexpensive and easy to work with. Ag/AgCl electrodes are not intended for use in high-pH environments, so to ensure the 1 M KOH solution did not cause the reference electrode potential to drift over time, potential drift tests were regularly performed. These were done by placing the Ag/AgCl electrode used as the reference electrode in a saturated KCl electrolyte with a second Ag/AgCl electrode. This second electrode was not used for testing and was always stored in an aqueous saturated KCl solution and was assumed to have a constant potential. Drift tests were performed at minimum once before and once after each cell that used a reference electrode was tested, and the potential difference between the two electrodes was always less than 5 mV, which was considered to be acceptable. The reference electrode remained at room temperature throughout testing, so no temperature correction for its potential was necessary.

The reference electrode was used throughout the full testing procedures for the feed

method study cells, including polarization curves and stability tests. All potentials measured with the reference electrode were converted to overpotentials using the methods covered in Section 2.4.4 for analysis. The materials and construction used for these cells is compared, along with the cell used by Xu et al. [53], in Table 3.11. Compared to Cells 1 to 5, the gasket layout was altered to accommodate the reference electrode connection, as described in Section 2.4.4. The results of the feed method testing will be discussed in the next section, whereas this section will look at the reference electrode measurements made on these cells operating with two-electrode feed to judge how well the reference electrode functioned. The cells discussed in this section and the next will be referred to as Cells 6 through 9.

Two polarization curves were measured under each feed method configuration for these cells. The average of these two curves for each cell under TEF, along with the separated electrode overpotentials are provided in Figure 3.18. The total cell voltage polarization curves for all three cells (Figure 3.18a) were very similar, highlighting again the repeatability of the cells. Initially, Cells 6, 7, and 8 were tested, but as the performance of Cell 7 was inconsistent, an additional cell, Cell 9, was also tested. Cell 9 did under-perform slightly, which was probably caused by small differences in the catalyst layers from the fabrication process. Note that for Cell 9, only TEF and COF polarization curves and stability tests were run, plus an additional test that will be discussed later in Figure 3.26.

The separate anode and cathode overpotential results (Figure 3.18b) show that Cells 6, 8, and 9 are close to one another, and as would be expected, show a positive overpotential in the anode and negative in the cathode. For Cell 7 however, the measured overpotentials were unusually high, and a positive cathode overpotential was measured, which is not physically possible; therefore, the results for Cell 7 contained a considerable error. The reason for this error was most likely related to the connection between the CCM and reference electrode. Cells 6 to 8 used a reinforced membrane strip (Aemion+ AF2-HLF8-15-X). Due to the reinforcement material, the in-plane conductivity of the membrane may have been different depending on which side contacted the CCM. This factor was not controlled for, and so Cell 7 may have used the less conductive side, with Cells 6 and 8 using the other side. For this reason, Cell 9 was tested using an unreinforced membrane strip. The potentiostat measured the potential difference between the anode and cathode, and the anode and reference electrode, so the higher measurements seen for Cell 7 would be consistent with a higher resistance in the reference electrode connection. These results show the importance of testing multiple cells to obtain repeatability, and since four cells were tested using a reference electrode, it can be confidently stated that there was an error in the Cell 7 polarization curves.

The cathode overpotential for Cells 6 and 9 initially had slightly positive overpotentials before becoming negative; however, the range of uncertainty covers the zero value and the overpotentials quickly become negative. The error in reference electrode measurements was

**Table 3.11** – Comparison of construction and operational parameters used for the cells in this work tested using a reference electrode and different feed methods along with the literature source used for reference electrode comparison.

Cell Component/Parameter	Eitzen Cells 6 to 8 [This work]	Eitzen Cell 9 [This work]	Xu et al. [53]
Membrane	Aemion+ AF2-HWP8-75-X	Aemion+ AF2-HWP8-75-X	Aemion AF1-HNN8-50-X
Membrane Strip	Aemion+ AF2-HLF8-15-X	Aemion+ AF2-HNN8-15-X	Aemion AF1-HNN8-50-X
Catalyst Layer Ionomer	Aemion+ AP2-HNN5-00-X	Aemion+ AP2-HNN5-00-X	Aemion AP1-HNN8-00-X
Anode Bipolar Plate	Ni 400 Serpentine	Ni 400 Serpentine	Ti Pillar-array
Anode PTL	Ni Felt (Bekipor)	Ni Felt (Bekipor)	Stainless Steel
Anode Catalyst	TKK IrO <sub>x</sub>	TKK IrO <sub>x</sub>	IrO <sub>x</sub>
Anode Catalyst Loading (mg/cm <sup>2</sup> )	1.0	1.0	2
Anode Ionomer Loading (wt.%)	4.8	4.8	9.1
Cathode Bipolar Plate	Ni 400 Serpentine	Ni 400 Serpentine	Ti Pillar-array
Cathode PTL	Ni Felt (Bekipor)	Ni Felt (Bekipor)	Toray Carbon Paper
Cathode Catalyst	TKK 46.7wt.% Pt/C	TKK 46.7wt.% Pt/C	Pt Black
Cathode Catalyst Loading (mg/cm <sup>2</sup> )	0.1	0.1	2
Cathode Ionomer Loading (wt.%)	9.6	9.6	9.1
Cell Feed Method	Cathode & Anode	Cathode & Anode	Cathode & Anode
Feed Electrolyte	1 M KOH	1 M KOH	Deionized Water
Cell Operating Temperature (°C)	60	60	50
Catalyst Layer Fabrication Method	CCM	CCM	IrOx CCM, Pt CCS
Cell area (cm <sup>2</sup> )	5	5	4

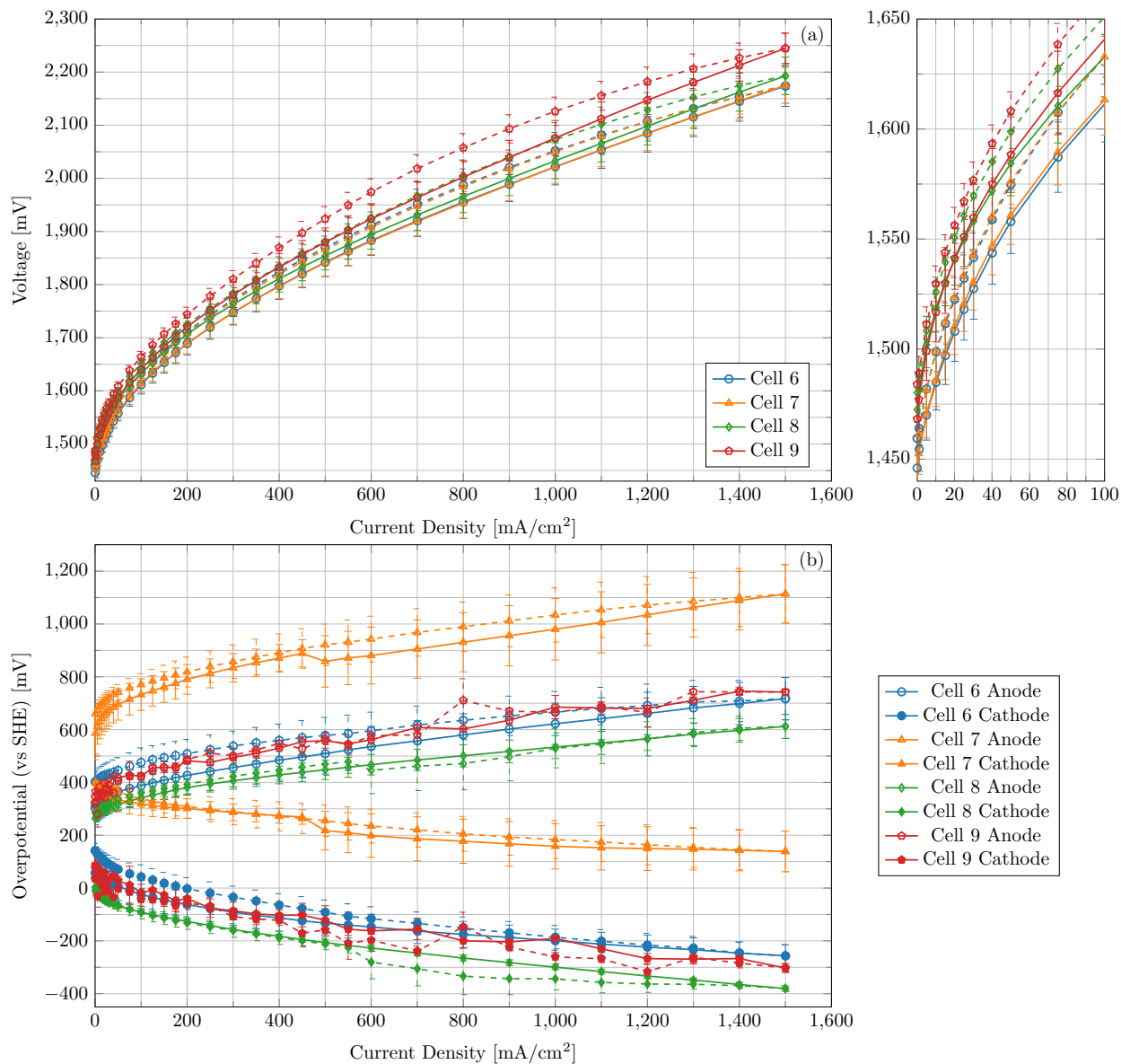


**Figure 3.18** – Average polarization curves measured on the feed method cells. Both electrodes fed with 1 M KOH solution. Error bars represent the minimum and maximum individual polarization curves from each cell. Backward curves plotted with dashed lines and no error bars. (a) Total cell overpotential. (b) Separated electrode overpotentials.

a combination of multiple factors including the the connection between the CCM and reference electrode, the ohmic voltage drop in the membrane, which might be included in the measurement depending on catalyst layer placement [67, 72, 73], and the errors associated with the estimation of the theoretical half-cell potential as it depends on the hydroxide and oxygen activities, which were only approximated. Ideally, the point of equal potential between the anode and cathode is sensed, but this distribution will shift and the sensed potential change due to different electrode kinetics and any small misalignment between the catalyst layers, smaller than can be controlled even with inkjet printing [67, 72, 73]. Other errors may have been introduced by the reference electrode connection itself, as there were two concentration gradients at electrolyte-electrolyte interfaces along the connection path: between the membrane strip and 1 M KOH solution, and between the solution and reference electrode itself. An unknown liquid junction potential might have established due to the concentration gradients.

These polarization curves were performed as described in Section 2.5.2, with current densities tested in a stepwise manner, each held for 90 s. Data obtained for Cell 9 was noisier than that for the other feed method cells due to the change in membrane strip material to the unreinforced Aemion+ AF2-HNN8-15-X. As this membrane strip was unreinforced, it may have dried out faster when exposed to air during cell assembly, in turn resulting in poor conductivity, increasing noise. To compensate for this, each point in all polarization curves for Cell 9 discussed in this work were calculated as an average of the measured potential for 90% of the current step instead of the standard 10%. A dehydrated membrane strip results in poor ionic conduction and the observed effect of this is noise in the measured potential, as demonstrated by the test results shown in Figure 2.14. An unreinforced strip was tested for this cell as the reinforcement layer was thought to be a possible reason for the poor Cell 7 results. The use of a very thin (15  $\mu\text{m}$ ) membrane strip would also result in lower conductivity compared to a thicker membrane, but Cells 6 and 8 also used 15  $\mu\text{m}$  membrane strips and did not see this poor conductivity, so this was not the cause of noise in the data.

Plots of the overpotential over time for the separate electrode polarization curves performed on Cells 6 to 8 are provided in Figure 3.19. Note that each constant-current step was held for 90 seconds, and the profile used is provided in Table 2.4. By analysing the measured voltage over these current holds, the short-term stability of reference electrode measurements can be assessed. The current holds for the separated polarization curves are relatively stable, but do not always follow the expected stepwise behaviour, with some steps blending together. For comparison, voltage versus time plots of the total cell potential are provided in Appendix E.4, and show more constant voltages over the steps. Backward sweeps of the anode and cathode overpotentials were not included here for clarity, but are also provided in Appendix E.4. Cell 9 was not included in this comparison, as the large amount of noise

in the data obscured any small changes in overpotential over time, however the same plots for Cell 9 are provided in Appendix E.4.

The inconsistency of the voltage observed over each current step shows that the error in the reference electrode measurements is not constant throughout the polarization curves. This change over time could have been caused by the build-up of electrical double layers at the electrolyte-electrolyte interfaces on the connection path between the CCM and reference electrode. Another possibility was that the membrane strip-CCM connection point shifted slightly during cell operation, as the membrane material may have swelled and contracted as its hydration increased or decreased. As the CCM had an uneven surface due to the woven reinforcement layer, the bumps in the CCM may have resulted in poor contact at this connection point. If there was then an abrupt movement, a sudden change in the potential sensed by the reference electrode could have occurred, such as that seen at the 5 and 45 minute marks for Cell 7. The change in overpotential throughout each step, although inconsistent compared to the total cell voltage, was smooth, indicating a gradual change. A lack of noise also shows that the membrane strips were not dehydrated. Voltage over time plots for Cell 9 are provided in Appendix E.4, and the separated overpotentials for that cell were very noisy which, as previously discussed, was likely caused by the unreinforced membrane strip used for Cell 9 dehydrating during cell assembly.

The initial anode overpotential was much larger for all cells, which makes sense as it is well known that the OER in the anode is the more sluggish reaction [108, 109]. It can be noted however, that the cathode overpotential seems to increase faster compared to the anode overpotential as the current density increased. This indicates that the anode is influenced more by kinetic effects, whereas the cathode is dominated by transport effects. The results obtained are consistent with the prior knowledge. To further validate the setup, a comparison of the separated electrode potentials for Cells 6 and 8 to those from Xu et al. [53] was done (Figure 3.20). The cell materials and feed method are different (Table 3.11), therefore only a qualitative comparison is possible. Overall, the magnitude of the cathode overpotentials are similar, while the anode overpotential reported by Xu et al. is larger, likely due to the pure water feed. The general shape of the curves was also different, with Xu et al. observing a larger change in the anode overpotential compared to the cathode overpotential over the tested current density range, whereas in this work, the change in both the anode and cathode overpotentials were similar.

The improved cathode performance may have been due to Xu et al. using a 20 times higher cathode catalyst loading compared to this work. It can be noted then, that since cathode loading does seem to have an impact on overall cell performance, the low cathode catalyst loading use in this work could be an explanation for why Fortin et al. and Koch et al. saw better cell performance (Figure 3.17). If the cathode overpotential was lowered

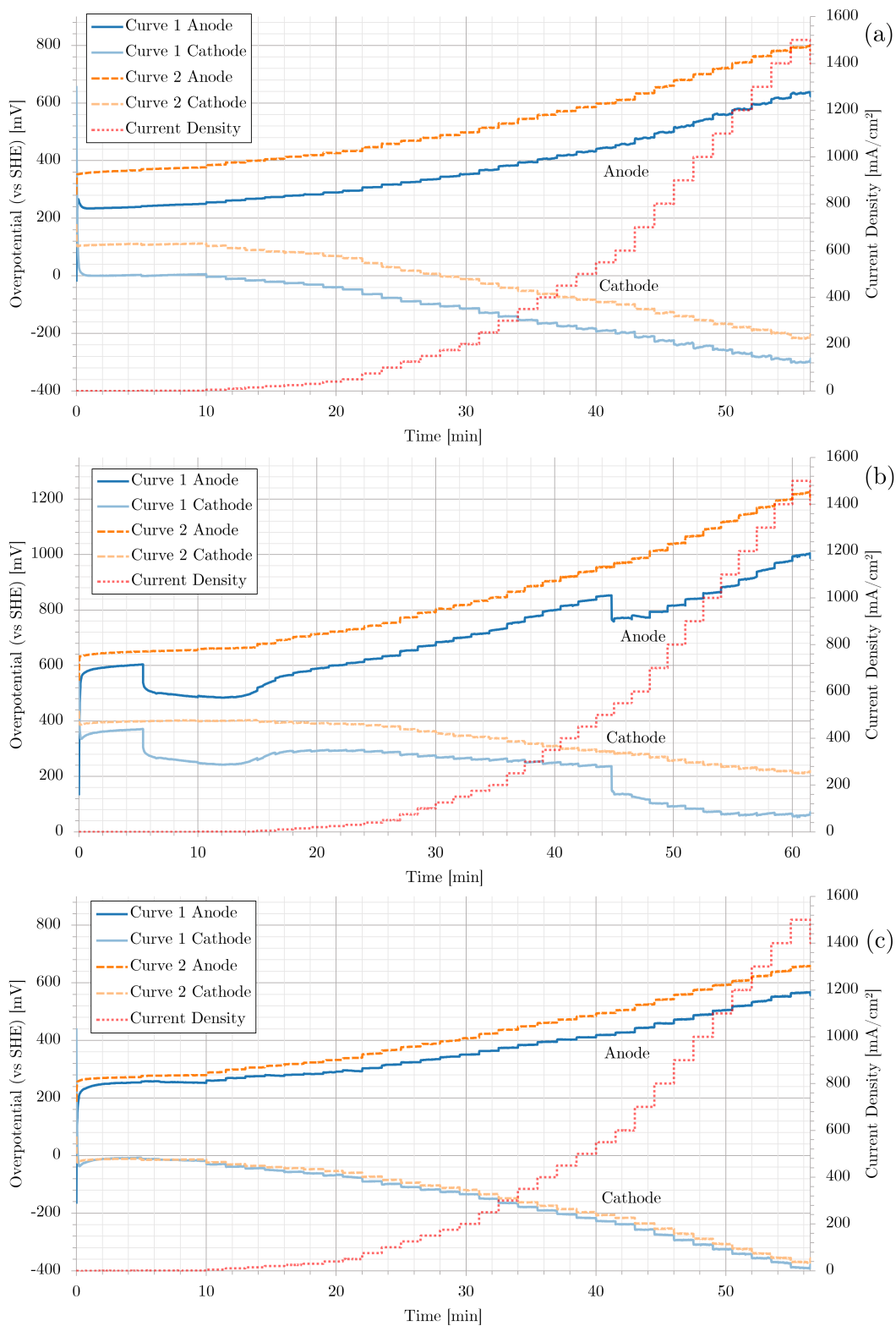


**Figure 3.19** – Plots of the separated electrode overpotential versus time during the two TEF polarization curves (denoted “Curve 1” and “Curve 2”) run on (a) Cell 6, (b) Cell 7, and (c) Cell 8 (forward sweeps).

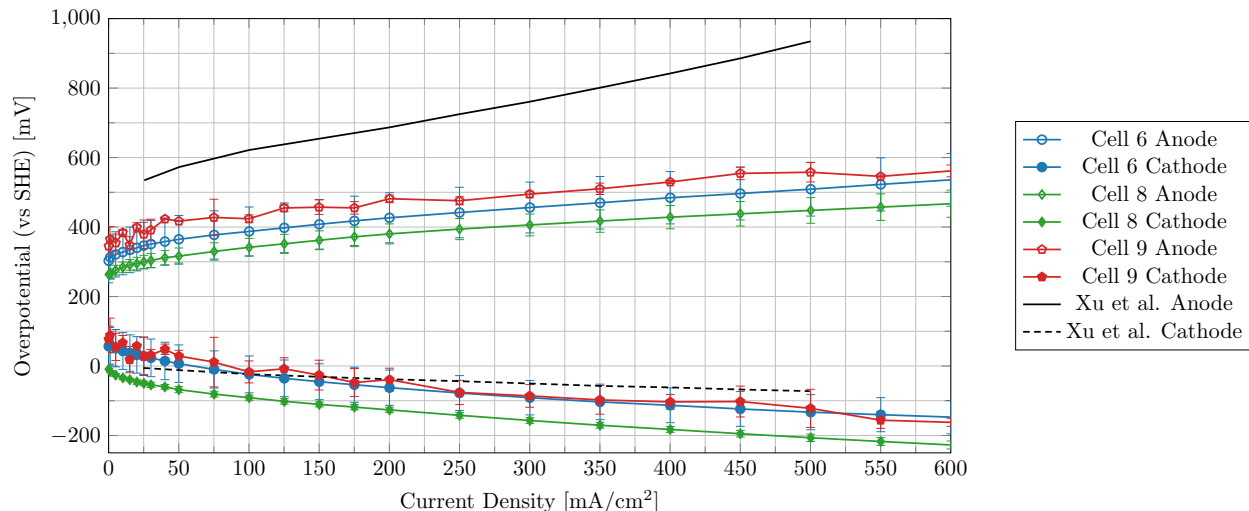


**Figure 3.20** – Comparison of the separated polarization curves measured on the feed method cells with both electrodes fed to the results from Xu et al. [53]. iR-free curves plotted with thinner, partly transparent lines.

by about 200 mV, as the Xu et al. results indicate it could be, the results from this work would be closer to those publications. Xu et al. also used an anode catalyst loading two times higher than this work, but this did not counteract the negative performance impact of the deionized water feed.

Another explanation for the drift in the reference electrode measurements could be that the value of  $E^{eq}$  was not constant throughout cell operation. The separate electrode overpotentials were calculated using Equation (2.8), where the values of  $E^{eq}$  were held constant and calculated using the Nernst equation (Equation (2.9)). During cell operation, if the activity of  $\text{OH}^-$  ions,  $\text{O}_2$ , and  $\text{H}_2\text{O}$  changed locally at the anode, then the value of  $E^{eq}$  would also change, but as this could not be measured, it was not accounted for in the overpotential calculation. As per Equation (2.9), a decrease in  $\text{OH}^-$  activity or an increase in  $\text{O}_2$  or  $\text{H}_2\text{O}$  activity would result in a decrease in the value of  $E^{eq}$ . The value of  $E^{eq}$  used in this work for the anode (the working electrode) was:  $E_{anode}^{eq} = 374$  mV, assuming  $a_{\text{OH}^-} = a_{\text{H}_2\text{O}} = a_{\text{O}_2} = 1$ . An unaccounted for decrease in this value would have resulted in the calculated  $\eta_{anode}$  and  $\eta_{cathode}$  both becoming more positive than they should have been. This exact effect was observed in multiple tests with the reference electrode (Figures 3.18 and 3.20).

The EIS measurements made on Cells 6 to 9 were also performed using the reference electrode, and so in addition to obtaining the HFR between the anode and cathode, the HFR between the reference electrode and the anode/cathode could also be obtained by fitting the equivalent circuit in Figure 2.19 to these EIS measurements (All individual HFR measurements between the anode or cathode and reference electrode are provided in Appendix E.6). A comparison of the average HFR between the anode/cathode and reference

**Table 3.12** – Average HFR measurements made on Cells 6, 7, and 8 between the anode and cathode compared to the average measurements between the anode/cathode and reference electrode.

Average HFR [ $\text{m}\Omega\cdot\text{cm}^2$ ]			
Between Anode and Cathode			
	TEF Curve 1	TEF Curve 2	TEF Stability
Cell 6	$105 \pm 8$	$100 \pm 6$	$101 \pm 8$
Cell 7	$98 \pm 5$	$101 \pm 4$	$100 \pm 5$
Cell 8	$104 \pm 5$	$104 \pm 3$	$104 \pm 9$

Between Anode and Reference			
	TEF Curve 1	TEF Curve 2	TEF Stability
Cell 6	$71 \pm 5$	$76 \pm 2$	$78 \pm 3$
Cell 7	$94 \pm 6$	$98 \pm 5$	$97 \pm 3$
Cell 8	$47 \pm 7$	$63 \pm 9$	$47 \pm 9$

Between Cathode and Reference			
	TEF Curve 1	TEF Curve 2	TEF Stability
Cell 6	$27 \pm 3$	$27 \pm 6$	$22 \pm 4$
Cell 7	$12 \pm 5$	$9 \pm 3$	$11 \pm 2$
Cell 8	$53 \pm 8$	$46 \pm 6$	$48 \pm 9$

electrode (Table 3.12) shows that while there was little change from the polarization curves to stability test for each individual cell, these values were inconsistent between cells. Note that while this data was collected for Cell 9, the reference electrode measurements were too noisy to obtain accurate HFR values. For comparison, the HFR measured between anode and cathode was also provided, which was very consistent between these cells, at a value just above  $100 \text{ m}\Omega\cdot\text{cm}^2$ . Both Cells 6 and 7 had higher HFR between the anode and reference than between the cathode and reference, although Cell 7 was more heavily weighted towards the anode-reference HFR, whereas Cell 8 was evenly split between the two.

These HFR results indicate that the resistance between the reference electrode and anode was not consistent between the cells. This likely did not change reference electrode voltage readings by much, as there would have been close to zero current passing through the reference electrode. This change in resistance could however, indicate that the reference electrode was sensing a different point on the CCM for each cell. This in turn would also change the point of the potential distribution in the cell membrane that it sensed. In this case, this supports the idea that the potential distribution contributed to some of the inconsistencies in the reference electrode measurements between cells.

While the reference electrode potential was consistent for Cells 6, 8, and 9 in the short term, it was not for the six hour stability tests, and so these results are not discussed here, but are provided in Appendix E.8. A possible explanation for the inconsistencies in these tests may have been that the change in the activities of the anode reaction species during cell operation resulted in a change in the reference electrode readings.

### 3.2.3 Cell Feed Method Study

For the study of AEMWE cell feed method, three cells (numbered 6, 7, and 8) were tested for repeatability in two-electrode feed (TEF), anode-only feed (AOF), and cathode-only feed (COF) configurations using the same characterization methods as the repeatability cells covered in Section 3.2.1. The objective of these tests was to characterize AEMWE cell performance under these operating configurations to determine how they influenced cell operation. From the literature that has tested electrode feed method in AEMWE cells [24, 45, 54, 55], it was expected that AOF feed would be the better single-electrode configuration, but there has not been much work done on this topic testing both feed methods, or investigating the reasons for this performance difference. Cells 6, 7, and 8 used the same construction and operational parameters as Cells 4 and 5 and are laid out in Table 3.11. Cell 9, which was mainly tested to investigate reference electrode operation, was also operated under TEF and COF configurations to obtain additional polarization curve and stability test data.

TEF was tested first and following this, the cathode-side of the cell was drained, and the feed line disconnected and capped. The short conditioning profile provided in Table 2.3 was run to displace air that had entered the system during the feed method change. On the same day, two polarization curves were run, followed the next day by a 6 hour, 300 mA/cm<sup>2</sup> stability test. The polarization curves and stability test were all followed by EIS measurements. After the AOF test, the same procedure was followed to change the cell over to COF, and the same tests run. Finally, after all these tests were finished, the cell was switched once more to TEF and the same tests were repeated to ensure the cell had not significantly degraded throughout feed method testing. When discussing both sets of TEF results, they have been denoted as “TEF 1” and “TEF 2” (if 1 or 2 is not specified, assume TEF 1 results).

The total cell potential polarization curve results for Cells 6 to 8 were repeatable, so the scan results from all three cells were averaged for each feed method (Figure 3.21, individual results in Appendix E.3). The polarization curves for Cell 9 were not used for this figure, as it was only operated using TEF and COF, but these results are discussed later, and the individual polarization curves are provided in Appendix E.3. The TEF and AOF methods resulted in nearly identical cell performance, whereas COF was quite a bit worse at high

current densities. For AOF, water must have been able to diffuse through the membrane at a high enough rate to replenish the water used in the HER. At low current densities, less than 100 mA/cm<sup>2</sup>, there were small differences between the three configurations, but it is too close to draw any solid conclusions for kinetic differences.

The poor performance of COF is surprising considering that the cathode is where the HER takes place, which consumes two water molecules per mole of H<sub>2</sub> produced. The COF method did not result in higher ohmic losses, therefore the performance loss was likely due to a lack of reactant hydroxide ions at the unfed anode. This would have required all the OH<sup>-</sup> ions needed as reactant for the OER at the anode be transported from the cathode, through the membrane and the ionomer in the catalyst layer to the reaction sites. The relatively low anode ionomer loading also did not help with this, as without the supporting electrolyte, all OH<sup>-</sup> ions had to be conducted from the membrane to the reaction sites using the ionomer in the catalyst layer. In addition to the lack of ions and supporting electrolyte, water is produced at the anode during the OER, and with COF, this water would not have been flushed out of the catalyst layer and could have built up. Ionomer recommends not to expose Aemion+ ionomer to pure water [49], and so COF operation may have damaged the catalyst layer. Not much permanent damage was done however, as performance was mostly recovered on subsequent tests, as demonstrated by the TEF 2 polarization curves (Figures E.12, E.14, E.15).

It is interesting that AOF performed very similarly to TEF, as in this configuration, the cathode, which uses water as a reactant for the HER, is not directly fed water. This means that water must be easily transported through the Aemion+ AF2-HWP8-75-X membrane. The need to transport water from anode to cathode only caused minor performance impacts at the current densities achieved in this work. In comparison to the performance decreases seen with COF, this also implies that Aemion+ membranes transport water more readily than OH<sup>-</sup> ions. By taking advantage of only needing to feed the anode, the setup required to operate an AEMWE cell could be simplified. This would reduce the complexity of the equipment used by reducing the number of required parts, such as electrolyte containers, heaters, and tubing, and removing the need to separate H<sub>2</sub> gas from the KOH electrolyte upon exiting the cell.

To further investigate the performance differences of COF, the separated anode and cathode overpotentials for TEF and COF were compared (Figure 3.22). The use of the reference electrode measurements here allowed for the effects of COF on the individual electrodes to be observed. These results show that the anode overpotential increased by a greater amount relative to the TEF overpotentials, meaning that most of the performance losses observed under COF were due to effects at the anode. This reinforces the previously discussed possibilities for the lower COF performance: a shortage of reactant OH<sup>-</sup> ions,

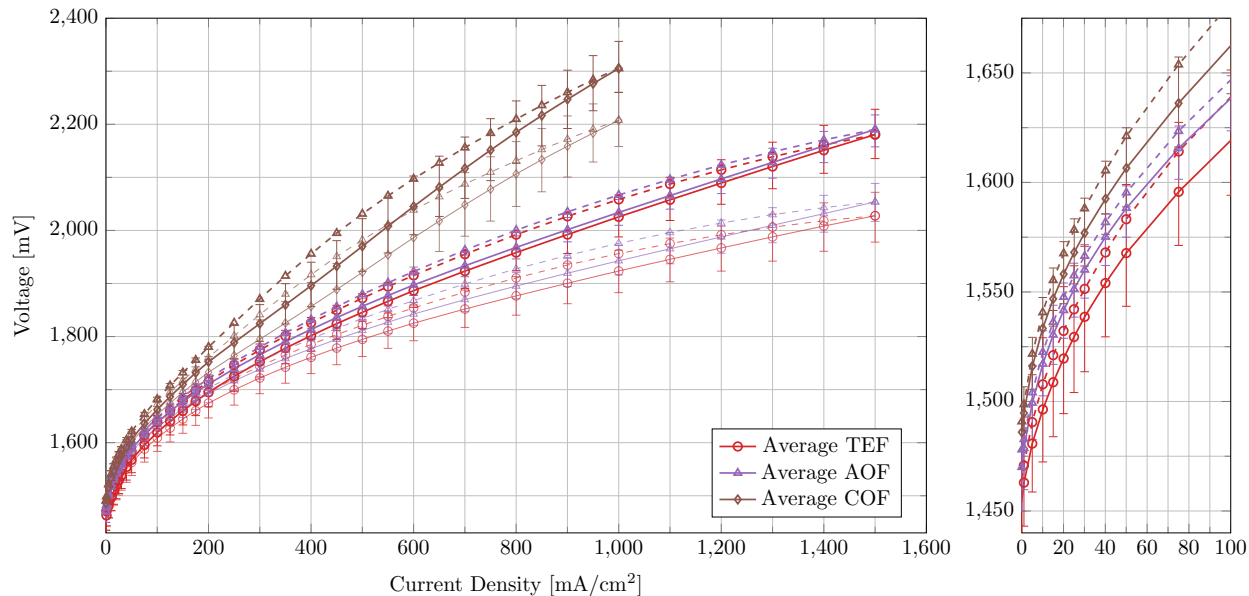


**Figure 3.21** – Average polarization curves across cells 6 to 8 for each of the feed methods tested. Error bars represent the minimum and maximum individual polarization curves from these cells. Backwards curves plotted as dashed lines without error bars, iR-free curves plotted with thinner, partly transparent lines.

or a loss of ionic conductivity. The additional anode losses also seem to be quite linear with current density, implying that the losses were ohmic, which would be consistent with a decrease in ionic conductivity. The little change in cathode overpotential is understandable, as it was fed under both of these feed methods. The individual polarization curves averaged to make Figure 3.22 are provided in Appendix E.3.

EIS measurements were performed on the feed method cells using the profiles laid out in Table 2.6. The resulting HFR values were obtained by fitting the equivalent circuit in Figure 2.18 to EIS data. The EIS and equivalent circuit fit done on Cell 6 following TEF curve 1 is given in Figure 3.23, and the obtained HFR values in Table 3.13 (similar tables for Cells 7, 8, and 9 are in Appendix E.5). These results showed that the HFR remained relatively constant with no strong trend over the tested current densities, and therefore the measurements made on the feed method cells were averaged and are provided in Table 3.14. The HFR was not only constant over the current density range, but also did not change much between the feed methods, as shown in Table 3.14, meaning that the feed methods did not have an impact on the cell resistance.

Stability tests were also run on these cells in each feed method configuration (Figure 3.24). Unlike the stability tests on the repeatability cells, these tests used a constant current of 300 mA/cm<sup>2</sup> and the voltage was measured. This includes two tests performed with both electrodes fed, denoted “TEF 1” and “TEF 2”, run first and last out of the four total tests

**Table 3.13** – Total cell HFR values obtained using equivalent circuit fits with the EIS measurements made on cell 6.

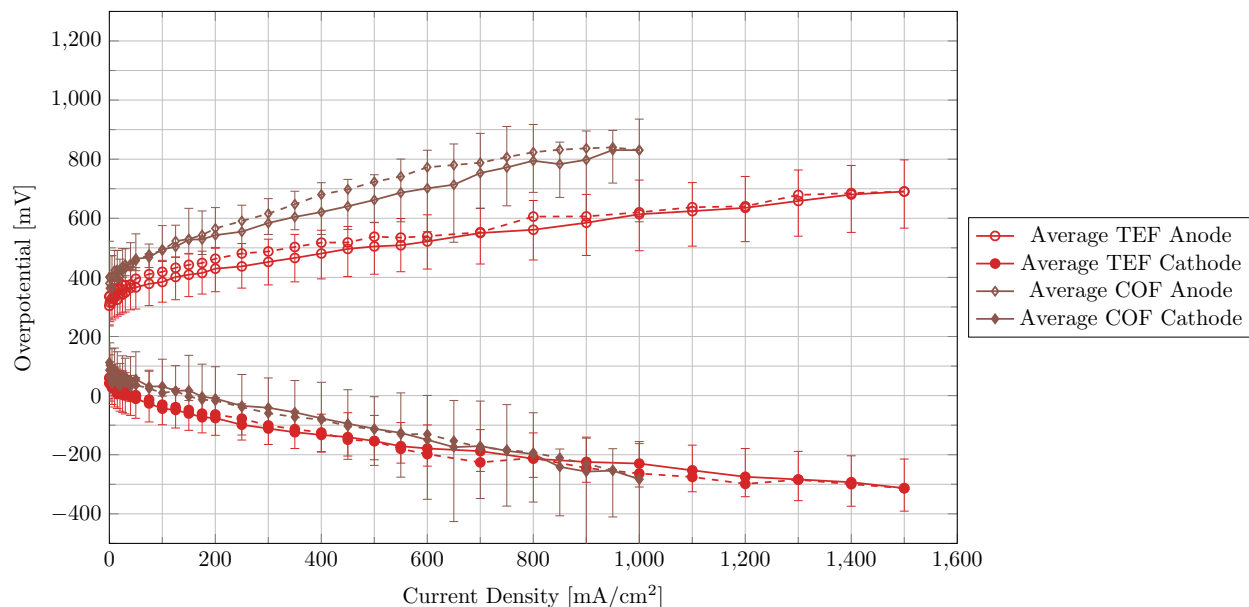
Current Density [mA/cm <sup>2</sup> ]	HFR [mΩ·cm <sup>2</sup> ]		
	TEF Curve 1	TEF Curve 2	TEF Stability
20	117	91	91
150	102	104	109
300	106	101	103
600	102	102	103
1000	100	100	101
Average	105	100	101

	AOF Curve 1	AOF Curve 2	AOF Stability
20	95	70	77
150	98	93	100
300	101	92	99
600	93	92	91
1000	85	83	86
Average	94	86	91

	COF Curve 1	COF Curve 2	COF Stability
20	86	73	98
150	100	99	101
300	105	98	98
600	107	104	91
900	110	104	100
Average	102	96	98



**Figure 3.22** – Average polarization curves across Cells 6, 8, & 9 of the separated electrode overpotentials for TEF and COF. Error bars represent the minimum and maximum individual polarization curves from these cells. Backwards curves plotted as dashed lines without error bars.

**Table 3.14** – Average total cell HFR values measured on the feed method cells following each polarization curve and stability test for all tested feed methods. Errors represent a 95% confidence interval.

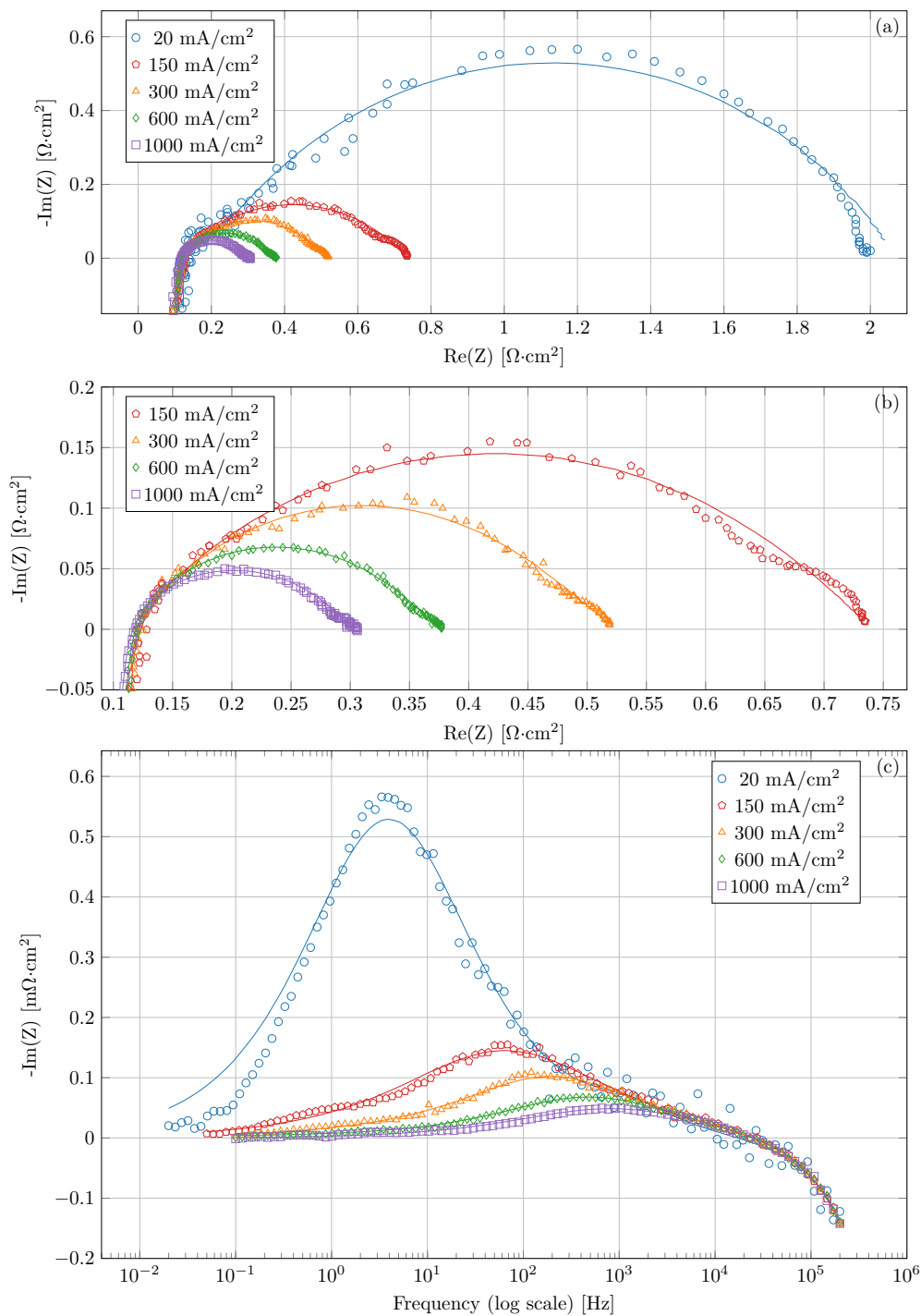
	Average HFR [ $\text{m}\Omega\cdot\text{cm}^2$ ]		
	TEF Curve 1	TEF Curve 2	TEF Stability
Cell 6	$105 \pm 8$	$100 \pm 6$	$101 \pm 8$
Cell 7	$98 \pm 5$	$101 \pm 4$	$100 \pm 5$
Cell 8	$104 \pm 5$	$104 \pm 3$	$104 \pm 9$
Cell 9	$104 \pm 4$	$101 \pm 8$	$107 \pm 5$

	Average HFR [ $\text{m}\Omega\cdot\text{cm}^2$ ]		
	AOF Curve 1	AOF Curve 2	AOF Stability
Cell 6	$94 \pm 7$	$86 \pm 12$	$91 \pm 12$
Cell 7	$94 \pm 6$	$92 \pm 7$	$94 \pm 4$
Cell 8	$98 \pm 7$	$97 \pm 5$	$94 \pm 9$

	Average HFR [ $\text{m}\Omega\cdot\text{cm}^2$ ]		
	COF Curve 1	COF Curve 2	COF Stability
Cell 6	$102 \pm 12$	$96 \pm 16$	$98 \pm 5$
Cell 7	$97 \pm 12$	$97 \pm 7$	$91 \pm 10$
Cell 8	$104 \pm 13$	$101 \pm 9$	$105 \pm 12$
Cell 9	$105 \pm 10$	$104 \pm 11$	$104 \pm 9$



**Figure 3.23** – Results of the EIS measurements made on cell 6 following TEF polarization curve 1 with equivalent circuit fits plotted as lines. (a) Nyquist plot of all 5 measurements. (b) Nyquist plot zoomed in to show the details of the higher current density measurements. (c)  $-\text{Im}(Z)$  versus  $\log(\text{frequency})$  plot of all 5 measurements.

on all the cells, respectively. The data is not averaged over the cells here because unlike the polarization curves, the stability tests were much less consistent between the three, especially for Cell 8, of which the stability test performance greatly decreased throughout the testing of that cell, as can be observed by comparing the two TEF tests.

From the stability test results of Cells 6 and 7, TEF always began at lower cell overpotentials compared to both single-electrode feeds, but TEF and AOF eventually converged, with AOF even being slightly better by the end of the six hours. The good stability with AOF confirms that water can easily be transported through the AEM and react in the cathode and membrane dry-out is not observed. COF on the other hand, always performed much worse and was less consistent by comparison. The similarities in the polarization curve results remained true in these longer tests as well, although AOF may be superior over an even longer time scale. This is not, however, due to permanent degradation in the cell, such as by a decrease in catalyst wash-out at the dry cathode, as the cell performance does recover over time when it is not in operation, as shown by the second TEF tests for Cells 6 and 7. The Cell 8 stability tests differed slightly from the other cells, but AOF still performed better than TEF, and the average degradation rates were consistent with Cells 6 and 7.

After running the standard set of tests on Cell 8 with each feed method, three additional stability tests were run at a higher current density,  $1000 \text{ mA/cm}^2$ , with each feed method, in the order of TEF, AOF, and then COF (Figure 3.25). The results of these tests indicate that while at  $300 \text{ mA/cm}^2$ , AOF might pull ahead over time, at this higher current density, the AOF is worse in comparison to TEF, with COF continuing to perform much worse compared to both. This change in AOF performance may be caused by a depletion of water in the cathode at the higher current density due to electro-osmotic drag and the usage of water being higher than diffusion through the membrane could replenish it. While the results of the original stability tests mostly align with the polarization curves results, where COF performs quite poorly, and AOF and TEF are similar, the higher-current density stability tests resulted in TEF pulling ahead of both AOF and COF. These results may have been influenced by cell degradation in the testing order, however, due to the extended operation at high current densities, and it would be interesting to observe similar tests run in a different order. It would be interesting to know the maximum current before AOF starts to perform worse than TEF in the long term.

The results of the stability tests on Cell 8 showed that AOF was stable at even high current. Current-hold tests were run on Cell 9 to try and repeat these results and determine if AOF was stable at any current. This was done by holding Cell 9 at five current density levels for one hour each in both feed configurations (Figure 3.26). Based on these results, AOF appeared to be stable at high current densities.

The stability test results for Cells 6 and 7 were trusted as those results agreed with each

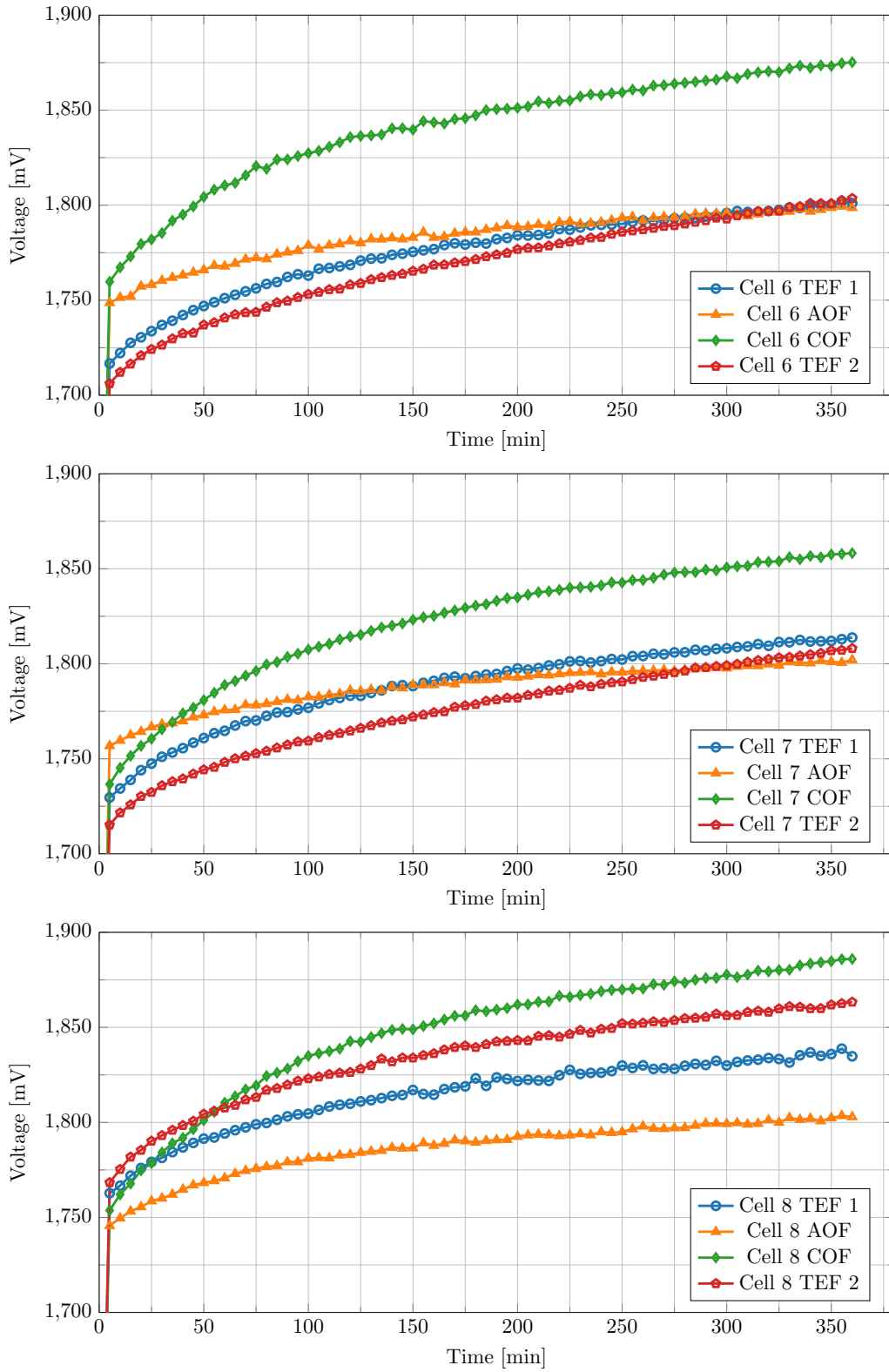


**Figure 3.24** – Six hour stability tests run on feed method cells at a constant  $300 \text{ mA/cm}^2$ . Tests were performed in the order of the legend.

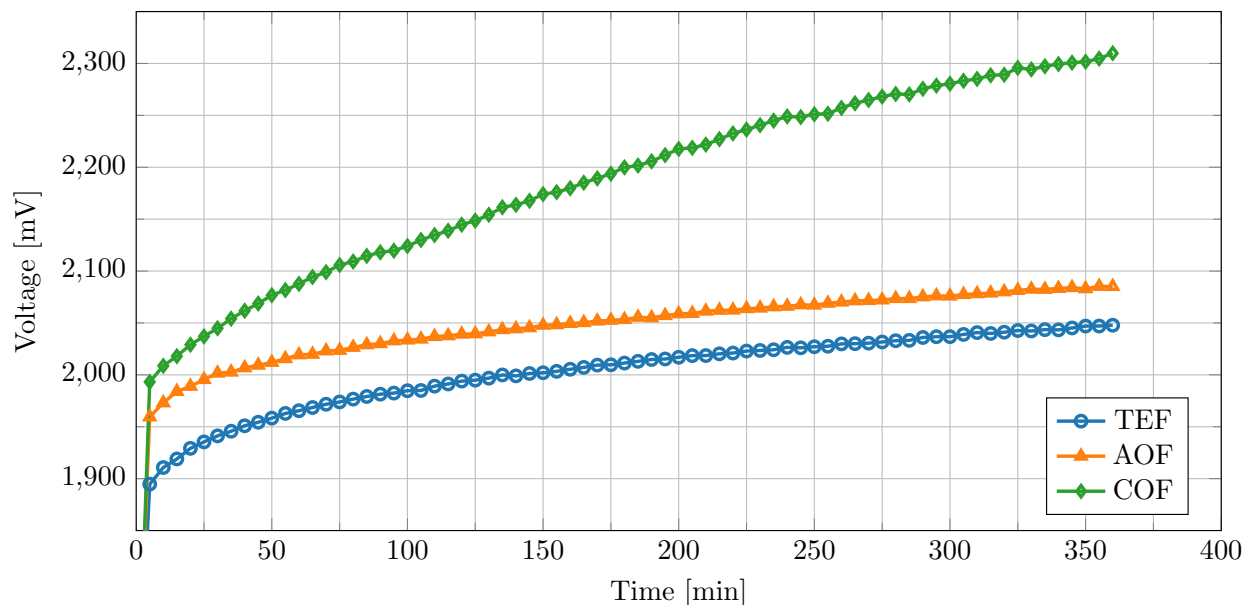


**Figure 3.25** – 6 hour stability tests run on Cell 8 at a constant  $1000 \text{ mA/cm}^2$ . Tests were run in the electrode-feed order of TEF, AOF, COF.

other and with the results for Cell 9 in Figure 3.26. In all these cases, TEF slightly outperformed AOF initially. Figure 3.26 showed that over the test period, the two feed methods started to converge, and over the stability tests for Cells 6 and 7, AOF eventually surpassed TEF. It is possible that over a long enough time frame, AOF may perform significantly better than TEF, but the length of tests necessary to show this could not be done in this work.

Cyclic voltammetry tests were also run on cells 6, 7, and 8 to calculate electrochemically active surface area. These results are provided in Appendix E.10 as they did not show a consistent trend, and so are not discussed in detail in this work.

It was a concern that the order of the feed configurations tests would significantly impact performance, so this was tested using two additional AEMWE cells, the first using AOF followed by COF, and the other in the opposite order. The polarization curves for these tests (Figure 3.27) show that the trends in single-electrode feed performance was independent of the order tested, with COF performing significantly worse at high current densities compared to AOF. Therefore, the order in which the three feed methods were should overall not influence the major observed effects that were discussed here. As was mentioned before, a final check on the feed method cells was also performed, where the TEF was re-characterized after the single-electrode tests to ensure cell degradation remained relatively small.

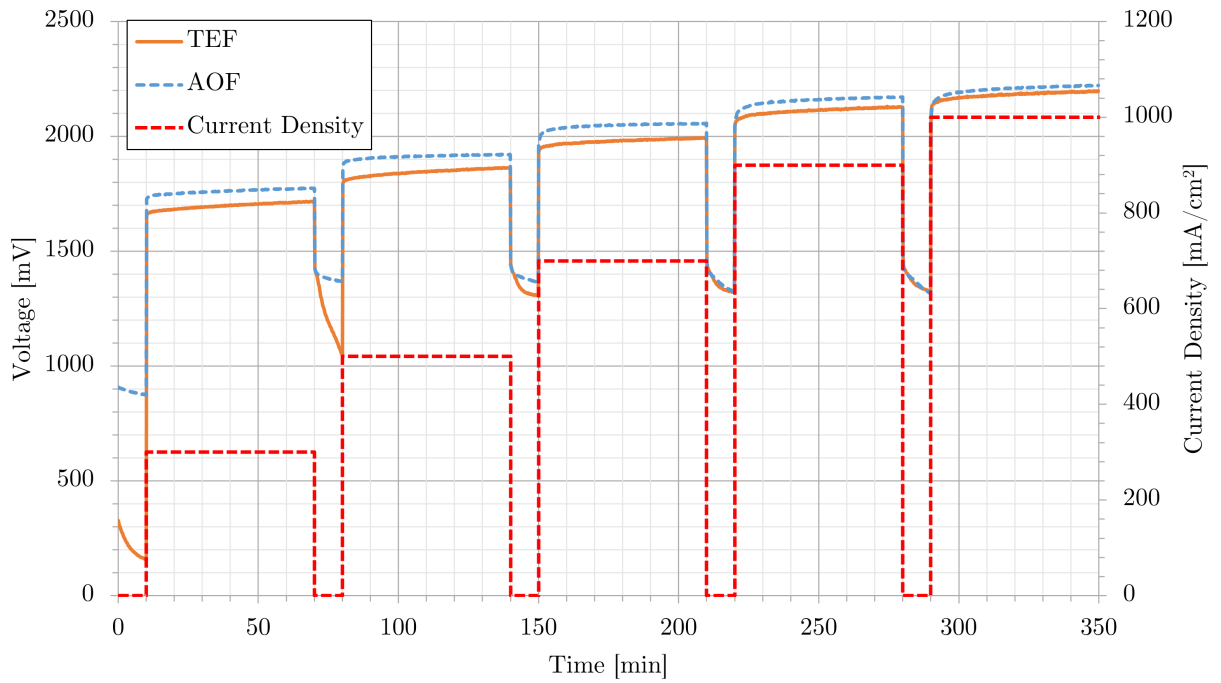


**Figure 3.26** – Test of five current density levels on Cell 9, each held for one hour under TEF and AOF.

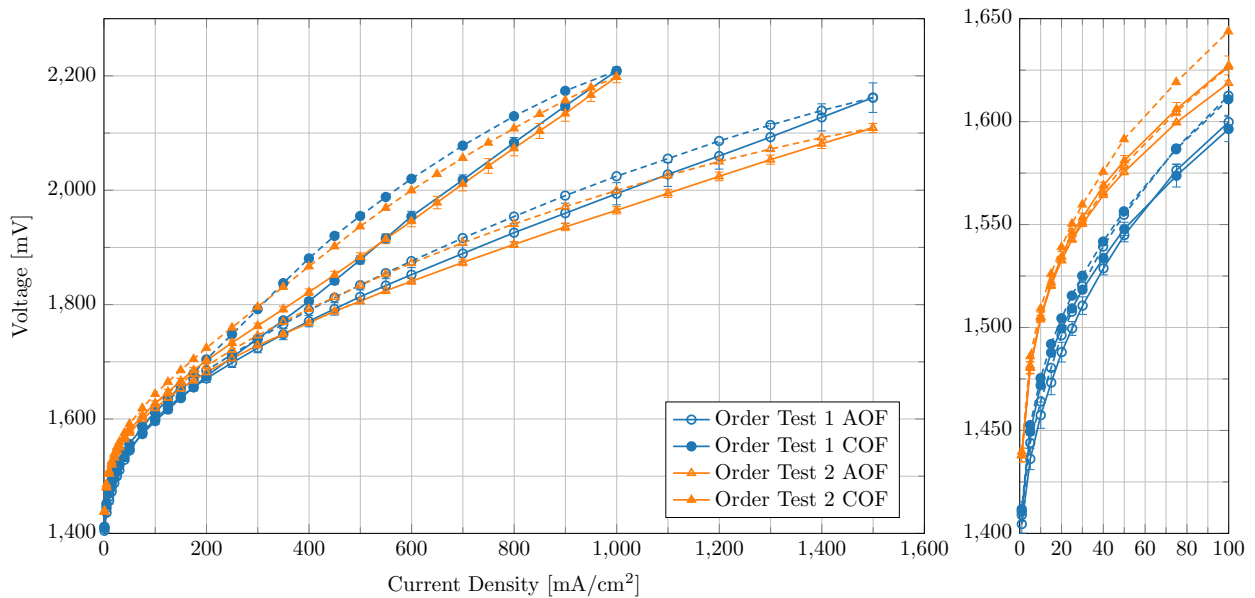


**Figure 3.27** – Polarization curves from test cells used to determine if the order of the feed method tests had a large effect. Test 1 was run AOF first, then COF, and test 2 was run in the opposite order. Error bars represent the minimum and maximum individual polarization curves from each cell. Backward sweeps plotted as dashed lines without error bars.

## 3.2.4 Summary of AEMWE Cell Testing

### Repeatability Cells

Five repeatability cells were initially tested to determine the cell components that would be used for the feed method study, and to ensure that repeatable results could be obtained with the materials used, mainly the new Aemion+ membranes and ionomer. The Aemion+ materials allowed for AEMWE cells to be run to higher current densities and resulted in a lower cell failure rate compared to cells previously tested in the ESDLab using first-generation Aemion by Storbakken [40]. The higher currents did however, result in the carbon paper PTL at the cathode side breaking when the cell was run above  $500 \text{ mA/cm}^2$ , likely due to carbon corrosion caused by higher overpotentials. This was fixed by replacing the carbon paper with a nickel felt PTL, and following this change, Cells 2 through 5 produced repeatable results.

Based on the polarization curve results for Cells 2 through 5 (Figure 3.13), the performance of these cells was comparable, although Cells 4 and 5 performed slightly better than Cells 2 and 3. EIS measurements determined that this difference was due to a decrease in HFR (Table 3.8), as the  $iR$ -free polarization curves were nearly identical for all four cells. As the change in bipolar plates only caused a minor decrease in HFR (Table 3.9), and the other small changes could not have caused this large a difference, it was determined that the change was due to the change in membrane from AF2-HLE8-50-X to AF2-HWP8-75-X. Although a thicker membrane would be expected to increase HFR, the change in reinforcement type had the opposite effect by allowing easier transport of hydroxide ions through the membrane.

Stability tests (Figure 3.15) provided information about the short-term stability of the cells. Cells 4 and 5 were less stable compared to 2 and 3, possibly due to the change in membrane reinforcement. Although this change likely decreased cell HFR, as the woven reinforcement did not seem to restrict the membrane as much, this may have also allowed additional swelling to occur. Still, the performance of Cells 4 and 5 remained above that of Cells 2 and 3 for the whole 6 hours of the test. In future, it would be interesting to compare these membrane reinforcement types in even longer-term tests.

### Reference Electrode Integration

The integration of a Ag/AgCl reference electrode to separate anode and cathode overpotentials in AEMWE cells was done, but the results were not consistent across all the cells. The general trends of the separate electrode polarization curves (Figure 3.18) were close to what was expected, but the measurements from Cell 7 were verifiably incorrect with positive cathode overpotentials throughout the curves. Due to the inconsistent results, another cell, Cell 9, was tested, and was consistent with Cells 6 and 8. From these results, some information

can be obtained, such as the observation that the cathode overpotentials are not negligible. The difference in the anode and cathode overpotentials however, differed from the results seen by Xu et al. [53], indicating that at the higher loadings used by Xu et al., the anode overpotential may begin to dominate over the cathode overpotential. A consistent result between this work and Xu et al. was the observation of a higher initial overpotential in anode compared to the cathode (Figure 3.20). In all cases, the cathode overpotential started at nearly 0 mV, but the anode overpotential started above 200 mV.

The inconsistent reference electrode measurements between cells are hypothesized to have occurred due to complications within the connection between the reference electrode and cell CCMs, or an unaccounted for change in  $E^{eq}$  of the electrodes during operation. However, tests to try and replicate issues with the reference electrode did not show major drifts. The exact placement of the membrane strip was difficult to control, including the points where it contacted the CCM and how far it extended into the bottle with the reference electrode. The strip was always placed in contact with the cathode side of the CCM, although the side of the strip itself that contacted the CCM was not controlled. Since the membrane strip was made from a reinforced membrane (Aemion+ AF2-HLF8-15-X), the properties of either side of it may have been slightly different. Xu et al. [53] avoided this issue by using a non-reinforced membrane strip, as did Cell 9 in this work. Other possible inconsistencies include how well the strip contacted the CCM as the AF2-HWP8-75-X membrane was not completely smooth, the formation of an electrical double layer and electrolyte-electrolyte interfaces on the connection path between the CCM and reference electrode, or a change in  $E^{eq}$  in the electrodes, that when not accounted for would have caused both the calculated anode and cathode overpotentials to become more positive.

To test the hypothesis that the reinforcement layer of the membrane was influencing the reference electrode measurements, Cell 9 was assembled and tested using an unreinforced membrane strip. This resulted in some additional complications, as the unreinforced membrane was more delicate, harder to work with, and seemed to dry-out faster. Cell 9 did however, resulted in electrode overpotentials similar to that of Cells 6 and 8. This does not necessarily prove that the reinforced membrane strip was the cause of the issues with Cell 7, but does contribute to the validity of the data obtained for the other cells, and demonstrates that these polarization curve results were repeatable.

No stability tests (current or voltage hold tests) with a reference electrode have been performed in existing literature for AEMWE cells. The 6 hour current holds done in this work with the reference electrode (Figure E.33) did not work as expected, as the measured reference electrode potential changed over the test period, and was not consistent between the tested cells. This was possibly related to swelling of the CCM resulting in the CCM-membrane strip connection shifting, a build-up of electrical double layers at electrolyte-

electrolyte interfaces, or a change in  $E^{eq}$  due to changes in the activities of the species involved in the anode reaction. These effects may take some time to reach an equilibrium state when a cell is running, and in that time, the potential sensed by the reference electrode could have changed. Further long-term testing with a reference electrode would be necessary to better understand these effects.

## Electrode Feed Method

For the AEMWE cell feed method study, three electrolyte feed configurations were tested: TEF, AOF, and COF, all repeated on three identical cells. From the polarization curves (Figure 3.21) and 6 hour, 300 mA/cm<sup>2</sup> stability tests (Figure 3.24), it was determined that the TEF and AOF methods performed very similarly, but the COF method performed worse. This was thought to have been due to a depletion of OH<sup>-</sup> ions at the anode side, which could have led to a lack of reactant for the OER, or a reduction in ionic conductivity in the anode catalyst layer. In both cases, this would mean that OH<sup>-</sup> ions could not be replenished quickly enough by transport through the AEM from cathode to anode. The membrane itself did not dry out and lose ionic conductivity as the HFR did not notably increase as it would have if this had occurred (Table 3.14). A decrease in the ionic conductivity of the catalyst layer however, would not have been detected by the HFR, as it only accounts for the most conductive phase of the catalyst layers, which is the electrical conductivity.

An alternative reason for the COF performance losses could have been an accumulation of water in the anode catalyst layer, which would have caused mass transport losses, and may have appeared linear in the polarization curves since the current densities the cells were run to were not very high and it would take time for this water to build up and block reaction sites. While the cells functioned fine with 1 M KOH electrolyte filling both electrodes, this would have been pure water, which has been shown to decrease AEMWE cell performance [14, 45, 50, 54, 63]. This would also explain why COF resulted in the largest performance decreases between subsequent polarization curves (Figures E.12, E.14, E.15). It would be interesting to see how an AEMWE cell would operate with COF configuration at higher current densities, as this could reveal more information on these losses, but to do so overall cell performance would have to be improved to lower the cell voltage.

When stability tests were run on Cell 8 at 1000 mA/cm<sup>2</sup> (Figure 3.25), the COF performance degraded much faster than the other feed methods, but it was determined that Cell 8 performed inconsistently in the stability tests. Compared to Cells 6 and 7 at 300 mA/cm<sup>2</sup>, the TEF stability test for Cell 8 performed notably worse, and additional testing on Cell 9 also contradicted the Cell 8 1000 mA/cm<sup>2</sup> stability tests. A test was run on Cell 9 where five current densities were held for an hour each using TEF and AOF, and at all current levels, TEF performed better. Consistent throughout the stability and the additional Cell

9 tests however, was that AOF performance decreased slower than the other feed methods. By the end of the Cell 6 and 7 stability tests, it had even surpassed the performance of TEF. It is possible that in the long term, AOF could be advantageous over TEF in reducing cell degradation without greatly reducing operational performance, but longer-term tests would need to be performed to confirm this.

A hysteresis between forward and backward polarization curves was consistently observed for all cells tested in this work. This was interesting as the performance mostly recovered when running the following test, meaning that this result must have been caused by a short-term change in the cell. For Cells 2 to 5, the fourth polarization curve was run the day after the first three, and performed comparably or even better than the first polarization curve. Similarly, the second round of TEF polarization curves (“TEF 2”) run on Cells 6 to 8 performed similarly to the first despite being run six days later and after AOF and COF testing. Individual polarization curve results are provided in Figure 3.12 and Appendix E.3. These results indicated that degradation seen early in testing was completely recovered when the cells were left to sit overnight. This degradation could not have been caused by catalyst loss, as that would be permanent, but could be a depletion in hydroxide ions or water in the membrane, which over time would be recovered while the cell was not in operation, and the CCM was surrounded by 1 M KOH electrolyte. If this was the case, measurements of HFR during a polarization curve may detect a slow increase in HFR as the membrane becomes less conductive, but that was not possible with the equipment used in this work.

# Chapter 4

## Conclusions and Future Work

### 4.1 Conclusions

Anion exchange membrane water electrolysis (AEMWE) cells were constructed and tested in this work using catalyst layers fabricated by inkjet printing. The first part of this work was concerned with the development of catalyst inks, using iridium oxide ( $\text{IrO}_x$ ) for the anode and platinum supported on carbon (Pt/C) for the cathode. One of each ink would be printed onto either side of an Aemion+ anion exchange membrane (AEM) to create a catalyst-coated membrane (CCM), which could then be assembled into an AEMWE cell. A step-by-step process was used to develop inks, beginning with a mixture of propylene glycol (PG) and isopropyl alcohol (IPA), then adding ionomer solution, and finally catalyst powder. At each step, the density, dynamic viscosity, and surface tension would be measured to ensure they were within the recommended ranges of the printer (Fujifilm Dimatix DMP-2831 with DMC-11610 cartridges). With this process, the first time each ink was made with catalyst, the desired properties were achieved, minimizing the waste of expensive catalyst nanopowder.

The process of creating new ink formulae developed in this work was successful in making printable catalyst inks. During the development of the ink formulation process however, it was found that although a base PG:IPA mass ratio of 2.5:1 had the desired properties, the addition of ionomer solution containing methanol and acetone solvents greatly lowered the dynamic viscosity, requiring PG:IPA mass ratios of 3.0:1 or 3.5:1 for printing. The highly volatile solvents also readily evaporated from solution, causing the viscosity to slowly increase over time. By minimizing evaporation, the inks were printed successfully, as demonstrated by both the  $\text{IrO}_x$  and Pt/C inks being used twice to print catalyst layers, and both times achieving the desired loadings in close to the number of expected layers. Overall, the process of ink development is quite time-consuming, as whenever a change is made to the materials used in an ink, resources must be dedicated to developing inks that have the correct rheology.

A total of nine in-situ AEMWE cells were discussed in this work, with the first five

being used to obtain repeatable results, and the latter four testing the implementation of a reference electrode into the cell hardware and the effect of single-electrode feed using aqueous 1 M potassium hydroxide (KOH) solution. The first five cells were used to develop the cell construction and testing protocols (polarization curves, electrochemical impedance spectroscopy (EIS), and potential or current holds) that would be used in the later studies, and was necessary since the cells used new Aemion+ membranes (AF2-HLE8-50-X and AF2-HWP8-75-X) and ionomer (AP2-HNN5-00-X). The first cell had issues with the cathode-side carbon paper porous transport layer (PTL) breaking, but after swapping it with nickel felt, cells two through five showed very similar results. This was despite the change in bipolar plates from titanium to nickel 400 alloy, and membrane from AF2-HLE8-50-X to AF2-HWP8-75-X following cell three. It was even found that the new, thicker membrane improved cell performance (the voltage required to obtain a given current density) by lowering high frequency resistance (HFR), likely due to the change in the reinforcement layer. As these cells performed consistently, the same cell construction was used for the reference electrode and feed method studies.

Integration of a reference electrode into the cell hardware was attempted in this work, and separate anode and cathode overpotential measurements were obtained. The integration process was similar to that done by Xu et al. [53], but the testing procedures were more extensive, with polarization curves, EIS, and six hour current holds repeated on four cells. While the overall cell voltage was again repeatable for these cells, the separated electrode overpotentials were only consistent in the short-term. Similar polarization curves were obtained on all but one of the cells, and the inconsistent cell was considered erroneous. Reference electrode measurements were not however, stable across any of the cells in the six hour stability tests. Discrepancies in these measurements were most likely due to a combination of issues with the CCM-reference electrode connection, and effects of cell operation, as the potentials did stabilize by the end of the six hour current holds, although they were not all consistent with each other. The repeatable polarization curve results were analysed, and it was noted that the change in anode and cathode overpotentials across the tested current densities were quite similar in magnitude when both electrodes were fed.

A comparison of two-electrode feed (TEF), anode-only feed (AOF), and cathode-only feed (COF) at the same time had until this point not been done in AEMWE cells. These feed methods were tested here, with the polarization curve results showing AOF performing as well as TEF, but with COF performing much worse comparatively. The results of the current-hold stability tests showed AOF and TEF had similar stability, with AOF performance decreasing slightly less compared to TEF. The reason for the COF performance differences were thought to be due to a depletion of hydroxide reactant at the anode side, resulting in a lack of reactant in the anode, or a loss of conductivity in the catalyst layer due to

a lack of supporting electrolyte. The former case would mean that hydroxide transport through the AEM was too slow to keep up with the reaction rate. This contrasted with AOF, where despite the fact that the cathode used water as a reactant, performance did not suffer, meaning that water could be transported through the membrane at a rate that kept up with the reaction. Using the repeatable reference electrode results, the separate anode and cathode overpotentials during the polarization curves were also analysed, showing that the performance loss during COF was due to an increase in anode overpotential, supporting the previous explanations.

## 4.2 Future Work

Inkjet printing provides advantages over other forms of catalyst layer fabrication, chiefly that the amount of ink wasted is quite small, lowering the waste of expensive catalyst materials. If it is desired to fabricate catalyst layers by this method, in addition to the work done here to ensure ink properties match the requirements for printing, it would be useful to also study the stability of the inks themselves, to better understand how long catalyst nanoparticles stay in suspension, and how this ink properties change over time. As this was not well understood for this work, inks were made and printed in quick succession, but it would be useful to make and store larger quantities of ink than was used in this work. If this could be done, inkjet printheads with more nozzles and larger ink reservoirs could be used to deposit ink at a faster rate, or fabricate more catalyst layers simultaneously. Both options would speed up the printing process, which is the main drawback of inkjet printing.

Additional work will be necessary to ensure that the use of reference electrodes with AEMWE cell hardware produces consistent results, especially over longer periods of cell operation. The issues in this work that were not observed by Xu et al. [53] may have been caused by the use of different membranes for the membrane strip, such as the reinforced Aemion+ AF2-HLF8-15-X used in this work, the exact placement of the strip, and how well it contacted the CCM. Using an unreinforced membrane strip also removes the possible influence of either side performing slightly differently, although the 15  $\mu\text{m}$  unreinforced membrane used in this work added the additional concern of membrane dehydration. A possible solution to the CCM-membrane contact challenge would be to eliminate the membrane strip altogether, instead having part of the CCM stick out of the cell directly. This would necessitate a relatively thin membrane be used for the CCM to prevent the cell from leaking, but membranes thinner than 50  $\mu\text{m}$  have been successfully used in AEMWE cells [30, 54, 55]. Investigations into the use of a connected membrane strip or the type of membrane over longer-term tests should be done to validate the use of reference electrodes in AEMWE cells.

In an effort to obtain consistent reference electrode results it would also be useful to un-

derstand why the reference electrode measurements drifted as observed in this work. Despite multiple cells tested in this work using the same construction, one cell (Cell 7) resulted in inconsistent polarization curve results, and this could not be repeated. If it were possible to repeat these poor results, then their causes could be investigated and steps taken to avoid them in the future.

Future single-electrode feed testing could be performed with the goal of optimizing the ionomer content in each electrode. This work did not investigate the catalyst layer ionomer content, but ideally the unfed electrode would contain additional ionomer to account for the lack of supporting electrolyte. This assumes that an electrolyte like 1 M KOH is used, and not deionized water. Feed method tests in this work were performed using only a single ionomer content in both electrodes, and it would be interesting to see how different membranes or ionomer materials affect this performance. For this, the anode catalyst layer may be a more interesting area for study, as changes to the ionomer content at that electrode have shown more significant changes to overall cell performance in cells using Aemion+ ionomer [30]. It may be possible that if anode ionomer loading was higher than the 5 wt.% used in this work, COF may not result in a smaller decrease in performance.

Testing of AOF over longer periods of time could verify whether it provides better cell performance compared to TEF in the long run, and why this performance difference occurs. In this work, AOF performance slightly surpassed that of TEF after 2 to 5 hours of operation at a constant 300 mA/cm<sup>2</sup>. This difference was however, quite small within the tested time frame. If either the test period were lengthened or the overall cell performance improved, a larger difference in performance may be observed, allowing for a more definitive conclusion on both how and why the AOF method affects AEMWE cell operation. The use of AOF may also be useful in future AEMWE cell studies on long-term cell operation, as it may provide better cell performance over a longer time frame.

Investigations into feeding both electrodes with different electrolytes could be done. If it was desirable to feed both electrodes, it is possible that a lower conductivity KOH solution or even deionized water could be used at the cathode without a major impact on cell performance. This would reduce the risk and additional complications associated with using 1 M KOH feed solution. The feed solutions that could be used would depend on the membrane and ionomer used as well, as with Aemion+, for example, it is recommended not to expose the ionomer material to pure water following conversion to hydroxide form [49].

Any of these possible studies on AEMWE cells could also be performed in conjunction with the use of non-PGM catalysts. This was not pursued in this work as using new catalyst materials to make inks would have been an additional challenge, and the use of standard catalyst materials allowed for better comparison with literature. The use of non-PGM catalysts is however, a goal of AEMWE cell development as this is a major benefit of the technology.

# References

- [1] Andreas Züttel et al. “Hydrogen: The Future Energy Carrier”. In: *Philosophical transactions. Series A, Mathematical, physical, and engineering sciences* 368 (July 28, 2010), pp. 3329–42. DOI: 10.1098/rsta.2010.0113.
- [2] Ram Ramachandran and Raghu K. Menon. “An Overview of Industrial Uses of Hydrogen”. In: *International Journal of Hydrogen Energy* 23.7 (July 1, 1998), pp. 593–598. ISSN: 0360-3199. DOI: 10.1016/S0360-3199(97)00112-2.
- [3] John A. Turner. “Sustainable Hydrogen Production”. In: *Science* 305.5686 (Aug. 13, 2004), pp. 972–974. DOI: 10.1126/science.1103197.
- [4] A. Midilli et al. “On Hydrogen and Hydrogen Energy Strategies: I: Current Status and Needs”. In: *Renewable and Sustainable Energy Reviews* 9.3 (June 1, 2005), pp. 255–271. ISSN: 1364-0321. DOI: 10.1016/j.rser.2004.05.003.
- [5] Merit Bodner, Astrid Hofer, and Viktor Hacker. “H<sub>2</sub> Generation from Alkaline Electrolyzer”. In: *WIREs Energy and Environment* 4.4 (2015), pp. 365–381. ISSN: 2041-840X. DOI: 10.1002/wene.150.
- [6] S Trasatti. “Water Electrolysis: Who First?” In: *Journal of Electroanalytical Chemistry* 476.1 (Oct. 1999), pp. 90–91. ISSN: 15726657. DOI: 10.1016/S0022-0728(99)00364-2.
- [7] Marian Chatenet et al. “Water Electrolysis: From Textbook Knowledge to the Latest Scientific Strategies and Industrial Developments”. In: *Chemical Society Reviews* (2022). DOI: 10.1039/D0CS01079K.
- [8] Hamish Andrew Miller et al. “Green Hydrogen from Anion Exchange Membrane Water Electrolysis: A Review of Recent Developments in Critical Materials and Operating Conditions”. In: *Sustainable Energy & Fuels* 4.5 (2020), pp. 2114–2133. DOI: 10.1039/C9SE01240K.
- [9] Marcelo Carmo et al. “A Comprehensive Review on PEM Water Electrolysis”. In: *International Journal of Hydrogen Energy* 38.12 (Apr. 22, 2013), pp. 4901–4934. ISSN: 0360-3199. DOI: 10.1016/j.ijhydene.2013.01.151.
- [10] Immanuel Vincent and Dmitri Bessarabov. “Low Cost Hydrogen Production by Anion Exchange Membrane Electrolysis: A Review”. In: *Renewable and Sustainable Energy Reviews* 81 (Jan. 1, 2018), pp. 1690–1704. ISSN: 1364-0321. DOI: 10.1016/j.rser.2017.05.258.

- [11] Lei Bi, Samir Boulfrad, and Enrico Traversa. “Steam Electrolysis by Solid Oxide Electrolysis Cells (SOECs) with Proton-Conducting Oxides”. In: *Chemical Society Reviews* 43.24 (2014), pp. 8255–8270. DOI: 10.1039/C4CS00194J.
- [12] Dirk Henkensmeier et al. “Overview: State-of-the Art Commercial Membranes for Anion Exchange Membrane Water Electrolysis”. In: *Journal of Electrochemical Energy Conversion and Storage* 18.2 (Aug. 24, 2020). ISSN: 2381-6872. DOI: 10.1115/1.4047963.
- [13] Grace A. Lindquist et al. “Performance and Durability of Pure-Water-Fed Anion Exchange Membrane Electrolyzers Using Baseline Materials and Operation”. In: *ACS Applied Materials & Interfaces* (Aug. 10, 2021). ISSN: 1944-8244. DOI: 10.1021/acsmi.1c06053.
- [14] Jiangjin Liu et al. “Elucidating the Role of Hydroxide Electrolyte on Anion-Exchange-Membrane Water Electrolyzer Performance”. In: *Journal of The Electrochemical Society* 168.5 (May 2021), p. 054522. ISSN: 1945-7111. DOI: 10.1149/1945-7111/ac0019.
- [15] *P2: Standard Reduction Potentials by Value*. Chemistry LibreTexts. Oct. 2, 2013. URL: [https://chem.libretexts.org/Ancillary\\_Materials/Reference/Reference\\_Tables/Electrochemistry\\_Tables/P2%3A\\_Standard\\_Reduction\\_Potentials\\_by\\_Value](https://chem.libretexts.org/Ancillary_Materials/Reference/Reference_Tables/Electrochemistry_Tables/P2%3A_Standard_Reduction_Potentials_by_Value) (visited on 2022-10-18).
- [16] Paige Shirvanian and Frans van Berkel. “Novel Components in Proton Exchange Membrane (PEM) Water Electrolyzers (PEMWE): Status, Challenges and Future Needs. A Mini Review”. In: *Electrochemistry Communications* 114 (May 1, 2020), p. 106704. ISSN: 1388-2481. DOI: 10.1016/j.elecom.2020.106704.
- [17] Himanshi Dhawan, Marc Secanell, and Natalia Semagina. “State-of-the-Art Iridium-Based Catalysts for Acidic Water Electrolysis: A Minireview of Wet-Chemistry Synthesis Methods : Preparation Routes for Active and Durable Iridium Catalysts”. In: *Johnson Matthey Technology Review* 65.2 (Apr. 1, 2021), pp. 247–262. DOI: 10.1595/205651321X16013966874707.
- [18] Xiao-Zi Yuan et al. *Electrochemical Impedance Spectroscopy in PEM Fuel Cells*. London: Springer London, 2010. ISBN: 978-1-84882-845-2 978-1-84882-846-9. DOI: 10.1007/978-1-84882-846-9.
- [19] Yuan-Cheng Cao, Xu Wu, and Keith Scott. “A Quaternary Ammonium Grafted Poly Vinyl Benzyl Chloride Membrane for Alkaline Anion Exchange Membrane Water Electrolyzers with No-Noble-Metal Catalysts”. In: *International Journal of Hydrogen Energy* 37.12 (June 1, 2012), pp. 9524–9528. ISSN: 0360-3199. DOI: 10.1016/j.ijhydene.2012.03.116.
- [20] Immanuel Vincent, Andries Kruger, and Dmitri Bessarabov. “Development of Efficient Membrane Electrode Assembly for Low Cost Hydrogen Production by Anion Exchange Membrane Electrolysis”. In: *International Journal of Hydrogen Energy* 42.16 (Apr. 20, 2017), pp. 10752–10761. ISSN: 0360-3199. DOI: 10.1016/j.ijhydene.2017.03.069.

- [21] Junwu Xiao et al. “Water-Fed Hydroxide Exchange Membrane Electrolyzer Enabled by a Fluoride-Incorporated Nickel–Iron Oxyhydroxide Oxygen Evolution Electrode”. In: *ACS Catalysis* 11.1 (Jan. 1, 2021), pp. 264–270. DOI: 10.1021/acscatal.0c04200.
- [22] Patrick Fortin et al. “High-Performance Alkaline Water Electrolysis Using Aemion™ Anion Exchange Membranes”. In: *Journal of Power Sources* 451 (Mar. 1, 2020), p. 227814. ISSN: 0378-7753. DOI: 10.1016/j.jpowsour.2020.227814.
- [23] Gaurav Gupta, Keith Scott, and Mohamed Mamlouk. “Performance of Polyethylene Based Radiation Grafted Anion Exchange Membrane with Polystyrene-b-Poly (Ethylene/Butylene)-b-Polystyrene Based Ionomer Using NiCo2O4 Catalyst for Water Electrolysis”. In: *Journal of Power Sources* 375 (Jan. 31, 2018), pp. 387–396. ISSN: 0378-7753. DOI: 10.1016/j.jpowsour.2017.07.026.
- [24] Yongjun Leng et al. “Solid-State Water Electrolysis with an Alkaline Membrane”. In: *Journal of the American Chemical Society* 134.22 (June 6, 2012), pp. 9054–9057. ISSN: 0002-7863. DOI: 10.1021/ja302439z.
- [25] Ahyoun Lim et al. “A Study on Electrode Fabrication and Operation Variables Affecting the Performance of Anion Exchange Membrane Water Electrolysis”. In: *Journal of Industrial and Engineering Chemistry* 76 (Aug. 25, 2019), pp. 410–418. ISSN: 1226-086X. DOI: 10.1016/j.jiec.2019.04.007.
- [26] Javier Parrondo et al. “Degradation of Anion Exchange Membranes Used for Hydrogen Production by Ultrapure Water Electrolysis”. In: *RSC Advances* 4.19 (2014), pp. 9875–9879. DOI: 10.1039/C3RA46630B.
- [27] Xiangdong Su et al. “Novel Piperidinium Functionalized Anionic Membrane for Alkaline Polymer Electrolysis with Excellent Electrochemical Properties”. In: *Journal of Membrane Science* 581 (July 1, 2019), pp. 283–292. ISSN: 0376-7388. DOI: 10.1016/j.memsci.2019.03.072.
- [28] Xu Wu and Keith Scott. “A Polymethacrylate-Based Quaternary Ammonium OH-Ionomer Binder for Non-Precious Metal Alkaline Anion Exchange Membrane Water Electrolysers”. In: *Journal of Power Sources* 214 (Sept. 15, 2012), pp. 124–129. ISSN: 0378-7753. DOI: 10.1016/j.jpowsour.2012.03.069.
- [29] Sabrina Campagna Zignani et al. “Investigation of NiFe-Based Catalysts for Oxygen Evolution in Anion-Exchange Membrane Electrolysis”. In: *Energies* 13.7 (7 Jan. 2020), p. 1720. DOI: 10.3390/en13071720.
- [30] Susanne Koch et al. “The Effect of Ionomer Content in Catalyst Layers in Anion-Exchange Membrane Water Electrolyzers Prepared with Reinforced Membranes (Aemion+™)”. In: *Journal of Materials Chemistry A* 9.28 (July 20, 2021), pp. 15744–15754. ISSN: 2050-7496. DOI: 10.1039/D1TA01861B.
- [31] Y.S. Park et al. “Commercial Anion Exchange Membrane Water Electrolyzer Stack through Non-Precious Metal Electrocatalysts”. In: *Applied Catalysis B: Environmental* 292 (2021). DOI: 10.1016/j.apcatb.2021.120170.

- [32] Li Wang et al. “High Performance Anion Exchange Membrane Electrolysis Using Plasma-Sprayed, Non-Precious-Metal Electrodes”. In: *ACS Applied Energy Materials* 2.11 (Nov. 25, 2019), pp. 7903–7912. DOI: 10.1021/acsaem.9b01392.
- [33] Sang Hyun Ahn et al. “Development of a Membrane Electrode Assembly for Alkaline Water Electrolysis by Direct Electrodeposition of Nickel on Carbon Papers”. In: *Applied Catalysis B: Environmental* 154–155 (July 1, 2014), pp. 197–205. ISSN: 0926-3373. DOI: 10.1016/j.apcatb.2014.02.021.
- [34] W. Guo et al. “Electrochemically Activated Ni@Ni(OH)<sub>2</sub> Heterostructure as Efficient Hydrogen Evolution Reaction Electrocatalyst for Anion Exchange Membrane Water Electrolysis”. In: *Materials Today Chemistry* 24 (June 1, 2022), p. 100994. ISSN: 2468-5194. DOI: 10.1016/j.mtchem.2022.100994.
- [35] S. Seetharaman et al. “Graphene Oxide Modified Non-Noble Metal Electrode for Alkaline Anion Exchange Membrane Water Electrolyzers”. In: *International Journal of Hydrogen Energy* 38.35 (Nov. 22, 2013), pp. 14934–14942. ISSN: 0360-3199. DOI: 10.1016/j.ijhydene.2013.09.033.
- [36] L. Zeng et al. “NiCo<sub>2</sub>O<sub>4</sub> nanowires@MnOx Nanoflakes Supported on Stainless Steel Mesh with Superior Electrocatalytic Performance for Anion Exchange Membrane Water Splitting”. In: *Electrochemistry Communications* 87 (Feb. 1, 2018), pp. 66–70. ISSN: 1388-2481. DOI: 10.1016/j.elecom.2018.01.002.
- [37] J Donald Joe, D B Siva Kumar, and P Sivakumar. “Production Of Hydrogen By Anion Exchange Membrane Using AWE”. In: *International Journal of Scientific & Technology Research* 3.6 (2014), p. 5.
- [38] T. Pandiarajan, L. John Berchmans, and S. Ravichandran. “Fabrication of Spinel Ferrite Based Alkaline Anion Exchange Membrane Water Electrolyzers for Hydrogen Production”. In: *RSC Advances* 5.43 (2015), pp. 34100–34108. DOI: 10.1039/C5RA01123J.
- [39] L. Zeng and T. S. Zhao. “Integrated Inorganic Membrane Electrode Assembly with Layered Double Hydroxides as Ionic Conductors for Anion Exchange Membrane Water Electrolysis”. In: *Nano Energy* 11 (Jan. 1, 2015), pp. 110–118. ISSN: 2211-2855. DOI: 10.1016/j.nanoen.2014.10.019.
- [40] Scott Storbakken. “Fabrication and Testing of Inkjet Printed Electrodes for Anion Exchange Membrane Water Electrolysis”. University of Alberta, Spr. 2022. DOI: 10.7939/r3-rb0h-p998.
- [41] S. Shukla et al. “Analysis of Low Platinum Loading Thin Polymer Electrolyte Fuel Cell Electrodes Prepared by Inkjet Printing”. In: *Electrochimica Acta* 156 (Feb. 20, 2015), pp. 289–300. ISSN: 0013-4686. DOI: 10.1016/j.electacta.2015.01.028.
- [42] Manas Mandal et al. “Analysis of Inkjet Printed Catalyst Coated Membranes for Polymer Electrolyte Electrolyzers”. In: *Journal of The Electrochemical Society* 165.7 (May 19, 2018), F543. ISSN: 1945-7111. DOI: 10.1149/2.1101807jes.

- [43] Alaa Y. Faid et al. “Highly Active Nickel-Based Catalyst for Hydrogen Evolution in Anion Exchange Membrane Electrolysis”. In: *Catalysts* 8.12 (12 Dec. 2018), p. 614. DOI: 10.3390/catal8120614.
- [44] Jaromír Hnát et al. “Development and Testing of a Novel Catalyst-Coated Membrane with Platinum-Free Catalysts for Alkaline Water Electrolysis”. In: *International Journal of Hydrogen Energy* 44.33 (July 5, 2019), pp. 17493–17504. ISSN: 0360-3199. DOI: 10.1016/j.ijhydene.2019.05.054.
- [45] Ji Eun Park et al. “High-Performance Anion-Exchange Membrane Water Electrolysis”. In: *Electrochimica Acta* 295 (Feb. 1, 2019), pp. 99–106. ISSN: 0013-4686. DOI: 10.1016/j.electacta.2018.10.143.
- [46] Richard G. Jones. *Compendium of Polymer Terminology and Nomenclature: IUPAC Recommendations, 2008*. Cambridge: Royal Society of Chemistry, 2009. 443 pp. ISBN: 978-1-84755-942-5.
- [47] S. Shukla et al. “Experimental and Theoretical Analysis of Ink Dispersion Stability for Polymer Electrolyte Fuel Cell Applications”. In: *Journal of The Electrochemical Society* 164.6 (Apr. 4, 2017), F600. ISSN: 1945-7111. DOI: 10.1149/2.0961706jes.
- [48] Shantanu T. Shukla. “Experimental Analysis of Inkjet Printed Polymer Electrolyte Fuel Cell Electrodes”. University of Alberta, Aut. 2016. DOI: 10.7939/R3XK8516J.
- [49] Omid Toussi. *Aemion+ Application Note: Handling, Dispersion, and Ink Formulation*. Ed. by Benjamin Britton. 2020.
- [50] Xu Wu and Keith Scott. “ $\text{Cu}_x\text{Co}_{3-x}\text{O}_4$  ( $0 \leq x < 1$ ) Nanoparticles for Oxygen Evolution in High Performance Alkaline Exchange Membrane Water Electrolysers”. In: *Journal of Materials Chemistry* 21.33 (2011), pp. 12344–12351. DOI: 10.1039/C1JM11312G.
- [51] Xu Wu et al. “A Reversible Water Electrolyser with Porous PTFE Based OH<sup>-</sup> Conductive Membrane as Energy Storage Cells”. In: *Journal of Power Sources* 246 (Jan. 15, 2014), pp. 225–231. ISSN: 0378-7753. DOI: 10.1016/j.jpowsour.2013.07.081.
- [52] Dongyu Xu et al. “Earth-Abundant Oxygen Electrocatalysts for Alkaline Anion-Exchange-Membrane Water Electrolysis: Effects of Catalyst Conductivity and Comparison with Performance in Three-Electrode Cells”. In: *ACS Catalysis* 9.1 (Jan. 4, 2019), pp. 7–15. DOI: 10.1021/acscatal.8b04001.
- [53] Qiucheng Xu et al. “Integrated Reference Electrodes in Anion-Exchange-Membrane Electrolyzers: Impact of Stainless-Steel Gas-Diffusion Layers and Internal Mechanical Pressure”. In: *ACS Energy Letters* 6.2 (Feb. 12, 2021), pp. 305–312. DOI: 10.1021/acsenergylett.0c02338.
- [54] Aleksandr Kiessling et al. “Influence of Supporting Electrolyte on Hydroxide Exchange Membrane Water Electrolysis Performance: Anolyte”. In: *Journal of The Electrochemical Society* (Aug. 2021). ISSN: 1945-7111. DOI: 10.1149/1945-7111/ac1dcd.

- [55] Aleksandr Kiessling et al. “Influence of Supporting Electrolyte on Hydroxide Exchange Membrane Water Electrolysis Performance: Catholyte”. In: *Journal of The Electrochemical Society* 169.2 (Feb. 2022), p. 024510. ISSN: 1945-7111. DOI: 10.1149/1945-7111/ac4fed.
- [56] Immanuel Vincent, Andries Krüger, and Dmitri Bessarabov. “Hydrogen Production by Water Electrolysis with an Ultrathin Anion-Exchange Membrane (AEM)”. In: (2018). DOI: 10.20964/2018.12.84.
- [57] Xu Wu and Keith Scott. “A Li-doped Co<sub>3</sub>O<sub>4</sub> Oxygen Evolution Catalyst for Non-Precious Metal Alkaline Anion Exchange Membrane Water Electrolysers”. In: *International Journal of Hydrogen Energy* 38.8 (Mar. 19, 2013), pp. 3123–3129. ISSN: 0360-3199. DOI: 10.1016/j.ijhydene.2012.12.087.
- [58] Li Xiao et al. “First Implementation of Alkaline Polymer Electrolyte Water Electrolysis Working Only with Pure Water”. In: *Energy & Environmental Science* 5.7 (2012), pp. 7869–7871. DOI: 10.1039/C2EE22146B.
- [59] Claudiu C. Pavel et al. “Highly Efficient Platinum Group Metal Free Based Membrane-Electrode Assembly for Anion Exchange Membrane Water Electrolysis”. In: *Angewandte Chemie International Edition* 53.5 (2014), pp. 1378–1381. ISSN: 1521-3773. DOI: 10.1002/anie.201308099.
- [60] Alaa Y. Faid et al. “Effect of Anion Exchange Ionomer Content on Electrode Performance in AEM Water Electrolysis”. In: *International Journal of Hydrogen Energy* 45.53 (Oct. 30, 2020), pp. 28272–28284. ISSN: 0360-3199. DOI: 10.1016/j.ijhydene.2020.07.202.
- [61] Garrett Huang et al. “Ionomer Optimization for Water Uptake and Swelling in Anion Exchange Membrane Electrolyzer: Hydrogen Evolution Electrode”. In: *Journal of The Electrochemical Society* 168.2 (Feb. 2021), p. 024503. ISSN: 1945-7111. DOI: 10.1149/1945-7111/abde7b.
- [62] Garrett Huang et al. “Ionomer Optimization for Water Uptake and Swelling in Anion Exchange Membrane Electrolyzer: Oxygen Evolution Electrode”. In: *Journal of The Electrochemical Society* 167.16 (Dec. 2020), p. 164514. ISSN: 1945-7111. DOI: 10.1149/1945-7111/abcde3.
- [63] Noor Ul Hassan et al. “KOH vs Deionized Water Operation in Anion Exchange Membrane Electrolyzers”. In: *Journal of The Electrochemical Society* 169.4 (Apr. 2022), p. 044526. ISSN: 1945-7111. DOI: 10.1149/1945-7111/ac5f1d.
- [64] Min Kyung Cho et al. “Alkaline Anion Exchange Membrane Water Electrolysis: Effects of Electrolyte Feed Method and Electrode Binder Content”. In: *Journal of Power Sources* 382 (Apr. 1, 2018), pp. 22–29. ISSN: 0378-7753. DOI: 10.1016/j.jpowsour.2018.02.025.
- [65] Eun Joo Park et al. “Chemically Durable Polymer Electrolytes for Solid-State Alkaline Water Electrolysis”. In: *Journal of Power Sources* 375 (Jan. 31, 2018), pp. 367–372. ISSN: 0378-7753. DOI: 10.1016/j.jpowsour.2017.07.090.

- [66] Ryan O’Hayre et al. *Fuel Cell Fundamentals*. John Wiley & Sons, May 2, 2016. 612 pp. ISBN: 978-1-119-11380-5. Google Books: 02JYCwAAQBAJ.
- [67] Wensheng He and Trung Van Nguyen. “Edge Effects on Reference Electrode Measurements in PEM Fuel Cells”. In: *Journal of The Electrochemical Society* 151.2 (Jan. 8, 2004), A185. ISSN: 1945-7111. DOI: 10.1149/1.1634272.
- [68] Johan Andre et al. “Development of a Reference Electrode for a PEMFC Single Cell Allowing an Evaluation of Plate Potentials”. In: *Journal of Fuel Cell Science and Technology* 7.4 (Apr. 8, 2010). ISSN: 1550-624X. DOI: 10.1115/1.4000674.
- [69] Alexandra Hartig-Weiß et al. “A Platinum Micro-Reference Electrode for Impedance Measurements in a PEM Water Electrolysis Cell”. In: *Journal of The Electrochemical Society* 168.11 (Nov. 2021), p. 114511. ISSN: 1945-7111. DOI: 10.1149/1945-7111/ac3717.
- [70] Elyse Johnston-Haynes. “Reference Electrode Development in Polymer Electrolyte Membrane (PEM) Electrolyzer Assembly for Novel Investigation of Electrodes”. M.A.Sc. Canada – Ontario, CA: Queen’s University (Canada), Apr. 2018. 102 pp. ISBN: 9798662401143.
- [71] Myunghee Jung and John W. Van Zee. “Using a Reference Electrode to Understand the Effect of Trace Fuel Contaminants on PEMFC Behavior”. In: *ECS Transactions* 25.1 (Sept. 25, 2009), p. 1585. ISSN: 1938-5862. DOI: 10.1149/1.3210714.
- [72] Graham Smith. “The Development of Characterisation Techniques and Electrodes for Alkaline Membrane Fuel Cells”. Imperial College London, Oct. 2015.
- [73] S. B. Adler et al. “Reference Electrode Placement and Seals in Electrochemical Oxygen Generators”. In: *Solid State Ionics*. Festschrift Dedicated to Prof. Brian Steele 134.1 (Oct. 1, 2000), pp. 35–42. ISSN: 0167-2738. DOI: 10.1016/S0167-2738(00)00711-6.
- [74] Madhu S. Saha et al. “Electrochemical Activity and Catalyst Utilization of Low Pt and Thickness Controlled Membrane Electrode Assemblies”. In: *Journal of The Electrochemical Society* 158.5 (Mar. 25, 2011), B562. ISSN: 1945-7111. DOI: 10.1149/1.3559188.
- [75] Fujifilm Dimatix. *Dimatix Materials Printer DMP-2800 Series User Manual*. Sept. 1, 2007.
- [76] Fujifilm Dimatix. *Jetable Fluid Formulation Guidelines*. May 16, 2013.
- [77] Brian Derby. “Inkjet Printing of Functional and Structural Materials: Fluid Property Requirements, Feature Stability, and Resolution”. In: *Annual Review of Materials Research* 40 (2010), pp. 395–414. ISSN: 1531-7331. DOI: 10.1146/annurev-matsci-070909-104502.
- [78] Gerard Cummins and Marc P.Y. Desmulliez. “Inkjet Printing of Conductive Materials: A Review”. In: *Circuit World* 38.4 (Jan. 1, 2012), pp. 193–213. ISSN: 0305-6120. DOI: 10.1108/03056121211280413.
- [79] MJ O’Neil, ed. *The Merck Index - An Encyclopedia of Chemicals, Drugs, and Biologicals*. ambridge, UK: Royal Society of Chemistry, 2013. 1868 pp.

- [80] W. M. Haynes, ed. *CRC Handbook of Chemistry and Physics*. 91st ed. Boca Raton: CRC Press, 2010–2011. 3-442.
- [81] *Water - Density, Specific Weight and Thermal Expansion Coefficients*. Engineering ToolBox. 2003. URL: [https://www.engineeringtoolbox.com/water-density-specific-weight-d\\_595.html](https://www.engineeringtoolbox.com/water-density-specific-weight-d_595.html) (visited on 2022-08-11).
- [82] Innovation Government of Canada. *Volume Correction Factors—Isopropyl Alcohol (Anhydrous)*. URL: <https://www.ic.gc.ca/eic/site/mc-mc.nsf/eng/lm00131.html> (visited on 2022-08-11).
- [83] Jarno Groenesteijn et al. “Micro Coriolis Mass Flow Sensor with Integrated Resistive Pressure Sensors”. In: Oct. 4, 2017.
- [84] *Wolfram—Alpha Widgets: ”Local Acceleration of Gravity” - Free Physics Widget*. URL: <https://tinyurl.com/3mkwarzx> (visited on 2022-11-24).
- [85] *Viscosity - Absolute (Dynamic) vs. Kinematic*. Engineering ToolBox. 2003. URL: [https://www.engineeringtoolbox.com/dynamic-absolute-kinematic-viscosity-d\\_412.html](https://www.engineeringtoolbox.com/dynamic-absolute-kinematic-viscosity-d_412.html) (visited on 2023-01-09).
- [86] D. Bohne, S. Fischer, and E. Obermeier. “Thermal, Conductivity, Density, Viscosity, and Prandtl-Numbers of Ethylene Glycol-Water Mixtures”. In: *Berichte der Bunsengesellschaft für physikalische Chemie* 88.8 (1984), pp. 739–742. ISSN: 0005-9021. DOI: 10.1002/bbpc.19840880813.
- [87] Jordi-Roger Riba and Bernat Esteban. “A Simple Laboratory Experiment to Measure the Surface Tension of a Liquid in Contact with Air”. In: *European Journal of Physics* 35.5 (Sept. 1, 2014), p. 055003. ISSN: 0143-0807, 1361-6404. DOI: 10.1088/0143-0807/35/5/055003.
- [88] Boon-Beng Lee, Pogaku Ravindra, and Eng-Seng Chan. “New Drop Weight Analysis for Surface Tension Determination of Liquids”. In: *Colloids and Surfaces A: Physicochemical and Engineering Aspects* 332.2 (Jan. 15, 2009), pp. 112–120. ISSN: 0927-7757. DOI: 10.1016/j.colsurfa.2008.09.003.
- [89] Jiangjiang Liu, Haifang Li, and Jin-Ming Lin. “Measurements of Surface Tension of Organic Solvents Using a Simple Microfabricated Chip”. In: *Analytical Chemistry* 79.1 (Jan. 1, 2007), pp. 371–377. ISSN: 0003-2700. DOI: 10.1021/ac0614011.
- [90] Boon-Beng Lee, Pogaku Ravindra, and Eng-Seng Chan. “A Critical Review: Surface and Interfacial Tension Measurement by the Drop Weight Method”. In: *Chemical Engineering Communications* 195.8 (Apr. 29, 2008), pp. 889–924. ISSN: 0098-6445. DOI: 10.1080/00986440801905056.
- [91] R. Miller, M. Bree, and V. B. Fainerman. “Hydrodynamic Effects in Measurements with the Drop Volume Technique at Small Drop Times—3. Surface Tensions of Viscous Liquids”. In: *Colloids and Surfaces A: Physicochemical and Engineering Aspects* 142.2 (Dec. 10, 1998), pp. 237–242. ISSN: 0927-7757. DOI: 10.1016/S0927-7757(98)00240-4.

- [92] Bryan C. Hoke and John C. Chen. “Binary Aqueous-Organic Surface Tension Temperature Dependence”. In: *Journal of Chemical & Engineering Data* 36.3 (July 1, 1991), pp. 322–326. ISSN: 0021-9568. DOI: 10.1021/je00003a019.
- [93] Arthur I. Vogel. “366. Physical Properties and Chemical Constitution. Part XX. Aliphatic Alcohols and Acids”. In: *Journal of the Chemical Society (Resumed)* (1948), p. 1814. ISSN: 0368-1769. DOI: 10.1039/jr9480001814.
- [94] Gonzalo Vazquez, Estrella Alvarez, and Jose M. Navaza. “Surface Tension of Alcohol Water + Water from 20 to 50 .Degree.C”. In: *Journal of Chemical & Engineering Data* 40.3 (May 1995), pp. 611–614. ISSN: 0021-9568, 1520-5134. DOI: 10.1021/je00019a016.
- [95] Bryan C. Hoke and Erin F. Patton. “Surface Tensions of Propylene Glycol + Water”. In: *Journal of Chemical & Engineering Data* 37.3 (July 1992), pp. 331–333. ISSN: 0021-9568, 1520-5134. DOI: 10.1021/je00007a016.
- [96] Anton Paar. *White Paper: Understanding the Concept of Dynamic Light Scattering*. URL: [anton-paar.com](http://anton-paar.com).
- [97] *ISO 22412:2017 Particle Size Analysis - Dynamic Light Scattering (DLS)*. 2017.
- [98] Richard Feynman. *The Feynman Lectures on Physics Vol. I Ch. 41: The Brownian Movement*. 1964. URL: [https://www.feynmanlectures.caltech.edu/I\\_41.html#Ch41-SUM](https://www.feynmanlectures.caltech.edu/I_41.html#Ch41-SUM) (visited on 2022-09-01).
- [99] John Drury Clark. *Ignition!: An Informal History of Liquid Rocket Propellants*. Rutgers University Press, Feb. 14, 1972. 232 pp. ISBN: 978-0-8135-8524-6. Google Books: wELgCgAAQBAJ.
- [100] John Varcoe et al. *Energy Environ Sci Vol7 P3135-3191 (2014)*. Nov. 8, 2014.
- [101] E. McCafferty. “Thermodynamics of Corrosion: Pourbaix Diagrams”. In: *Introduction to Corrosion Science*. Ed. by Edward McCafferty. New York, NY: Springer, 2010, pp. 95–117. ISBN: 978-1-4419-0455-3. DOI: 10.1007/978-1-4419-0455-3\_6.
- [102] Cynthia G. Zoski. *Handbook of Electrochemistry*. Elsevier, Dec. 11, 2006. 935 pp. ISBN: 978-0-08-046930-0. Google Books: XWU\_gNZ3yxwC.
- [103] IUPAC. *Compendium of Chemical Terminology, 2nd Ed. (the “Gold Book”)*. 2nd ed. Compiled by A. D. McNaught and A. Wilkinson. Online Version (2019-) Created by S. J. Chalk. Blackwell Scientific Publications, Oxford, 1997. ISBN: 0-9678550-9-8.
- [104] Weitian Wang et al. “Exploring the Impacts of Conditioning on Proton Exchange Membrane Electrolyzers by In Situ Visualization and Electrochemistry Characterization”. In: *ACS Applied Materials & Interfaces* 14.7 (Feb. 23, 2022), pp. 9002–9012. ISSN: 1944-8244. DOI: 10.1021/acsmi.1c21849.
- [105] Manas Kumar Mandal. “Understanding the Physical Phenomena Limiting the Inkjet Printed PEM Water Electrolyzer Performance”. University of Alberta, 2022.
- [106] Omid Toussi. *Aemion+ Electrolysis Offerings - Anion Exchange Membranes & Polymers*. Ed. by Benjamin Britton. 2021.

- [107] Marta Moreno-González et al. “One Year Operation of an Anion Exchange Membrane Water Electrolyzer Utilizing Aemion+® Membrane: Minimal Degradation, Low H<sub>2</sub> Crossover and High Efficiency”. In: *Journal of Power Sources Advances* 19 (Jan. 1, 2023), p. 100109. ISSN: 2666-2485. DOI: 10.1016/j.powera.2023.100109.
- [108] Xiaohong Xie et al. “Oxygen Evolution Reaction in Alkaline Environment: Material Challenges and Solutions”. In: *Advanced Functional Materials* 32.21 (2022), p. 2110036. ISSN: 1616-3028. DOI: 10.1002/adfm.202110036.
- [109] Raja Rafidah Raja Sulaiman, Wai Yin Wong, and Kee Shyuan Loh. “Recent Developments on Transition Metal-Based Electrocatalysts for Application in Anion Exchange Membrane Water Electrolysis”. In: *International Journal of Energy Research* 46.3 (2022), pp. 2241–2276. ISSN: 1099-114X. DOI: 10.1002/er.7380.
- [110] Anthony J Wheeler et al. *Introduction to Engineering Experimentation*. Vol. 480. Pearson, 2010.
- [111] Xuehai Tan et al. “Decoupling Structure-Sensitive Deactivation Mechanisms of Ir/IrO<sub>x</sub> Electrocatalysts toward Oxygen Evolution Reaction”. In: *Journal of Catalysis* 371 (Mar. 1, 2019), pp. 57–70. ISSN: 0021-9517. DOI: 10.1016/j.jcat.2019.01.018.

# Appendix A

## Equipment Information

# A.1 Cannon Instrument Company Zeitfuchs Cross-Arm Viscometer Certificate of Calibration

2139 High Tech Road  
 State College, PA 16803  
 814-353-8000 • 800-676-6232 • Fax 814-353-8007  
[cannon@cannoninstrument.com](mailto:cannon@cannoninstrument.com)  
[www.cannoninstrument.com](http://www.cannoninstrument.com)

## Certificate of Calibration

ZEITFUCHS CROSS-ARM VISCOMETER			
Size	2	Serial Number	B562
Constant	Expanded Uncertainty* (k=2)	Kinematic Viscosity Range	
mm <sup>2</sup> /s <sup>2</sup> , (cSt/s)	%	mm <sup>2</sup> /s, (cSt)	
0.009463	0.16	2 - 10	

\* In alignment with the Calibration and Measurement Capabilities of National Metrology Institutes, the expressed uncertainty is relative to the viscosity of water, and therefore the uncertainty of the viscosity of water (ISO/TR 3666 (1998), 0.17%) is not taken into account.

### CALIBRATION DATA AT 40°C - The viscometer constant is the same at all temperatures.

Viscosity Standard	Kinematic Viscosity mm <sup>2</sup> /s, (cSt)	Efflux Time Seconds	Constant mm <sup>2</sup> /s <sup>2</sup> , (cSt/s)
12	2.418	255.54	0.009460
13	3.829	404.56	0.009465

Average = 0.009463

Kinematic viscosities of the standards used in calibrating were established in Master Viscometers as described in Ind. Eng. Chem. Anal. Ed. 16,708(1944), ASTM D 2162, and the Journal of Research of the National Bureau of Standards, Vol. 52, No. 3, March 1954, Research Paper 2479.

Kinematic viscosities are traceable to the viscosity of, water ISO 3666, at 20°C (ITS-90). Temperature measurements are traceable to NIST fixed-point calibration of SPRTs.

The gravitational constant, g, is 980.1 cm/sec<sup>2</sup> at the Cannon Instrument Company. The gravitational constant varies up to 0.1% in the United States. To make this small correction in the viscometer constant, multiply the above viscometer constant by the factor [g (at your laboratory) / 980.1].

Calibrated by DLH on 3/15/2021  
 Issue Date 3/15/2021

under supervision of   
 D. T. Trowbridge Ph.D Laboratory Technical Director  
 J. T. Mastropiero Deputy Laboratory Technical Director  
 M. T. Zubler Director of Quality Assurance



# A.2 Pine Research Ag/AgCl Reference Electrode

### Electrode Storage

Aqueous reference electrodes must be stored properly to prevent damage when not in use. The ceramic frit should never be allowed to dry out. Follow these steps to properly store this reference electrode:

1. Rinse the reference electrode with distilled water (aqueous) or clean solvent (non-aqueous).
2. Suspend the reference electrode in 4M KCl. A 20 mL scintillation vial with a 4 mm OD hole drilled in the cap serves as an idea storage vessel. Ensure the frit is fully submerged in solution.
3. Always store the reference electrode upright and never in direct sunlight.

### Performance Verification

#### Reference Electrode Impedance

Reference electrode input impedance should be less than 10 kΩ. The most likely cause of high reference electrode input impedance is a blocked or partially blocked ceramic frit (H). Ceramic frits can become blocked by precipitation of salts in the microporous structure. In some cases, the frit clog can be cleared but often, the frit cannot be cleared and the electrode must be replaced.

#### Checking the Reference Potential

The standard potential of a reference electrode can be checked relative to another of the same reference electrode. Pine recommends that all users keep a "master" reference electrode that is never used in experiments and is always properly stored.

To check the reference potential of a reference electrode, submerge the experimental and master electrodes in filling solution. Measure the potential difference between the electrodes using either a simple voltmeter or a potentiostat in two electrode, open circuit potential mode. The difference should be less than 5 mV if the reference electrode standard potential is correct. If the difference is > 5 mV, the reference electrode should be disposed.

**This reference electrode will last a long time if proper care and storage conditions are met. Should the electrode become unusable, it cannot be refreshed or regenerated. It should be discarded and replaced.**

### Reference Electrode Conversions

From	NHE	MOE 20% KBr	Ag/AgCl sat'd KCl	SCE sat'd KCl	MSE sat'd H <sub>2</sub> SO <sub>4</sub>
To	0	98	199	241	650
NHE					
MOE 20% KBr	-98		101	143	552
Ag/AgCl sat'd KCl	-199	-101		42	451
SCE sat'd KCl	-241	-143	-42		409
MSE sat'd H <sub>2</sub> SO <sub>4</sub>	-650	-442	-451	-409	

Add listed value (in mV) to convert.  
 NHE = Normal Hydrogen; MOE = Mercury Oxide;  
 SCE = Calomel; MSE = Mercury Sulfate

### Optional Accessories

Additional reference electrode are available from Pine Research, including aqueous, non-aqueous, and standard size applications. Ensure proper operation and lifetime of the reference electrode with a storage system. Use of an isolation tube or salt bridge when temperature or ion contamination are of concern.

### Parts List

The following are included in the box:

- Single junction Ag/AgCl reference electrode
- 3.5mm OD fluorocarbon (FKM) O-Ring
- Polymer shipping cap

### Contact Us / Support

2741 Campus Walk Ave, Building 100  
 Durham, NC, 27705 USA

[www.pineinstruments.com](http://www.pineinstruments.com)  
[pineinstruments@pineinstruments.com](mailto:pineinstruments@pineinstruments.com)  
 +1 (919) 782-8320

## Reference Electrode

### Product Guide

This brief reference guide describes how to unpack, use, clean, store, and test the product. Please contact us with any additional questions.

## Part #: RRPEAGCL and RRPEAGCL2

### LowProfile (3.5 mm) Single Junction Ag/AgCl Reference Electrode (Saturated KCl)

### Quick Facts

**Reaction** AgCl(s) + e ⇌ Ag(s) + Cl<sup>-</sup>  
**Standard Potential (E°)** +199 mV vs. NHE  
**Filling Solution** 4M KCl gel  
**Temperature Tolerance** 10°C to 80°C  
**Avoid Use With** NH<sub>3</sub> buffers, sulfides, [base] > 0.1M OH<sup>-</sup>  
**Typical Variance** ±3 – 5 mV  
**Typical Input Impedance** < 10 kΩ

**Cannot be refilled/refreshed!**

DRP 10043 / REV002 (MAY 2016)  
 Copyright © 2009-2016 Pine Research Instrumentation

### Unpack the Electrode

Newly purchased reference electrodes are packed to ensure safe shipment. To unpack the electrode (refer to diagram on adjacent page): Remove the Parafilm around polymer shipping cap (G) and glass body (B). Rinse the reference electrode with distilled water to remove any solution that may have leaked during shipment. You can dispose of the polymer shipping cap (G); it should not be used for storage.

### Electrode Usage Tips

For optimal use, review the following tips for proper reference electrode use:

1. During an experiment, ensure the ceramic frit (H) is fully submerged in solution.
2. Ensure the clip connected to the brass contact pin (A) is not corroded and is firmly attached.
3. Ensure reference electrodes are always connected properly to the potentiostat. Current should never pass through a reference electrode.
4. The fluorocarbon (FKM) O-Ring (D) can carefully be moved along the length of the glass body (B) for optimal solution immersion depth.

### Refresh Reference Electrodes

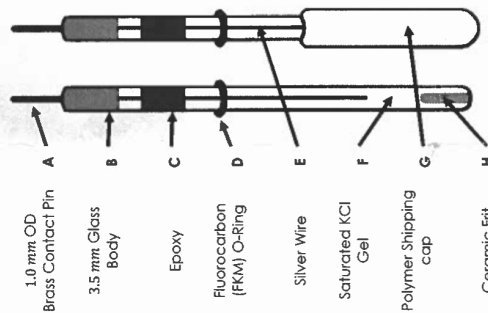
When the ceramic frit has been plugged (by precipitates or crystals), a higher than normal input impedance may cause problems such as potentiostat instability. The RRPEAGCL and RRPEAGCL2 reference electrodes cannot be refreshed. Dispose properly and replace with a new electrode.

### Electrode Sizes

This reference electrode is available in two lengths: 60 mm and 74 mm.

- 60 mm Ag/AgCl reference electrode was developed specifically for use in the Honeycomb Spectroelectrochemical Cell Kit.
- 74 mm Ag/AgCl reference electrode is ideal for use in the compact voltammetry cell kit (with Pt and Au ceramic screen printed electrodes) and the Low Volume series cells.

### Reference Electrode Diagram



The filling solution in the RRPEAGCL and RRPEAGCL2 reference electrodes is a solid, KCl saturated gel making the flow of chloride ion from these electrodes slow compared to liquid junction reference electrodes.

### Additional Resources

Search YouTube for "Pine Research Instrumentation" for instructional videos on this product.

LowProfile Reference Electrodes are also available in a Non-Aqueous version. This electrode, also called a pseudo reference electrode, can be customized to be used as a standard reference in non-aqueous media.

### Other Reference Electrodes

#### Ag/AgCl Double Junction (saturated KCl)

- Part #: RREF0024
- $E^{\circ}$  = 199 mV vs. *NHE*\*
- Filling Solution: 10% *KNO*<sub>3</sub>
- Temperature Range: 10°C to 80°C

#### Calomel/SCE (saturated KCl)

- Part #: RREF0022
- $E^{\circ}$  = 241 mV vs. *NHE*
- Filling Solution: 4*M* KCl
- Temperature Range: 10°C to 50°C

#### Mercury Sulfate (saturated *K*<sub>2</sub>*SO*<sub>4</sub>)

- Part #: RREF0025
- $E^{\circ}$  = 650 mV vs. *NHE*
- Filling Solution: saturated *K*<sub>2</sub>*SO*<sub>4</sub>
- Temperature Range: 10°C to 60°C
- Contains no chloride ion

#### Mercury Sulfate Double Junction (saturated *K*<sub>2</sub>*SO*<sub>4</sub>)

- Part #: RREF0026
- $E^{\circ}$  = 650 mV vs. *NHE*\*
- Filling Solution: saturated *K*<sub>2</sub>*SO*<sub>4</sub>
- Temperature Range: 10°C to 60°C
- Contains no chloride ion

#### Mercury Oxide (20% KOH)

- Part #: RREF0038
- $E^{\circ}$  = 98 mV vs. *NHE*\*
- Filling Solution: saturated 20% KOH
- Temperature Range: 10°C to 80°C
- Contains no chloride ion

#### Ag/Ag<sup>+</sup> Pseudo Electrode Kit

- Part #: AKREF0033
- Ideal for use in non-aqueous solvents
- Unstable reference potential unless made into a Ag/AgNO<sub>3</sub> reference

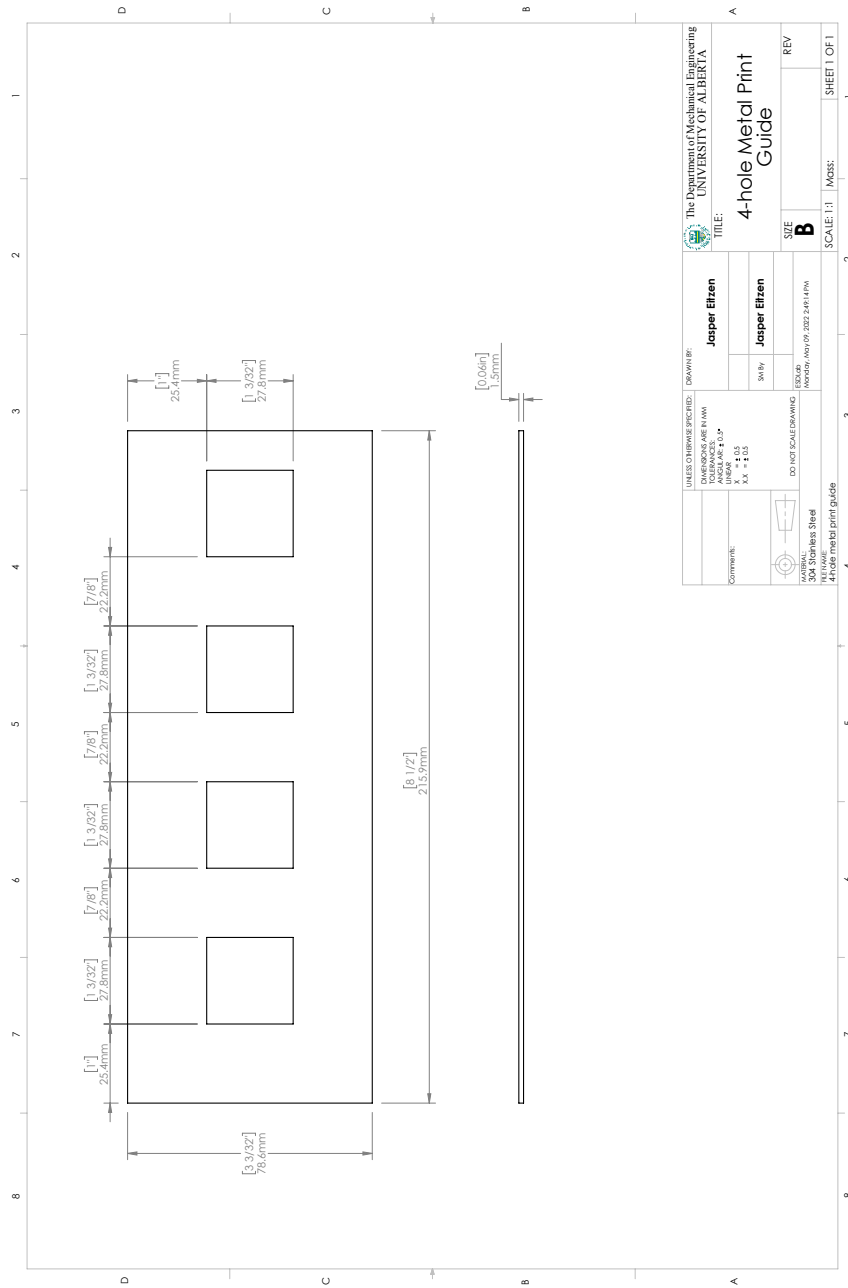
#### LowProfile (3.5 mm) Reference Electrodes

- Ag/AgCl in 60 mm and 74 mm lengths
- Ag/Ag<sup>+</sup> in 60 mm and 74 mm lengths

\*Double junction electrodes are subject to additional potential/drop across the second frit.

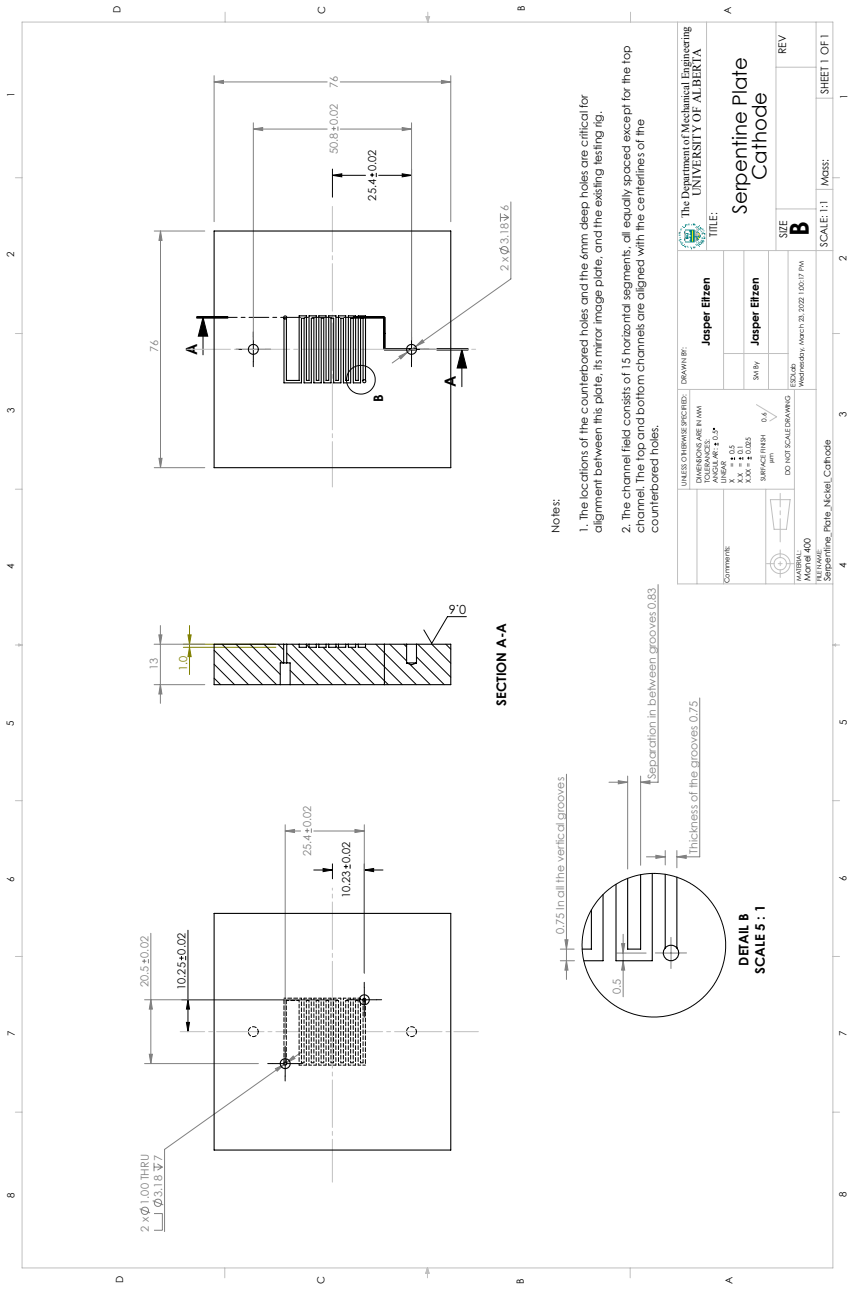
**Be prepared! Always have a spare reference electrode to use!**

# A.3 Metal Print Guide Solidworks Drawing



UNLESS OTHERWISE SPECIFIED, DIMENSIONS ARE IN MM ANGLES ARE IN °		DRAWN BY: <b>Jasper Eitzen</b>		The Department of Mechanical Engineering UNIVERSITY OF ALBERTA	
COMMENT:		DATE: 10/20/2023		TITLE: <b>4-hole Metal Print Guide</b>	
MATERIAL: 304 Stainless Steel		SCALE: 1:1		REV	
BY: Jasper Eitzen		DATE: 10/20/2023		SHEET 1 OF 1	
DESCRIPTION: 4-hole metal print guide		SCALE: 1:1		SHEET 1 OF 1	





**SECTION A-A**

**DETAIL B  
SCALE 5 : 1**

- Notes:**
1. The locations of the counterbored holes and the 6mm deep holes are critical for alignment between this plate, its mirror image plate, and the existing testing rig.
  2. The channel field consists of 15 horizontal segments, all equally spaced except for the top channel. The top and bottom channels are aligned with the centres of the counterbored holes.

UNLESS OTHERWISE SPECIFIED:		DRAWN BY:	The Department of Mechanical Engineering UNIVERSITY OF ALBERTA	
DIMENSIONS ARE IN MM		Jasper Eltahan	TITLE:	
ANGLES ARE 1:1 UNLESS NOTED			Serpentine Plate Cathode	
TOLERANCES ARE:		DATE:	SIZE	
FRACTIONS: ± 0.05		20/01/2020	B	
DECIMALS: ± 0.025		DESIGNED BY:	REV	
HOLE POSITION: ± 0.025		Jasper Eltahan		
SURFACE FINISH: Ra 3.2		DATE:	SCALE: 1:1	
DO NOT SCALE DRAWING		20/01/2020	Mass:	
MATERIAL: Monel 400		PROCESSED BY:	SHEET 1 OF 1	
Serpentine Plate_Nickel_Cathode				

## Appendix B

# Measurement Error and Confidence Interval Calculations

Two types of experimental uncertainty are present in every measurement, random or precision uncertainty and systematic or bias uncertainty. To obtain the total uncertainty of a calculated quantity, the precision and bias uncertainties of all measured values must be propagated. For a quantity,  $f$ , the total uncertainty can be represented as [110]

$$\Delta f = \sqrt{B_f^2 + P_f^2} \quad (\text{B.1})$$

where  $\Delta f$  is the total uncertainty in  $f$ ,  $B_f$  is the bias uncertainty in  $f$ , and  $P_f$  is the precision uncertainty in  $f$ .

For any resulting value of  $f$  calculated using multiple measurements, the precision uncertainty can be calculated as a function of the standard deviation of  $f$  [110] by

$$P_f = t \frac{S_f}{\sqrt{n}} \quad (\text{B.2})$$

where  $t$  is Student's  $t$ -value obtained from Table B.1,  $S_f$  is the sample standard deviation of  $f$ , and  $n$  is the number of measurements made.

The bias uncertainty can be calculated for the value of  $f$  by propagating the bias uncertainty of each of the measured values. If  $f$  is dependent on a set of variables such that  $f(x_1, x_2, \dots, x_N)$ , this can be done by taking the root sum of squares of the bias uncertainties for each independent variable  $x_i$  [110] as follows:

$$B_f^2 = \sum_{i=1}^N \left( \frac{\partial f}{\partial x_i} B_{x_i} \right)^2 \quad (\text{B.3})$$

where  $B_{x_i}$  is the sample standard deviation of  $x_i$ , and  $\partial$  is the partial derivative. Note that Equation (B.3) assumes that the bias uncertainty in all independent variables  $x_i$  are independent of each other.

**Table B.1** – Table of Student’s  $t$ -values [110]

Degrees of Freedom	Confidence Interval (%)				
	80	90	95	98	99
1	3.078	6.314	12.706	31.820	63.657
2	1.886	2.920	4.303	6.965	9.925
3	1.638	2.353	3.182	4.541	5.841
4	1.533	2.132	2.776	3.747	4.604
5	1.476	2.015	2.571	3.365	4.032
6	1.440	1.943	2.447	3.143	3.707
7	1.415	1.895	2.365	2.998	3.499
8	1.397	1.860	2.306	2.897	3.355
9	1.383	1.833	2.262	2.821	3.250
10	1.372	1.812	2.228	2.764	3.169
11	1.363	1.796	2.201	2.718	3.106
12	1.356	1.782	2.179	2.681	3.055
13	1.350	1.771	2.160	2.650	3.012
14	1.345	1.761	2.145	2.625	2.977
15	1.341	1.753	2.131	2.602	2.947
16	1.337	1.746	2.120	2.584	2.921
17	1.333	1.740	2.110	2.567	2.898
18	1.330	1.734	2.101	2.552	2.878
19	1.328	1.729	2.093	2.539	2.861
20	1.325	1.725	2.086	2.528	2.845
21	1.323	1.721	2.080	2.518	2.831
22	1.321	1.717	2.074	2.508	2.819
23	1.319	1.714	2.069	2.500	2.807
24	1.318	1.711	2.064	2.492	2.797
25	1.316	1.708	2.060	2.485	2.787
26	1.315	1.706	2.056	2.479	2.779
27	1.314	1.703	2.052	2.473	2.771
28	1.313	1.701	2.048	2.467	2.763
29	1.311	1.699	2.045	2.462	2.756
30	1.310	1.697	2.042	2.457	2.750

## B.1 Density Measurement Uncertainty

The density of a material is calculated given the material's mass and volume as per Equation 2.2, where  $\rho = \frac{m}{V}$ . In this work, the density of a fluid is calculated based on the measured mass,  $m$ , of a set volume of fluid,  $V=1.00$  mL. The measurement of fluid mass is carried out six times, and so Equation (B.2) can be used to calculate the precision uncertainty in density,  $P_\rho$ , for a 95% confidence interval as follows:

$$P_\rho = 2.571 \times \frac{S_\rho}{\sqrt{6}}$$

As there is no bias uncertainty in the instruments used, this calculated precision uncertainty is the total uncertainty.

## B.2 Dynamic Viscosity Measurement Uncertainty

Dynamic viscosity was calculated given the measured values of kinematic viscosity and density as per Equation 2.3:  $\mu = tC\rho$ . The time value,  $t$ , was measured, the calibration constant,  $C$  was obtained from the viscometer certification of calibration, given in Appendix A.1, and the density,  $\rho$ , was calculated based on the procedure outlined in Section 2.2.1. For measurements of viscosity, two replications of the experiment were run, and so at a 95% confidence interval, the precision uncertainty in dynamic viscosity,  $P_\mu$ , was calculated using Equation (B.2):

$$P_\mu = 12.706 \times \frac{S_\mu}{\sqrt{2}}$$

As with the density measurements, the instruments used for the viscosity measurements did not contain a bias uncertainty and so the precision uncertainty is the total uncertainty.

## B.3 Surface Tension Measurement Uncertainty

Surface tension was calculated in this work using the drop weight method. The calculation of surface tension using this method is done with Equation (2.5):  $\gamma = \frac{mg}{2\pi r C_T}$ . The average mass of a single droplet is measured using the procedures laid out in Section 2.2.3, and this value is also used in the calculation of the correction factor,  $C_T$ . Capillary diameter was also measured before droplet mass measurements were made. For the PG:IPA solutions, four surface tension measurement replicates were done, and three were done for ink solutions. Equation (B.2) can then be used to calculate the 95% confidence interval as follows:

$$P_\gamma = 4.303 \times \frac{S_\gamma}{\sqrt{3}}$$

where for the PG:IPA solutions, values of  $n = 4$  and  $t = 3.182$  were used.

As with the density and dynamic viscosity measurements, the instruments used for the viscosity measurements do not contain a bias uncertainty and so the precision uncertainty is the total uncertainty.

## B.4 HFR Uncertainty

HFR was calculated by taking EIS measurements following polarization curves and stability tests at the tested current densities. The EIS test profiles used are provided in Tables 2.5, 2.6, and C.2. It was found that the value of HFR did not change with current density, and so these values were averaged. Along with this, a 95% confidence interval on these average values was calculated using Equation (B.2):

$$P_{HFR} = 2.776 \times \frac{S_{HFR}}{\sqrt{5}}$$

There was no reason to expect a bias uncertainty, and so it was not accounted for in the HFR uncertainty calculation.

## Appendix C

# Altered Test Profiles for Cells Operating Under Cathode-Only Feed

As cell losses were significantly higher when operating under cathode-only feed, some testing profiles had to be adjusted to compensate. To account for the additional losses, cells were only operated up to a current density of  $1000 \text{ mA/cm}^2$  in an effort to keep the cell potential under 2.3 V. Table C.1 provides the profile used for polarization curves and Table C.2 provides the profiles used for EIS with cathode-only feed.

**Table C.1** – Galvanostatic profile used to obtain polarization curves under cathode-only feed. For curves run forward and backward, backward steps are denoted in parenthesis beside their forward counterparts.

Step (Backward Step)	Time [s]	Current [mA]	Current Density [mA/cm <sup>2</sup> ]
0 (62)	300	0	0
1 (61)	300	5	1
2 (60)	90	25	5
3 (59)	90	50	10
4 (58)	90	75	15
5 (57)	90	100	20
6 (56)	90	125	25
7 (55)	90	150	30
8 (54)	90	200	40
9 (53)	90	250	50
10 (52)	90	375	75
11 (51)	90	500	100
12 (50)	90	625	125
13 (49)	90	750	150
14 (48)	90	875	175
15 (47)	90	1000	200
16 (46)	90	1250	250
17 (45)	90	1500	300
18 (44)	90	1750	350
19 (43)	90	2000	400
20 (42)	90	2250	450
21 (41)	90	2500	500
22 (40)	90	2750	550
23 (39)	90	3000	600
24 (38)	90	3250	650
25 (37)	90	3500	700
26 (36)	90	3750	750
27 (35)	90	4000	800
28 (34)	90	4250	850
29 (33)	90	4500	900
30 (32)	90	4250	850
31	90	5000	1000

**Table C.2** – Galvanostatic EIS profiles used following each polarization curve and stability test run on the studied AEMWE cells when operating in Cathode-only feed.

Current Density (mA/cm <sup>2</sup> )	Amplitude (mA/cm <sup>2</sup> )	Starting Frequency (kHz)	Ending Frequency (mHz)	Points Measured per Frequency Decade
20	4	200	20	15
150	15	200	50	15
300	30	200	100	15
600	60	200	100	15
900	90	200	100	15

# Appendix D

## Additional Equations used in this Work

### D.1 Conversion of Ink Recipes from a Weight Percent Basis to a Mass Basis

All ink recipes used in this work were defined using a weight percent basis so that they could be scaled to any desired amount when made. The mass of each ink component needed to make an ink then needed to be calculated from the weight percent recipe. This was done by first selecting the total mass of ink that would be made, then solving a system of linear equations to calculate the mass of each component in the ink. This process is quite simple, as each linear equation can be solved sequentially.

The ink recipes used in this work are defined in Tables 3.2 and 3.4 for the IrO<sub>x</sub> and Pt/C inks, respectively. These tables provide the wt.% of each component in the ink individually, however, when developing these formulae, only the minimum number of variables needed to fully define the formulae were used. These variables were the wt.% of propylene glycol (PG) ( $w_{PG}$ ), the wt.% of solid content ( $w_{solids}$ ) as well as the wt.% of ionomer within the solid content ( $w_{ionomer}$ ). These values from the ink formulae are provided in Table D.1 below, and all variables used in this section are defined in Table D.2. The PG content was based on the PG-IPA ratio, the total solid content was limited to prevent clogging of the printhead nozzles [40], and the ionomer content was chosen based on the justifications provided in Section 1.2.1. Additionally, as ionomer solid was added as part of an ionomer solution, the amount of ionomer solid in the solution ( $w_{ionomer\ solution\ solid}$ ) had to be known. The ionomer solution used in this work was made from 2 wt.% of solid ionomer dissolved into a 50%/50% by volume solution of methanol and acetone. The amount of ionomer solid in this solution could be changed if it was desired to change the amount of methanol and acetone in the ink, but this was not done in this work.

**Table D.1** – Ink formulae definitions.

Component	Amount in IrO <sub>x</sub> ink [wt.%]	Amount in Pt/C ink [wt.%]
PG ( $w_{PG}$ )	69.1	69.5
Solid Content ( $w_{solid}$ )	3.25	1.25
Ionomer in Solid Content ( $w_{ionomer}$ )	5.0	10.0
Ionomer in Solution ( $w_{ionomer\ solution\ solid}$ )	2.0	2.0

**Table D.2** – Definitions for the variables used to convert ink recipes from a weight percent basis to a mass basis.

Component	Mass	Weight Percent
Total Ink Solution	$m_{total}$	$W_{total}$
PG in Ink	$m_{PG}$	$W_{PG}$
IPA in Ink	$m_{IPA}$	$W_{IPA}$
Total Solid Content in Ink	$m_{solid}$	$W_{solid}$
Catalyst in Ink	$m_{catalyst}$	$W_{catalyst}$
Ionomer in Total Solid Content	$m_{ionomer}$	$W_{ionomer}$
Ionomer Solution in Ink	$m_{ionomer\ solution}$	$W_{ionomer\ solution}$
Ionomer in Ionomer Solution	$m_{ionomer\ solution\ solid}$	$W_{ionomer\ solution\ solid}$
Solvent in Ionomer Solution	$m_{ionomer\ solution\ solvent}$	$W_{ionomer\ solution\ solvent}$

Based on these set variables, for a given total mass of ink to be made,  $m_{total}$ , the following system of linear equation was solved to calculate each component:

$$m_{PG} = (m_{total})(w_{PG})$$

$$m_{solid} = (m_{total})(w_{solid})$$

$$m_{catalyst} = (m_{solids})(1 - w_{ionomer})$$

$$m_{ionomer\ solution} = \frac{m_{ionomer}}{w_{ionomer\ solution\ solid}}$$

$$m_{IPA} = m_{total} - (m_{pg} + m_{catalyst} + m_{ionomer\ solution})$$

Then, using the calculated values of  $m_{PG}$ ,  $m_{catalyst}$ ,  $m_{ionomer\ solution}$ , and  $m_{IPA}$ , the desired mass of ink can be made.

The mass of ionomer and solvent used in the ionomer solution must also be calculated. The solvent used was a 50%/50% by volume mixture of methanol and acetone, made simply by measuring equal volumes of each with a syringe. To account for filtration losses at least 3 times the required amount of ionomer solution was made, which is reflected in the calculation:

$$m_{ionomer\ solution\ solid} = 3m_{ionomer}$$

$$m_{ionomer\ solution\ solvent} = 3m_{ionomer} \times \frac{1 - w_{ionomer\ solution\ solid}}{w_{ionomer\ solution\ solid}}$$

## D.2 Calculation of the Mass of Solid Potassium Hydroxide needed to make an Aqueous 1 M Solution

Aqueous 1 M KOH solutions were used to convert the Aemion-based CCMs used in this work, as a feed solution for the tested AEMWE cells, and as part of the ionic connection between the cells and reference electrode. These solutions were made using solid KOH (Fischer Scientific P250-1 Potassium Hydroxide) and deionized water. The formula used to calculate the required mass of solid KOH to add to the water was:

$$m_{KOH} = cMV = (1 \text{ mol/L})(56.1056 \text{ g/mol}) \cdot V$$

where  $c$  is the concentration of the solution,  $M$  is the molar mass of KOH, and  $V$  is the desired volume in litres.

# Appendix E

## Additional Experimental Results

### E.1 Cell Voltage and Current During Conditioning

This section contains plots of cell current density and voltage during the conditioning process for cells 1 to 5, 7, 8, and 9 (The plot for cell 6 is in the main body in Figure 2.16). For cell conditioning, the current density was set, and the cell voltage measured. The conditioning procedure was still under development during the testing of cells 1 and 2, which is why the procedure used on those cells is different. Cells 3, 4, and 5 used the in-house built system (BK Precision 9202 power supply and Arduino UNO), whereas cells 6, 7, and 8 used a Biologic SP-300 potentiostat, which is why the voltage measurements at 0 mA/cm<sup>2</sup> differ for these cells. These different setups were discussed in Section 2.4.2. The reason these differ is that the Biologic potentiostat actively held the cell at 0 mA/cm<sup>2</sup>, not allowing the reverse reaction to proceed in the cell, whereas the in-house setup simply turned off the power supply.

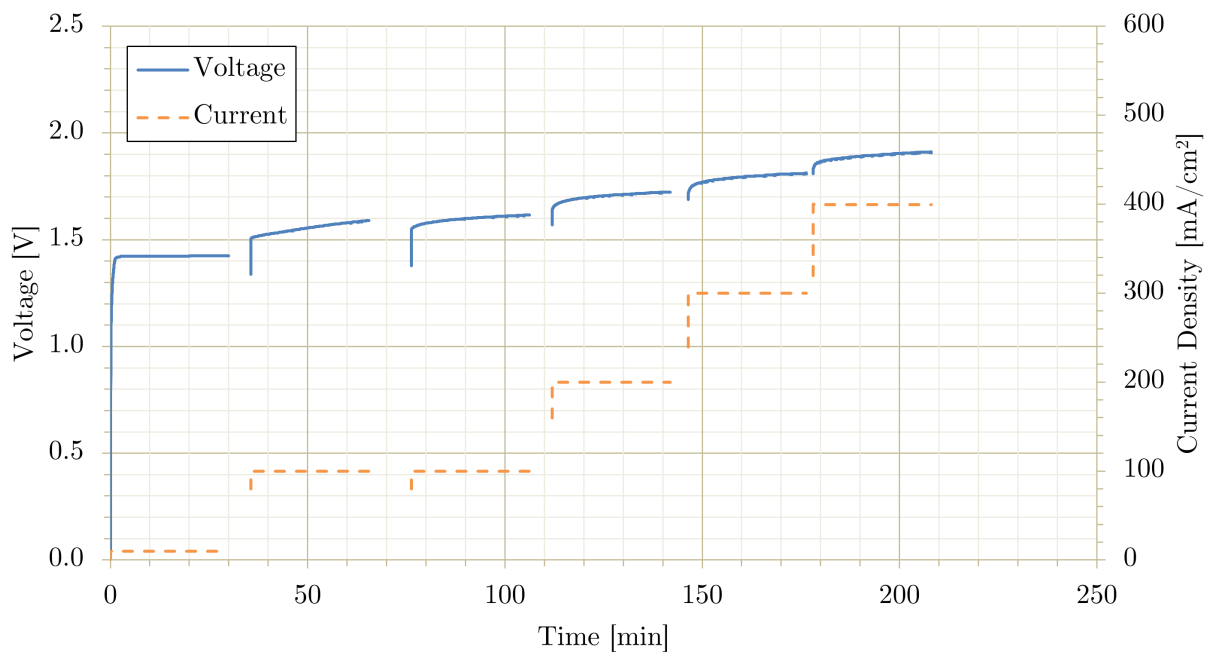


**Figure E.1** – Conditioning process for Cell 1. Current was applied and the cell voltage was measured. This cell was tested before the final conditioning profile was decided.

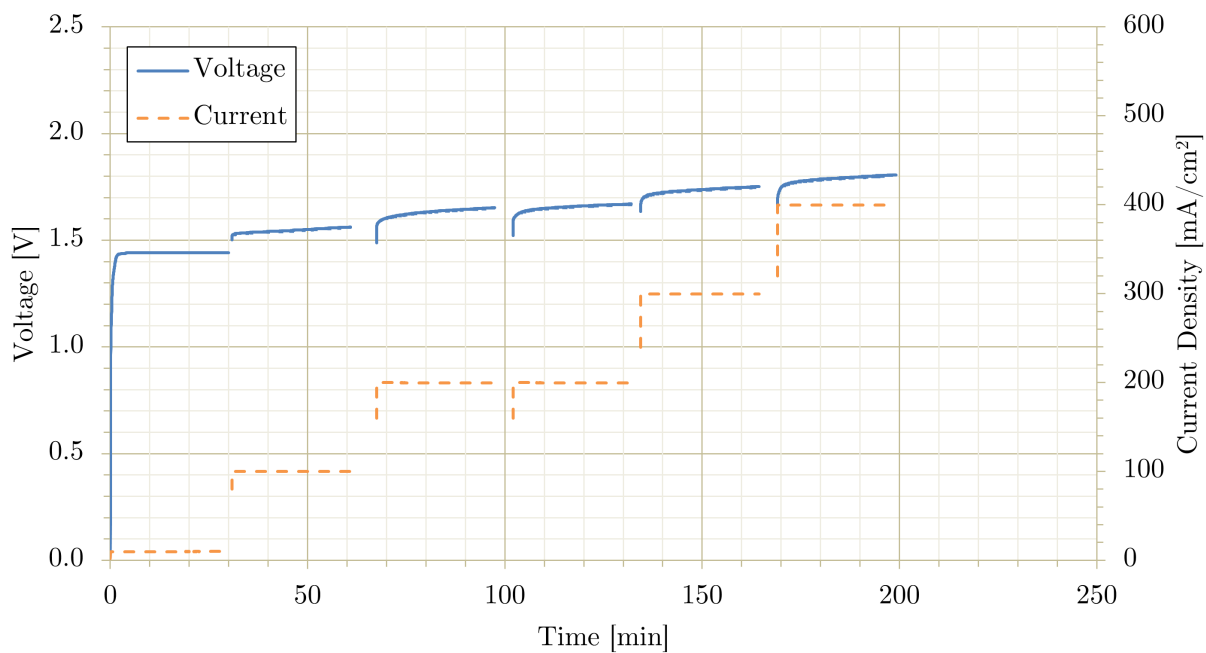


**Figure E.2** – Conditioning process for Cell 2. Current was applied and the cell voltage was measured. This cell was tested before the final conditioning profile was decided.

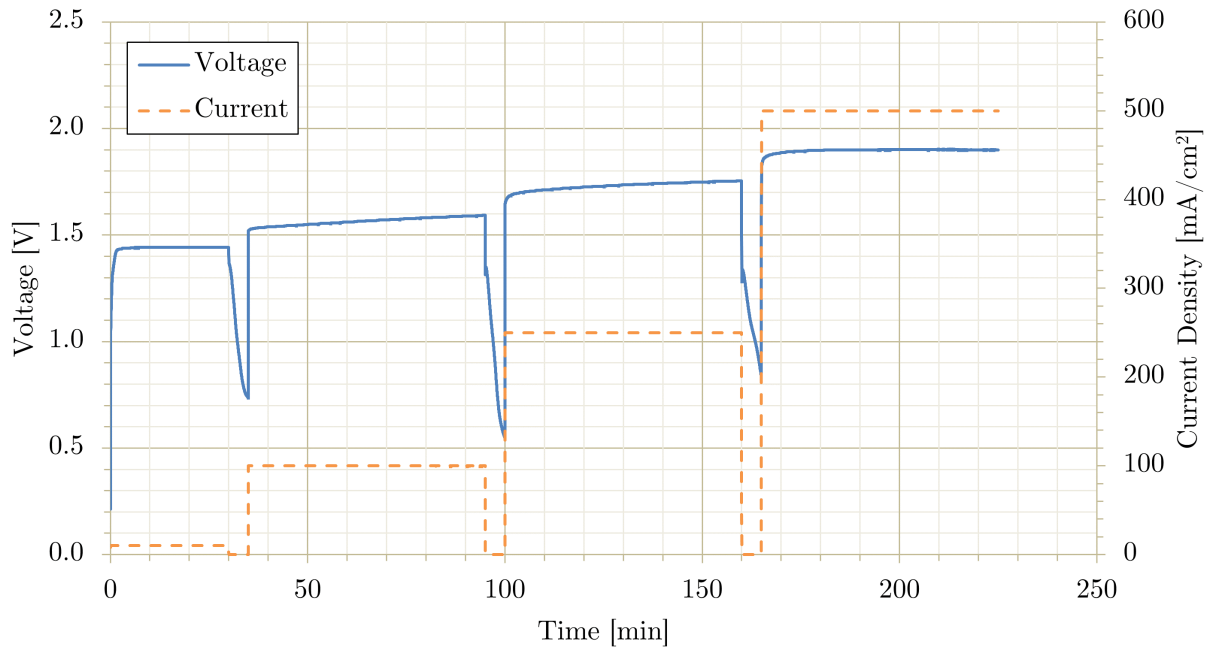


**Figure E.3** – Conditioning process for Cell 3. Current was applied based on the profile in Table 2.2, and the cell voltage was measured

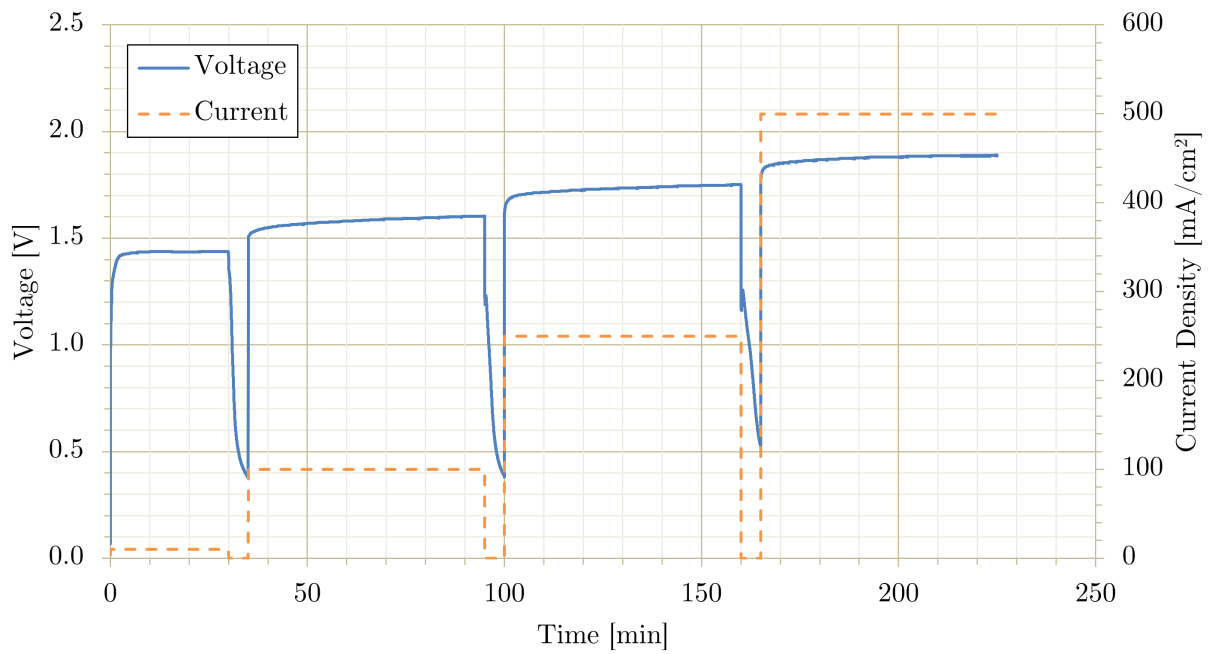


**Figure E.4** – Conditioning process for Cell 4. Current was applied based on the profile in Table 2.2, and the cell voltage was measured

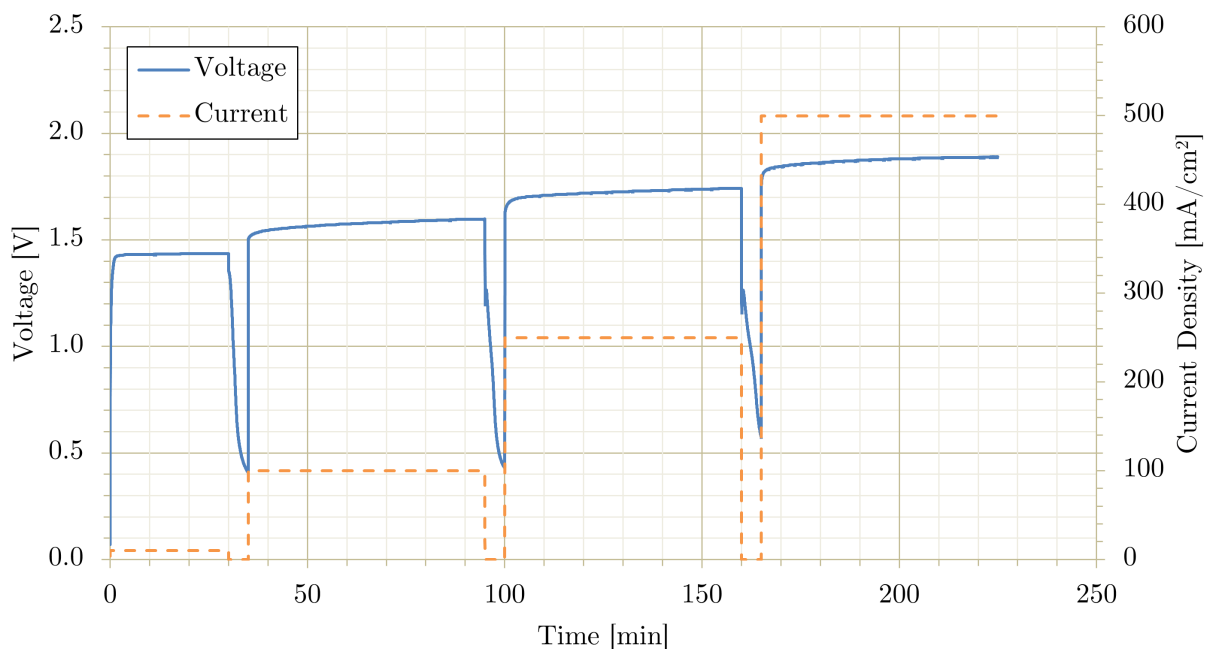


**Figure E.5** – Conditioning process for Cell 5. Current was applied based on the profile in Table 2.2, and the cell voltage was measured

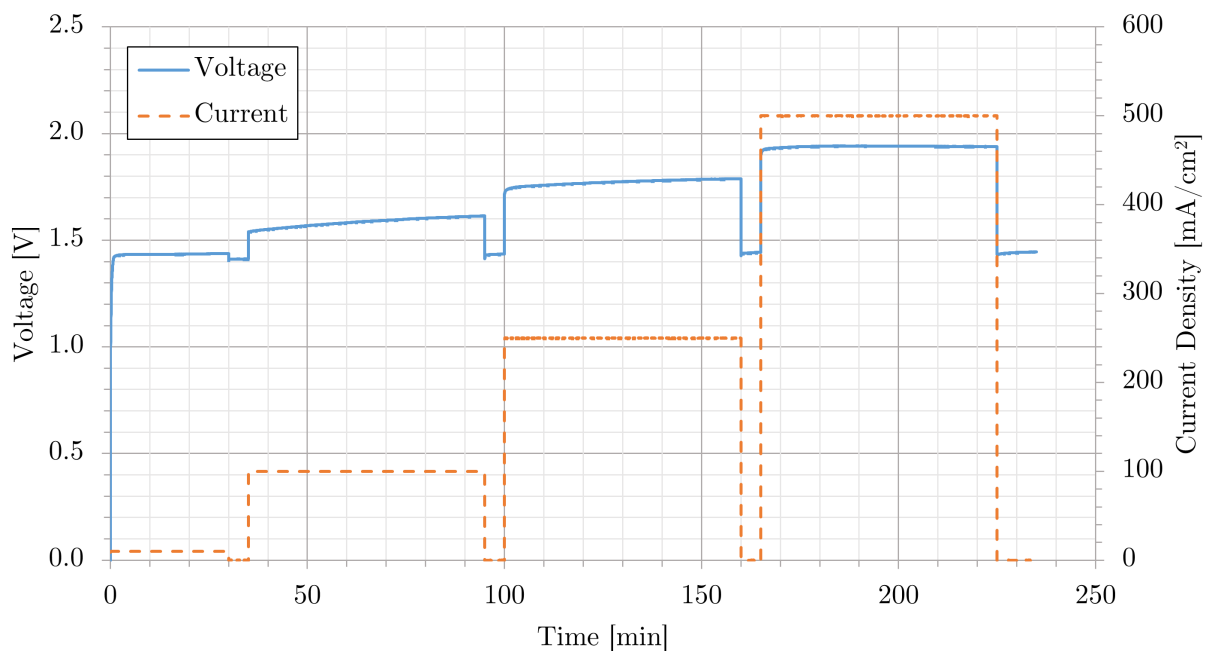


**Figure E.6** – Conditioning process for Cell 7. Current was applied based on the profile in Table 2.2, and the cell voltage was measured.

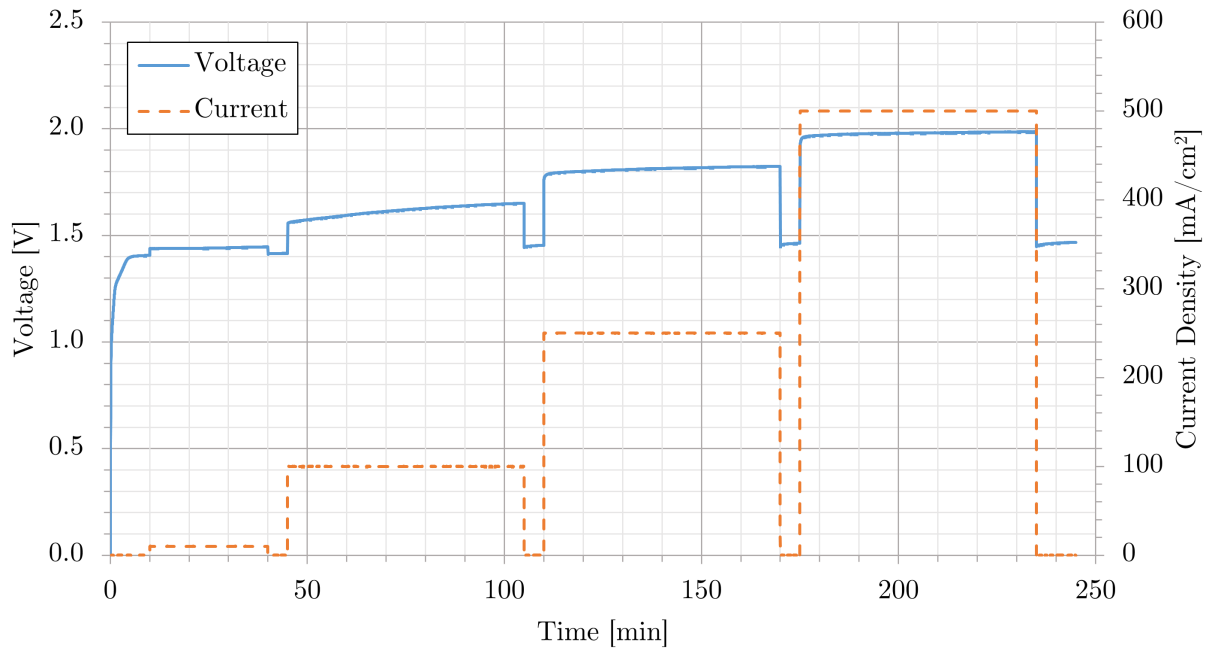


**Figure E.7** – Conditioning process for Cell 8. Current was applied based on the profile in Table 2.2, and the cell voltage was measured.

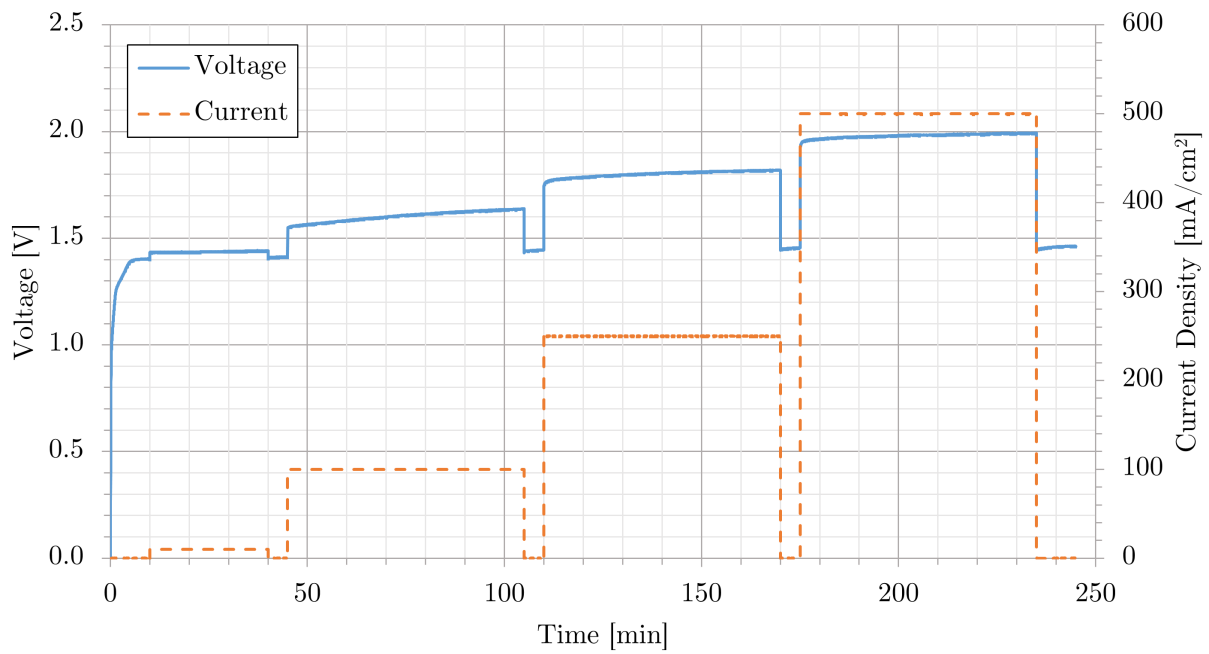


**Figure E.8** – Conditioning process for Cell 9. Current was applied based on the profile in Table 2.2, and the cell voltage was measured.

## E.2 Individual Viscosity Measurements for Ink Development Solutions

It was noticed during the development of the inks containing Aemion+ AP2-HNN5-00-X ionomer used in this work that consecutive viscosity measurements had a larger error for solutions that contained dissolved ionomer compared to those that did not. This was probably due to the evaporation of the highly volatile acetone and methanol used to dissolve the ionomer material. As these were the lowest-viscosity components of these solutions, as they evaporated, viscosity would therefore increase, and this trend was observed over consecutive viscosity measurements. This is demonstrated in Table E.1, where the inks with and without catalyst follow this trend to a much greater degree than the PG:IPA mixtures.

The full Pt/C ink had the smallest percent difference between the two measurements as it was tested following the identification of this trend, and so special care was taken to ensure minimal exposure to air during characterization. This was successful in reducing the difference between the two measurements, but the viscosity did still increase a small amount, meaning that there was still some solvent evaporation.

**Table E.1** – Individual, consecutive measurements of dynamic viscosity made during ink development.

Solution	Dynamic Viscosity [mPa·s]		
	Measurement 1	Measurement 2	% Difference
1.0:1 PG:IPA Mixture	5.40	5.41	0.21
1.5:1 PG:IPA Mixture	7.31	7.32	0.21
2.0:1 PG:IPA Mixture	8.91	8.94	0.31
2.5:1 PG:IPA Mixture	10.38	10.42	0.39
3.0:1 PG:IPA Mixture	11.79	11.84	0.43
3.5:1 PG:IPA Mixture	12.77	12.86	0.69
IrO <sub>x</sub> No-catalyst Ink (3.0:1 PG:IPA)	10.46	10.59	1.18
IrO <sub>x</sub> No-catalyst Ink (3.5:1 PG:IPA)	11.14	11.26	1.03
IrO <sub>x</sub> Full Ink	11.15	11.31	1.42
Pt/C No-catalyst Ink (3.5:1 PG:IPA)	11.90	12.04	1.16
Pt/C No-catalyst Ink (3.0:1 PG:IPA)	11.93	12.22	2.47
Pt/C Full Ink	9.15	9.22	0.85

### E.3 Individual Polarization Curve Results

This section contains all individual polarization curve results for Cells 2, 3, 4, 6, 7, 8, and 9 discussed in this work. The individual polarization curves for Cell 5 are provided in Figure 3.12 in the main body.

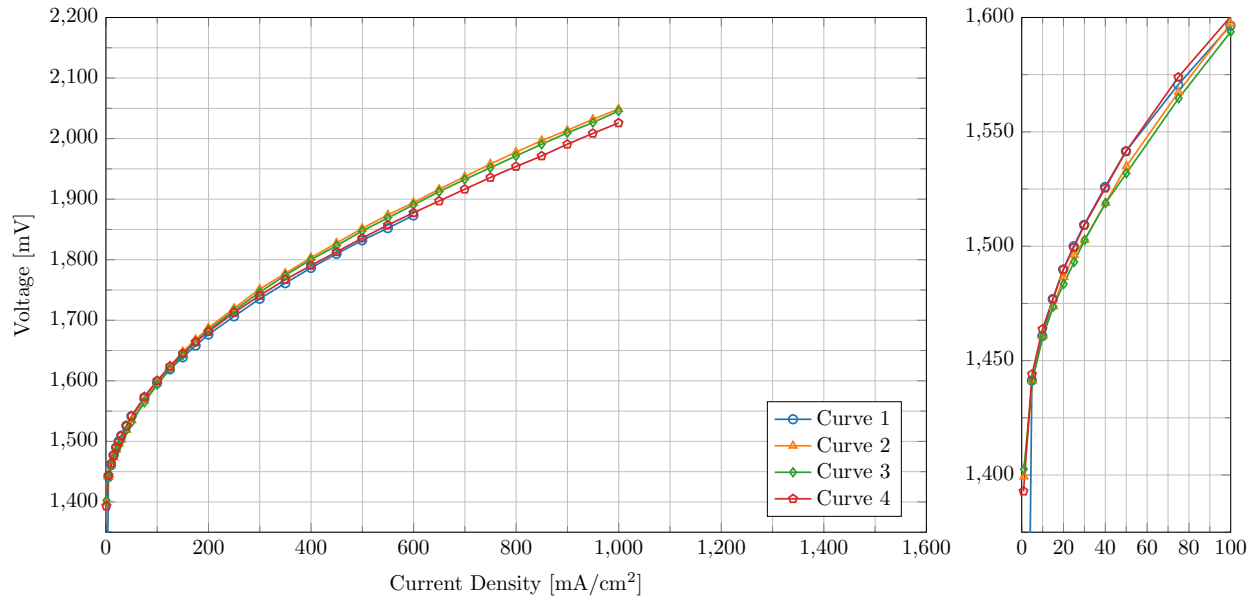
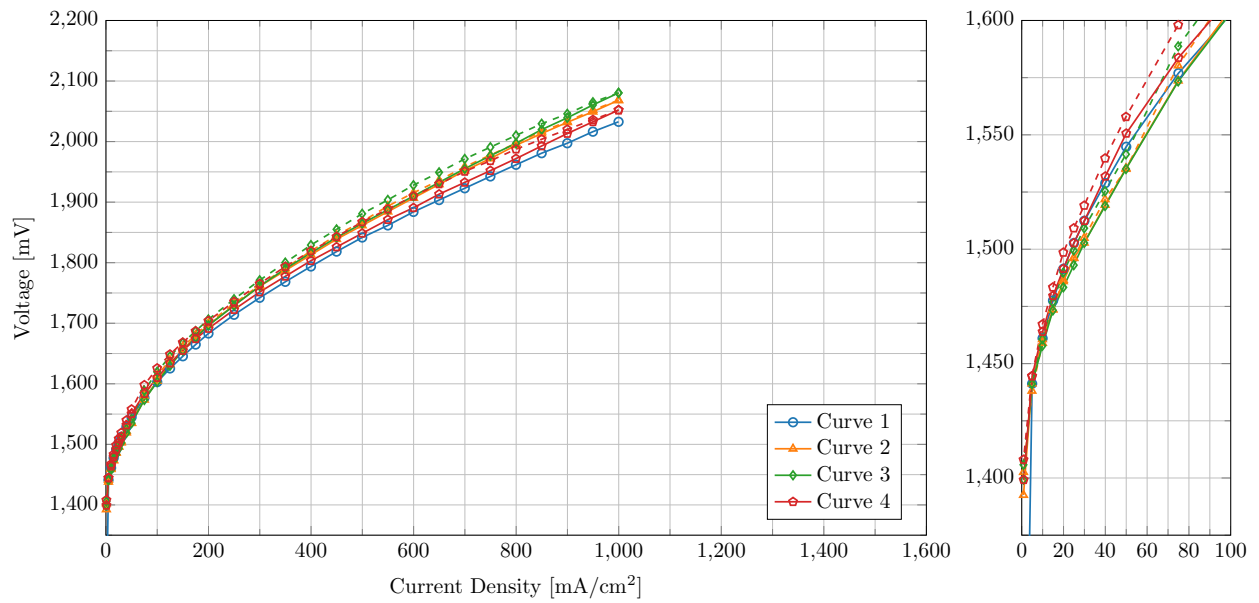
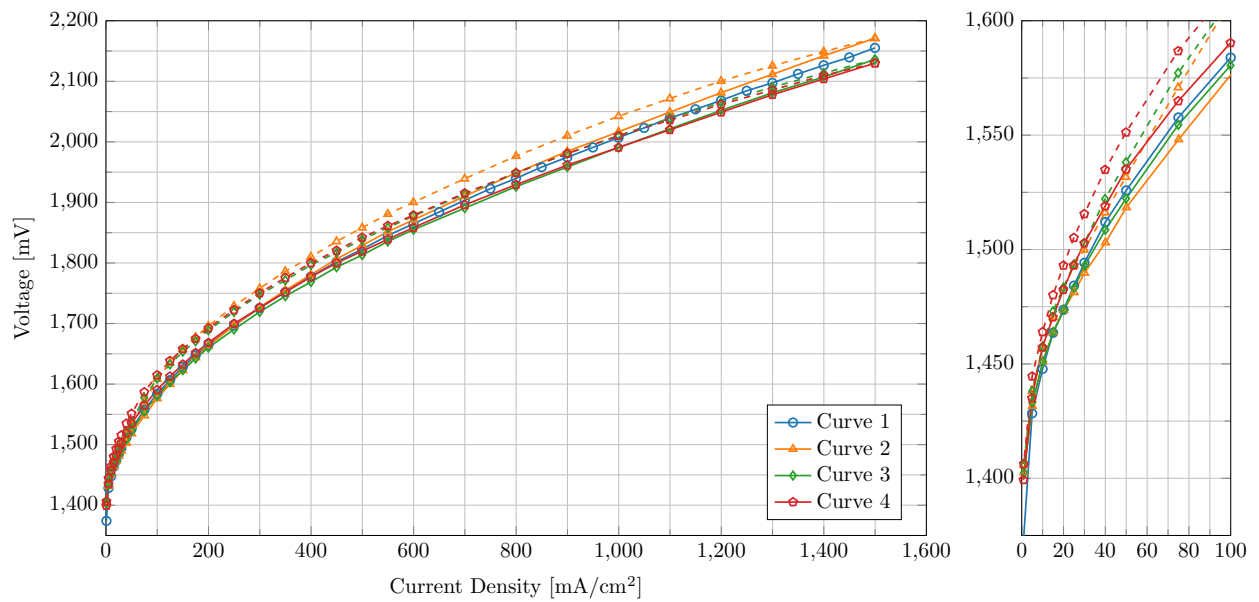


Figure E.9 – Polarization curves measured on Cell 2.



**Figure E.10** – Polarization curves measured on Cell 3. Backward curves plotted with dashed lines.



**Figure E.11** – Polarization curves measured on Cell 4. Backward curves plotted with dashed lines.

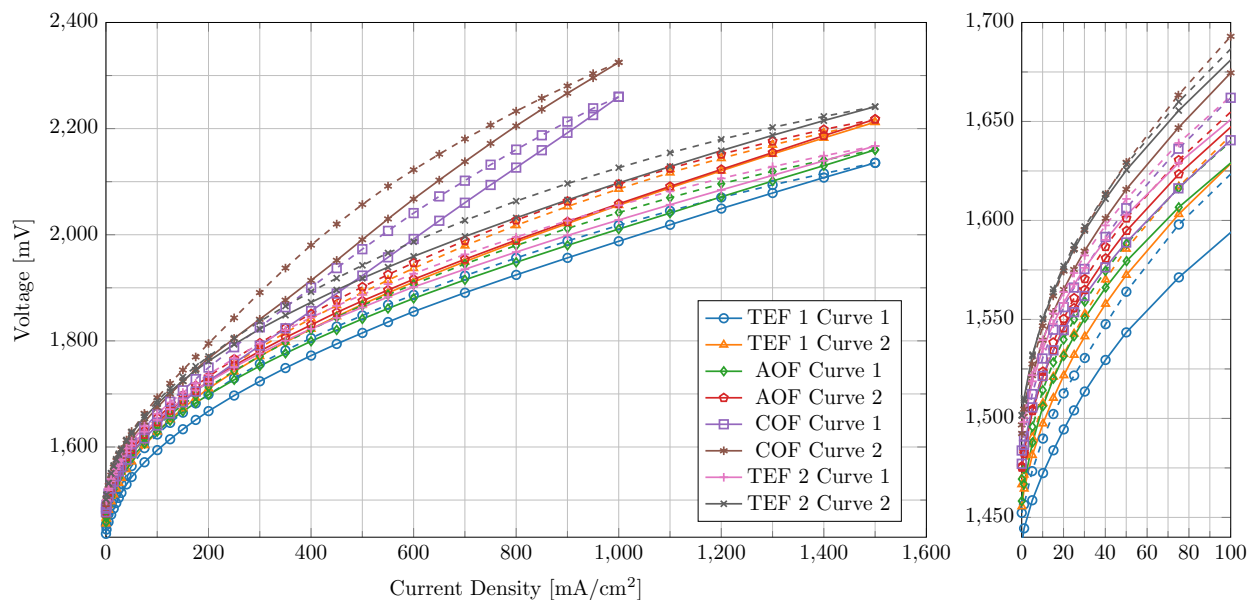


**Figure E.12** – Polarization curves measured on Cell 6 with all electrode feed configurations. Backward curves plotted with dashed lines.

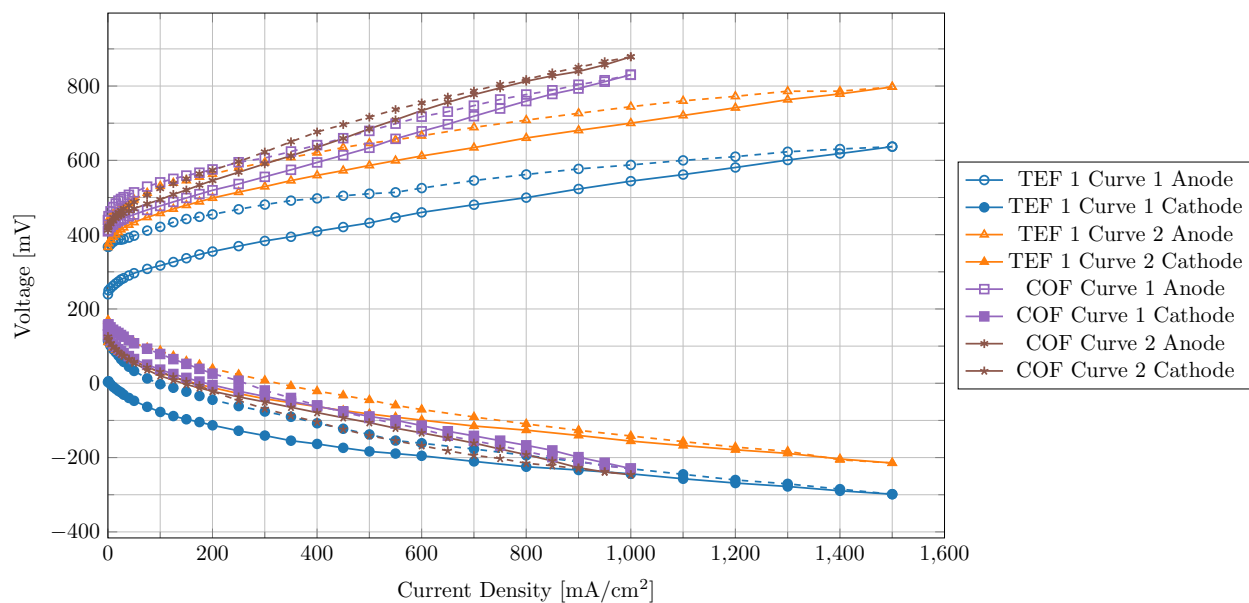


**Figure E.13** – Polarization curves of the separate anode and cathode overpotentials measured on Cell 6 with TEF and COF configurations. Backward curves plotted with dashed lines.

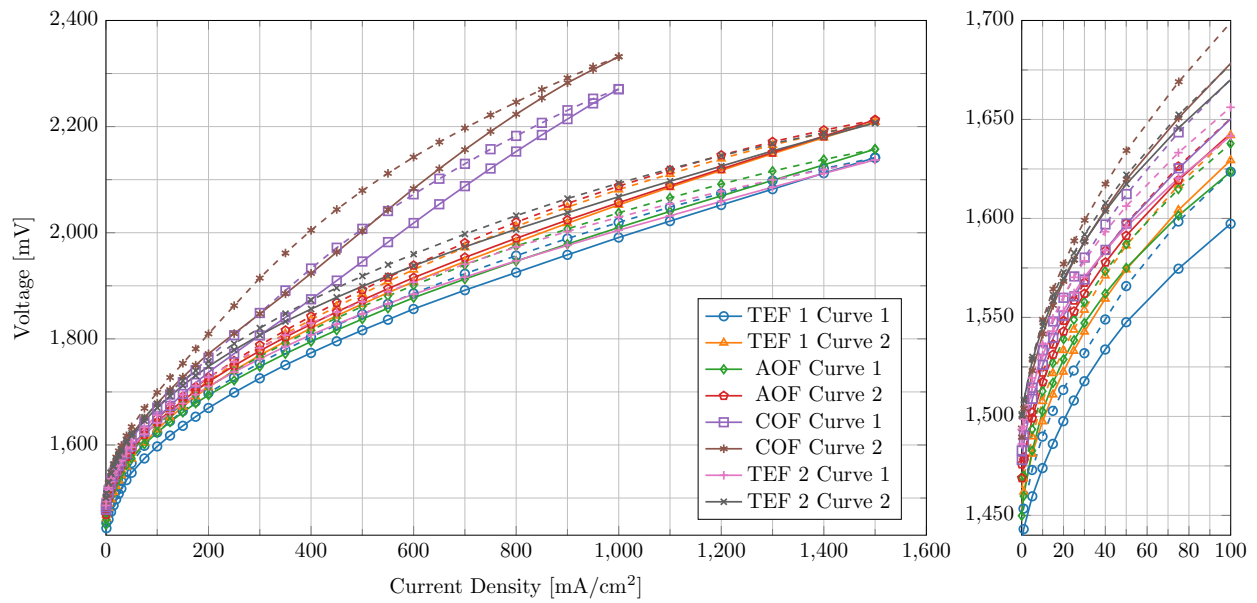


**Figure E.14** – Polarization curves measured on Cell 7 with all electrode feed configurations. Backward curves plotted with dashed lines.

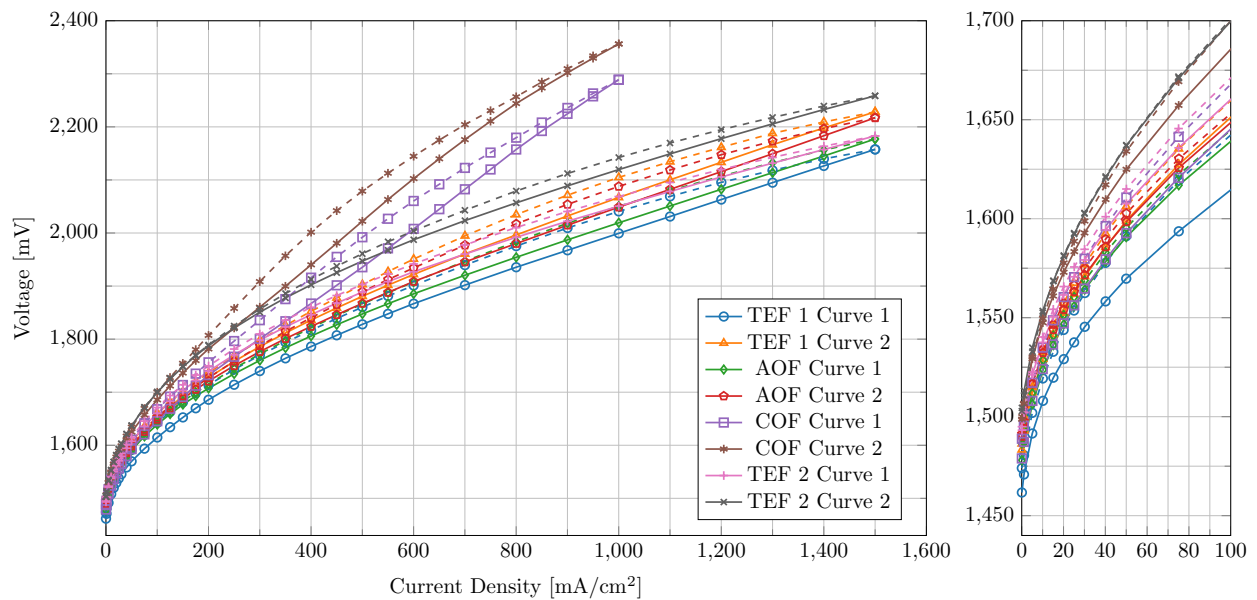


**Figure E.15** – Polarization curves measured on Cell 8 with all electrode feed configurations. Backward curves plotted with dashed lines.

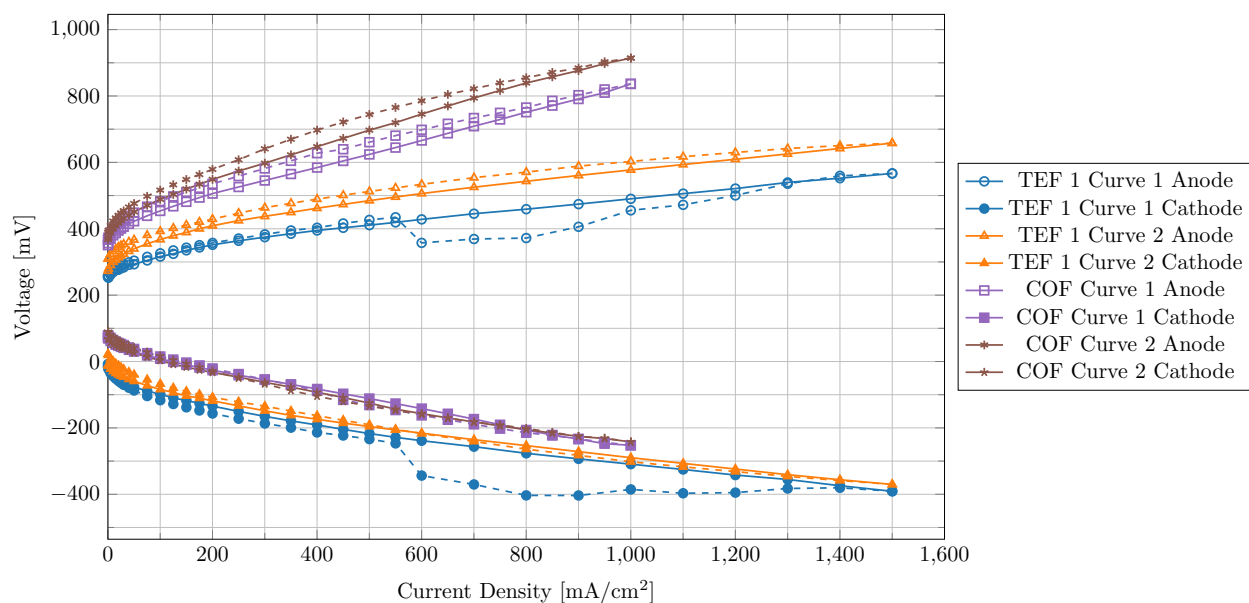


**Figure E.16** – Polarization curves of the separate anode and cathode overpotentials measured on Cell 8 with TEF and COF configurations. Backward curves plotted with dashed lines.

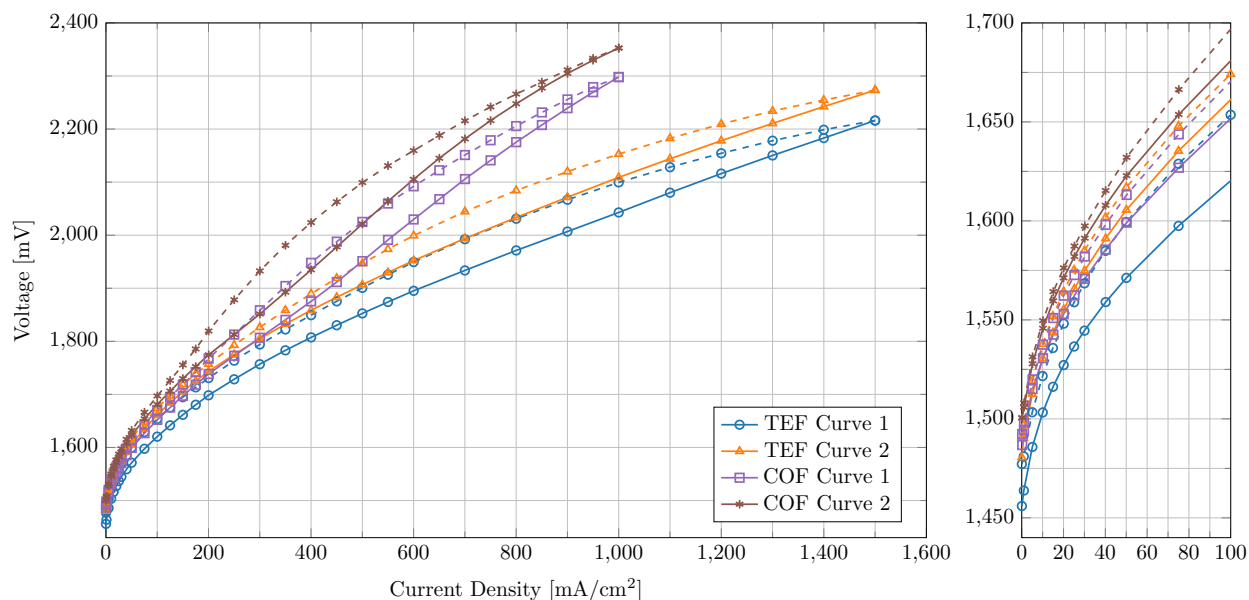


**Figure E.17** – Polarization curves measured on Cell 9 with TEF and COF configurations. Backward curves plotted with dashed lines.

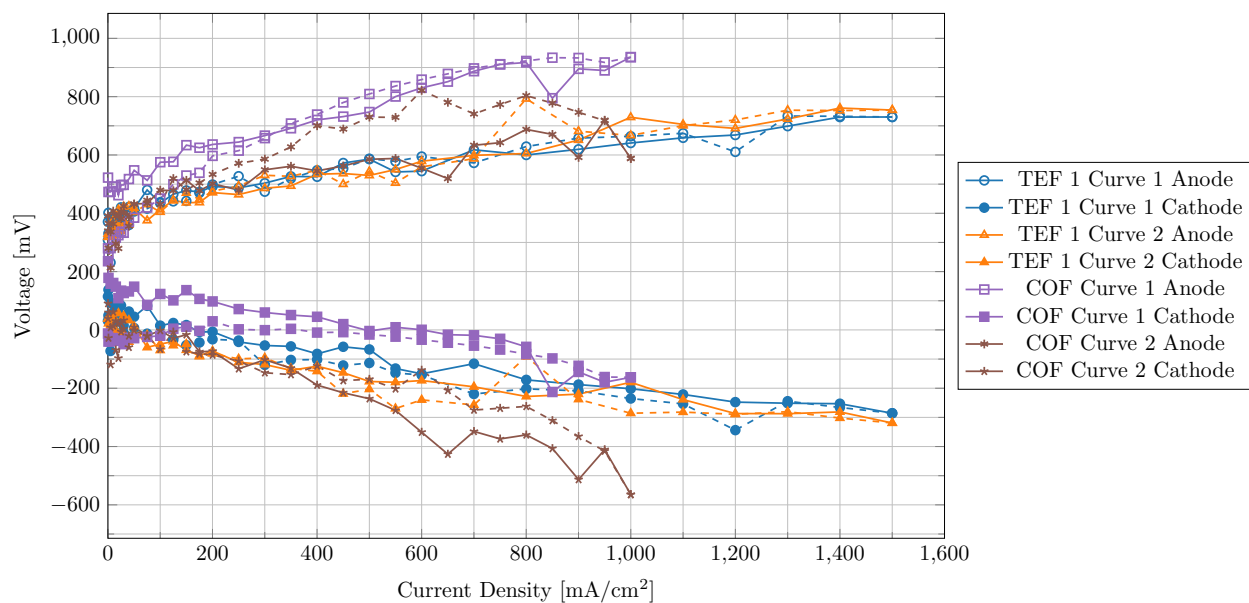


**Figure E.18** – Polarization curves of the separate anode and cathode overpotentials measured on Cell 9 with TEF and COF configurations. Backward curves plotted with dashed lines.

## E.4 Polarization Curve Voltage over Time Plots

Plots of the overpotential measured over time for forward sweeps of the the separate electrode, TEF polarization curves for Cells 6, 7, and 8 were provided in Figure 3.19 and discussed in the main body of this work. In this section, the same plots for the total cell voltage, as well as the backward sweeps of the separated electrode overpotentials are provided for comparison. All the same plots for Cell 9 are also provided here. These were not discussed in the main body as the reference electrode data was very noisy, although the general trends in the data can still be seen. Note that for the backward sweeps, the time scale continues from where the forward sweeps finish.

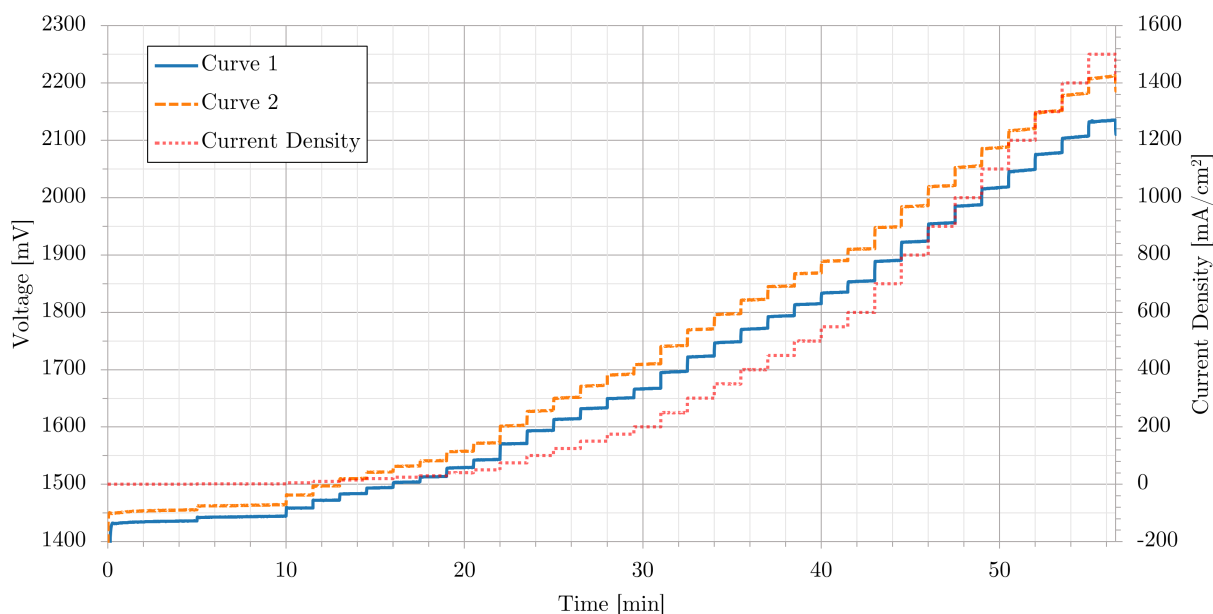


**Figure E.19** – Plot of the voltage versus time during the two TEF polarization curves (denoted “Curve 1” and “Curve 2”) run on Cell 6 (forward sweep).

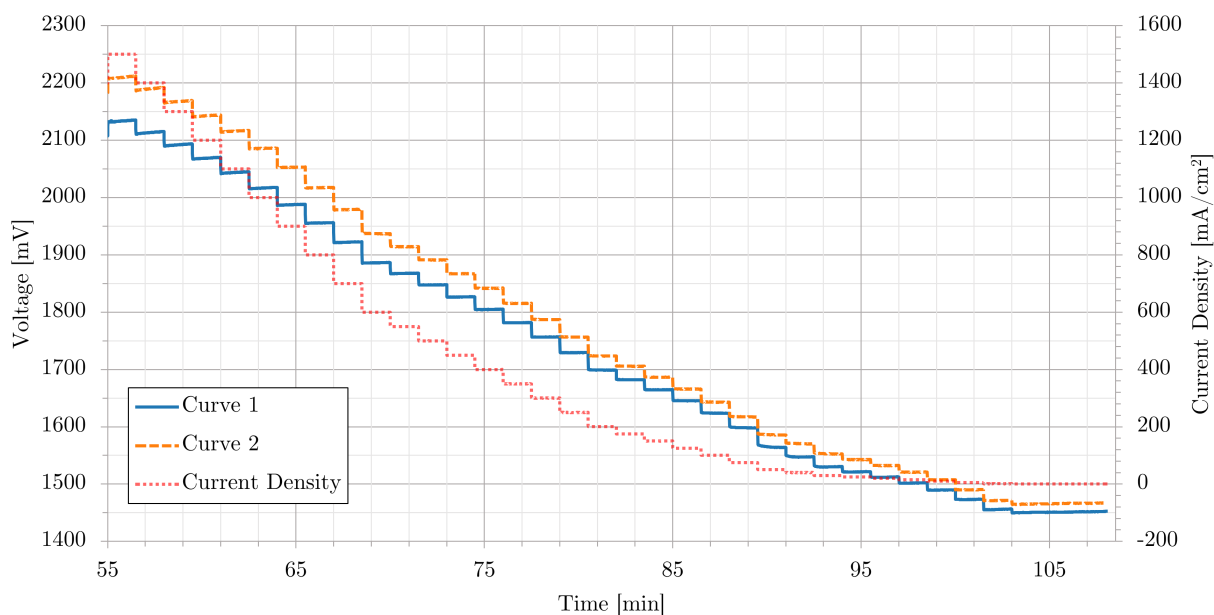


**Figure E.20** – Plot of the voltage versus time during the two TEF polarization curves (denoted “Curve 1” and “Curve 2”) run on Cell 6 (backward sweep).

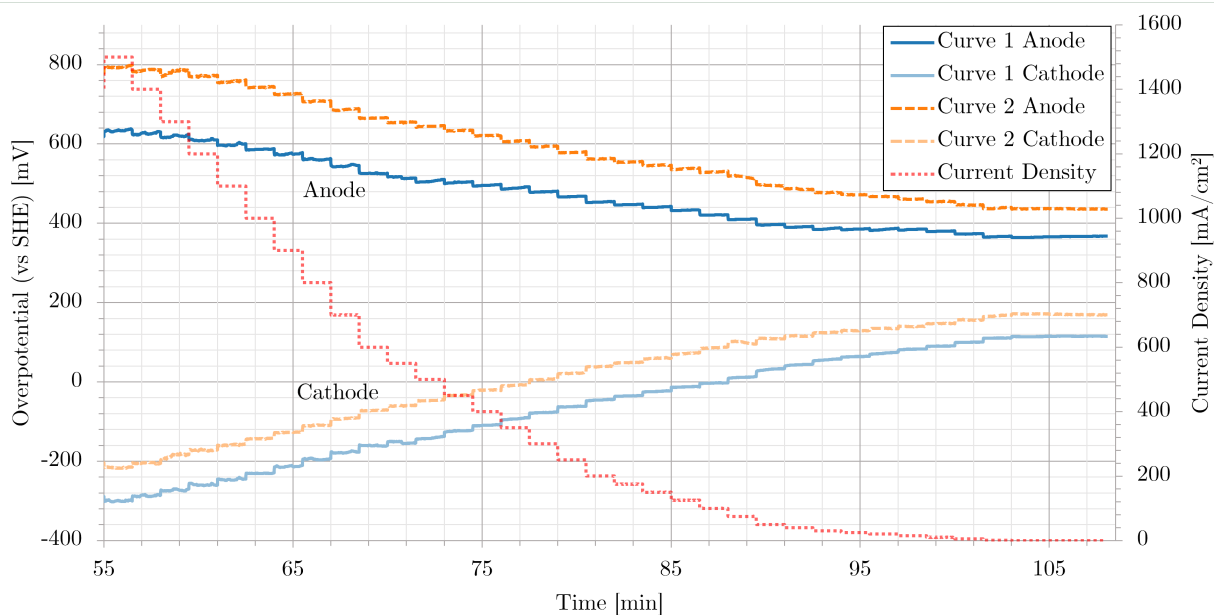


**Figure E.21** – Plot of the separated electrode overpotential versus time during the two TEF polarization curves (denoted “Curve 1” and “Curve 2”) run on Cell 6 (backward sweep).

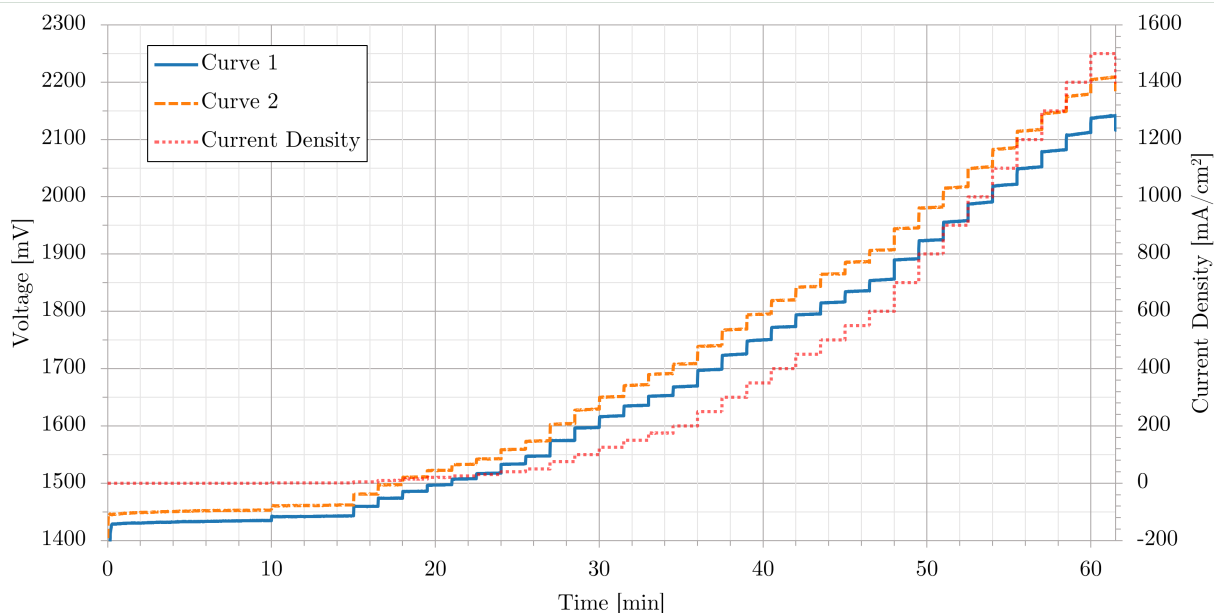


**Figure E.22** – Plot of the voltage versus time during the two TEF polarization curves (denoted “Curve 1” and “Curve 2”) run on Cell 7 (forward sweep).

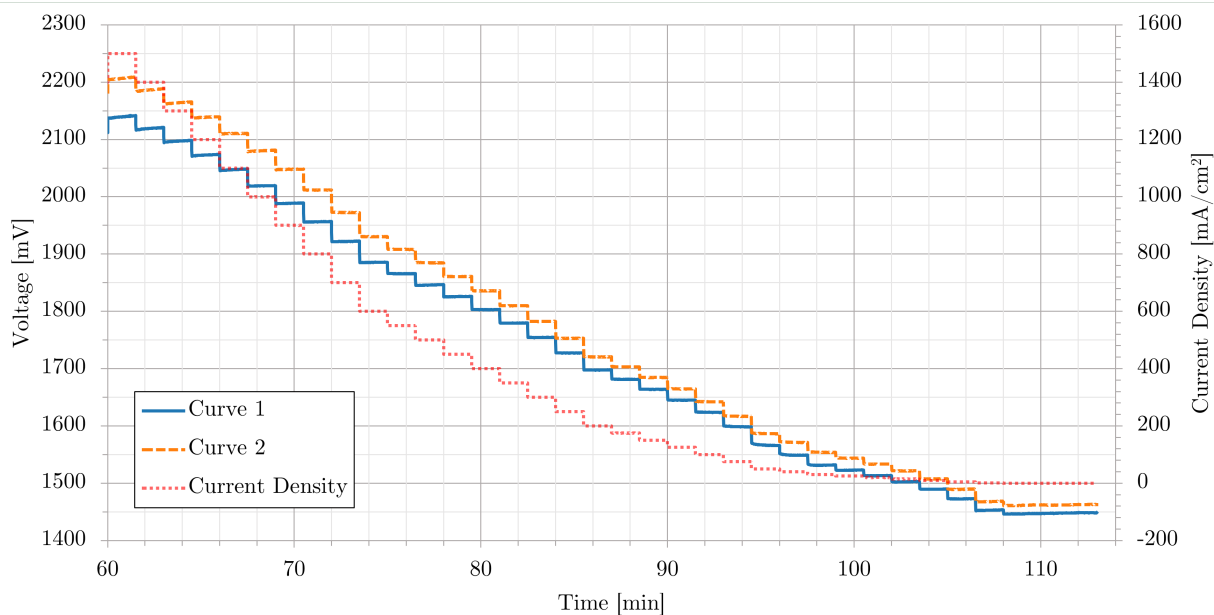


**Figure E.23** – Plot of the voltage versus time during the two TEF polarization curves (denoted “Curve 1” and “Curve 2”) run on Cell 7 (backward sweep).

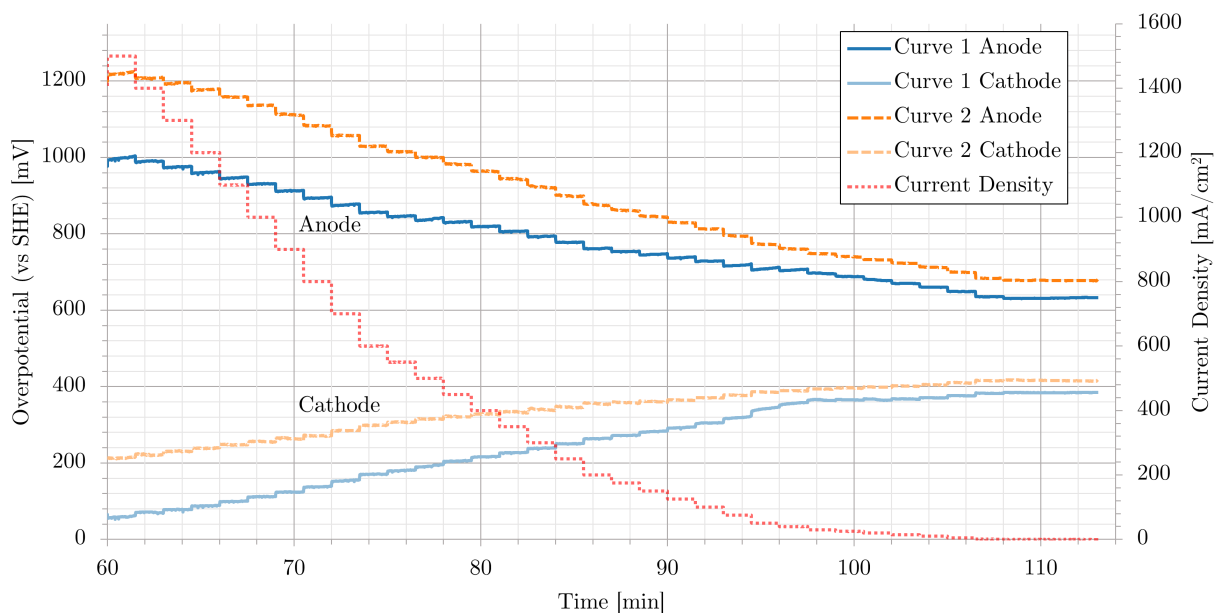


**Figure E.24** – Plot of the separated electrode overpotential versus time during the two TEF polarization curves (denoted “Curve 1” and “Curve 2”) run on Cell 7 (backward sweep).

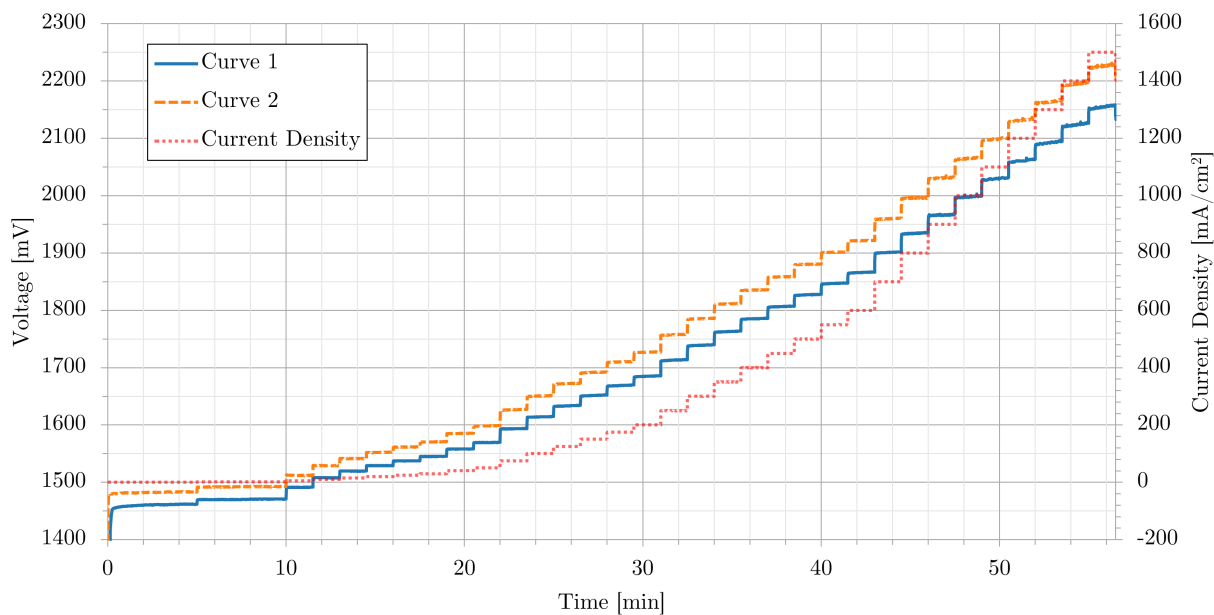


**Figure E.25** – Plot of the voltage versus time during the two TEF polarization curves (denoted “Curve 1” and “Curve 2”) run on Cell 8 (forward sweep).

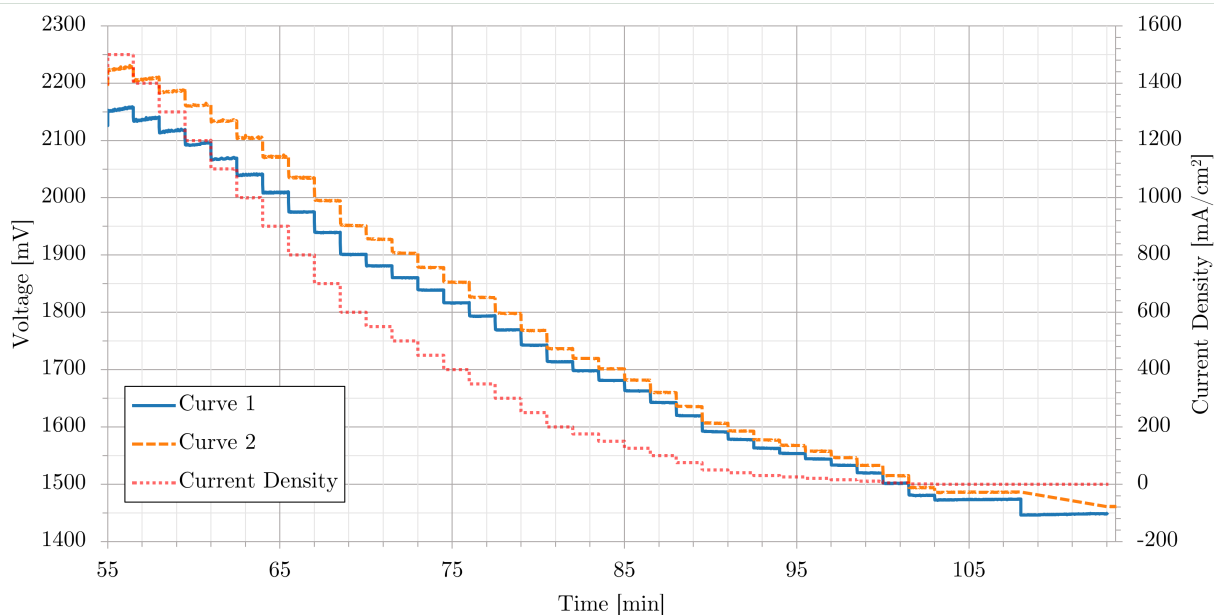


**Figure E.26** – Plot of the voltage versus time during the two TEF polarization curves (denoted “Curve 1” and “Curve 2”) run on Cell 8 (backward sweep).

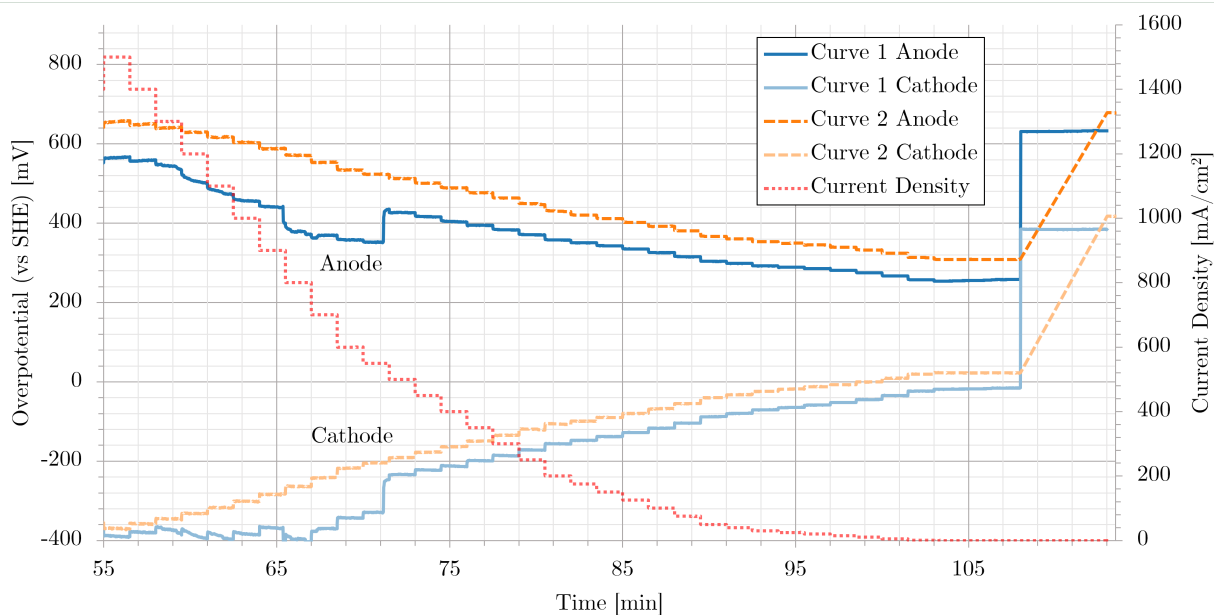


**Figure E.27** – Plot of the separated electrode overpotential versus time during the two TEF polarization curves (denoted “Curve 1” and “Curve 2”) run on Cell 8 (backward sweep).

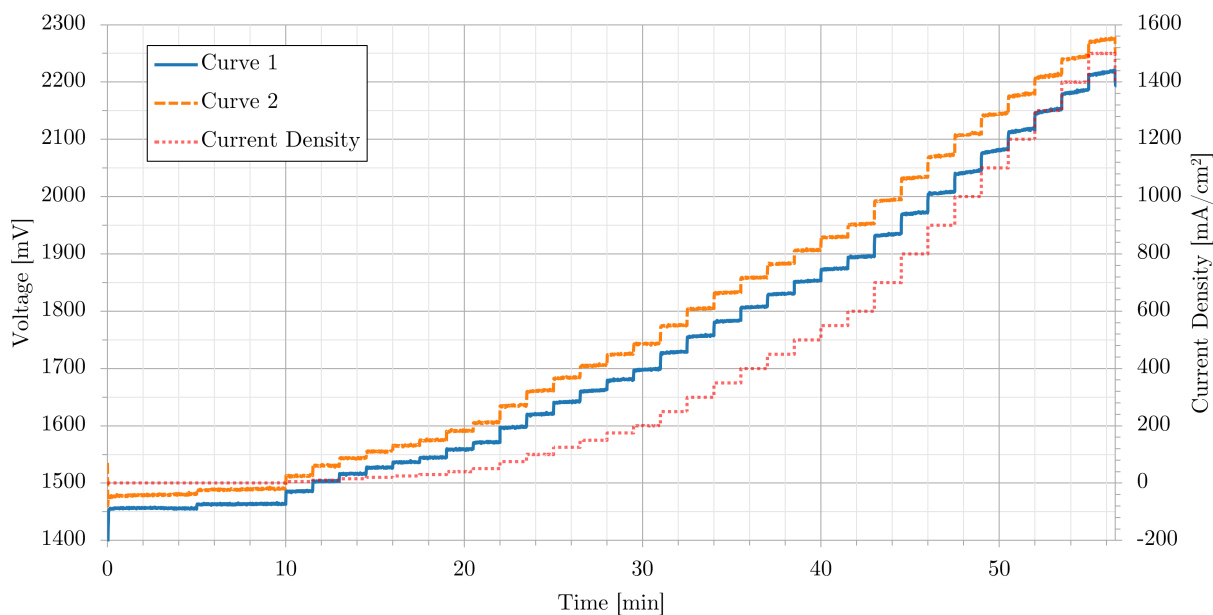


**Figure E.28** – Plot of the voltage versus time during the two TEF polarization curves (denoted “Curve 1” and “Curve 2”) run on Cell 9 (forward sweep).

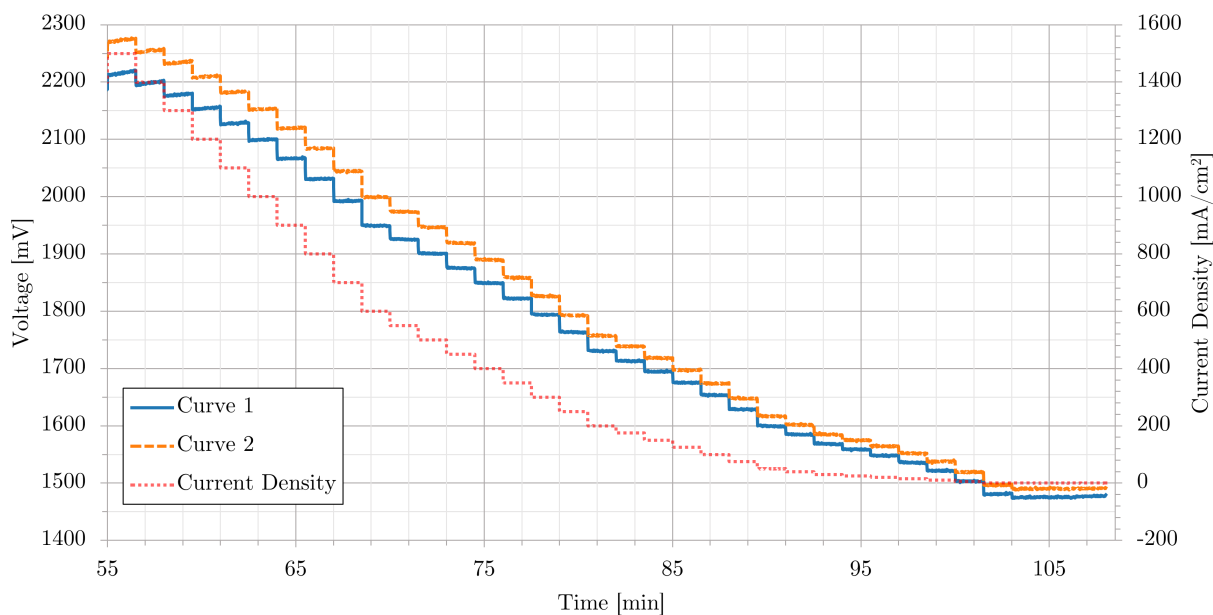


**Figure E.29** – Plot of the voltage versus time during the two TEF polarization curves (denoted “Curve 1” and “Curve 2”) run on Cell 9 (backward sweep).

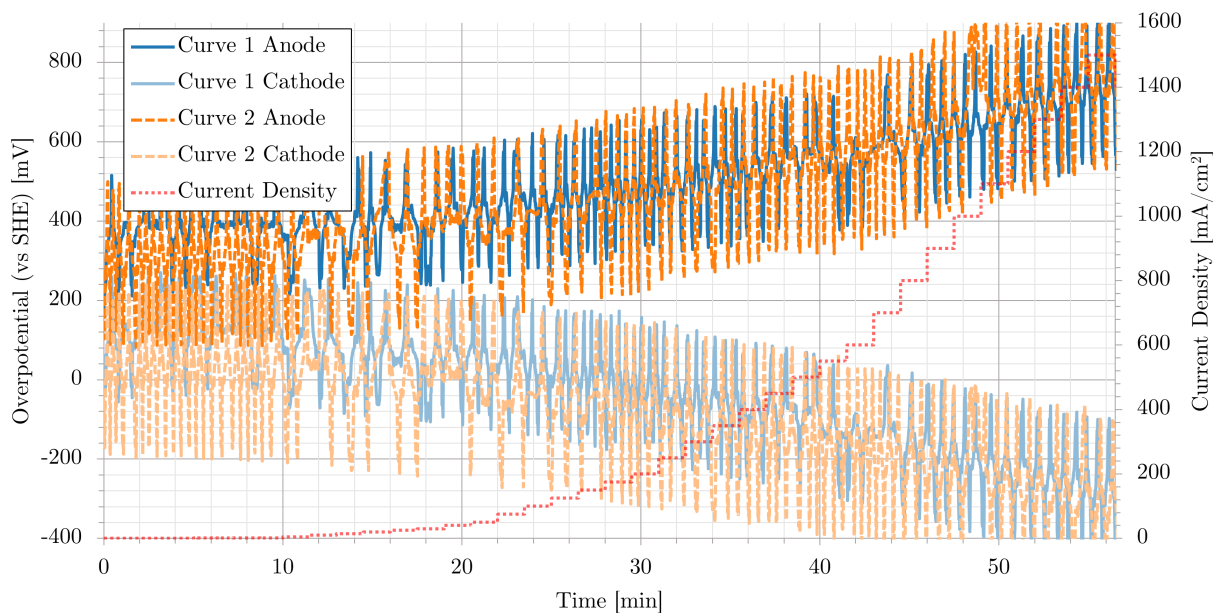


**Figure E.30** – Plot of the separated electrode overpotential versus time during the two TEF polarization curves (denoted “Curve 1” and “Curve 2”) run on Cell 9 (forward sweep).

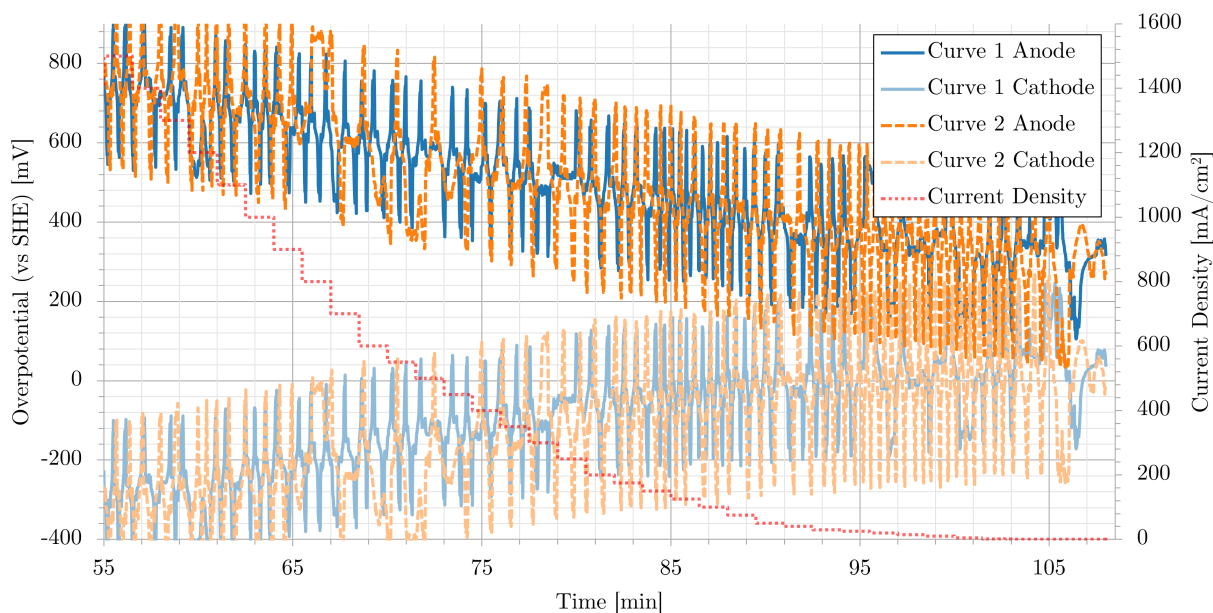


**Figure E.31** – Plot of the separated electrode overpotential versus time during the two TEF polarization curves (denoted “Curve 1” and “Curve 2”) run on Cell 9 (backward sweep).

## E.5 Individual HFR Measurements - measured between anode and cathode

This section contains the individual HFR measurements for Cells 2, 3, 4, 7, 8, and 9 discussed in this work. The individual HFR measurements for Cells 5 and 6 are provided in Table 3.7 and 3.13 in the main body, respectively. For Cells 6 to 9, the HFR measured for all tested feed methods is also provided.

**Table E.2** – HFR values obtained using equivalent circuit fits with the EIS measurements made on cell 2.

Current Density [mA/cm <sup>2</sup> ]	HFR [mΩ·cm <sup>2</sup> ]				Stability
	Curve 1	Curve 2	Curve 3	Curve 4	
20	157	155	157	157	158
300	157	157	158	159	150
600	153	151	152	154	152
Average	156	154	156	157	153

**Table E.3** – HFR values obtained using equivalent circuit fits with the EIS measurements made on cell 3.

Current Density [mA/cm <sup>2</sup> ]	HFR [mΩ·cm <sup>2</sup> ]				Stability
	Curve 1	Curve 2	Curve 3	Curve 4	
20	160	160	166	169	166
300	161	159	160	163	165
600	155	155	157	156	159
Average	158	158	161	163	163

**Table E.4** – HFR values obtained using equivalent circuit fits with the EIS measurements made on cell 4.

Current Density [mA/cm <sup>2</sup> ]	HFR [mΩ·cm <sup>2</sup> ]				Stability
	Curve 1	Curve 2	Curve 3	Curve 4	
20	109	108	107	112	117
300	111	111	114	114	119
600	111	111	110	108	117
Average	110	110	110	112	117

**Table E.5** – Total cell HFR values obtained using equivalent circuit fits with the EIS measurements made on cell 7.

Current Density [mA/cm <sup>2</sup> ]	HFR [mΩ·cm <sup>2</sup> ]		
	TEF Curve 1	TEF Curve 2	TEF Stability
20	94	101	96
150	103	104	106
300	103	103	101
600	97	101	102
1000	95	96	97
Average	98	101	100

	AOF Curve 1	AOF Curve 2	AOF Stability
20	95	96	96
150	100	96	96
300	96	97	94
600	92	85	96
1000	86	87	89
Average	94	92	94

	COF Curve 1	COF Curve 2	COF Stability
20	83	92	77
150	91	89	94
300	100	98	95
600	105	101	98
1000	105	103	93
Average	97	97	91

**Table E.6** – Total cell HFR values obtained using equivalent circuit fits with the EIS measurements made on cell 8.

Current Density [mA/cm <sup>2</sup> ]	HFR [mΩ·cm <sup>2</sup> ]		
	TEF Curve 1	TEF Curve 2	TEF Stability
20	99	101	94
150	106	107	106
300	107	106	109
600	106	105	111
1000	100	101	99
Average	104	104	104

	AOF Curve 1	AOF Curve 2	AOF Stability
20	106	99	87
150	99	101	102
300	99	99	100
600	95	94	91
1000	91	91	87
Average	98	97	94

	COF Curve 1	COF Curve 2	COF Stability
20	90	93	90
150	97	99	102
300	106	99	107
600	113	110	112
1000	114	107	114
Average	104	101	105

**Table E.7** – Total cell HFR values obtained using equivalent circuit fits with the EIS measurements made on cell 9.

Current Density [mA/cm <sup>2</sup> ]	HFR [mΩ·cm <sup>2</sup> ]		
	TEF Curve 1	TEF Curve 2	TEF Stability
20	101	91	109
150	102	104	102
300	104	100	112
600	108	106	109
1000	103	103	105
Average	104	101	107

	COF Curve 1	COF Curve 2	COF Stability
20	96	91	96
150	107	101	98
300	98	111	109
600	111	110	109
1000	113	109	110
Average	105	104	104

## E.6 Individual HFR Measurements - measured between one electrode and reference electrode

This section contains the individual HFR measurements made between the anode or cathode and the reference electrode for Cells 6, 7, and 8 discussed in this work. The individual HFR measurements for Cell 5 are provided in Table 3.7 in the main body. Results for Cell 9 are not presented here as EIS measurements between the anode/cathode and reference electrode were too noisy to obtain consistent HFR values.

**Table E.8** – Separate anode and cathode HFR values obtained using equivalent circuit fits with the EIS measurements made on Cell 6.

Measurement Between Anode and Reference Electrode			
Current Density [mA/cm <sup>2</sup> ]	HFR [mΩ·cm <sup>2</sup> ]		
	TEF Curve 1	TEF Curve 2	TEF Stability
20	79	78	76
150	70	76	80
300	70	76	81
600	70	73	79
1000	68	78	76
Average	71	76	78

Measurement Between Cathode and Reference Electrode			
Current Density [mA/cm <sup>2</sup> ]	HFR [mΩ·cm <sup>2</sup> ]		
	TEF Curve 1	TEF Curve 2	TEF Stability
20	23	35	19
150	30	24	21
300	29	27	26
600	25	24	19
1000	28	25	25
Average	27	27	22

**Table E.9** – Separate anode and cathode HFR values obtained using equivalent circuit fits with the EIS measurements made on Cell 7.

Measurement Between Anode and Reference Electrode			
Current Density [mA/cm <sup>2</sup> ]	HFR [mΩ·cm <sup>2</sup> ]		
	TEF Curve 1	TEF Curve 2	TEF Stability
20	100	104	100
150	97	100	97
300	93	94	97
600	91	95	93
1000	90	99	97
Average	94	98	97

Measurement Between Cathode and Reference Electrode			
Current Density [mA/cm <sup>2</sup> ]	HFR [mΩ·cm <sup>2</sup> ]		
	TEF Curve 1	TEF Curve 2	TEF Stability
20	16	9	8
150	16	11	12
300	8	9	13
600	7	12	12
1000	12	5	10
Average	12	9	11

**Table E.10** – Separate anode and cathode HFR values obtained using equivalent circuit fits with the EIS measurements made on Cell 8.

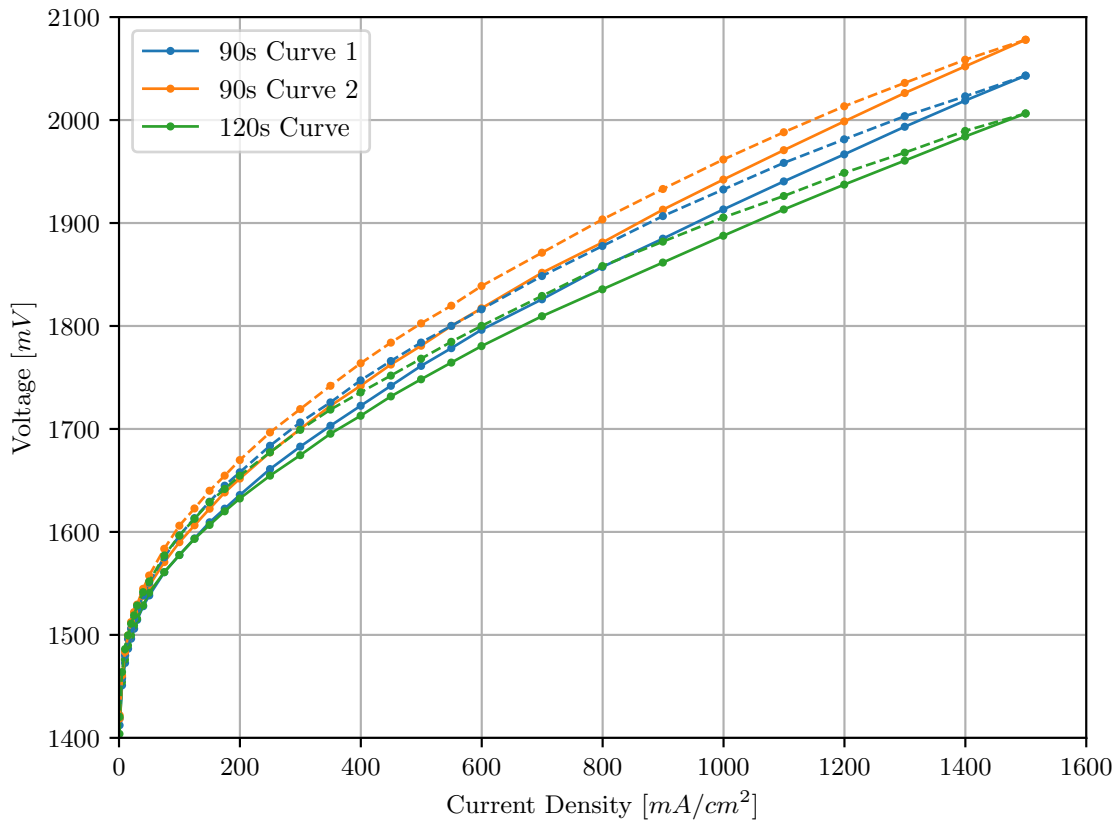
Measurement Between Anode and Reference Electrode			
Current Density [mA/cm <sup>2</sup> ]	HFR [mΩ·cm <sup>2</sup> ]		
	TEF Curve 1	TEF Curve 2	TEF Stability
20	53	67	42
150	42	73	57
300	41	59	50
600	45	57	46
1000	52	59	40
Average	47	63	47

Measurement Between Cathode and Reference Electrode			
Current Density [mA/cm <sup>2</sup> ]	HFR [mΩ·cm <sup>2</sup> ]		
	TEF Curve 1	TEF Curve 2	TEF Stability
20	57	48	58
150	56	50	53
300	58	49	46
600	52	44	44
1000	42	39	41
Average	53	46	48

## E.7 Polarization Curve Step Time Test

Polarization curves were run using both 90 and 120 second steps to understand if this would change the results of the polarization curves. These curves are provided in Figure E.32, and show that there was minimal difference in the polarization curves based on the scan rate, as the difference between the first 90 second curve and the 120 second curve is similar to the difference between the two 90 second curves.



**Figure E.32** – Comparison between the results of 90 and 120 second polarization curve step lengths on the same cell.

## E.8 Stability Tests with the Reference Electrode

Stability tests were performed following polarization curves for each feed method cell, the reference electrode was also used along with these tests to separate the electrode overpotentials. The results of the stability tests with TEF (Figure E.33) were consistent for the total cell voltage, but the separated electrode overpotentials were not and drifted quite a bit throughout the tests. Initially, there was quite a large spread in the overpotentials, however over time they did begin to convert and stabilize. Over time, the poor measurements from Cell 7 become reasonable, and those of Cell 6 and 9 drifted higher, out of the expected range. By the end of the six hours they were within about 100 mV of each other, although the Cell 6 results were higher than expected. The cathode overpotential for Cell 6 also became positive, which should not be possible, as that would mean oxidation was occurring there, and as the cell was still operating nominally, these results must be erroneous, or the measured values drifted due to some effect of cell operation.

The results from Cell 9 are also provided here, although just like for the polarization curves, the reference electrode data was very noisy. Still, there is a visible trend in the data. The anode and cathode overpotentials begin between those of Cells 7 and 8 before rising and falling twice. This resulted in the cathode overpotential sometimes reaching positive values. There was obviously quite a bit of error in these measurements, possibly caused by a dry-out of the unreinforced membrane strip over the long operational period. This error was so large that just before the 175 min mark, the potentiostat automatically stopped cell operation due to a spike in the reference electrode measurement, and the test had to be restarted, which is why there is a sudden drop in the overall cell voltage at this point.

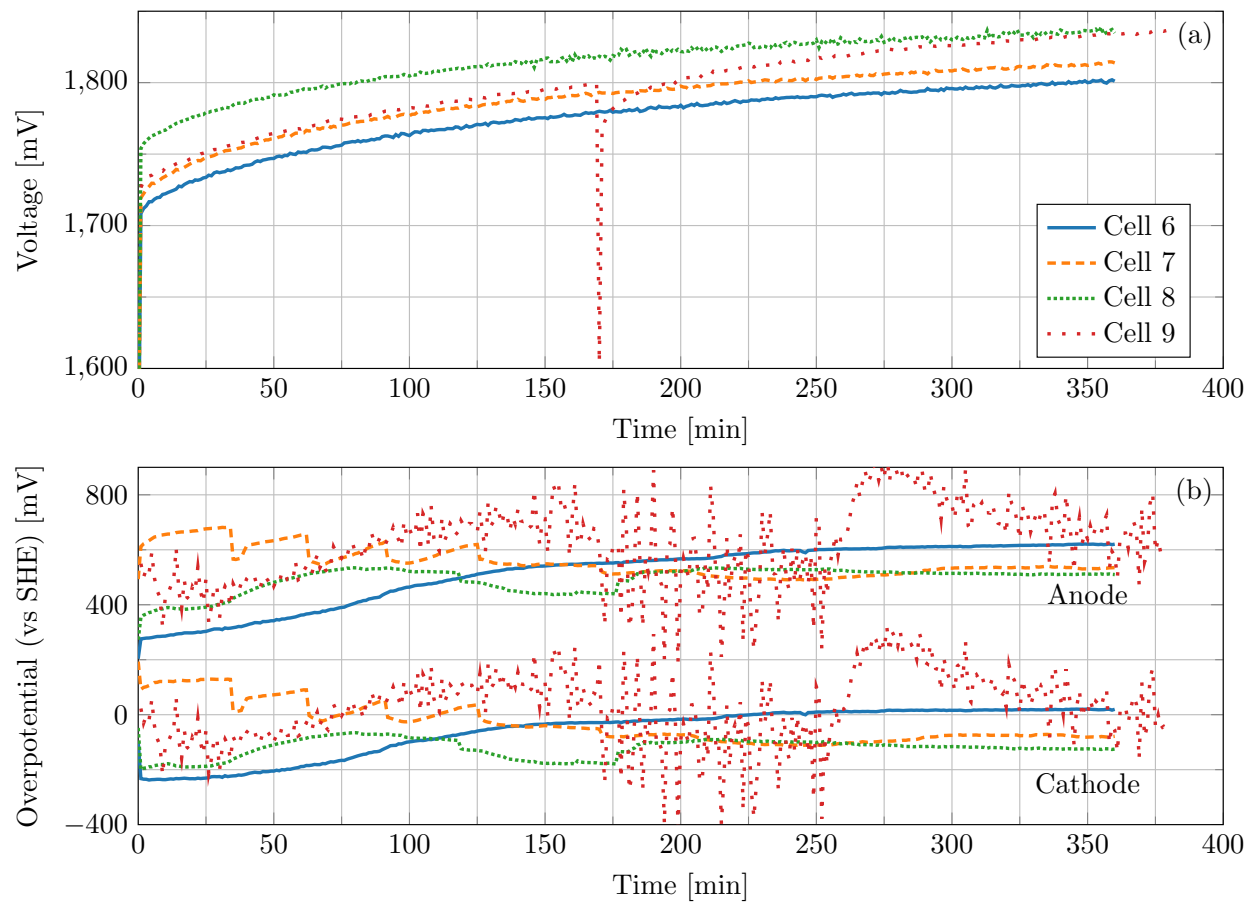


**Figure E.33** – Stability test results for the feed method cells with electrolyte feed to both electrodes. Tests were run at a constant  $300 \text{ mA/cm}^2$  for 6 hours. (a) Total cell potential. (b) Separated electrode overpotentials.

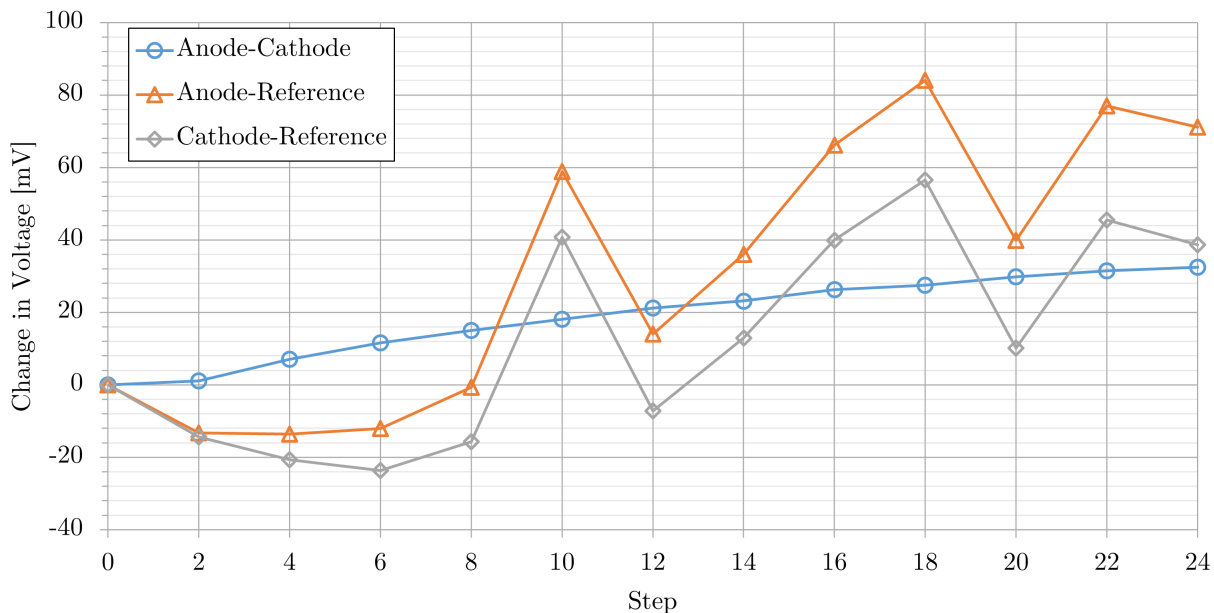


**Figure E.34** – Change in the average voltage measured on Cell 9 for the 10 mA/cm<sup>2</sup> current holds for the OCV drift test following the profile in Table E.11.

An experiment was run on Cell 9 to test the hypothesis that the value of  $E^{eq}$  changed over time, specifically at the anode as the anode versus reference electrode potential was measured directly. If this was the case, it could explain the drift in the reference electrode measurements during the stability tests. This test consisted of twelve 30 minute, 1000 mA/cm<sup>2</sup> current holds, each followed by a 5 minute, 10 mA/cm<sup>2</sup> current hold (test profile in Table E.11), with the resulting change in voltage of the 10 mA/cm<sup>2</sup> holds provided in Figure E.34 (Note that the steps in the figure are numbered based on their respective step in Table E.11). The voltage measurements of the anode during these lower current holds was analysed to try and observe the drift in the reference electrode measurements. As demonstrated by these results, over the test period, the measured anode and cathode potentials with respect to the reference electrode increased more than the cell voltage. This means that there must have been an effect caused by more than just the expected degradation of the cell performance. This confirms the idea that the potential measured between the anode and reference electrode drifted over time, likely due to a change in OH<sup>-</sup> concentration during cell operation. The observed drift however, was quite small at about 40 mV more than the change in cell potential, small than the about 100 mV drift observed during the stability tests. When performing stability tests on AEMWE cells in future, it would be useful to perform these short 10 mA/cm<sup>2</sup> holds before and after the tests to observe any change in OCV that may have occurred.

**Table E.11** – Test profile used to characterize the drift in OCV on Cell 9.

Step	Time [min]	Current Density [mA/cm <sup>2</sup> ]
0	5	10
1	30	1000
2	5	10
3	30	1000
4	5	10
5	30	1000
6	5	10
7	30	1000
8	5	10
9	30	1000
10	5	10
11	30	1000
12	5	10
13	30	1000
14	5	10
15	30	1000
16	5	10
17	30	1000
18	5	10
19	30	1000
20	5	10
21	30	1000
22	5	10
23	30	1000
24	5	10

## E.9 Cell Component Resistance Measurements

The resistance of the cell components, not including the CCMs, used in the AEMWE cells in this work was measured so that the resistance of just the CCMs could be calculated as  $R_{CCM} = HFR - R_{components}$ . Cell component resistance was measured by assembling cells without a CCM, applying a current to the cell, and measuring the voltage. Tests were run for both configurations used for the repeatability cells and these results were then plotted in Figure E.35. The slope of these results was taken as the resistance of the cell components,  $R_{components}$ . In order to achieve a similar level of compression to the actual cells, three sheets of 75  $\mu\text{m}$  thick copper foil was used in place of the membrane to fill space while providing minimal resistance.

Based on the slopes of the resulting data, the cell component resistance was  $5.32 \text{ m}\Omega\cdot\text{cm}^2$  when using the titanium bipolar plates and  $1.51 \text{ m}\Omega\cdot\text{cm}^2$  when using the nickel 400 bipolar plates. The switch from titanium to nickel 400 bipolar plates therefore led to a small reduction in the area-specific resistance.

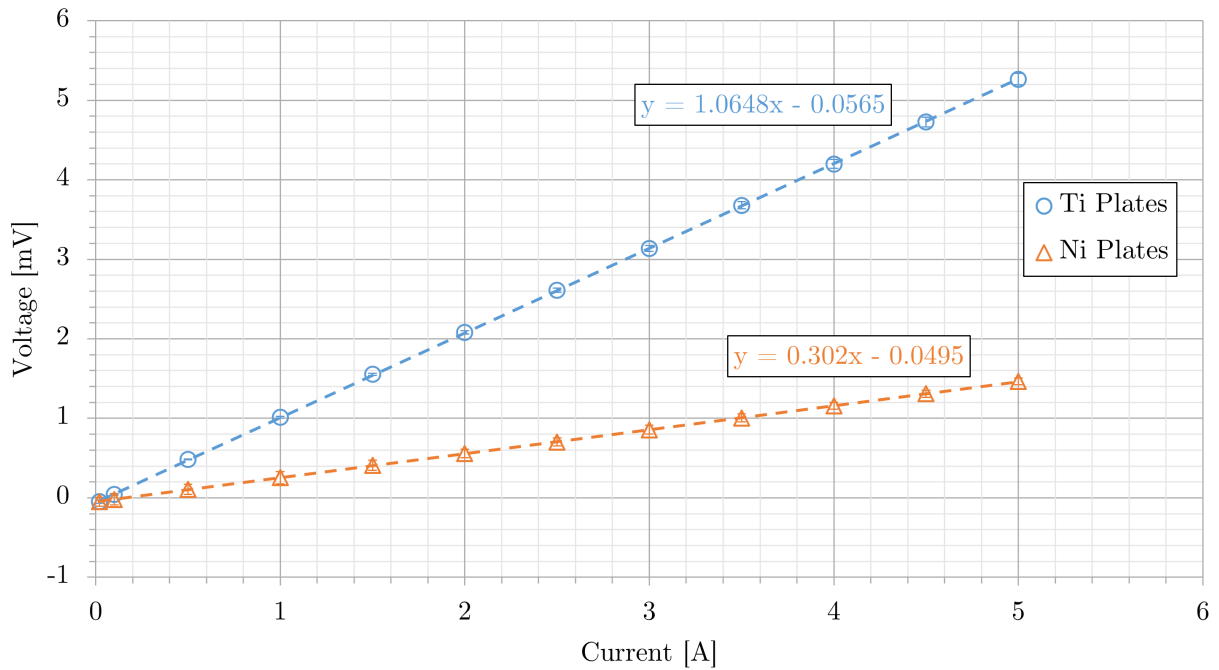


**Figure E.35** – Cell component resistance tests performed by assembling cells without a CCM and applying a series of current holds.

## E.10 Electrochemically Active Surface Area Measurements

Cyclic voltammetry tests (scan rate of 40 mV/s) were run on cells 6 through 8 discussed in this work in order to calculate the electrochemically active surface area (ECSA) of these cells. Measurements were also made before and after characterization for each cell. Note that the “pre-test” measurements were made following cell conditioning and before the first polarization curve. The methods covered by Tan et al. [111] were followed to calculate the ECSA, and the potential range of 0.4 V to 1.25 V of the cyclic voltammetry measurements was used.

**Table E.12** – ECSA values calculated for the feed method cells using cyclic voltammetry measurements.

Test	ECSA (m <sup>2</sup> /g)
Cell 6 Pre-Test	2.18
Cell 6 Post-Test	5.25
Cell 7 Pre-Test	1.50
Cell 7 Post-Test	1.02
Cell 8 Pre-Test	2.31
Cell 8 Post-Test	1.94

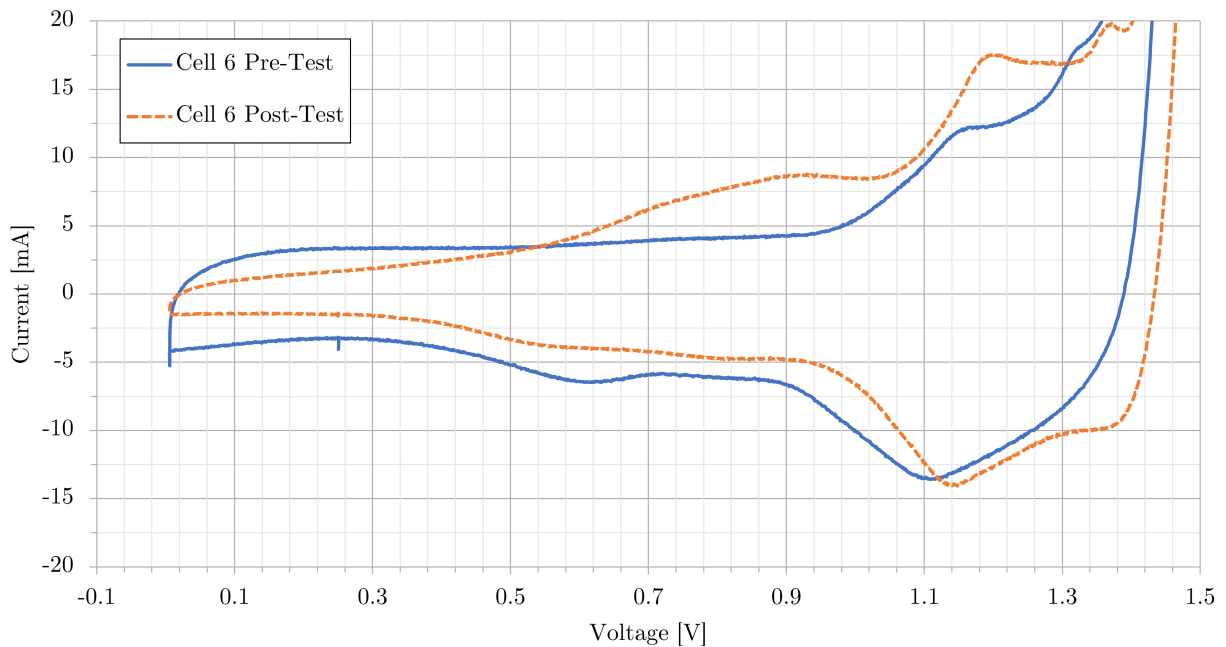


**Figure E.36** – Cyclic voltammetry measurements run on Cell 6 before and after characterization.

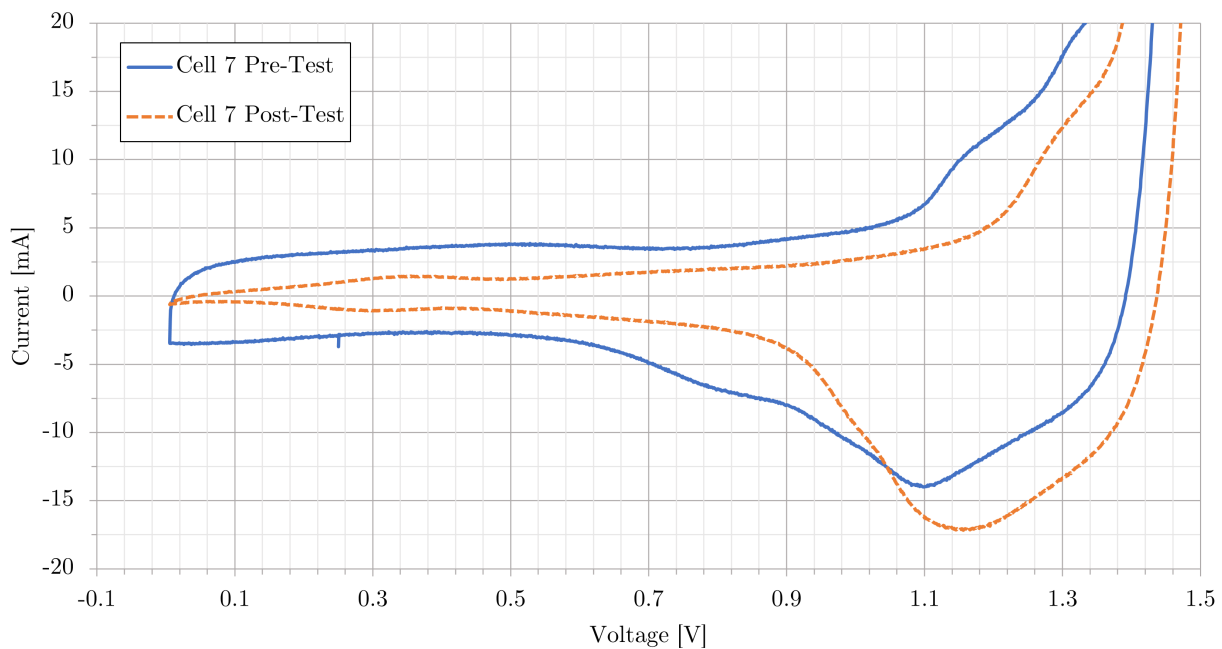


**Figure E.37** – Cyclic voltammety measurements run on Cell 7 before and after characterization.

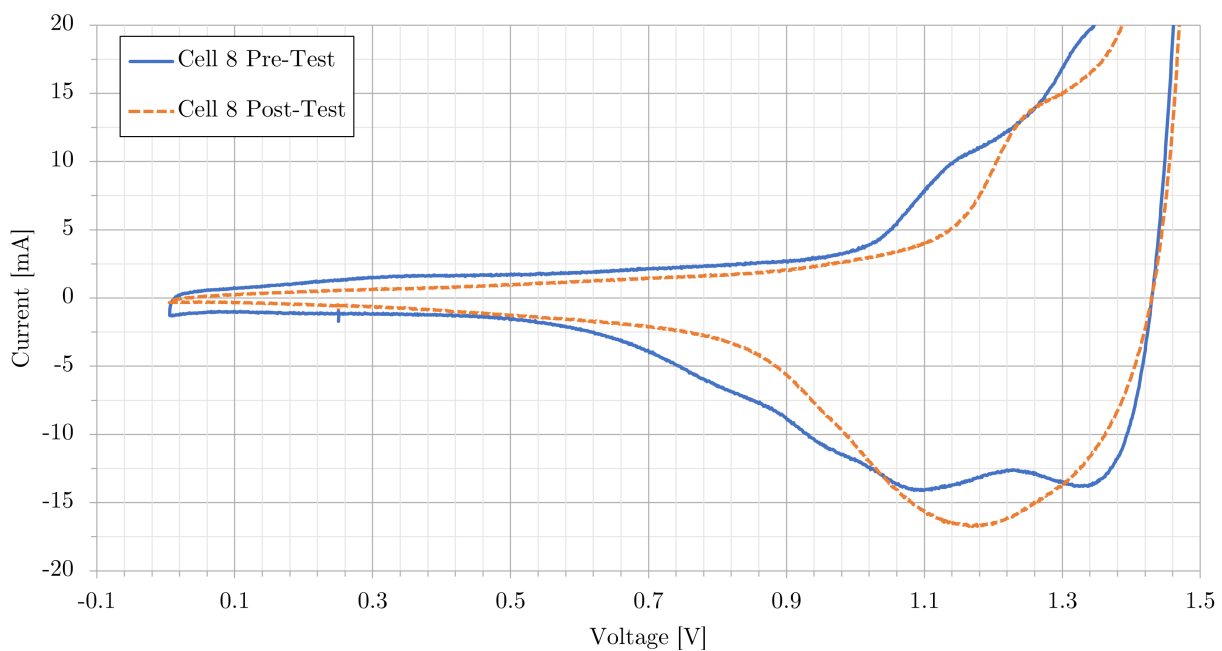


**Figure E.38** – Cyclic voltammety measurements run on Cell 8 before and after characterization.